



HAL
open science

SiGe photonics circuits exploiting nonlinear optics and electro-optic effects in the mid-infrared

Miguel Montesinos Ballester

► **To cite this version:**

Miguel Montesinos Ballester. SiGe photonics circuits exploiting nonlinear optics and electro-optic effects in the mid-infrared. Optics / Photonics. Université Paris-Saclay, 2021. English. NNT : 2021UPAST119 . tel-03483165

HAL Id: tel-03483165

<https://theses.hal.science/tel-03483165>

Submitted on 16 Dec 2021

HAL is a multi-disciplinary open access archive for the deposit and dissemination of scientific research documents, whether they are published or not. The documents may come from teaching and research institutions in France or abroad, or from public or private research centers.

L'archive ouverte pluridisciplinaire **HAL**, est destinée au dépôt et à la diffusion de documents scientifiques de niveau recherche, publiés ou non, émanant des établissements d'enseignement et de recherche français ou étrangers, des laboratoires publics ou privés.

SiGe photonics circuits
exploiting nonlinear optics and
electro-optic effects in the
mid-infrared

*Circuits photoniques SiGe exploitant
l'optique non linéaire et les effets
électro-optiques dans l'infrarouge moyen*

Thèse de doctorat de l'université Paris-Saclay

École doctorale n° 575,
Electrical, Optical, Bio-physics and Engineering (EOBE)
Spécialité de doctorat: électronique et optoélectronique, nano-
et microtechnologies
Unité de recherche: université Paris-Saclay, CNRS, Centre de
Nanosciences et de Nanotechnologies, 91120, Palaiseau, France
Réfèrent: faculté des sciences d'Orsay

**Thèse présentée et soutenue à Paris-Saclay,
le 10 Novembre 2021, par**

Miguel MONTESINOS BALLESTER

Composition du jury:

Jean-Jacques Greffet Professeur, Laboratoire Charles Fabry – IOGS	Président
Guy Millot Professeur, Université de Bourgogne Franche-Comté – ICB	Rapporteur & Examineur
Jean-Baptiste Rodriguez Chargé de recherche (HDR), CNRS – IES	Rapporteur & Examineur
Jérôme Faist Professeur, ETH Zürich – IQE	Examineur

Direction de la thèse:

Delphine Marris-Morini Professeur, Université Paris-Saclay – C2N	Directrice de thèse
Carlos Alonso-Ramos Chargé de recherche, CNRS – C2N	Co-Encadrant

Synthèse en français

Introduction

La gamme spectrale de l'infrarouge moyen (MIR), communément définie entre 2 et 20 μm de longueur d'onde, a suscité un grand intérêt au cours des deux dernières décennies, en raison de ses caractéristiques uniques pour la détection et la sécurité. D'une part, la région de 3 à 13 μm de longueur d'onde (aussi appelée « fingerprint region ») permet une détection à haute sensibilité de la plupart des molécules, grâce à leur mode de vibration fondamentaux qui conduisent à des lignes d'absorption spécifiques dans cette gamme spectrale. D'autre part, le MIR contient également deux fenêtres de transparence atmosphérique (3-5 et 8-14 μm de longueur d'onde), qui se superposent également aux radiations thermiques. Par conséquent, le MIR présente un intérêt considérable pour de multiples applications à fort impact.

En particulier, cette thèse a principalement visé les applications de détection. Bien que des capteurs à large bande et à haute résolution soient déjà disponibles, ils se basent sur une configuration en espace libre, devenant ainsi volumineux et coûteux, et ne sont appropriés que pour l'industrie et les laboratoires. Par conséquent, l'intégration sur puce de capteurs MIR permettrait d'obtenir des dispositifs compacts et économiques qui pourraient être largement utilisés dans une myriade d'applications.

Plateforme MIR à large bande

Plusieurs plates-formes intégrées ont été développées au cours des deux dernières décennies, parmi lesquelles les plates-formes à base de Si et Ge qui sont une approche intéressante pour fournir des dispositifs compacts, fonctionnant dans une large gamme de spectre MIR. En particulier, cette thèse s'appuie sur des travaux antérieurs réalisés à partir de guides d'onde SiGe à gradient d'indice (Fig. 1(a)), dans lesquels différents dispositifs passifs ont déjà été démontrés.

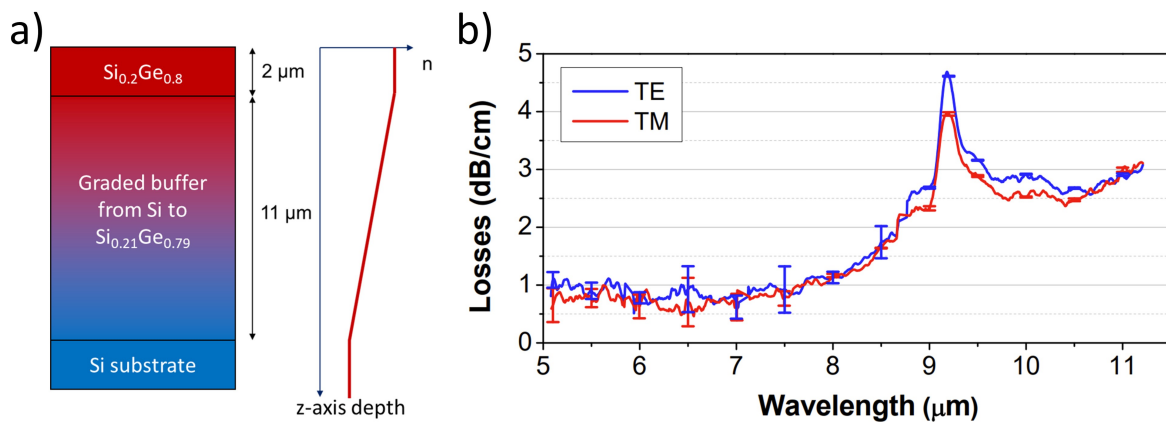


Figure 1: (a) Schéma de la plate-forme à gradient d'indice et profil d'indice de réfraction en fonction de sa profondeur. (b) Pertes de propagation en fonction de la longueur d'onde pour les polarisations TE et TM obtenues expérimentalement par la méthode du cut-back.

À cet effet, j'ai développé et optimisé un nouveau processus de fabrication, permettant d'obtenir des profils de guides d'ondes relativement profonds ($> 4 \mu\text{m}$) pour améliorer le confinement optique aux plus grandes longueurs d'onde. Comme on peut observer sur la Fig. 1(b), de pertes de propagation inférieures à 4.6 dB/cm sont obtenues de 5 à 11 μm de longueur d'onde, qui sont compatibles avec la plupart des applications MIR intégrées. Comme le montre la Fig. 2, j'ai également procédé à la caractérisation expérimentale de deux dispositifs MZI, confirmant ainsi les performances à large bande de cette plateforme.

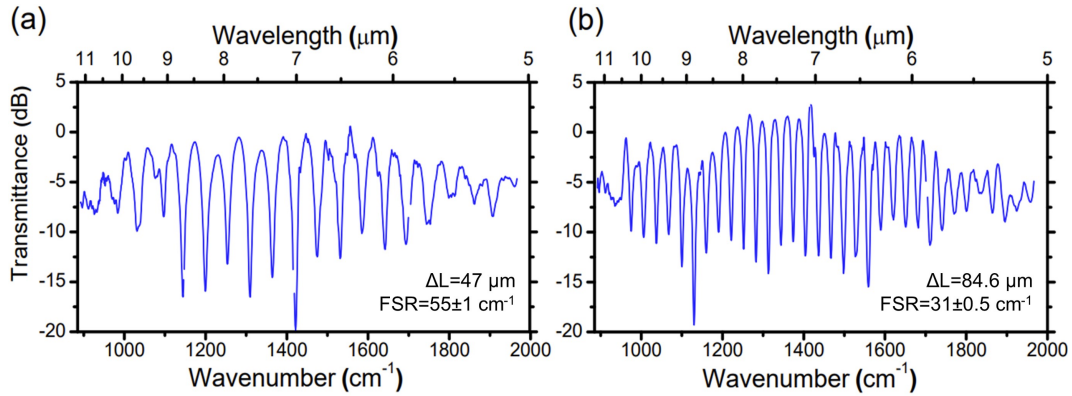


Figure 2: Transmission optique normalisée en polarisation TM en fonction de la longueur d'onde (axe des x du haut) ou du nombre d'onde (axe des x du bas) de deux MZI asymétriques avec un déséquilibre de bras de (a) 47 μm et (b) 84.6 μm . Un filtre de Savitzky-Golay d'ordre 4 avec une fenêtre de 100 nm est appliqué.

Ensuite, pour progresser vers une plateforme MIR plus complète, j'aborde dans ce manuscrit le développement des trois importants composants actifs et non linéaires, en fournissant également leur modèle numérique.

Spectromètre intégré

Tout d'abord, j'aborde une approche de spectromètre intégré basée sur une configuration hétérodyne spatiale, dans laquelle j'accorde thermiquement le déséquilibre du retard du chemin pour surmonter le compromis classique entre la résolution, la largeur de bande opérationnelle et le nombre de structures interférométriques requises. Comme je le montre dans les équations ci-dessous, la largeur de bande opérationnelle peut être multipliée par le nombre de températures mesurées (N_T), tout en gardant le même nombre de dispositifs (N_L) et même en améliorant légèrement la résolution. Pour démontrer expérimentalement l'avantage de cette approche, j'ai fabriqué et caractérisé ce spectromètre intégré. Comme on peut le voir sur la Fig. 3, contrairement à ce qui se passe lorsqu'aucun ajustement thermique n'est effectué, un signal d'entrée monochromatique peut être correctement récupéré dans toute la gamme spectrale caractérisée, et une amélioration du rapport signal-bruit est également observée. Ces résultats facilitent la mise en oeuvre de spectromètres compacts et robustes fonctionnant dans la région des empreintes digitales du MIR.

$$resolution = \frac{1}{\Delta L_{max} n_g + L_H \Delta n_{g,T,max}} \quad [cm^{-1}]$$

$$bande\ passante = \frac{1}{\Delta L_{max} n_g + L_H \Delta n_{g,T,max}} \frac{N_T N_L}{2} \quad [cm^{-1}]$$

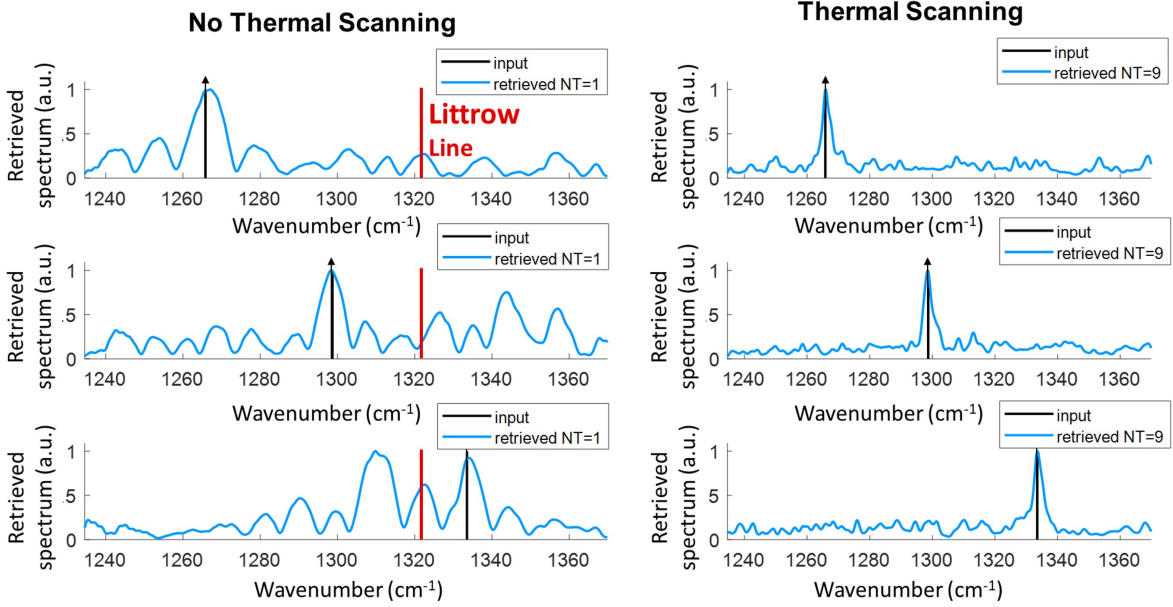


Figure 3: Densité du spectre de puissance expérimental (PSD) récupéré pour une entrée monochromatique à trois positions différentes de 7.3 à 8.1 μm de longueur d’onde, représentée par une flèche noire verticale: (a) lorsqu’aucun balayage thermique n’est mis en oeuvre ($N_T = 1$) et (b) pour neuf mesures à différentes de température ($N_T = 9$).

Génération de supercontinuum

Ensuite, je tire parti des phénomènes non linéaires, et en particulier de la génération de supercontinuum (SCG), pour étendre la gamme de spectre couverte par un seul dispositif. À cet égard, j’ai modélisé ce phénomène SCG et caractérisé expérimentalement sa génération avec différentes puissances de pompe et longueurs d’onde. Comme le montre la Fig. 4, je rapporte dans ce manuscrit une expansion de 2 octaves, allant d’une longueur d’onde de 3 à 13 μm , et en utilisant un guide d’onde en SiGe graduel de 5.5 mm de long. Cette démonstration expérimentale est deux fois plus large que les travaux précédents rapportés dans la littérature, fournissant une source MIR large bande, cohérente et compacte, et ouvrant des perspectives passionnantes pour la détection simultanée de multiples molécules sur puce.

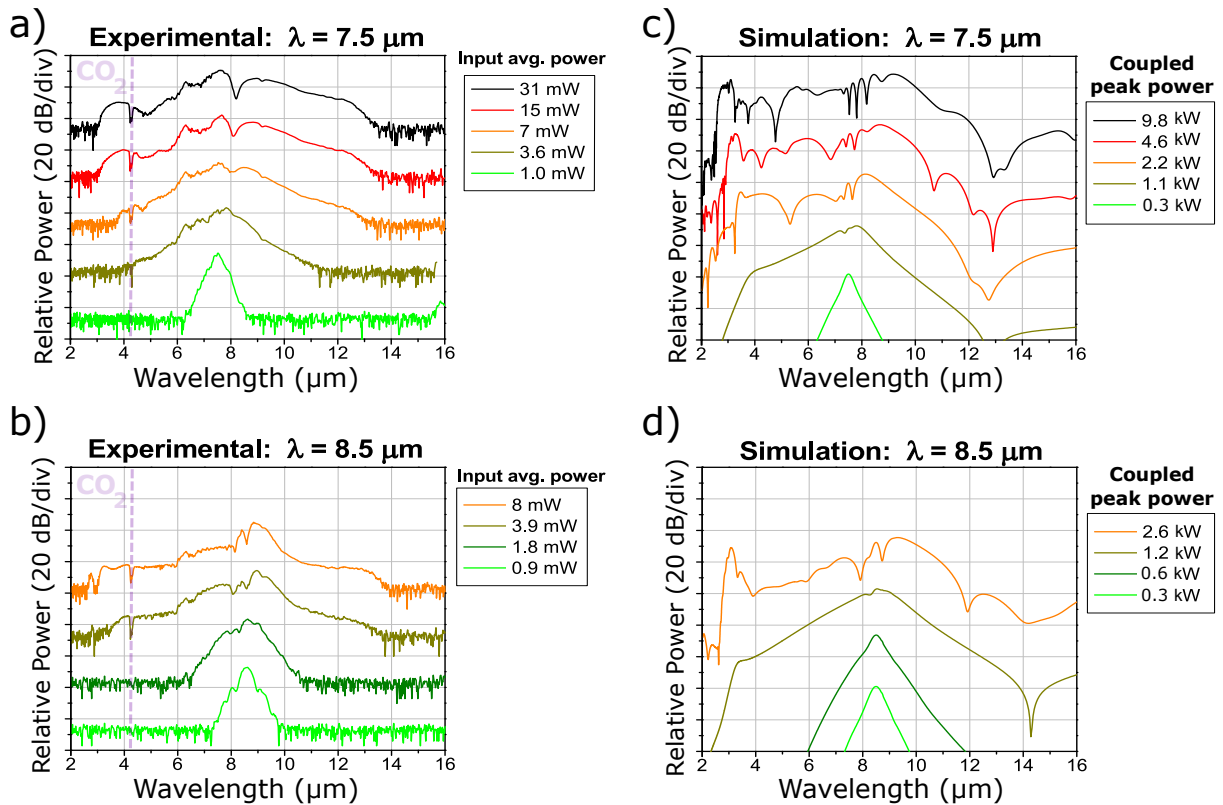


Figure 4: Spectre expérimental et simulé pour un guide d'onde de 5.5 mm de long. (a-b) Mesures expérimentales pour une longueur d'onde de pompe d'entrée de 7.5 et 8.5 μm et différentes puissances moyennes injectées. Une ligne pointillée verticale à 4.25 μm indique l'absorption atmosphérique de CO_2 . (c-d) Résultats simulés pour les mêmes longueurs d'onde d'entrée et des puissances de crête injectées équivalentes. Chaque trace a été décalée verticalement de 30 dB.

Modulateur électro-optique intégré

La dernière démonstration que j'aborde dans cette thèse est un modulateur électro-optique (EOM). Ce dispositif est essentiel pour mettre en oeuvre la détection synchrone et améliorer ainsi considérablement la sensibilité des systèmes de détection intégrés. Dans un premier temps, j'évalue expérimentalement l'effet de dispersion de plasma de porteurs libres (FCPD) dans une large gamme de spectre MIR, ce qui manquait dans la littérature. Comme on peut le voir sur la Fig. 5, les résultats que j'obtiens grâce à une modélisation appropriée et des mesures tout-optique confirment les prédictions précédentes de FCPD rapportées dans la littérature. Il est aussi intéressant de noter qu'un effet FCPD plus efficace est observé à de plus grandes longueurs d'onde MIR.

Ces résultats permettent de poursuivre la conception d'un dispositif EOM au moyen de l'effet FCPD. Ainsi, dans une deuxième partie, je propose, évalue numériquement et fabrique un dispositif EOM, basé sur une diode Shottky dans un guide d'onde SiGe et avec un substrat Si fortement dopé. Ensuite, je caractérise premièrement le dispositif EOM en modulation statique de 6.4 à 10.7 μm longueur d'onde, et en configuration de déplétion de porteurs et d'injection

de courant. Comme nous pouvons l'observer sur la Fig.6 pour la transmission normalisée lorsque différentes tensions et courants sont appliquées, un rapport d'extinction maximal de 1.33 dB est obtenu pour une longueur d'onde de $10.7 \mu\text{m}$ et avec une injection de courant de 170 mA. Il s'agit, à ce jour, de la modulation électro-optique la plus efficace rapportée sur puce à des longueurs d'onde supérieures à $8 \mu\text{m}$.

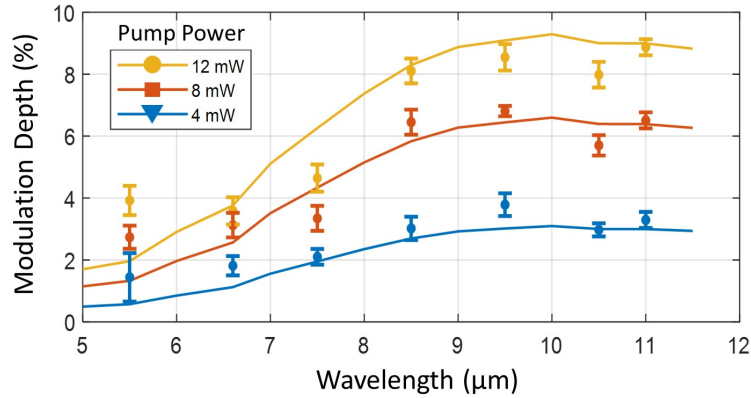


Figure 5: Modulation tout-optique expérimentale en fonction de la longueur d'onde et pour trois puissances de pompe NIR couplées au guide d'onde SiGe à une longueur d'onde de $1.33 \mu\text{m}$. Les données expérimentales sont représentées par des points et les résultats simulés par des lignes continues.

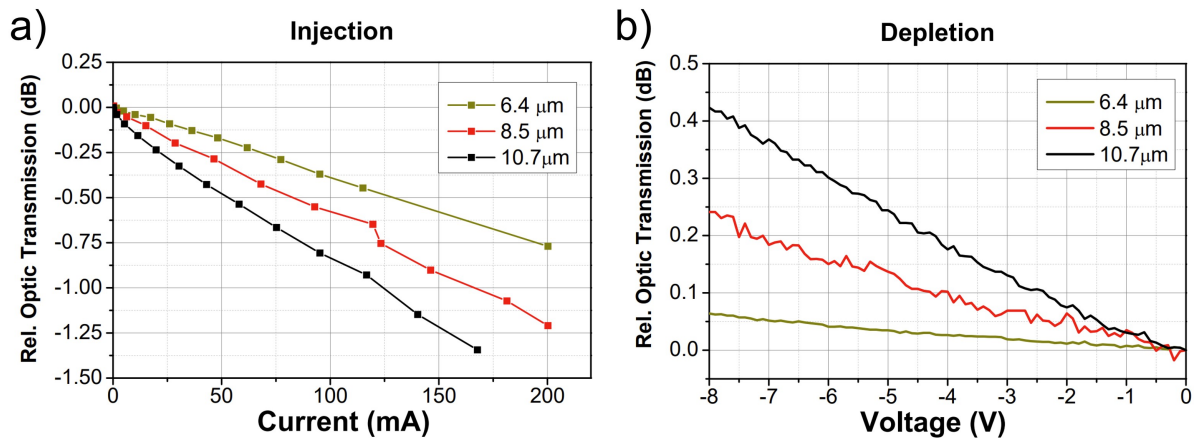


Figure 6: Caractérisation de l'EOM statique: (a) Transmission optique normalisée en fonction du courant injecté. (b) Transmission optique normalisée en fonction de la tension appliquée en configuration de déplétion.

Pour étudier la vitesse de modulation de ce dispositif, j'ai également effectué une caractérisation dynamique avec un laser fonctionnant en continu à $8 \mu\text{m}$. L'amplitude de la raie correspondant à la modulation, détectée dans l'analyseur de spectre électrique en fonction de la fréquence du signal est reportée sur la Fig. 7. Pour le régime d'injection de courant, l'amplitude de modulation diminue presque linéairement à des fréquences supérieures à 50 MHz. Par contre, en régime de déplétion de porteurs, une amplitude de modulation presque plate est obtenue

jusqu'à 225 MHz, tandis que le niveau de bruit empêche une caractérisation correcte au-delà de cette fréquence, en raison du montage expérimental utilisé.

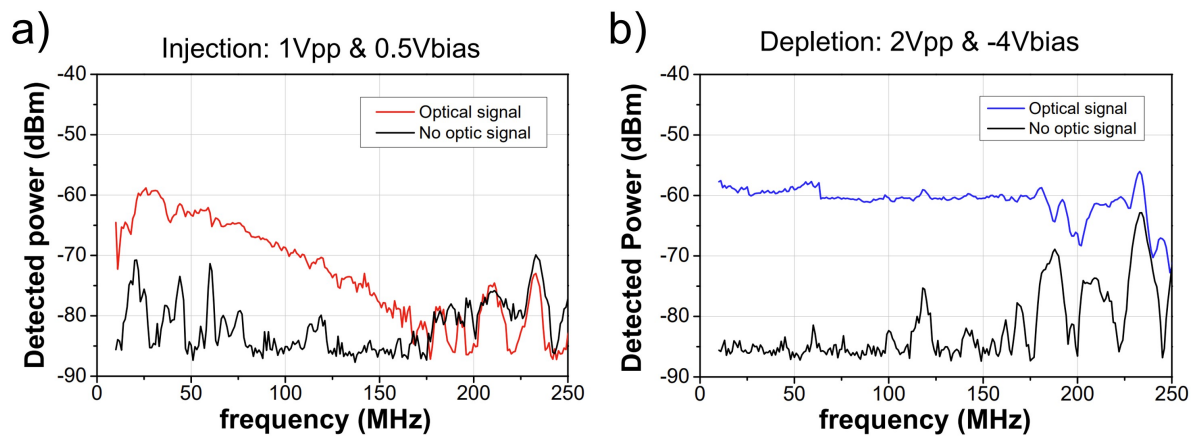


Figure 7: Amplitude du signal photodétecté en fonction de la fréquence du signal sinusoïdal appliqué à l'EOM: (a) en régime d'injection de courant avec une polarisation de 0.5 V et un signal électrique de 1 Vpp et (b) en régime de déplétion avec une polarisation de -4 V et 2 Vpp. Le bruit de fond obtenu lorsque la source MIR n'est pas allumée est également reporté en couleur noire.

Conclusion

En conclusion, cette thèse a abordé avec succès le développement de guides d'ondes intégrés et de trois composants associés et manquants en la littérature (spectromètre à transformée de Fourier, génération de supercontinuum et modulateur électro-optique), fonctionnant dans une large bande spectrale MIR. Par conséquent, ce travail ouvre des perspectives passionnantes dans une grande gamme d'applications à fort impact, et ouvre la voie au développement à long terme de systèmes de capteurs multimoléculaires compacts.

Acknowledgements

First of all, I would like to thank my main thesis director Delphine for giving me the confidence and the freedom to explore new solutions, to participate in numerous conferences and project meetings (Inspire and LightUp) and to collaborate with different colleagues and institutions. Delphine has given me personal support, always being very comprehensive and kind. Thanks to her high scientific and leading qualities, I could achieve great results during my thesis, always feeling comfortable and motivated from the first moment. She greatly managed that, neither a laboratory relocation, nor a Covid pandemic affected my PhD thesis. I can only say thank you Delphine for giving me the opportunity to do a thesis with you.

I would also like to express my deepest gratitude to Carlos, to be not only my co-director of thesis but also a friend. Thank you for all the highly valuable scientific discussion we have had during my thesis and all the times I have bothered you with my questions. I also really appreciate all the awesome personal support and the moments we have shared: conferences (Singapore, San Francisco, etc.), hosting me when the RER-B was not working, doing some sport together, shopping, etc.

I thank Laurent and Eric, for all the precious pieces of advice and talks we have had, especially on the coffee time. Also, I really appreciate all the great discussions and teaching of Xavier about device fabrication, sharing with me part of your experience in the silicon photonics technology. Without you it would have been impossible to achieve all the results I got during my PhD. Then, I would like to thank all my colleagues that I have had during my thesis. I have learned a lot from them: Joan and Qiankun taught me all the mid-infrared characterization, Vladyslav rapidly introduced me to multiple fabrication processes (specially in Milano), or I had very high-valuable discussions with Christian about nonlinear phenomena. I would like to particularly thank Elena for all the scientific and personal support during all my PhD, not only while we shared an office in IEF lab with me, but also after you left the C2N lab. Elena welcomed me to the group very warmly and helped me a lot with all the crazy paperwork I had to do, among others. I do not forget many other colleagues of Minaphot group, with who I shared nice scientific and personal moments. I am also very grateful to my nice colleagues from Italy and the successful collaboration we have continued. In summary, I could not imagine a better group to do a PhD as Minaphot, which host great scientific professionals and even better personalities.

I cannot forget and I would like to thank my first supervisor Domenico and former colleagues, and now friends, Mariam and Mario. They introduced me to the photonics community and taught me a lot before starting my PhD. Together with my second supervisor Bart and the PhD student on that time Koen, I got highly interested in the field, and set the initial milestones of my thesis. The support and experience you have shared with me have strongly helped to rapidly achieve nice results during my thesis.

In a personal level, I acknowledge the long-life friends I have kept in Spain, and I am truly grateful for all the amazing friends I have found in France: Javid, Zhila, Carlos, Laura, Jasone, Carmen, Fernando ... We have spent amazing moments in the good times, and we have been a mutual support for each other (in particular the PhD students) in the bad times. I am especially grateful for having met Pardis, as he has been a great support during my PhD, with who I have shared great moments and managed to survive a Covid pandemic together, among others.

Finally, I would like to thank one of the fundamental pillars of my life, my family, and for all the unconditional support I received from them.

For these and many other reasons, I can only say:

Thank you very much to all of you!

Merci beaucoup à tous !

¡Muchas gracias a todos!

Contents

Synthèse en français	i
Acknowledgements	vii
Contents	ix
List of abbreviations	xi
1. Introduction	1
1.1. Motivations and context of the MIR spectrum	1
1.1.1. Fingerprint region	2
1.1.2. MIR atmospheric transparency windows	3
1.1.3. MIR coherent lights sources	4
1.2. Spectroscopy sensing	5
1.2.1. Narrowband spectroscopy sensing techniques	5
1.2.2. Broadband spectroscopy sensing techniques	7
1.2.3. Dual-comb spectroscopy	10
1.3. MIR platforms and materials	11
1.3.1. Non Si-based photonic integrated platforms	12
1.3.2. Si-based photonic integrated platforms	12
1.3.3. SiGe-based photonic integrated platforms	13
1.4. Outline of thesis	16
2. Broadband MIR platform	19
2.1. Ge-rich graded-index SiGe platform	19
2.2. Fabrication of graded-index SiGe integrated waveguides	23
2.2.1. Fabrication processes developed in Polifab	24
2.2.2. Fabrication processes developed in C2N	25
2.3. Propagation loss characterization of SiGe waveguides	27
2.3.1. Experimental setup for propagation loss measurements and results	27
2.3.2. Study of propagation loss contributions	30
2.4. Experimental demonstration of a wideband MZI device	35
2.5. Conclusions and routes for improvement of broadband MIR graded-index SiGe platforms	37
3. Integrated Fourier-transform spectrometer in the MIR	39
3.1. State-of-the-art and working principle of integrated FTS	39
3.1.1. Stationary wave integrated FTS	40

3.1.2.	Heterodyne integrated FTS	41
3.1.2.1.	Spatial-heterodyne integrated FTS	41
3.1.2.2.	Scanning interferometry integrated FTS	43
3.2.	Integrated thermally-tuned spatial-heterodyne FTS: working principle and theoretical modeling	45
3.3.	Application of calibration matrix method in TT-SH-FTS	49
3.4.	Numerical simulations and performance evaluation of integrated TT-SH-FTS in the MIR regime	51
3.5.	Experimental validation of MIR integrated TT-SH-FTS	53
4.	On-chip supercontinuum generation in the MIR	59
4.1.	State of the art and basic dynamics of SCG	59
4.1.1.	Context and motivations for on-chip SCG in the MIR	59
4.1.2.	Basic nonlinear dynamics of SCG	62
4.2.	SCG design with graded-index SiGe waveguides	64
4.3.	Numerical SCG simulations	66
4.4.	On-chip 2-octaves SCG: experimental results	68
4.5.	Simulated SCG coherence	73
4.6.	Conclusions and routes for improvement of SCG in SiGe waveguides	74
5.	Integrated MIR electro-optical modulator	75
5.1.	Motivation and state-of-the-art for broadband integrated EOM in the MIR regime	75
5.2.	Broadband validation of FCPD absorption in the MIR	77
5.2.1.	Modeling of free-carrier absorption in Ge-rich SiGe waveguides	78
5.2.2.	Experimental characterization of all-optical modulation in the MIR	83
5.3.	Integrated EOM in the MIR	85
5.3.1.	Design of the integrated EOM structure	85
5.3.2.	Integrated EOM fabrication and experimental insertion losses	87
5.3.3.	Schottky diode mesa study and electrical characterization	90
5.3.4.	Experimental characterization of integrated EOM in the MIR: modulation efficiency and bandwidth	93
5.3.5.	Numerical modeling of FCPD effect modulation in depletion regime	96
5.3.6.	Routes for improvement and new MIR integrated EOM designs	97
5.4.	Conclusion of integrated EOM operating the MIR	98
6.	Conclusions and perspectives	101
6.1.	General conclusions	101
6.2.	Perspectives and future works	102
	Bibliography	105
	A. Publication List	123

List of abbreviations

AWG	A rrayed W aveguide G rating
CMOS	C omplementary M etal- O xide S emiconductor
CW	C ontinuous W ave
DW	D ispersiv e W ave
EOM	E lectro- O ptic M odulator
FCPD	F ree- C arrier P lasma D ispersion
F-P	F abry- P erot
FSR	F ree S pectral R ange
FTS	F ourier- T ransform S pectrometer
Gpbs	G iga b its p er s econd
GOI	G ermanium- O n- I nsulator
ICP-RIE	I nductively C oupled P lasma- R eactive I on E tching
ICL	I nterband C ascade L aser
IPA	I so P ropyl A lcohol
LEPECVD	L ow E nergy P lasma E nhanced C hemical V apour D eposition
LWIR	L ong- W ave I nfra R ed (spectrum here defined as 8–15 μm wavelength range)
MCT	M ercury C admium T elluride
MEMS	M icro- E lectro- M echanical S ystems
MIR	M id I nfra R ed (spectrum here defined as 2–20 μm wavelength range)
MMI	M ulti- M ode I nterferometer
MWIR	M iddle- W ave I nfra R ed (spectrum here defined as 3–8 μm wavelength range)
MZI	M ach- Z ehnder I nterferometer
NDIR	N on- D ispersiv e I nfra R ed
NEMS	N ano- E lectro- M echanical S ystems
NIR	N ear I nfra R ed (spectrum here defined as 0.78–2 μm wavelength range)
OFC	O ptical F requency C omb
PIC	P hotonic I ntegrated C ircuit
ppb	p art- p er- b illion
ppt	p art- p er- t rillion
PSD	P ower S pectrum D ensity
QCL	Q uantum C ascade L aser
RF	R adio F requency
SCG	S uper C ontinuum G eneration

Contents

SEM	Scanning Electron Microscope
SIMS	Secondary Ion Mass Spectrometry
SOI	Silicon-On-Insulator
SOS	Silicon-On-Sapphire
SWIR	Short-Wave InfraRed (spectrum here defined as 1.4–3 μm wavelength range)
TDD	Threading Dislocation Density
TDLAS	Tunable Diode Laser Absorption Spectroscopy
TE	Transverse Electric
TM	Transverse Magnetic

1

Introduction

During the last two decades, the mid-infrared (MIR) spectral range has aroused a high interest in the photonics community, due to its unique features for sensing and security purposes. Indeed, commercial sensing systems are already available, but are mainly based on a free-space configuration, thus being bulky and expensive. To overcome these issues and provide compact and wide-spread MIR devices, several integrated photonics platforms have been explored, and a whole set of passive building blocks have been reported in the literature. However, the further demonstration of broadband functionalities operating at the longest MIR wavelengths is still at its infancy. In this regard, the aim of this PhD manuscript is to explore and experimentally demonstrate different active and nonlinear building blocks that are key to progress in the development of a fully integrated and broadband MIR system. The successful demonstration of these on-chip functionalities would pave the way towards the implementation of widely used MIR devices in a plethora of applications, such as medical diagnostics, hyper-spectral imaging or remote sensing. Therefore, this introduction chapter first presents the MIR spectral band, together with its unique features that have motivated the development of the different sensing techniques and integrated platforms that are subsequently discussed. Finally, the outline of the following chapters is also detailed.

1.1. Motivations and context of the MIR spectrum

In the photonics framework, the MIR range is typically defined between 2 and 20 μm wavelength, as depicted in Fig. 1.1. Therefore, it is likewise defined in this manuscript hereafter. Furthermore, based on the radiation transparency of the atmosphere, the infrared spectrum is alternatively divided in three different sub-bands: the short-wave infrared (SWIR) commonly defined from 1.4 to 3 μm wavelength, the middle-wave infrared (MWIR) between 3 to 8 μm and the long-wave infrared (LWIR) from 8 to 15 μm [1]. In particular, the MWIR and LWIR are highly interesting due to two key factors: the fingerprint region and two related atmospheric transparency windows. Both aspects are discussed in the following.

1. Introduction

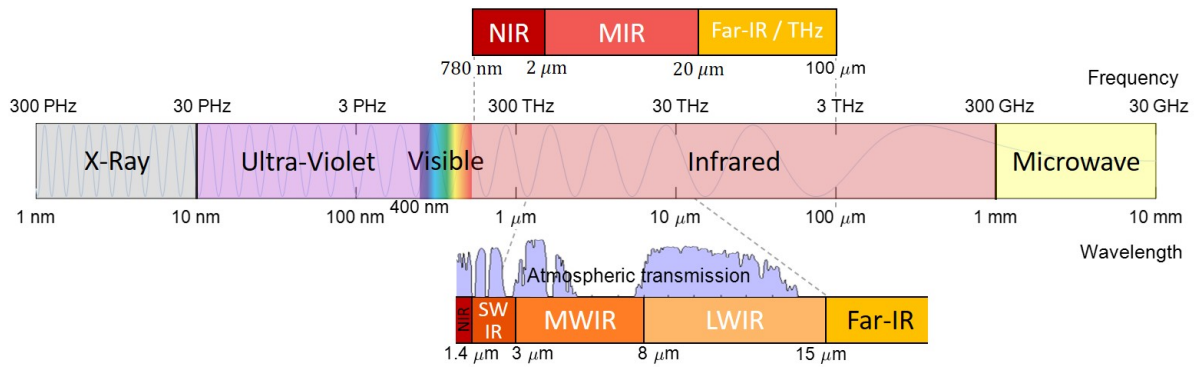


Figure 1.1.: Schematic of the electromagnetic radiation spectrum. The infrared band is divided in the near-, mid- and far-infrared. The MIR band is sub-divided in the SWIR, MWIR and LWIR.

1.1.1. Fingerprint region

The MIR contains the commonly called molecular fingerprint region, here defined as the spectral range between 3 and 13 μm wavelength. It means that in the MIR spectral range, and in particular at wavelength longer than 3 μm , most of molecules have an intense and distinctive spectral absorption pattern. This fact is due to the excitation of fundamental vibrational modes, as the molecules stretch along their bonds or vibrate around their mass center. As depicted in Fig. 1.2(a) for a CO_2 molecule, there are two main vibrational modes: stretching (symmetric and antisymmetric) and bending in four different kind of motions, two in-plane (scissoring and rocking) and two out-of-plane (wagging and twisting) [2]. In the near-infrared (NIR) regime, the spectral absorption lines are not caused by fundamental vibrational modes, but by vibrational overtones. Therefore, the spectral absorption pattern in the MIR is much stronger than in the NIR regime [3].

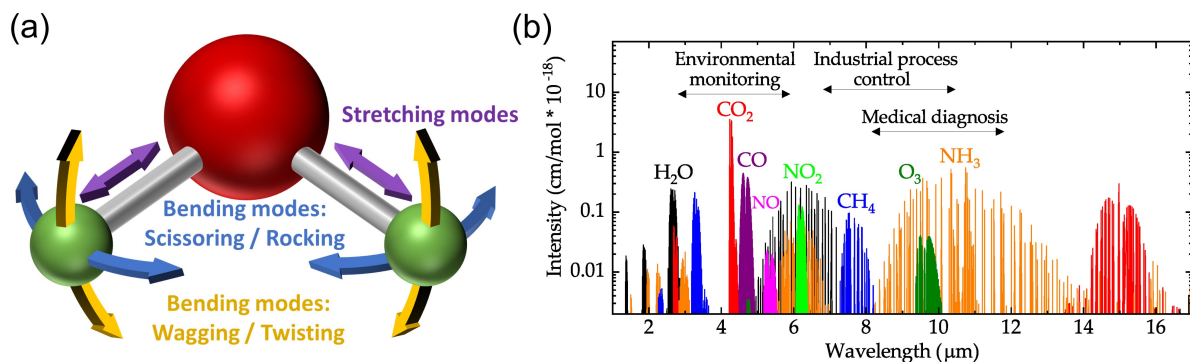


Figure 1.2.: (a) Illustration of vibrational modes of a CO_2 molecule. (b) Relative intensity absorption spectrum of selected molecules in the fingerprint region. Image taken from Ref. [4].

In this sense, the strong and specific molecular absorption in the MIR range has compelling interest to identify in a non-intrusive way the presence of a large number of molecular compounds in a medium with a high sensitivity, potentially up to part per billion (ppb) or even part per trillion (ppt) level. For instance, the absorption spectra of different important molecules are

shown in Fig. 1.2(b). Due to these unique absorption features, the MIR is highly relevant for sensing and monitoring applications in any context. For example, the MIR can be used for food safety control purposes, as salmonella bacteria shows different absorption lines in this spectral range [5]. Moreover, carbon-dioxide presents strong absorption lines centered at $4.25 \mu\text{m}$ wavelength and, since it is a greenhouse gas, it can be used as an indicator of environmental pollution. But not only, ammonia (NH_3), nitrous oxide (N_2O), carbon monoxide (CO), methane (CH_4) and other alkanes also have strong absorption lines in the MIR [6]. In particular, alkanes show strong absorption lines for wavelengths longer than $7 \mu\text{m}$, making the $7\text{-}13 \mu\text{m}$ spectral range especially interesting, while it has not yet been extensively exploited by integrated devices. The MIR range can thus be used for many sensing applications, such as ecological monitoring, industrial process controls or warfare agent detection. In the Fig. 1.3 we can see an example of the main growing markets in MIR sensing applications [7].

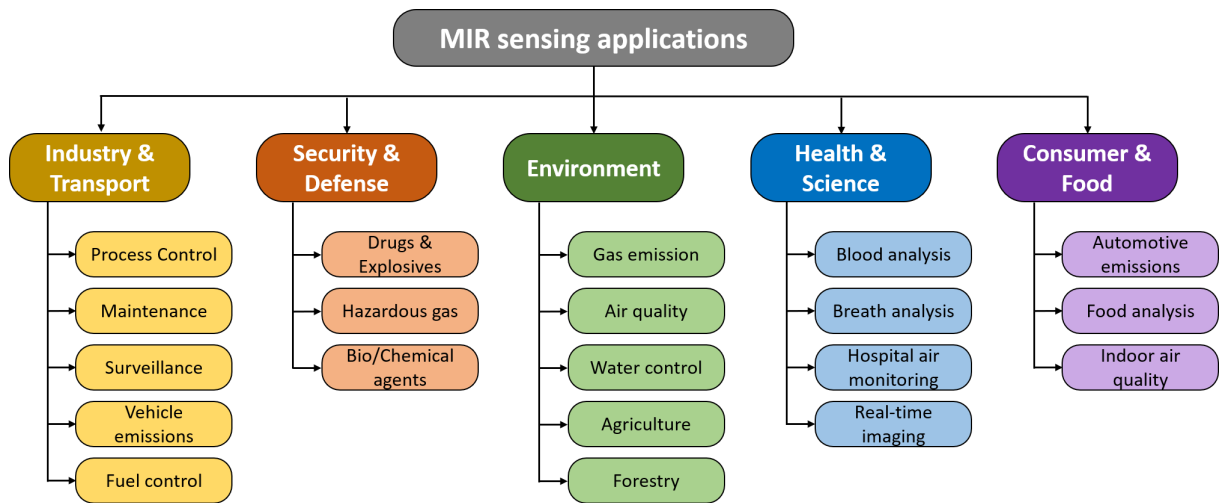


Figure 1.3.: Scheme of growing markets for MIR sensing applications, adapted from Ref. [7].

1.1.2. MIR atmospheric transparency windows

In the visible spectral range the light is relatively not absorbed by the molecules present in the atmosphere and is the reason why we capture the light scattered in objects by the eyes to see them in different colors (i.e., different radiation wavelengths), even though they are relatively far away. Similarly, the MIR contains two atmospheric transparency windows: $3\text{-}5 \mu\text{m}$ (in the MWIR) and $8\text{-}14 \mu\text{m}$ wavelength (in the LWIR) [8]. It means that part of the MWIR and almost the entire LWIR are relatively not absorbed by the atmosphere, even benefiting from a lower Rayleigh scattering when compared to the visible or NIR spectral ranges [9]. Hence, significant advances have been made in free-space communications during the last two decades by exploiting these two MIR transparency windows. As one of the first works, a high-speed and free-space communication demonstration was reported in 2001 at $8.1 \mu\text{m}$ wavelength by direct laser modulation [10]. Since then, several demonstrations have been subsequently reported in the literature. For example, a later work at the same wavelength showed an improvement of

1. Introduction

the Mie scattering when compared to the NIR regime in 2009 [11]. Also, a more recent free-space gigabit transmission was demonstrated at room temperature at 4.65 μm wavelength in 2017 [12], or a 10-Gbps transmission was reported at 3.6 μm wavelength thanks to frequency down-conversion in 2018 [13].

Moreover, the two transparency windows are relevant for many other applications, such as hyper-spectral imaging. In fact, the maximum of the thermal spectral radiation is located in the MIR regime, as seen in Fig. 1.4. Therefore, this spectral range is an ideal candidate for thermal-based purposes, showing a compelling interest for many critical applications, such as security surveillance or warfare counter-measurements [14–16].

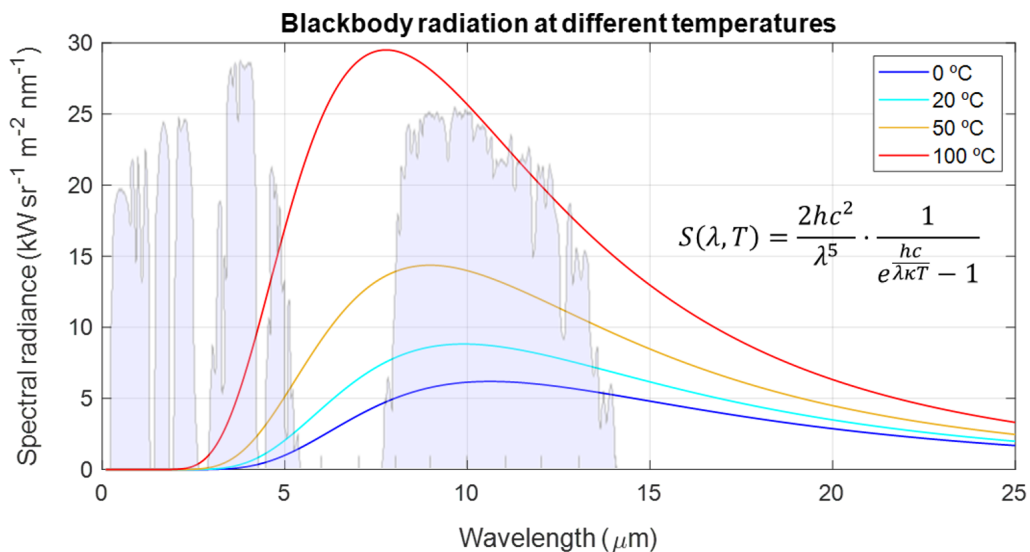


Figure 1.4.: Blackbody radiation at different temperatures as a function of the wavelength. In background: normalized atmospheric transmission [6]. Inset: blackbody radiation equation [17].

1.1.3. MIR coherent lights sources

Despite the strong interest of the MIR regime (due to the two above-mentioned factors), it was the development of MIR laser sources in the 90’s which strongly triggered an extensive development of photonic integrated platforms and associate devices working in this spectral range. The first milestone was the demonstration of a quantum cascade laser (QCL) operating in the MIR, carried out by J. Faist et al. in 1994 [18]. Unlike classical semiconductor lasers that are based on electron-hole recombination across a certain bandgap between the valence and conduction band, QCL sources rely on intersubband electron transitions through a cascade of quantum well heterostructures to perform a coherent electromagnetic radiation. In fact, current QCLs have been demonstrated to be a mature technology, typically covering from 3 to 30 μm wavelength range.

Moreover, interband cascade lasers (ICLs) operating in the MIR have also been reported in the literature, relying on interband transitions (instead of intersubband as QCLs) and typ-

ically covering from 3 to 6 μm wavelength [19]. For instance, this type of lasers have been demonstrated at 3.75 μm wavelength in 2008, operating in continuous wave (CW) and at room temperature [20]. In fact, MIR light sources have reached an impressive level of technological maturity during the past decade, including some other technologies such as fiber lasers or optical frequency comb (OFC) generation [21–24]. Also, strain or lattice engineering of group IV materials has been recently demonstrated, as an emerging and exciting solution to provide silicon-compatible MIR lasers [25]. Nevertheless, achieving a broadband source with a single device is often challenging, typically covering up to 10 cm^{-1} spectral range.

1.2. Spectroscopy sensing

Due to the impressive progress in MIR laser sources and the high interest of this spectral range for sensing applications, multiple detecting approaches have been reported in the literature. Most of these methods rely on spectroscopy techniques to perform remote and non-intrusive sensing capabilities. It means to identify the molecular composition of any substance through the study of the light-matter interaction as a function of the wavelength. For practical reasons, most of the absorption spectroscopy techniques have been first developed in the NIR range and in a free-space configuration, while in most of cases their working principles have been later applied to integrated photonic circuits (PICs). Therefore, to better illustrate their operational approach and for concept simplicity, it is interesting to first introduce those techniques in a free-space configuration, too. In this regard, some of the main absorption spectroscopy techniques reported in the literature are presented below, which have been classified in this manuscript in three main categories: narrowband, wideband and dual-comb spectroscopy.

1.2.1. Narrowband spectroscopy sensing techniques

Narrowband spectroscopy techniques for sensing applications are typically based on the interaction of a monochromatic MIR source with a medium to be sensed. In this regard, the three following approaches show different strategies to exploit the light-matter interaction between the MIR source and the molecules present in a medium.

- **Ring-down method:** Classically in this method, a monochromatic and squared-pulsed laser source is coupled into a free-space resonant cavity, based on two highly reflective mirrors (as depicted in Fig. 1.5). Then, the temporal response of the output beam is analyzed in both cases, with and without the analyte inside the cavity. Finally, the molecular concentration is obtained from the exponential decay difference when the molecules are present or not [26–29]. Also, if the laser source wavelength is tuned together with the cavity length, to ensure resonance condition, a spectral response can be obtained. The cavity ring down method is a very sensitive approach to identify the electromagnetic absorption of a substance that has been occasionally used for gas sensing with a sensitivity

1. Introduction

up to ppt level.

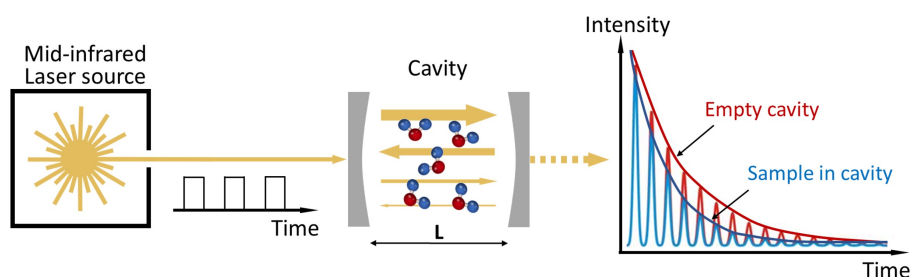


Figure 1.5.: Working principle scheme of ring-down method in a free-space configuration.

- **Photo-acoustic spectroscopy:** This is a technique that indirectly obtains the molecular absorption by mean of acoustic detection [30–32]. As shown in Fig. 1.6 for the classical approach, a monochromatic MIR laser source is modulated in amplitude and sent to a photo-acoustic cell. The modulation frequency can be given, for example, by direct laser modulation. Then, if the analyte (most of the time as gases) pumped to the photo-acoustic cell has a vibrational resonance that corresponds to the operational wavelength, the light is absorbed by the molecules and translated to vibrational motion. This vibration of the excited molecules is then translated to heat, leading to a gas expansion. Hence, as the MIR beam amplitude is modulated, an acoustic wave is generated. Also, if the modulation frequency matches the acoustic resonance of the cell, the sensitivity of the detecting system can be greatly enhanced. Finally, this acoustic wave is detected by a microphone that, for instance, can be fabricated by micro- or nano-mechanical (MEMS and NEMS) diaphragm gauges [33]. This system has the main advantage of implementing an indirect photodetection that works at room temperature and is independent of the MIR wavelength, but mainly depends on the acoustic cavity resonance that is matched with the modulation frequency of the MIR source, thus avoiding the use MIR photodetectors that are often required to be cooled down to cryogenic temperatures. High sensitivity (up to ppb or even ppt levels) can be achieved with this approach, while performing a low detecting time response for a single operational wavelength (in the order of milliseconds). Also, a spectral response can be obtained by tuning the wavelengths of the MIR source sent to the photo-acoustic cell.

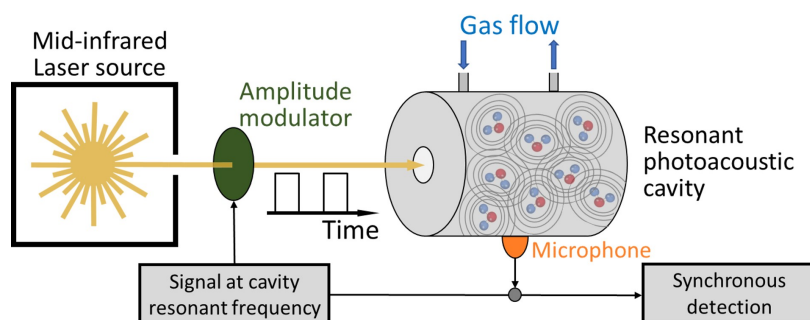


Figure 1.6.: Working principle scheme of photo-acoustic detection spectroscopy sensing.

- **Tunable diode laser absorption spectroscopy (TDLAS):** In this method, a monochromatic input pulse is scanned over a large MIR bandwidth and sent through a medium to be sensed [34–38]. Then, the output beam is collected in a broadband photodetector. In this way, as depicted in Fig. 1.7, the transmission spectrum is sequentially constructed. Finally, the presence of different molecules in the medium are identified by analyzing the output spectral absorption pattern.

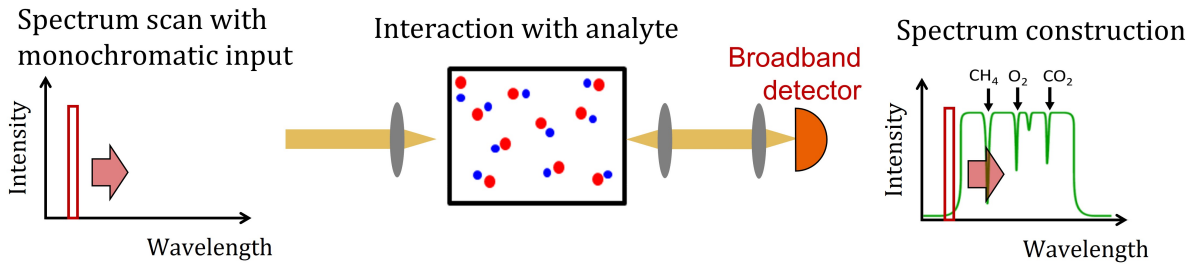


Figure 1.7.: Generic schematic of TDLAS working principle.

These methods can provide high sensitivity, while broadband operation could be achieved by widely tuning the laser source wavelength. However, single laser sources typically cover a relatively narrow spectral range. The on-chip combination of multiple lasers has been proposed as a solution in the literature [39], but it may increase the system complexity and its related fabrication. Also, the time response of these approaches may be degraded, as the laser must be sequentially generated and detected at each sampling point of the wide spectral range. In this regard, alternative broadband implementations are often preferred for multi-molecule detection purposes, as is the case in this manuscript.

1.2.2. Broadband spectroscopy sensing techniques

As an alternative to narrowband spectroscopy techniques, different broadband approaches have been reported in the literature [40]. As depicted in Fig. 1.8, these approaches are commonly based on the generation of a wide MIR spectrum that, after interacting with a medium, is retrieved in a spectrometer system. Then, the different molecules are identified by analyzing the resulting absorption spectral pattern. Although the generation of a broadband MIR spectrum with a single source may be challenging, different techniques have been proposed in the literature. Interestingly, some of those approaches takes advantage of nonlinear phenomena, such as supercontinuum generation (SCG), to extend the operational spectral band of a single device.

This type of broadband spectroscopy techniques is highly interesting to perform multi-molecule sensing as, the broader is the light source spectrum, the more absorption lines will be possible to identify, and thus the more molecules will be possible to simultaneously detect. Moreover, the spectrometer system must be capable to accurately retrieve the output spectrum, in order to properly distinguish between the different absorption lines corresponding to different mo-

1. Introduction

olecules. Thus, high-resolution together with broadband performance features are critical for MIR spectrometers. In the following, three different spectrometer approaches are presented.

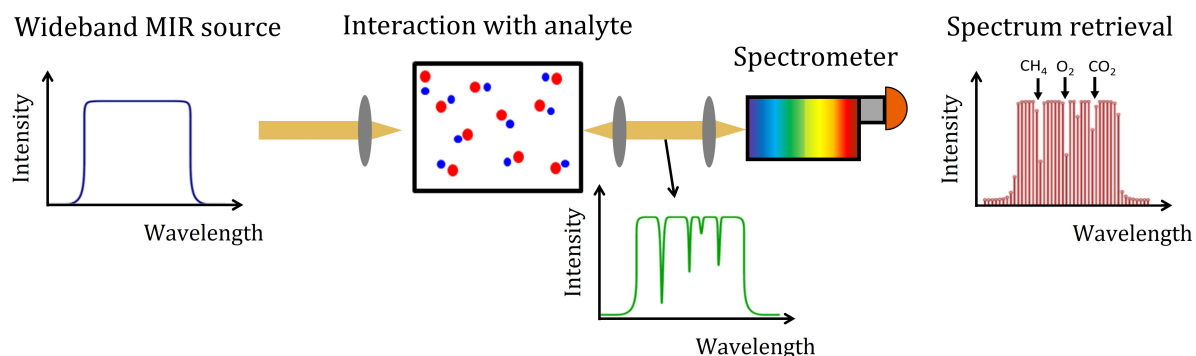


Figure 1.8.: Generic schematic of broadband absorption spectroscopy techniques. A wide light source interacts with an analyte and the resulting spectrum is retrieved in a spectrometer system, in order to identify the presence of multiple molecules by analyzing the absorption pattern.

- **Non-dispersive infrared (NDIR) spectroscopy:** In this method, the spectrometer approach is commonly based on the implementation of either an array of narrowband filters and detectors, as illustrated in Fig. 1.9(a), or a single narrowband but widely tunable filter, with only one broadband photodetector, as depicted in Fig. 1.9(b) [41–43]. Alternatively, some works have demonstrated the possibility to implement reconstructive spectrometry techniques by mean of a broadband scattering media, shown as an encoder array in Fig. 1.9(c) [44, 45]. These approaches can perform high resolution, also in an integrated and compact way. However, a large number of filters and detectors are often needed to achieve high performance features. Also, the maximal tunability of a single PIC filter is often limited to a narrow spectral range.

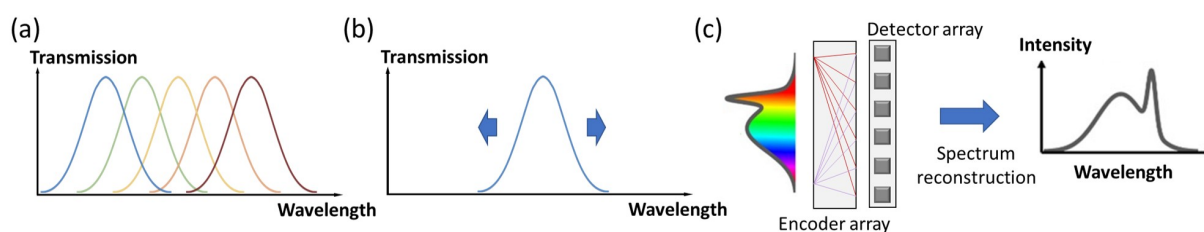


Figure 1.9.: NDIR spectrometer system schematics. (a) A narrowband filter array is used to select each spectrum sampling point. (b) A widely tunable filter is used to select the detected wavelength. (c) Reconstructive filtering methods schemes can also be used to retrieve the input spectrum.

- Dispersive infrared spectroscopy:** Dispersive-based spectrometers typically rely on the diffraction of a light beam to spatially separate and detect the different wavelength contributions [46–48]. For instance, if a light beam is sent to a grating array in a free-space configuration, the light is reflected, diffracted and then collected in a detector array, each one detecting a different wavelength, as seen in Fig. 1.10(a). In a similar way, the grating array can mechanically move to select a single wavelength that is collected in a broadband photodetector and thus construct the output spectrum, as illustrated in Fig. 1.10(b). In both approaches, the retrieval spectral resolution depends on the physical length between the grating array and the detector, meaning the maximal diffraction of the light beam in the monochromator system. Dispersive infrared spectroscopy also includes the use of an integrated array waveguide grating (AWG). In this device, a wideband input spectrum is divided in different channels, in which a phase delay is increasingly accumulated along a set of waveguides, due to the waveguide dispersion. In this way, each output channel collects a different wavelength contribution, as depicted in Fig. 1.10(c) [49, 50]. In this way, each output waveguide of the AWG corresponds to a sampling point of the retrieved spectrum.

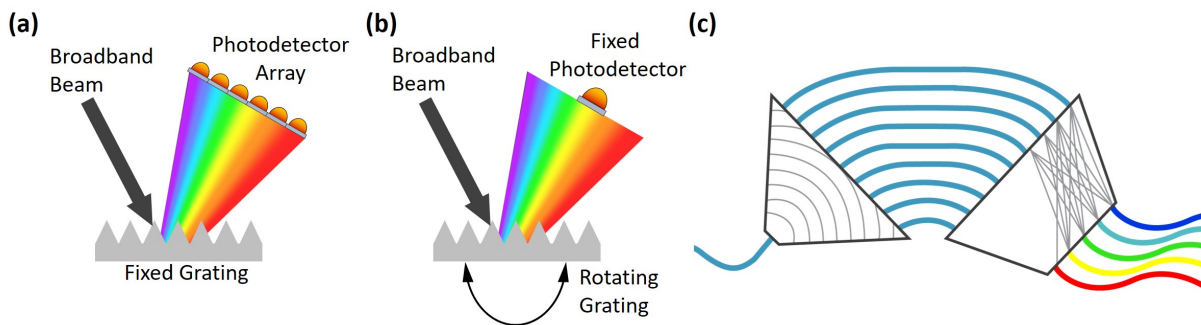


Figure 1.10.: Schematic of dispersive spectrometer systems. (a) A fixed grating array is used to diffract a broadband input beam and thus select each spectral sampling point in a photodetector array. (b) A rotating grating and a fixed photodetector can alternatively be used to retrieve the input spectrum. (c) Integrated AWGs can also be exploited to separate a wideband input into different wavelength contributions, each one in an output waveguide.

- Fourier transform spectrometer:** A widely used approach to perform absorption spectroscopy is based on a Fourier-transform spectrometer (FTS). Classical FTS are based on a free-space Michelson interferometer, in which one mirror is fixed and the other is mechanically displaced to tune the arm length difference [51–53]. The output light intensity is then collected in a broadband photodetector as a function of the path-length unbalance, thus generating an interference pattern. For instance, if a monochromatic source is sent, a sinusoidal pattern is obtained, as seen in Fig. 1.11(a). Then, if an inverse Fourier-transform is applied to that sinusoidal interference signal, the monochromatic input spectrum is thus retrieved. On one hand, the sampling rate of the interference pattern is given by the moving mirror displacement step, which is related to the free spectral range (FSR).

1. Introduction

It means the operational spectral band that can be properly retrieved free of aliasing, given by Nyquist-Shannon theorem. On the other hand, the maximal unbalance in the Michelson interferometer (i.e., the maximal displacement of the moving mirror) is related to the spectrometer resolution. Interestingly, if a broadband light source is sent to the system (instead of a monochromatic input), the whole input spectrum can be directly retrieved, at the same time and by mean of a single photodetector. Finally, as shown in Fig. 1.11(b), if the wideband MIR source is sent through an analyte to be sensed, the spectral absorption pattern can be obtained to later identify the presence of different molecules.

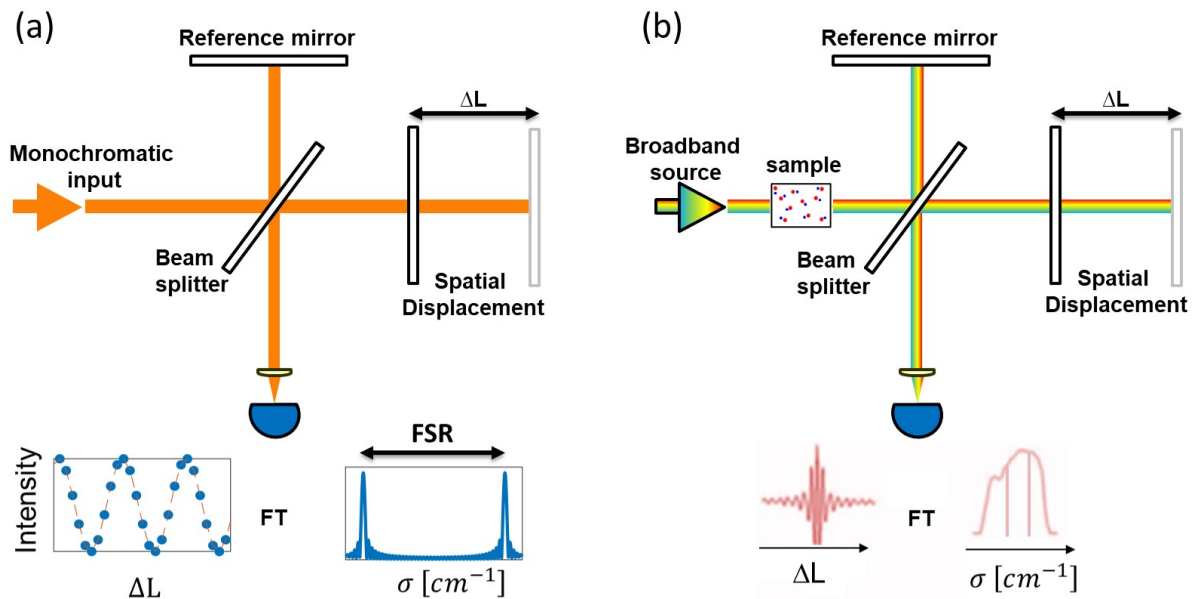


Figure 1.11.: Working principle of a Fourier-transform spectrometer for: (a) monochromatic input operation and (b) broadband input operation after interacting with a medium.

1.2.3. Dual-comb spectroscopy

As another alternative, dual-comb spectroscopy has aroused a high interest in the photonics sensing community during the last decade, due to its broadband and remarkable high-resolution performances.

To understand its working principle, it must be first mentioned that an optical frequency comb consists in the generation of a stable train of narrow pulses in time domain, that is translated to a wide series of discrete, equally spaced and coherent lines in the optical frequency domain. Since its recent discovery in 2005 (which merited the Nobel prize in physics [54]), this phenomenon has aroused a high interest in the photonics community. Hence, a large variety of subsequent OFC demonstrations have been reported by mean of different approaches. For example, thanks to a monolithically integrated micro-resonator, T. Kippenberg's group at EPFL demonstrated for the first time the commonly called Kerr OFC in 2007 [55]. Alternatively, electro-optic modulation has also demonstrated its potential to generate tunable OFCs [56, 57]. However, these two techniques (Kerr and electro-optic OFC generation) have been mainly developed in

the NIR regime, where a subsequent wavelength conversion to the MIR is often implemented. In addition, other direct OFC generation techniques have been successfully reported in the literature in the MIR regime [58], and most notably by mean of QCLs [59].

The significant progress of OFCs has consequently opened interesting perspectives for sensing purposes, and in particular for dual-comb spectroscopy. This technique has been extensively studied during the last two decades [60–67], as it enables a direct link between the optical and radiofrequency (RF) domain. As depicted in Fig. 1.12, dual-comb spectroscopy technique is based on the generation of two OFCs with different spacing between lines (f_{rep}), that are later recombined in a fast photodetector. The different repetition rate of each OFC leads to an increasing separation between the mixed comb lines, creating an array of beatnotes in the photodetector, and thus generating a frequency comb in the RF domain. This RF comb can be later studied through an electrical spectrum analyzer equipment, which is more convenient than in the optical domain. Interestingly, if one of the OFCs is sent through a medium to be sensed (or both OFCs), the molecular absorption fades one of the OFC lines, and consequently its related RF line, too. Therefore, the full absorption spectrum is directly obtained in the RF domain. In this manner, the direct link between optical and frequency domain is established.

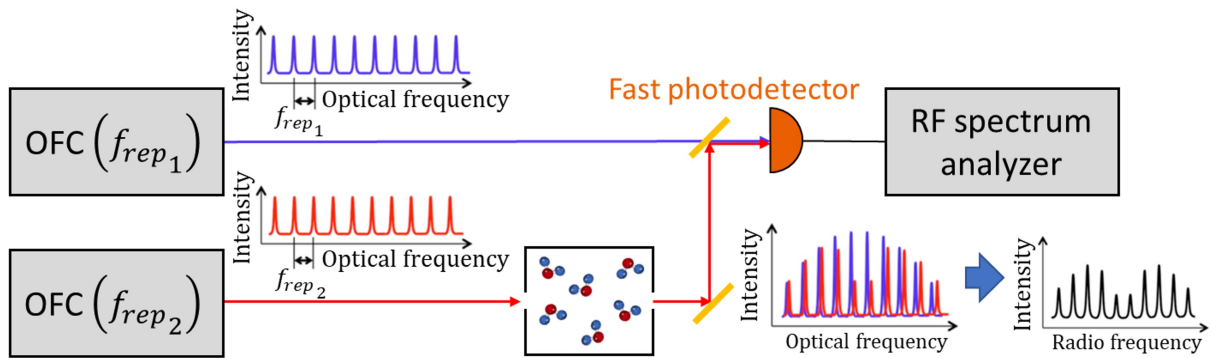


Figure 1.12.: Working principle scheme of dual-comb spectroscopy for sensing applications.

1.3. MIR platforms and materials

The on-chip photonic integration of MIR sensing schemes would open exciting perspectives, providing cost-effective devices with a significant increase of robustness and compactness. Therefore, the first objective of this thesis will be to develop a PIC platform capable to host a wide MIR range and potentially covering the full fingerprint region (3-13 μm wavelength range). Nevertheless, only a few materials are suitable to provide broadband integrated platforms covering the LWIR regime ($>8 \mu\text{m}$ wavelength). As seen in Fig. 1.13, different materials present different transparency windows, limited at the lowest wavelengths by the electronic excitation (when the photon energy is higher than the material bandgap) and at longest wavelengths by multiphonon absorption. Therefore, the material properties play a fundamental role in the PICs design.

1.3.1. Non Si-based photonic integrated platforms

Among the different materials commonly used in PICs, lithium niobate has interesting nonlinear properties, as it is a non-centrosymmetric material. However, its transparency window is limited for wavelengths longer than $5\ \mu\text{m}$ [68]. In contrast, III-V materials can have a wide transparency window, such as GaAs material covering from 1.6 to $16\ \mu\text{m}$ wavelength, while benefiting from the inherent laser source integration [8,69]. Therefore, some works have been reported by mean of GaAs platforms, including an integrated Mach-Zehnder interferometer (MZI) for sensing purposes operating in the 5.8 - $6.3\ \mu\text{m}$ wavelength range [70]. Chalcogenide compounds also exhibits a remarkably wide transparency window in the MIR, even covering the full MIR range (2 - $20\ \mu\text{m}$ wavelength). Hence, some related works have been reported in the literature, as a high quality-factor ring resonator ($Q=2\times 10^5$) at $5.2\ \mu\text{m}$ wavelength [71] or supercontinuum generation from 2 to $10\ \mu\text{m}$ wavelength by mean of rib chalcogenide waveguides [72].

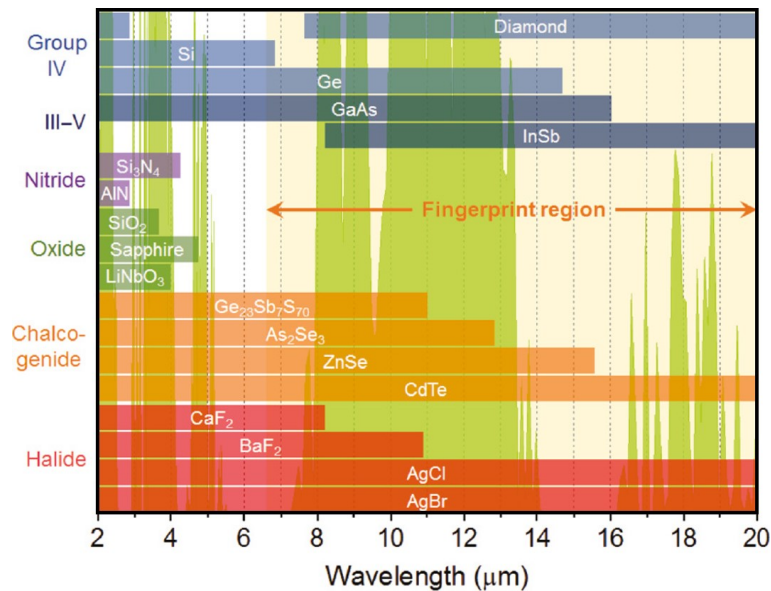


Figure 1.13.: Transparency window of selected materials in the MIR. The horizontal bars represents the transmittance at $-1\ \text{dB}$ and the green background the atmospheric transmission spectrum. Figure taken from Ref. [8].

1.3.2. Si-based photonic integrated platforms

PICs operating in the MIR have experienced an intense development during the last decade. Interestingly, although III-V and chalcogenide materials show wideband features, Si-based platforms have been proposed as a powerful solution to achieve high-performance and cost-effective devices in the MIR regime. The development of silicon photonic platforms in the MIR regime has compelling interest, as they can take advantage of currently available, high-performance and large-scale technologies that have been promoted by the complementary metal oxide semiconductor (CMOS) industry. Silicon-on-insulator (SOI) platforms are widely used for NIR applications, profiting from a high index contrast between silicon ($n\sim 3.5$) and silicon dioxide

($n \sim 1.5$), thus allowing compact devices. This kind of platforms have also been explored in the MIR range. For example, propagation losses as low as 0.6-0.7 dB/cm have been reported at 3.39 μm [73] or an on-chip FTS has been demonstrated at 3.75 μm [74]. However, SiO_2 presents a transparency window limit around 3.5 μm wavelength, thus preventing the use of SOI platforms for applications operating at the middle and longest MIR wavelengths.

To overcome this limitation and extend the operational bandwidth, several approaches have been explored, such as minimizing the optical overlap with the SiO_2 cladding [75]. Nevertheless, the optical mode expansion at longer wavelengths still prevents the use of SOI waveguides in the LWIR regime. Also, different Si-based MIR platforms have been developed by the integration of other materials, including Si-on-silicon nitride (Si_3N_4) or Si-on-sapphire (SOS) platforms [76, 77]. However, silicon nitride and sapphire also show a transparency window limit at approximately 4.5 and 5 μm wavelength, respectively.

Alternatively, suspended-Si has also been proposed as a MIR platform, by mean of under-etching the buried oxide to perform suspended structures. Thanks to a sub-wavelength design, suspended-Si has shown propagation losses of 3.4 dB/cm at 3.4 μm [78]. Nevertheless, the transparency window limit of Si at 7.5 μm wavelength typically prevents the use of this kind of platforms in the LWIR regime as well. Moreover, the liberation of suspended membranes requires the use of acids (typically hydrofluoric acid), which is often preferred to avoid as increases the fabrication complexity and may not be compatible with other fabrication process steps. In this sense, most of the Si-based works reported in the literature have been carried out below 8 μm wavelength. In fact, the development of Si-based platforms operating in the LWIR is highly challenging, as most of the commonly used materials (including Si) present an intrinsic material absorption in this regime.

1.3.3. SiGe-based photonic integrated platforms

Despite the posed challenges, the extension of the operational bandwidth of Si-based circuits to the LWIR, and potentially covering the full fingerprint region (3-13 μm wavelength) and the two atmospheric transparency windows (3-5 and 8-14 μm wavelength), is highly desirable. In this regard, to overcome the above-mentioned limitation, silicon-germanium (SiGe) platforms have aroused as an interesting alternative. Indeed, this kind of platforms have demonstrate the extension of the operational bandwidth to the LWIR, as Ge material show a transparency window up to approximately 15 μm wavelength [8, 79–83]. Moreover, Ge is commonly used in large-scale CMOS industry and is therefore fully compatible with high-performance and cost-effective CMOS fabrication processes [8]. In the following, different Ge-based works are presented. To illustrate a comparative of the present manuscript with the these other works reported in the literature, the Table 1.1 shows the basic features of the selected platforms based on Si and Ge material.

The first demonstration of Ge-on-Si (GOS) strip waveguide was done in 2012 at 5.8 μm wavelength, achieving an average propagation loss of 3.5 dB/cm (measured with a Fabry-Perot

1. Introduction

cavity) [84]. Since then, several GOS works have been reported in the literature. For example, MZI or multiplexers based on planar-concave-gratings and AWGs have been developed by G. Roelkens' group in Gent University [85–87]. Also, G. Z. Mashanovich's group in Southampton University has demonstrated the lowest propagation loss in the MIR by mean of GOS waveguides so far, with 0.6 dB/cm at 3.8 μm wavelength [88]. Going deeper in the MIR, a more recent work from the same research group has demonstrated a minimum propagation loss of 2.5 dB/cm at 7.5 μm wavelength [89]. In 2018, the research group of D. J. Paul in Glasgow University demonstrated propagation losses below 5 dB/cm between 7.5 and 11 μm wavelength in GOS rib waveguides for both TE and TM polarization, by mean of a Fabry-Perot resonance technique [90]. A minimal loss as low as 1 dB/cm was reported in TE polarization, while cutoff propagation (more than 50% of optical power in the Si substrate) prevented TM measurements for wavelengths longer than 10 μm . Based on this platform, the same group has recently demonstrated the potential of Ge-based platforms for spectroscopy sensing in the fingerprint region [91] and a polarization rotator operating between 9 and 11 μm wavelength, too. Finally, it must be also mentioned a very recent demonstration based on a GOS platform, which reported a propagation loss from 6 to 17 dB/cm in the 7-11 μm wavelength range, together to a micro-resonator characterized by thermo-optic effect in 2021 [92]. In this work, a cutoff limitation has also been observed in TM polarization for wavelengths longer than approximately 9 μm .

Ref.	Platform	Losses	Wavelengths	Method	Polarization
[84]	GOS	3.5 dB/cm	5.8 μm	F-P cavity	TM
[85]	GOS	2-4 dB/cm	5.2 - 5.4 μm	Cut-back	TE
[87]	GOS	2.5-4 dB/cm	5.15-5.45 μm	Cut-back	TE & TM
[88]	GOS	0.6 dB/cm	3.8 μm	Cut-back	TE
[89]	GOS	3-20 dB/cm	7.5-8.5 μm	Cut-back (camera)	TE
[90]	GOS	1-5 dB/cm	7.5-11 μm	F-P cavity	TE & TM*
[92]	GOS	6-17 dB/cm	7-11 μm	Cut-back	TE & TM*
[93]	Si _{0.6} Ge _{0.4}	0.5-1.5 dB/cm	3.75-4.75 μm	Cut-back	TE
[94]	grad-SiGe	1-2 dB/cm	4.5-7.5 μm	F-P cavity	TM
[95]	grad-SiGe	2-3 dB/cm	5.5-8.5 μm	Cut-back	TE & TM
This work	grad-SiGe	0.5-4.6 dB/cm	5-11.2 μm	Cut-back	TE & TM

Table 1.1.: Propagation loss features of selected SiGe-based platforms. *Not for the entire wavelength range.

Simultaneously to GOS approaches, Ge-on-SOI platforms have also been reported, benefiting from a higher thermal and electrical isolation. Hence, thermo-optic phase shifters and thermally-tunable racetrack resonators have been demonstrated at 5 μm wavelength [96, 97]. Ge-on-insulator and Ge-on-silicon nitride platforms have also been proposed, taking advantage of higher a refractive index contrast than GOS [98, 99]. However, the intrinsic material absorption of SiN or SiO₂ (when compared to Si and Ge) is expected to limit the operational MIR bandwidth.

It must be also noted that, an air-cladded Ge membrane platform would benefit from the wide transparency window of Ge (from approximately 2 to 15 μm wavelength). In this sense, photonic crystal cavities [100], nanocavities [101] and micro-resonators [102] have been demonstrated in suspended-Ge platforms by M. Takenaka's group in Tokyo University around 2 μm wavelength, showing a quality-factor up to $Q \sim 57,000$. Also, a consortium led by Malaga University (Spain) proposed a suspended Ge-membrane with a sub-wavelength design that experimentally performed 5.3 dB/cm losses at 7.7 μm wavelength. This kind of platforms may be a definitive way to benefit from the broad transparency window of Ge. However, the fabrication process complexity increases due to the cladding removal and experimental demonstrations in the LWIR are still missing in the literature.

Alternatively, the use of SiGe-alloy platforms presents the advantage of material engineering to optimize the waveguide refractive index profile and thus tailor the optical mode confinement. For instance, strip SiGe-alloy waveguides with a constant composition at 60% of Ge have been demonstrated, performing propagation losses as low as 0.5 dB/cm at 4.75 μm wavelength [93]. Also, the first demonstration of a graded-index SiGe platform for MIR applications was done by S. Nicoletti's group at CEA-Leti in 2014 [94]. In this work, the Ge concentration gradually increases and decreases from 0% to 40% in Si-cladded waveguides, demonstrating 2 dB/cm propagation losses at 7.4 μm wavelength. Later, an AWG operating around 4.5 μm wavelength was also demonstrated by mean of this platform [103].

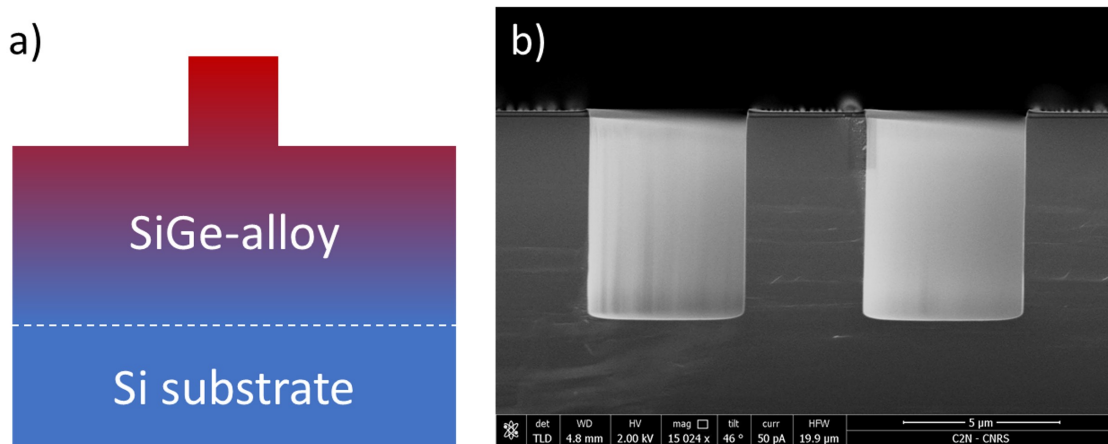


Figure 1.14.: (a) Cut-view schematic of a graded-index SiGe platform. (b) Scanning electron microscope (SEM) cut-view image of a graded-SiGe waveguide fabricated during this thesis.

In the context of PICs for MIR sensing applications, Ge-rich graded-index SiGe platforms with air cladding (Fig. 1.14) have also been proposed in 2017 [104], in a collaboration between Paris-Sud (now Paris-Saclay) and Politecnico di Milano Universities. Since the optical mode is guided through Ge-rich layers and far from Si substrate, this type of platforms is expected to perform a wide operational spectral range, potentially up to 15 μm wavelength and covering the full transparency window of Ge. Later in 2018, this collaboration proposed three different graded-index profiles [95], showing 2-3 dB/cm propagation losses up to 8.5 μm wavelength in both TE and TM polarization. Subsequently, a whole set of passive building blocks operating in

1. Introduction

the MIR up to $8.5 \mu\text{m}$ wavelength have been demonstrated: dual-polarization MZI [105], Fabry-Perot resonant cavity [106], racetrack resonators [107], integrated FTS [108] or a theoretical polarization rotator [109]. Moreover, it has also been noted the interest of this kind of platforms for nonlinear phenomena [110] or free-space communications [111].

1.4. Outline of thesis

The work I present in this PhD manuscript leverages on previous works on Ge-rich graded-index SiGe waveguides to go a step further towards a more complete MIR platform, in the framework of an ongoing collaboration between C2N (Paris-Saclay University-CNRS, France) and L-NESS (Politecnico di Milano, Italy) laboratories. Since previous works were only dedicated to passive devices, I address in this manuscript the design, fabrication and characterization of thermally-tuned, nonlinear and electro-optic effect devices operating in a wide MIR spectral range (including the LWIR), that were crucially missing in the literature. The development of these building blocks would pave the way towards the future realization of the integrated sensor conception envisaged in this thesis and shown in Fig. 1.15. Therefore, the work I report in this manuscript significantly contributes to the long-term development of cost-effective, portable and robust MIR devices that can be widely used in a plethora of applications, and especially in multi-molecule sensing purposes in any context.

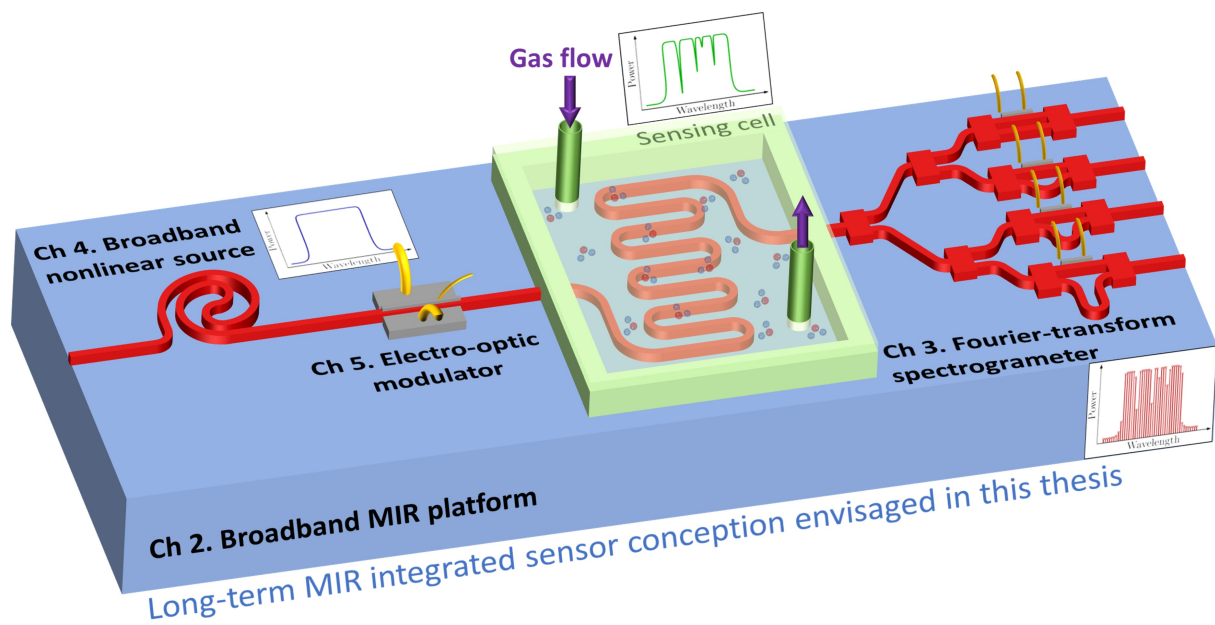


Figure 1.15.: Overview of the long-term integrated sensor conception envisaged in this PhD thesis. The contribution of the four main chapters of this manuscript is also indicated.

In this manuscript I have experimentally demonstrate a broadband MIR platform and three related building blocks. Therefore, this manuscript is divided in the following four main chapters:

- **Chapter 2. Broadband MIR platform:** This chapter addresses the different challenges to achieve a broadband MIR platform capable to operate up to the LWIR regime, and beyond the Si absorption. Optical confinement performances will first be studied by numerical analyses. Then, I will discuss different fabrication processes and experimentally investigate the propagation losses of the fabricated waveguides. Finally, I will characterize two MZI devices to confirm the broadband operation of graded-SiGe platforms.
- **Chapter 3. Integrated Fourier-transform spectrometer in the MIR:** Classic integrated spatial-heterodyne FTS is a robust approach to implement on-chip spectrometers for sensing applications, thanks to calibration matrix methods. However, this implementation typically show a tradeoff between the number of required intereferometric structures, bandwidth and resolution. In this regard, I will propose in this chapter a novel approach that overcomes this limitation, breaking this classical tradeoff. This breakthrough is achieved by mean of thermally tune the path-length unbalance in a MZI array. I will provide a theoretical model and simulated results, to later fabricate a device and report an experimental demonstration that confirms the advantages of this new approach.
- **Chapter 4. On-chip supercontinuum generation in the MIR:** In this chapter I will explore the use of nonlinear phenomena, and in particular SCG, to provide a wide MIR source with a single device. I will provide accurate numerical simulations, to later fabricate and experimentally characterize the SCG at different pump powers and wavelengths. Then, I will analyze the remarkably broad spectral expansion results, obtained thanks to the unique and flexible dispersion features of the graded-index SiGe waveguides. Finally, spectral coherence simulations will also be provided.
- **Chapter 5. Integrated MIR electro-optical modulator:** Electro-optical modulator (EOM) operating in a wide MIR range are crucial for sensitivity enhancement via synchronous detection. In this regard, I will first report in this chapter a broadband evaluation of the free-carrier plasma dispersion (FCPD) absorption effect in the MIR, which was previously missing in the literature. By mean of all-optical modulation modeling and measurements, I will experimentally confirm previous FCPD predictions. These results allow the further exploration of integrated EOMs in the MIR range. Hence, I will subsequently propose an absorption EOM design. Then, I will fabricate and characterize the EOM device from 6.4 to 10.7 μm wavelength in static and dynamic modulation regimes, and in carrier depletion and current injection configurations. Finally, I will also provide a numerical model in depletion configuration that allows future optimized EOM designs.

1. Introduction

2

Broadband MIR platform

The graded-index SiGe platform and the integrated waveguide fabrication process is presented in the following chapter, to later show its propagation loss characterization and investigate different sources of losses. Finally, to validate the potential of this platform for wideband on-chip devices, an experimental MZI demonstration is also reported.

2.1. Ge-rich graded-index SiGe platform

The development of MIR platforms based on Si and Ge material, and in particular operating in the LWIR, presents important challenges. In one hand, the overlap between the optical mode and the Si substrate must be minimized, in order to avoid multiphonon absorption in the LWIR regime (Fig. 2.1(a)). On the other hand, achieving a good material quality is decisive. The epitaxial growth of Ge on top of Si is critical, as there is a 4.2% lattice mismatch between Si and Ge material. As depicted in Fig. 2.1(b), this lattice mismatch leads to a high misfit dislocation density, especially in the interface between Si and Ge in GOS platforms. Therefore, a high threading dislocation density (TDD) is created in the deposited material layer, thus increasing the propagation losses.

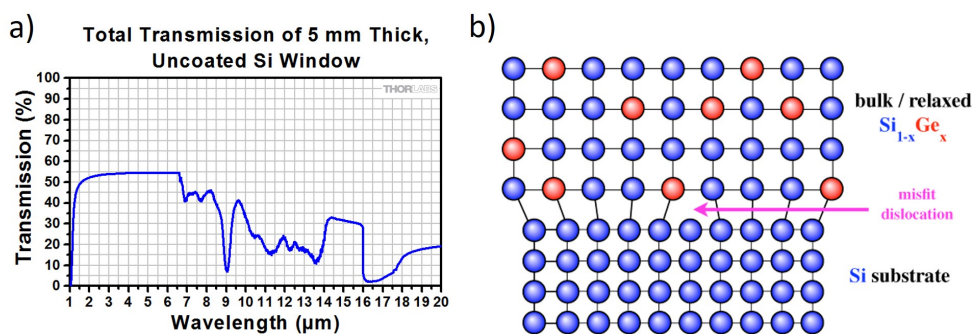


Figure 2.1.: (a) Optical transmission through 5 nm-thickness of silicon as function of the wavelength. Figure taken from Ref. [112]. (b) Misfit dislocation schematic due to 4.2% mismatch between Si and Ge. Figure taken from Ref. [113].

2. Broadband MIR platform

To overcome these limitations, this work relies on a graded-index SiGe platform that smoothly adapts the lattice mismatch along a relatively thick deposited layer. Interestingly, as it was reported in Ref. [95], this epitaxial growth is highly versatile and different graded-index profiles with different thicknesses can be implemented. Among the different possibilities, this work has mainly focused on a 13 μm -thickness graded-SiGe platform on top of a Si substrate, as depicted in Fig. 2.2(a). In this platform, the Ge concentration linearly increases from 0% to 79% along a 11 μm -thickness layer, followed by a 2 μm constant composition layer at 80% of Ge. The epitaxial growth is done by low-energy plasma-enhanced chemical vapor deposition (LEPECVD) at 5-10 nm/s, which is carried out by G. Isella's group in L-NESS laboratory of Politecnico di Milano University (Como, Italy). The smooth lattice transition along the 11 μm thickness leads to low TDD, with typical values of $3 \times 10^6 \text{cm}^{-2}$ and 3.5 nm root-mean square surface roughness [114].

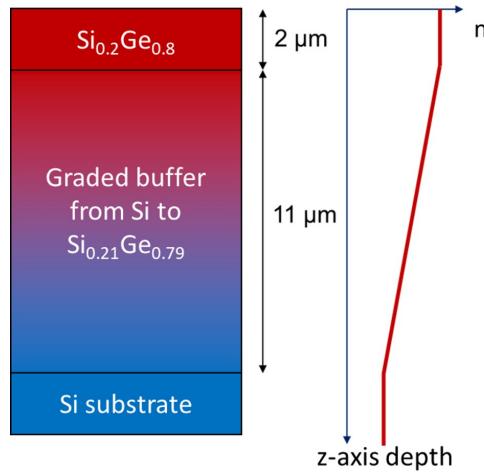


Figure 2.2.: (a) Cut-view scheme of the graded-index platform and representation of the refractive index profile as a function of the vertical z -axis depth.

In order to accurately simulate the optical mode profiles in this kind of platforms, the refractive index of Si (n_{Si}) and Ge (n_{Ge}) are obtained at each wavelength by the fitting equations Eq. 2.1 and Eq. 2.2 reported in Ref. [80] (data taken from Refs. [115, 116]), where the wavelength λ is expressed in μm . Then, the vertical refractive index profile $n(z)$ is calculated by weighting the $\text{Si}_{1-x}\text{Ge}_x$ alloy as in Eq. 2.3, where $x(z)$ is the Ge concentration as a function of the vertical position (z) in the layer stack. This index profile is then introduced in a mode solver software (Mode, Lumerical) to perform the optical simulations.

$$n_{Si}^2(\lambda) = 11.6858 + \frac{0.939816}{\lambda^2} + \frac{0.00810461 \times 1.1071^2}{\lambda^2 - 1.1071^2} \quad (2.1)$$

$$n_{Ge}^2(\lambda) = 9.28156 + \frac{6.7288 \times \lambda^2}{\lambda^2 - 0.664116^2} + \frac{0.21307 \times \lambda^2}{\lambda^2 - 62.21013^2} \quad (2.2)$$

$$n(z) = n_{Ge} x(z) + n_{Si} (1 - x(z)) \quad (2.3)$$

Thanks to this modeling, the optical properties of the integrated waveguides can be subsequently investigated. In the following, I will compare two waveguide designs with a squared profile (same width and height) of 4 and approximately 6 μm . The first dimension (4 μm) has been commonly used in previous works [104, 105, 108, 110], while the second one (approximately 6 μm) has been optimized in this manuscript.

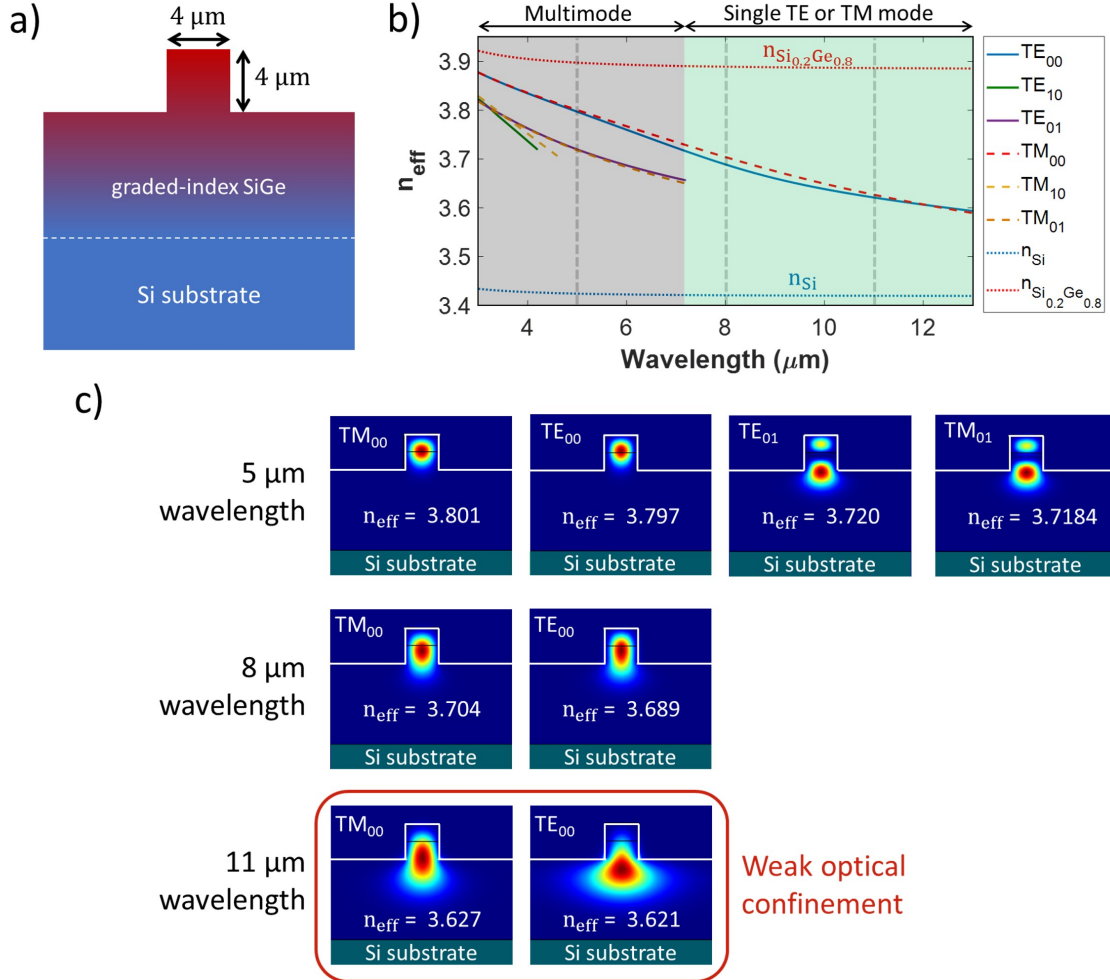


Figure 2.3.: (a) Schematic of the waveguide dimensions used for simulations. (b) Effective refractive index as a function of the wavelength of the first three TE and TM optical modes. The refractive index of the Si and Si_{0.2}Ge_{0.8} alloy are also included. In green background: single TE and TM mode operation. In grey background: multimode operation. In vertical dash lines: wavelength of 5, 8 and 11 μm . (c) Simulated optical profiles of the different modes obtained at 5, 8 and 11 μm wavelength. The modes have been ordered by increasing effective refractive index (n_{eff}) in each simulated wavelength (row) from left to right.

As seen in Fig. 2.3, different simulations are performed for a waveguide dimension of 4 μm width and height. The effective refractive index (n_{eff}) values of the first six optical modes are reported in Fig. 2.3(b). The refractive index (n) of the Si_{0.2}Ge_{0.8} alloy (higher Ge concentration in the waveguide) and Si material (the substrate) have also been included in this figure, as an illustration of the upper and lower n_{eff} limits of the guided modes. A low polarization depend-

2. Broadband MIR platform

ence is observed and the fundamental TE and TM modes can be guided in a wide MIR range. However, as depicted in grey background color in Fig. 2.3(b), multimode operation is obtained in both polarizations at wavelengths lower than $7.2 \mu\text{m}$. Then, to study the confinement properties of the waveguide, the field profiles of the different modes at $5, 8$ and $11 \mu\text{m}$ wavelength (represented as vertical dashed lines in Fig. 2.3(b)) are obtained and reported in Fig. 2.3(c). As observed in this figure, although this waveguide dimension can propagate the fundamental TE and TM modes up to wavelengths as long as $11 \mu\text{m}$, the optical mode is not strongly confined inside the waveguide profile at the longest MIR wavelengths. This fact present different drawbacks. First, the optical mode expansion towards the Si substrate increases the propagation losses due to Si multiphonon absorption in the LWIR regime. Second, the radiation loss in sharp bends is also increased, thus requiring larger device structures. Third, the effective modal area is also increased at the longest wavelengths, hence reducing the light-matter interaction. This last fact is detrimental for nonlinear effects or optical sensing purposes, among others.

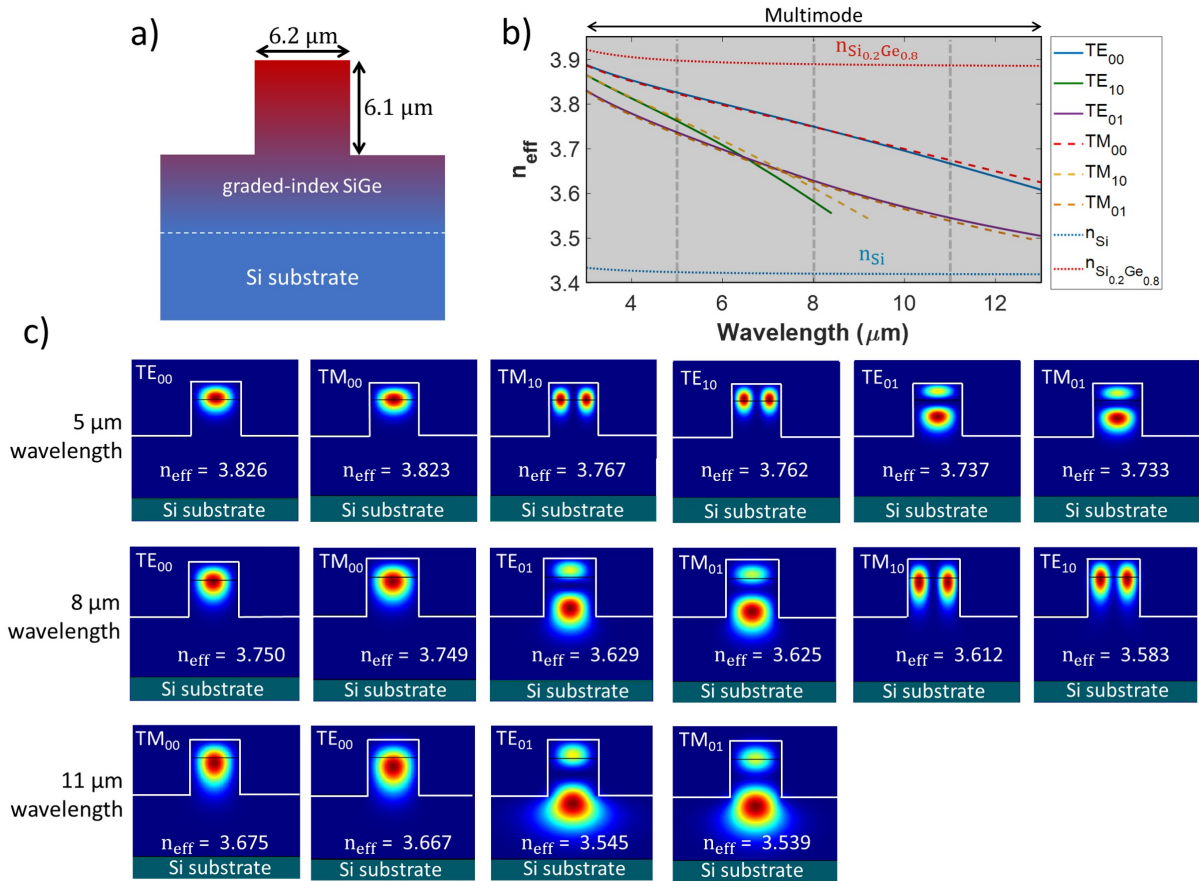


Figure 2.4.: (a) Schematic of the waveguide dimensions used for simulations. (b) Effective refractive index as a function of the wavelength of the first three TE and TM optical modes. The refractive index of the Si and $\text{Si}_{0.2}\text{Ge}_{0.8}$ alloy are also included. In grey background: multimode operation. In vertical dash lines: wavelength of $5, 8$ and $11 \mu\text{m}$. (c) Simulated optical profiles of the different modes obtained at $5, 8$ and $11 \mu\text{m}$ wavelength. The modes have been ordered by increasing effective refractive index (n_{eff}) in each simulated wavelength (row) from left to right.

In order to improve the confinement features of the SiGe waveguide at the longest MIR wavelengths, I have investigated deeper and wider profiles. As seen in Fig. 2.4(a), similar simulations are performed for an optimized waveguide dimensions of $6.2 \mu\text{m}$ width and $6.1 \mu\text{m}$ height (as they will be later fabricated). A low polarization sensitivity and broadband MIR guiding properties are likewise obtained, as observed in Fig. 2.4(b). In contrast, multimode operation is obtained for wavelengths shorter than $13 \mu\text{m}$, as reported in grey background color in the same figure. Nevertheless, although single mode operation may be a desired scenario, this kind of multimode behavior does not impede the use of the fundamental TE and TM modes in most of applications, as it has been demonstrated in previous works [105–108] or in Ref. [117]. Moreover, as observed in Fig. 2.4(c), a high optical confinement with a relatively low effective modal area is achieved in the upper Ge-rich layers, for both fundamental modes, and up to wavelengths as long as $11 \mu\text{m}$. The overlap with the Si substrate is also minimized, thus avoiding high propagation losses due to multiphonon absorption. Therefore, despite the multimode operation, this waveguide dimension interestingly enables low propagation losses and high optical confinement at the longest MIR wavelengths.

Furthermore, the graded-index profile introduces an extra degree of freedom to perform refractive index and confinement engineering. Interestingly, when analyzing the mode profile simulations at different wavelengths, a self-adaptation of the optical mode towards high Ge concentrations is appreciated. As it will be later discussed in Chapter 4, this fact leads to a remarkably wide anomalous dispersion condition, while achieving a relatively high confinement. This unique feature makes this kind of platforms ideal for nonlinear phenomena implementations, such as supercontinuum generation (SCG).

2.2. Fabrication of graded-index SiGe integrated waveguides

In previous works, this graded-SiGe platform has experimentally demonstrated low propagation losses up to $8.5 \mu\text{m}$ wavelength, by mean of $4 \mu\text{m}$ width and depth waveguides [95]. However, achieving higher etching depths with a vertical waveguide profile and low sidewall roughness present several challenges. Indeed, a maximum of $4 \mu\text{m}$ etching depth could be achieved in previous fabrications. Therefore, in order to provide high confinement features and optimize nonlinear phenomena in the LWIR regime, among other possible purposes, new fabrication processes must be developed.

During the first year of my PhD thesis and the closed period of new cleanroom facilities in C2N laboratory, I developed during one month the main fabrication processes in the facilities of Politecnico di Milano University (Polifab), together with V. Vakarín (former postdoc of C2N). Then, I also developed and optimized a complete fabrication process in C2N facilities, in a close collaboration with X. Le Roux (C2N engineer). The general fabrication process flow is illustrated in Fig. 2.5. In the following, the fabrication processes that I developed in both cleanrooms are detailed.

2. Broadband MIR platform

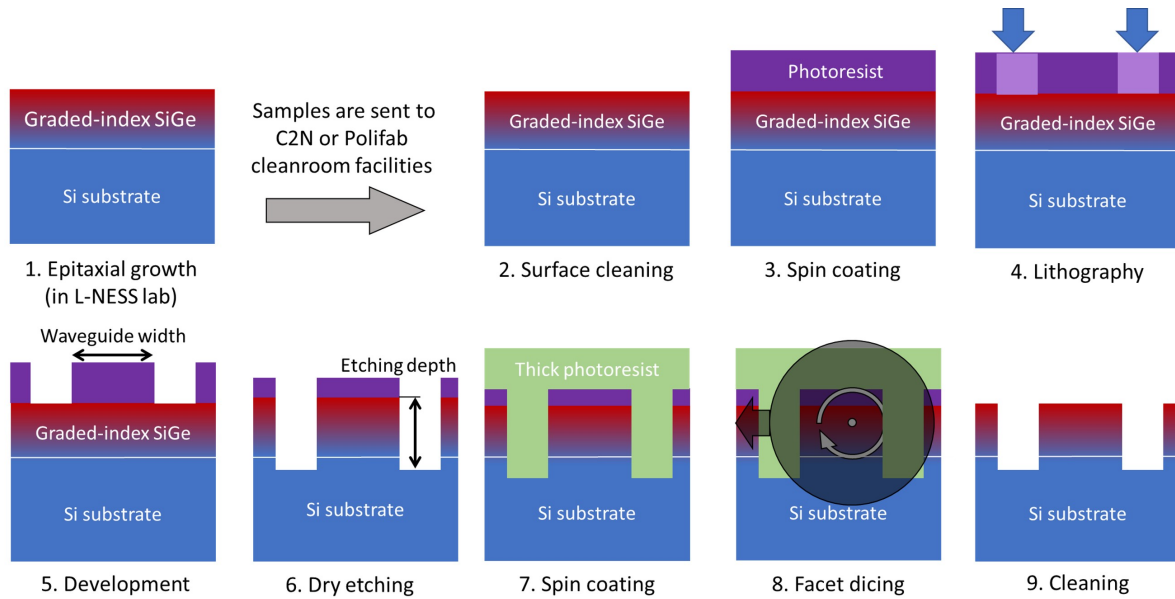


Figure 2.5.: Schematic of the general fabrication process flow of integrated SiGe waveguides.

2.2.1. Fabrication processes developed in Polifab

First, the graded-index platform is growth on a 4-inch Si wafer in L-NESS laboratory (Como, Italy). Then, the wafer is sent to next cleanroom facilities (C2N or Polifab) to continue its fabrication process. The typical sample size is 2×2 cm, which is manually cleaved from the 4-inch wafer on which the SiGe-alloy layers were monolithically grown. The sample surface is cleaned by 10 minutes ultrasonic bath in acetone and another 10 minutes in isopropanol (IPA).

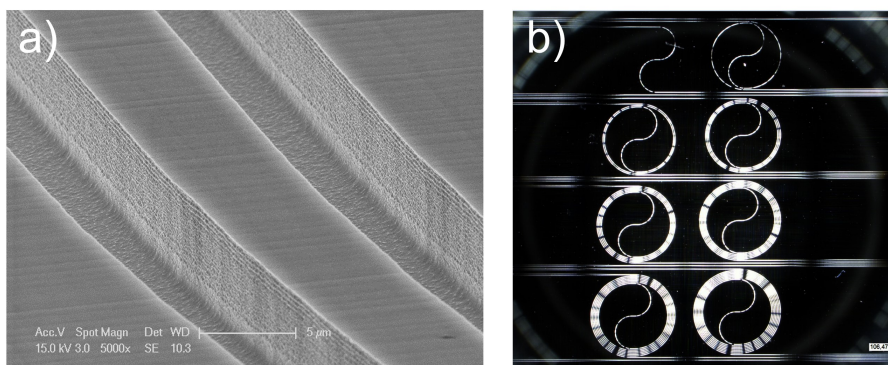


Figure 2.6.: Images of waveguides fabricated in Polifab. (a) SEM image of the $6.1 \mu\text{m}$ -height and $6.2 \mu\text{m}$ -width waveguide. (b) Top-view optical microscope image of different spiral waveguides with increasing propagating length.

Then, the four following fabrication steps were developed in Polifab. First, a spin coating process is used to deposit a Ti-primer layer, followed by AZ-5214-E photoresist. Second, the structures are patterned with a laser lithography equipment (Heidelberg MLA100). Third, the pattern is developed in a AZ-726-MF bath during 75 seconds. Fourth, the waveguide sides are etched by mean of an inductively coupled plasma reactive ion etching (ICP-RIE). In this pro-

cess, the gas flow injected to the equipment chamber alternates from SF₆ to C₄F₈ in a sequenced scheme, thus performing the commonly called Bosch process. As seen in the scanning electron microscope (SEM) image of Fig. 2.6(a), the different fabrication parameters were optimized to achieve a good waveguide profile with acceptable sidewalls roughness. Also, different waveguides with increasing length from 0.55 to 14.8 cm were fabricated in a spiral shape, as seen in Fig. 2.6(b), with a waveguide dimensions of 6.2 μm width and 6.1 μm height.

2.2.2. Fabrication processes developed in C2N

Additionally, I have also developed a complete fabrication process in new cleanroom facilities of C2N. In this, the sample is likewise cleaned at its arrival, after the graded-index platform growth. Next, an electronic photoresist is spin coated on top of the sample, in order to benefit from its higher resolution when compared to optical photoresists. However, due to the selectivity of the subsequent dry etching step, a minimum deposited thickness of 1 μm is required to properly achieve relatively deep waveguide profiles (> 4 μm etching depth). Initially, ZEP-520A photoresist was explored in a multi-layer approach. However, 3 to 4 layers were needed, and the resulting high strain caused cracks in the photoresist material, thus preventing a good deposition quality. Alternatively, AR-P 6200.18 (CSAR-62) photoresist was investigated. Interestingly, an optimized spin coating process at 1250 rpm provides a resist deposition thickness of approximately 1.3 μm with a good uniformity, thus largely achieving the initial 1 μm thickness required. Therefore, CSAR-62 is hereafter chosen for the electronic lithography step. Finally, 5 minutes post-bake at 180 °C is performed.

Then, I have also calibrated the subsequent electronic lithography step in two different electron-beam (e-beam) equipment (Raith EBPG 5200 and NanoBeam nB4), identifying the optimal setting parameters, such as nominal dose or beam step size. Since CSAR-62 is a positive photoresist, 5 μm paths are typically defined at both sides of the waveguide. After the electronic exposition, the areas where the resist has been illuminated are removed in a 2 minute bath in ZED-N50 developer, followed by 1 minute in IPA. As seen in Fig. 2.7(a), good photoresist mask profiles are achieved.

As next step, a dry etching process has also been developed. To perform anisotropic etching, an ICP-RIE process is used in a continuous manner. In this, a combined flux of C₄F₈ and SF₆ gasses is injected into the chamber of the equipment (ICP-SPTS) to feed the generated plasma. As seen in Fig. 2.7(b), the process setting are optimized to achieve a vertical waveguide profile with a low sidewalls roughness. Also, an average photoresist etching rate value of 4 nm/s is obtained, with a typical SiGe etching rate of 26 nm/s. In this regard, with 1.3 μm thickness of deposited CSAR-62, a maximal depth of 8.4 μm could be theoretically achieved. However, it is highly recommended to keep a thin layer of photoresist remaining after the etching process, in order to ensure a correct protection of the waveguide surface. Therefore, in practice, a maximal depth of 8 μm is expected for the currently developed process, which is remarkably two-fold the previous fabrication limit. Also, since Ge has a higher etching rate than Si material, and its

2. Broadband MIR platform

concentration is modified along the platform depth, the obtained etching rate value is not linear with the resulting depth. Therefore, it must be noted that each graded-index platform should be independently considered for the etching fabrication step.

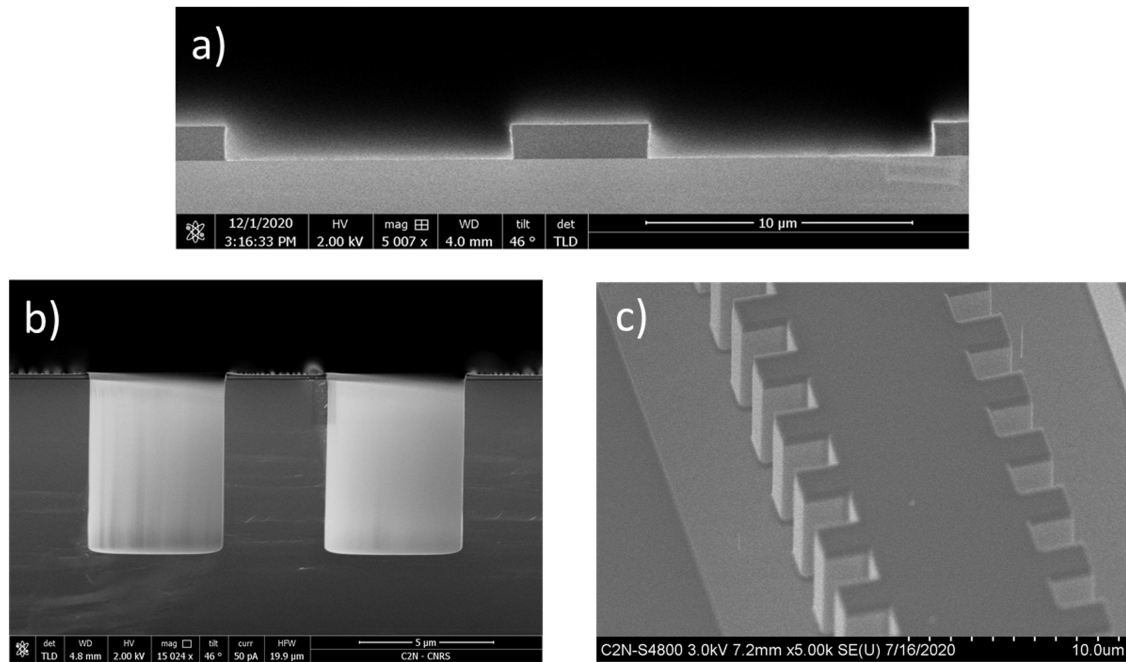


Figure 2.7.: SEM images of fabricated structures in C2N. (a) Cut-view of 1.3 μm -thickness CSAR-62 photoresist mask. (b) Cut-view of 6.5 μm -height and 5 μm -width waveguide. A 150 nm photoresist thickness is remaining after the etching step. (c) Top-view of periodic horizontal structures with top remaining photoresist after dry etching step.

Thanks to the fabrication process here developed, not only straight waveguides can be patterned, but also more complex structures can be implemented. For instance, as seen in Fig. 2.7(c), periodic sidewall structures with good profile features are also achieved. This sort of periodic structures is convenient for the fabrication of Fabry-Perot resonant cavities or integrated rejection filters, among other possible implementations.

To allow an edge coupling to the waveguide from a free-space beam, the facets of the waveguides must be diced. However, the fabricated structures must be protected during this mechanical process. Therefore, a thick photoresist (AZ-4562) is first spin coated on top of the sample. Then, the waveguide facets are mechanically diced by D. Bouville (C2N engineer) with a 6000 grid-size blade (DISCO-P1A-SERIES), to provide an optically-polish quality result. Finally, the protecting and remaining (CSAR-62 left after the etching process) photoresists are removed with a 5 minutes acetone bath, followed by 5 minutes in 2-butanone and 5 minutes in IPA. To ensure a good sample cleaning, 10 minutes of plasma oxygen cleaning is also performed. As optional final step, piranha (H_2O_2 and sulfuric acid) cleaning bath can also be implemented to ensure a proper cleaning. The resulting input facet after the dicing step is shown in Fig. 2.8. It must also be noted that, to allow an efficient edge coupling, a 50 μm -width waveguides are placed at input and output facet of the device, followed by 1.5 mm-length taper transitions.

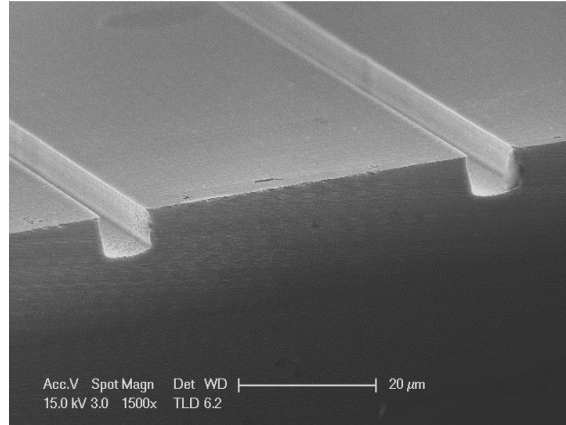


Figure 2.8.: SEM image of the 50 μm -width input waveguide facet after the dicing step in C2N.

Interestingly, these devices are achieved with a single lithography and etching steps, thus simplifying the fabrication process. Moreover, this kind of graded-index SiGe waveguides are based on Si-compatible fabrication processes and materials. These facts allow the development of cost-effective integrated devices and systems that can be widely spread.

2.3. Propagation loss characterization of SiGe waveguides

2.3.1. Experimental setup for propagation loss measurements and results

In order to characterize the propagation losses of the fabricated waveguides, I built up an experimental setup in new C2N facilities. As seen in Fig. 2.9(a), a tunable MIR laser (Mircat, Daylight Solutions) is placed on an optical table, with a monochromatic wavelength range from 5.1 to 11.2 μm . Then, the light is injected and collected in the waveguides thanks to a pair of ZnSe aspherical lenses. The output beam is collected in a Mercury Cadmium Telluride (MCT) photodetector (DSS-MCT(14)020, Horiba) cooled down with liquid nitrogen. As the MIR laser is operating in pulsed regime with 5% duty cycle at 100 kHz frequency, the trigger signal is directly used in a lock-in amplifier system to enhance the signal-to-noise (SNR) ratio. It must be noted that the voltage detected in the lock-in equipment, and shown in further figures, is directly related to the optical power collected in the MCT detector. Then, to sequentially set the laser source wavelength and collect the signal detected in the lock-in amplifier, a Labview program is adapted from previous works. Also, the output beam of the laser equipment is fixed to TM polarization. However, high-efficient polarization rotators that cover the entire spectral band of the laser source (5.1 to 11.2 μm wavelength) have not been commercially developed, and to rotate the sample in order to change the injected polarization is not a desired scenario. Therefore, to allow dual polarization measurements in the entire spectral band without any wavelength-dependent consideration, I used the polarization rotator schematic shown in Fig. 2.9(b). This system is based on a set of broadband gold-coated mirrors that can be placed in the optical beam path by mean of a pair of flip mirrors.

2. Broadband MIR platform

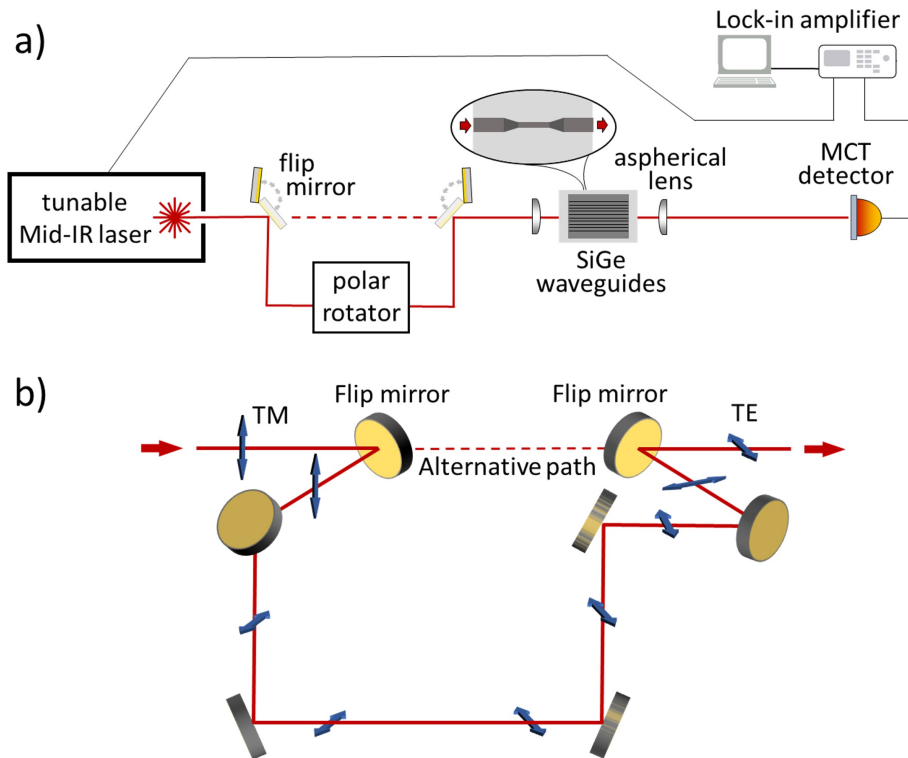


Figure 2.9.: (a) General view schematic of the propagation loss characterization setup. (b) Broadband free-space polarization rotator system based on gold mirrors. Blue arrows represent the electric field orientation.

By mean of this characterization setup, the transmission spectra of the fabricated waveguides of $6.2 \mu\text{m}$ width and $6.1 \mu\text{m}$ height are experimentally obtained, to later calculate its propagation losses by cut-back method. To that end, the measured wavelength is progressively selected in the tunable laser to build up the transmission spectrum, with a wavelength step of 5 nm . In fact, the MIR light source equipment (Mircat, Daylight Solutions) is composed by four different tunable QCLs, as seen in Fig. 2.10(a). The transition wavelengths between the four light sources are depicted as dashed vertical lines. This characterization is repeated for different waveguides, with an increasing length from 0.55 to 14.8 cm (as previously fabricated). For the sake of clarity, the waveguide length has been normalized with the shortest 0.55 cm -length straight reference waveguide. Moreover, for each measured transmission, the aspherical lenses position, and in particular the focal length, is optimized at several wavelengths, in order to allow an efficient and broadband coupling. A spectral spacing below of $1 \mu\text{m}$ is set between optimized wavelength positions. Also, these wavelengths in which the coupling is optimized are fixed within the whole set of measurements, in order to later perform a correct propagation loss characterization. The different transmission results for TM polartization are shown in Fig. 2.10(b). As observed in this figure, since the experimental setup is based in a free-space configuration and the MIR spectral range lies to multiple atmospheric absorption lines, the resulting transmission spectra are highly noisy between 5 and $7.5 \mu\text{m}$ wavelength. In contrast, a clear spectrum trace is obtained in the second MIR atmospheric transparency window ($8\text{-}14 \mu\text{m}$ wavelength).

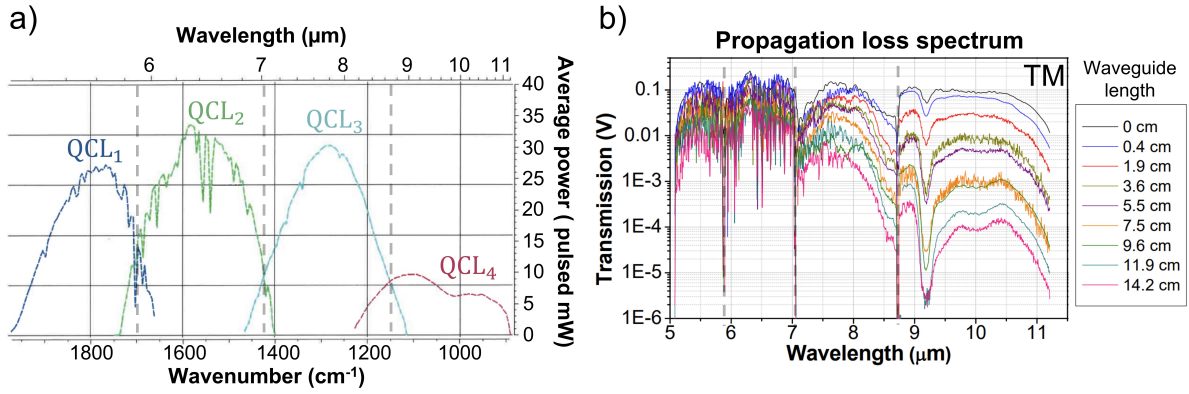


Figure 2.10.: (a) Optical transmission of the MIR source used for propagation loss measurements. (b) Optical transmission as a function of the wavelength, in TM polarization and for different waveguide lengths. The voltage detected in the lock-in amplifier is directly related to the optical power collected. In vertical dashed lines: transitions between the four QCLs in the equipment.

Then, cut-back method calculations are performed. To that end, a linear fit of the optical transmission as a function of the normalized waveguide length is done at each wavelength sampling point. The Fig. 2.11 shows a fit example of three different wavelengths: 6, 8 and 10 μm. The slope of the linear regression gives the optical propagation losses, which is commonly presented in logarithmic scale as dB/cm. Also, the error obtained from this linear fit can be later used to estimate the incertitude of the propagation loss measurements. As observed in this figure, the experimental data show a good linearity, meaning low incertitude in the measurements. Indeed, as several waveguides are fabricated with an increasing length up to a relatively long normalized distance (i.e., 14.2 cm), the measuring incertitude is significantly reduced.

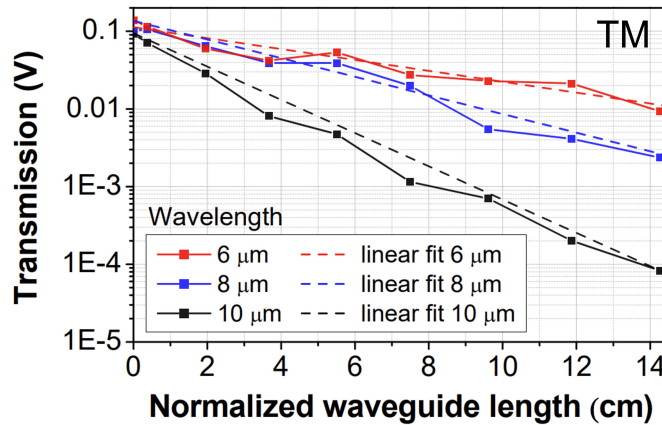


Figure 2.11.: Linear fit of the optical transmission as a function of the normalized propagating length at 6, 8 and 10 μm wavelength in TM polarization.

I have performed this characterization method for TE and TM polarization, and the results are reported in Fig. 2.12. To minimize the resulting measurement noise, mainly due to the absorption lines between 5 and 7.5 μm wavelength, a noise filtering is implemented. In this

2. Broadband MIR platform

regard, I have chosen a Savitzky-Golay (savgol) filter with 30 sampling points window (150 nm wavelength span) and 3rd polynomial order. Unlike other filtering approaches, such as moving average, savgol filters preserve the mean value and performs a better smooth in discrete absorbing media, as is the case here. Error bars at selected wavelengths are also obtained as $\hat{\epsilon}=(1-R^2)\alpha$, where $\hat{\epsilon}$ is the estimated error, α is the propagation loss experimentally obtained and R^2 is the coefficient of determination (R-squared) calculated as the Pearson product-moment correlation from previous linear regression calculations.

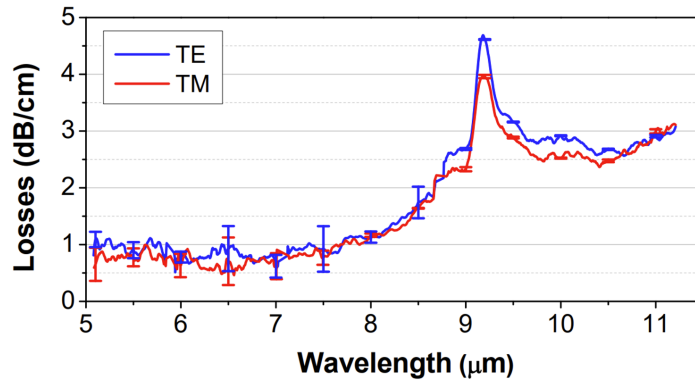


Figure 2.12.: Propagation losses as a function of the wavelength for TE and TM polarizations. Error bars are obtained from the R-squared coefficient of the linear fit in cut-back method calculations.

As shown in Fig. 2.12, propagation losses between 0.5 and 1.2 dB/cm are achieved from 5 to 8 μm wavelength and below 3 dB/cm between 9.5 and 11.2 μm wavelength. Interestingly, similar results are obtained in both TE and TM polarization, avoiding the typical TM cutoff limitation of GOS platforms at the longest wavelengths. As it is later explained, an increase of the propagation loss up to 4 and 4.6 dB/cm in TM and TE polarization is observed at 9.2 μm wavelength, respectively. Nevertheless, the propagation loss remains moderate over the entire characterized spectral range, allowing its use for most of on-chip MIR applications.

2.3.2. Study of propagation loss contributions

Despite the good propagation loss results obtained, it is still interesting to investigate different sources of losses to better understand the gradient-index platform limitations and further explore possible routes for improvement. In this regard, I have investigated the following sources of optical propagation loss:

- **Silicon substrate absorption:** Silicon material present multiphonon absorption at wavelengths beyond 7.5 μm . Therefore, numerical simulations of the optical mode profile are performed (as previously detailed) to identify the optical mode overlap with the Si substrate. The overlap value is directly given by the mode solver (Mode, Lumerical) as a power fraction of the optical mode that superposes the selected region, as in Eq. 2.4 [118]. As seen in Fig. 2.13, the simulated mode overlap value remains below 0.01% in the entire

2.3. Propagation loss characterization of SiGe waveguides

spectral range reported (i.e., from 5 to 11 μm wavelength). Therefore, the Si substrate contribution is considered negligible and hereafter not considered as a source of propagation losses.

$$overlap = Re \left[\frac{\left(\int \vec{E}_1 \times \vec{H}_2^* \cdot d\vec{S} \right) \left(\int \vec{E}_2 \times \vec{H}_1^* \cdot d\vec{S} \right)}{\int \vec{E}_1 \times \vec{H}_1^* \cdot d\vec{S}} \right] \frac{1}{Re \left(\int \vec{E}_2 \times \vec{H}_2^* \cdot d\vec{S} \right)} \quad (2.4)$$

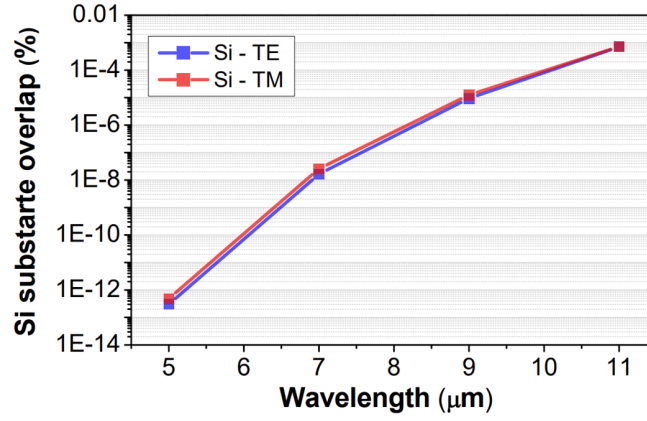


Figure 2.13.: Optical mode overlap in % with the Si substrate as a function of the wavelength for both TE and TM polarizations and for 6.1 μm -height and 6.2 μm -width SiGe waveguides.

- **Interstitial oxygen in Si:** Oxygen impurities in silicon is known to cause Si-O-Si vibrations, leading to an absorption peak centered at 9.04 μm wavelength (1106 cm^{-1} wavenumber) [119]. Interstitial oxygen ($\text{Si}_i:\text{O}$) in SiGe alloy has also been studied in the literature and the absorption peak has been identified to experience a red-shift displacement, possibly due to the expansion of Si-Si bonds in the SiGe lattice [120, 121]. This effect has also been observed in GOS platforms [90]. Therefore, the increase of propagation losses around 9.2 μm wavelength is considered to have its origin in oxygen impurities during the epitaxial growth of the SiGe alloy, carried out by LEPECVD.

To validate this analysis, secondary ion mass spectrometry (SIMS) measurements are externally performed by Eurofins Scientific. As seen in Fig. 2.14 in blue color, the oxygen concentration depends on the vertical axis depth. First, a constant concentration of $1.5 \times 10^{17} \text{ cm}^{-3}$ is measured in the top 2 μm -thickness constant composition layer of $\text{Si}_{0.2}\text{Ge}_{0.8}$ alloy. Then, a concentration peak of $2.7 \times 10^{17} \text{ cm}^{-3}$ is observed in the interface between the constant composition and the graded-index SiGe layers. Finally, the oxygen concentration decreases with the platform depth.

Numerical simulations are also performed to analyze the optical profile of the fundamental TE and TM polarization modes. In these, a slightly deeper optical propagation of

2. Broadband MIR platform

TM than TE polarization is observed. Therefore, a higher overlap between the optical TE mode and higher oxygen impurities concentrations in the upper part of the waveguide is assumed to be the origin of slightly higher propagation loss around $9.2 \mu\text{m}$ wavelength in TE (4.6 dB/cm) than TM polarization (4 dB/cm).

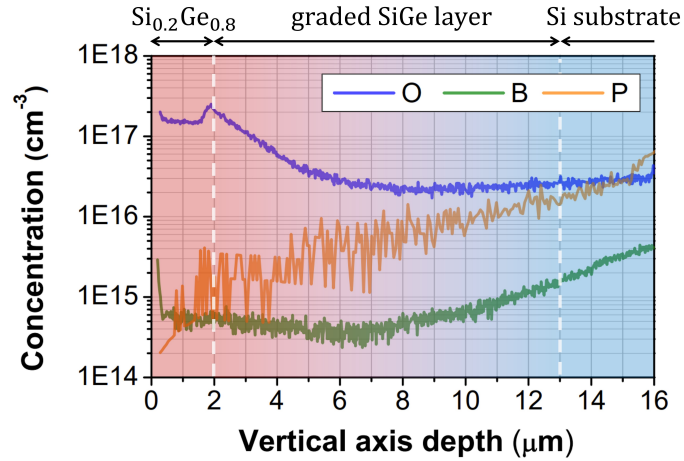


Figure 2.14.: SIMS characterization results of oxygen (blue), phosphorous (yellow) and boron (green) concentration as function of the vertical axis depth. The zero in the horizontal axis depth means the top sample surface. The layer stack of the graded-index platform has also been depicted in a colored background, separated by vertical dashed lines.

- **Free-carrier absorption:** In the classical Drude model, the free-carrier plasma-dispersion (FCPD) effect increases as a function of the squared of the wavelength, thus showing a stronger effect in the MIR than in the NIR regime. However, this classical model does not consider quantum phenomena and the FCPD effect experimentally increases as a function of the wavelength with different fluctuations. In fact, the free-electrons experience intraband transitions by absorbing the MIR light. Then, the hot electrons lose the energy excess by different scattering processes. In contrast, the free-holes experience transitions from the heavy to the light-hole band. This is also the reason why free-holes show a higher FCPD effect than free-electrons. This FCPD has been first pseudo-empirically model in the MIR [122] and later experimentally confirmed [123] in the literature.

In this regard, boron (p-type) and phosphorous (n-type) dopant concentration profiles are also obtained by SIMS measurements and reported in Fig. 2.14. A mean concentration value of $2 \times 10^{15} \text{cm}^{-3}$ is estimated for electrons and $5 \times 10^{14} \text{cm}^{-3}$ for holes in the top $6 \mu\text{m}$ platform depth. Therefore, n-type dopant is identified as dominant. As the optical mode is mainly confined in the upper $6 \mu\text{m}$ thickness, a residual $1.5 \times 10^{15} \text{cm}^{-3}$ electron concentration value is considered for the SiGe platform, and used in next propagation loss calculations. Based on this electron concentration value and the model reported in Ref. [122], the propagation loss contribution due to free-carriers is expected to increase from 0.2 dB/cm at $5 \mu\text{m}$ wavelength to 1.2 dB/cm at $11.5 \mu\text{m}$. The calculated values are shown in green color in Fig. 2.15.

- Sidewall roughness:** Since the fabricated waveguides are relatively deeply etched, with a height of $6.1 \mu\text{m}$, the effect of the sidewall roughness on the propagation loss is also considered. To that end, I have used the model reported by Payne & Lacey in Ref. [124] for planar waveguides and later developed for SOI strip waveguides in Ref. [125]. The propagation loss contribution is calculated as in Eq. 2.5, where n_c is the waveguide core refractive index (here taken as a constant weighted value of $\text{Si}_{0.2}\text{Ge}_{0.8}$), σ the sidewall roughness standard deviation, d is half the waveguide width, $g(V)$ is a value is determined by the waveguide geometry (as in Ref. [125]) and $f(x)$ is determined by the geometry and correlation length (as in Ref. [125]). Therefore, it is needed to estimate 2 parameters: correlation length (L_c) and the roughness standard deviation (σ).

$$\alpha_{\text{roughness}} = \frac{4.34}{2\pi} \frac{\sigma^2}{k_0 \sqrt{2} d^4 n_c} g(V) f(x) \quad (2.5)$$

To obtain both parameters (L_c and σ), the following analysis is made. First, Si multiphonon absorption is only expected for wavelengths longer than $7.5 \mu\text{m}$. Hence, free-carrier absorption and sidewall roughness are assumed to be the main propagation loss contributions between 5 and $7.5 \mu\text{m}$ wavelength. As previously discussed, the residual free-carrier effect is estimated by SIMS measurements and evaluated models [122, 123]. Therefore, the sidewall roughness is considered as the main remaining contribution in this wavelength range. In this regard, L_c and σ are fitted, in order to match the experimental losses with the combination of free-carriers and sidewall roughness in the $5.0\text{-}7.5 \mu\text{m}$ wavelength range. In this manner, values of $L_c=100 \text{ nm}$ and $\sigma=9 \text{ nm}$ are obtained. Those values are in good agreement with other works in MIR waveguides reported in the literature [89]. Finally, the combined contribution of sidewall roughness and free-carrier absorption is shown in black color in Fig. 2.15.

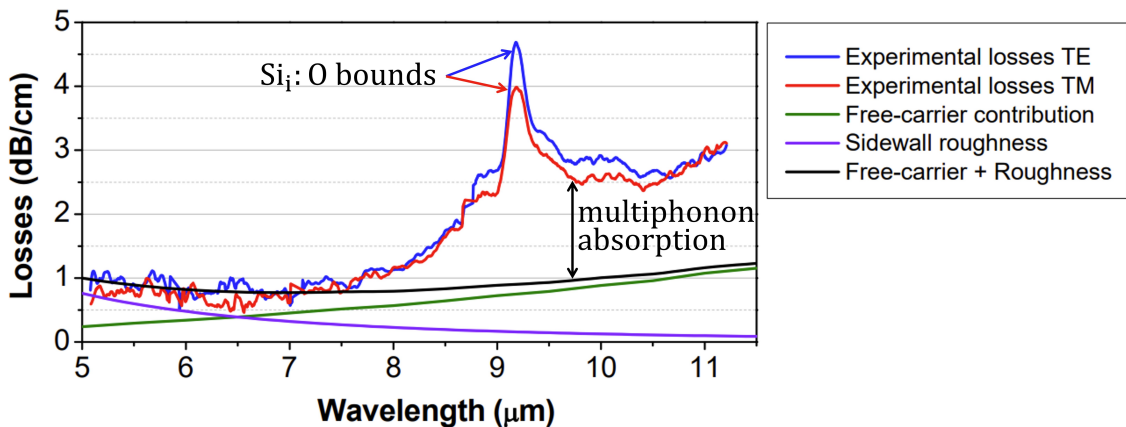


Figure 2.15.: Experimental propagation loss of fabricated waveguides and expected contributions. In purple: sidewall roughness contribution with 9 nm standard deviation and 100 nm correlation length. In green: $1.5 \times 10^{15} \text{ cm}^{-3}$ electron concentration. In black: combination of both sidewall roughness and free-carrier contributions.

2. Broadband MIR platform

- **Multiphonon absorption of silicon:** Silicon material show intrinsic multiphonon absorption at wavelengths longer than $7.5 \mu\text{m}$ [126], while Ge show absorption for wavelengths longer than approximately $15 \mu\text{m}$ [127]. The absorption spectra of SiGe alloys have also been reported with different concentrations [121]. However, a detailed study of graded-SiGe absorption in the LWIR regime is still missing in the literature. Hence, the propagation loss contribution due to the multiphonon absorption of the graded-SiGe alloy is considered as the residual difference between the experimental results and the rest of contributions considered here: sidewall roughness, free-carriers and interstitial oxygen absorption localized at $9.2 \mu\text{m}$ wavelength. In this sense, the multiphonon absorption in the SiGe waveguides is assumed to increase the propagation losses up to a maximum value of approximately 1.7 dB/cm for wavelengths between 7.5 and $11.5 \mu\text{m}$, while it can be considered as negligible at lower wavelengths.

From these investigations, the following analysis is deduced. On the one hand, the propagation losses between 5.0 and $7.5 \mu\text{m}$ wavelength are mainly due to sidewall roughness and free-carrier absorption, taking values lower than 1 dB/cm for both polarizations. On the other hand, for wavelengths longer than $7.5 \mu\text{m}$, the losses are mainly caused by free-carriers and Si multiphonon absorption, taking values below 3 dB/cm between 9.5 and $11 \mu\text{m}$ wavelength. Additionally, an absorption peak centered at $9.2 \mu\text{m}$ wavelength is observed, as a result of oxygen impurities during the epitaxial growth. It must be noted that, due to the smooth adaptation of the lattice mismatch between Si and Ge material along the graded-index SiGe layer, low threading dislocation densities are expected and thus have not been considered in this analysis. Propagation loss values lower than 4.6 dB/cm are achieved for the entire spectrum range here reported, and for both polarizations. Noticeably, these values are compatible with most of MIR applications.

In future works, I expect that these results can still be improved. First, the Si multiphonon absorption in the LWIR regime can be reduced by modifying the SiGe gradient-index profile. For instance, by increasing the Ge concentration up to 100% , it is expected to minimize the optical overlap with high Si concentrations and thus reduce the propagation losses at the longest MIR wavelengths. Second, the absorption peak due to interstitial oxygen can be minimized by modifying the epitaxial growth process of the SiGe-alloy layers, such as placing a specific gas filter in the LEPECVD equipment. Third, the free-carrier concentration due to residual dopants (B and P) can be either reduced or finely tuned to achieve a doping compensation effect. Finally, the waveguides used for the experimental characterization were fabricated by laser lithography in Polifab facilities. The fabrication of waveguides with e-beam lithography and an optimized dry etching process in C2N is also expected to reduce the propagation losses due to sidewall roughness at the lowest wavelengths. Therefore, if these improvements are addressed, propagation losses of 0.5 dB/cm are expected between 5 and $7.5 \mu\text{m}$ wavelength, while around 2 dB/cm are foreseen between 7.5 and $11 \mu\text{m}$ wavelength.

2.4. Experimental demonstration of a wideband MZI device

The Ge-rich graded-index SiGe platform here proposed has shown low propagation losses in a wide MIR spectral range. As next step, the demonstration of broadband devices would confirm the potential of this kind of platforms for MIR applications. To that end, I address the experimental characterization of a broadband MZI device in this section.

Indeed, a MZI device was designed by mean of this graded-SiGe platform in Ref. [105], demonstrating a good operation between 5.1 and 8.5 μm wavelength. In that work, an optimized multimode interference (MMI) design was used as a splitter and combiner, based on waveguides of 4 μm height and width. The design schematic and an optical top-view image of the fabricated MMI are shown in Fig. 2.16(a). Interestingly, the fabricated MMI had a simulated operational band (at -1 dB loss limit) from approximately 5.5 to 11.0 μm wavelength, as seen Fig. 2.16(b). However, the full spectral band could not be experimentally demonstrated in Ref. [105]. Furthermore, this MMI design was also exploited in Ref. [108] for an integrated spectrometer demonstration, in which an array of MZIs with increasing path-length unbalance was implemented, as seen in Fig. 2.16(c). Nevertheless, the experimental bandwidth in which this MZI array was characterized was likewise limited at the longest wavelength to 8.5 μm . Therefore, the extension of these demonstrations towards longer MIR wavelengths is highly interesting to confirm the viability of this platform to implement broadband devices, capable to operate in the LWIR range of the MIR spectral band.

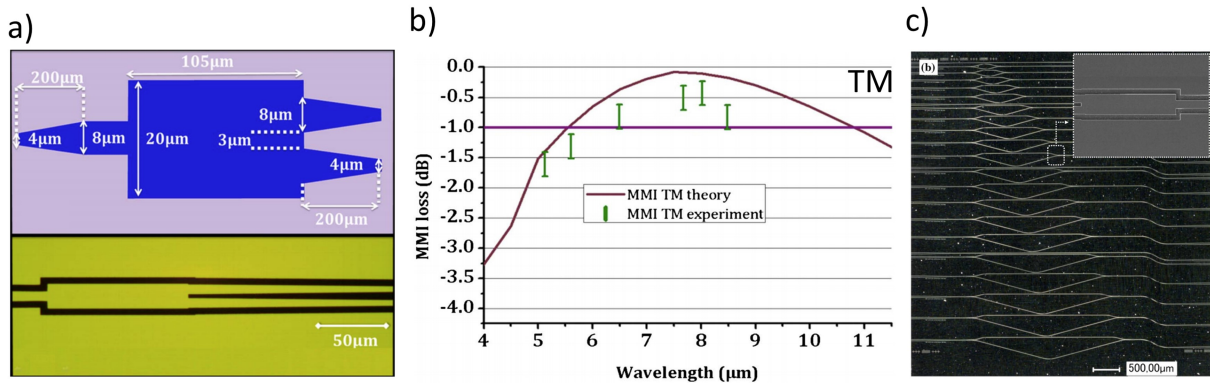


Figure 2.16.: (a) Top-view schematic and optical image of an optimized MMI design with 4 μm width and height graded-index SiGe waveguides. (b) Spectral transmission of the corresponding MMI structure in TM polarization. In brown: simulated and normalized losses as a function of the wavelength. In purple: a horizontal line indicates the -1 dB operational bandwidth. In green dots: measured losses distribution. (c) Optical microscope image of an MZI array. Inset: SEM image of the MMI design used as splitter and combiner. Figures taken from [105, 108].

In this regard, the experimental setup used for previous propagation loss measurements is also used to obtain the optical transmission of the already available MZIs. Hence, the fabricated waveguides are 4 μm width and height, and a similar MMI design as in Fig. 2.16(a) is used as splitter and combiner. A good MZI operation is expected up to 11 μm wavelengths, due to the MMI bandwidth. Also, as it was previously demonstrated in numerical simulations (Fig. 2.3),

2. Broadband MIR platform

this waveguide dimension is capable to guide the TM polarization up to 11 μm wavelength, while single mode operation is only achieved for wavelengths longer than 7.2 μm . Then, to experimentally demonstrate the wideband features of graded-SiGe platforms, I have characterized a straight waveguide and two asymmetric MZIs with arm-length unbalance of 47 and 84.6 μm in TM polarization, and from 5.1 to 11.2 μm wavelength. Next, the transmission of both MZIs is normalized with respect the straight waveguide, and the results are reported in Fig. 2.17. Similar to previous figures, a savgol filter is also applied. In this case, a 4th polynomial order and 100 nm window are chosen (instead of 3rd order and 150 nm), in order to better follow the resonances.

As seen in Fig. 2.17, clear resonances are shown in both MZIs between approximately 5.5 and 10.5 μm wavelength (i.e., from 950 to 1800 cm^{-1} wavenumber). From the different resonance positions, the FSR_{σ} can be extracted, taking values of 55 ± 1 and 31 ± 0.5 cm^{-1} for 47 and 84.6 μm path-length unbalance, respectively. It must be noted that the FSR in wavenumber is fixed, while it increases as a function of the wavelength (proportional to λ^2). To obtain the FSR_{σ} in-certificate, I have use the data collected to obtain the standard deviation as $\sqrt{\frac{\sum(FSR_i - FSR_{mean})^2}{N}}$, where FSR_i is the the experimental value at each peak resonance, FSR_{mean} the mean value and N the number of peak resonances considered. Moreover, from these values, the average group index value of the fundamental TM mode along the measured MIR wavelength range can also be calculated as $n_g = \frac{1}{\Delta L FSR_{\sigma}}$, taking a value of 3.861 (mean value of both MZIs).

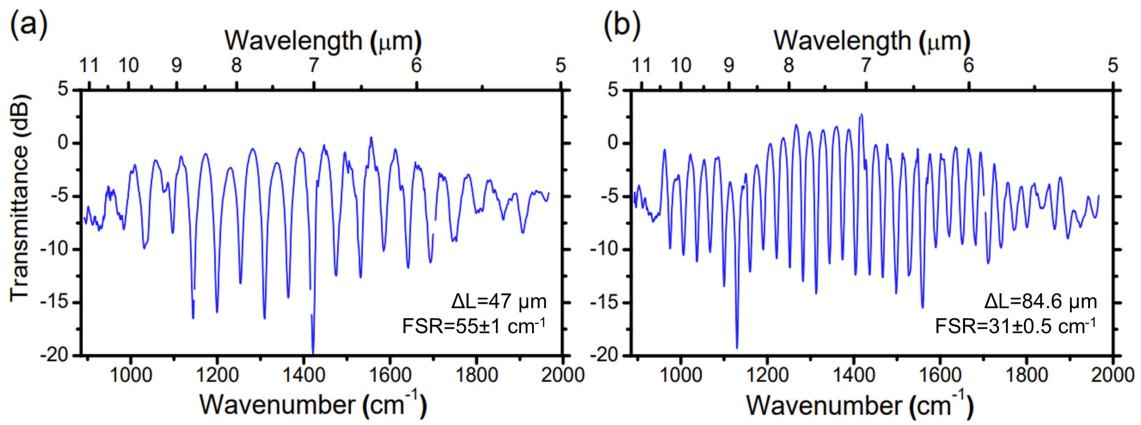


Figure 2.17.: Optical transmission in TM polarization as a function of wavelength (top x-axis) and wavenumber (bottom x-axis), normalized with a straight waveguide of two asymmetric MZIs with arm unbalance of (a) 47 μm and (b) 84.6 μm . A savgol filter with 20 samples window (i.e., 100 nm wavelength span) and 4th order polynomial filter is applied.

Interestingly, these results reveal different facts. On one hand, the wideband operation of the designed MMI and fabricated MZI devices is experimentally confirmed, showing the great potential of Ge-rich graded-index platforms to provide broadband devices in the MIR regime. On the other hand, even though single mode operation was only expected for wavelengths longer than 7.2 μm (Fig. 2.3), the MZI devices did not suffer from strong coupling to higher-order modes at the shortest wavelengths. Otherwise, strong resonances would have not been appreciated between 5.5 and 7.2 μm wavelength in Fig. 2.17.

2.5. Conclusions and routes for improvement of broadband MIR graded-index SiGe platforms

In summary, in this chapter I have developed a Si-based PIC platform capable to host a wide MIR spectral range, and almost covering the full fingerprint region, with an acceptable propagation loss for most of MIR applications. To that end, a model of the Ge-rich graded-index SiGe platform has been first provided, in order to perform accurate optical simulations. Thanks to this model, an optical mode profile analysis has been reported for two waveguide dimensions. This study reveals that relatively high etching depths must be achieved ($> 4 \mu\text{m}$ depth), in order to obtain a high mode confinement at the longest MIR wavelengths. This fact is crucial for further efficient nonlinear demonstrations, among others.

In this regard, a full fabrication process has been developed in new C2N cleanroom facilities, while alternative fabrication steps were also developed in Polifab cleanroom. Then, I deployed an experimental setup in new C2N laboratory facilities, in which the spectral range has been extended to longer wavelengths (up to $11.2 \mu\text{m}$) when compared to previous works. Thanks to this new fabrication process and characterization setup, waveguide propagation losses lower than 4.6 dB/cm have been achieved between 5.1 and $11.2 \mu\text{m}$ wavelength for both TE and TM polarizations. Notably, these results are compatible with most of integrated MIR applications and, to the best of my knowledge, this is the lowest propagation loss experimentally demonstrated up to $11 \mu\text{m}$ wavelength by mean of SiGe-based waveguides.

At the end of this chapter, I have also addressed the experimental characterization of two MZI devices, showing clear resonances between 5.5 and $10.5 \mu\text{m}$ wavelength. Interestingly, even if multimode operation is expected at wavelengths shorter than $7.2 \mu\text{m}$, strong coupling to higher-order modes is not observed. These results confirm the possibility to operate in multimode regime in SiGe waveguides, while also demonstrating the broadband performance of MMI structures used in MZI devices. Therefore, these results confirm the great potential of Ge-rich graded-SiGe platforms to develop broadband MIR on-chip systems.

In conclusion, the results that I have presented in this chapter are particularly interesting for sensing applications, as the fabricated waveguides have air cladding and are expected to host the full fingerprint region of the MIR ($3\text{-}13 \mu\text{m}$ wavelength). Therefore, in the aim to progress towards the development of an on-chip multi-molecule sensor, it is highly interesting to exploit this graded-index SiGe platform to develop further integrated building-blocks that are essential but still missing in the literature.

2. Broadband MIR platform

3

Integrated Fourier-transform spectrometer in the MIR

This chapter is devoted to the development of a compact and high-resolution integrated spectrometer operating in a wide MIR range, by mean of a Fourier-transform spectrometer (FTS) implementation. In the following, different integrated FTS demonstrations will be presented. A novel FTS approach will be then proposed, which overcomes the classical tradeoff limitation of previous works. An analytic model will be presented, followed by a robust and flexible retrieval method process. The advantages of this new approach will then be illustrated with numerical simulations. Finally, the fabrication of this device will be addressed and experimental results provided, confirming the advantages of this new integrated FTS approach.

3.1. State-of-the-art and working principle of integrated FTS

While free-space spectrometers have been generally introduced in Chapter 1, this thesis has been devoted to the development of integrated devices, as they would provide compact and robust sensing systems. In this regard, several integrated spectrometer approaches have been reported in the literature, such as AWG or echelle gratings [86,87]. However, the maximal resolution of these dispersion-based approaches is intrinsically limited by the diffraction limit of the device. Furthermore, its performance can be highly affected by fabrication imperfections, too. Alternatively, integrated FTS schemes have aroused as an interesting approach to implement high-performance spectrometers, as they benefit from different advantages when compared to its dispersion-based counterparts: Connes, Fellgett and Jacquinot advantages [128–130]. Therefore, the photonics integration of FTS systems with high bandwidth and resolution is highly interesting and, consequently, multiple integrated FTS approaches have been reported in the literature. Although they have generally been developed for the first time in the NIR regime, two main integrated approaches are highlighted in this manuscript and discussed below: stationary wave and heterodyne FTS. To better compare the later selected works, their main figures of

3. Integrated Fourier-transform spectrometer in the MIR

merit are summarized in Table 3.1: central wavelength, operational bandwidth, resolution and size (number of structures used). Since some of them are reported in the NIR and others in the MIR, it is often preferred to compare the resolution and bandwidth of the different spectrometers in wavenumber rather than in wavelength, as the FTS spectral response (as well as the FSR of a MZI) is constant as a function of the wavenumber, while it increases as a function of the wavelength.

Ref.	Design	Size	Resolution	Bandwidth	Wavelength
[131]	SWIFT	1 waveguide	16.6 cm^{-1}	400 cm^{-1}	1550 nm
[132]	SWIFT	1 waveguide	76 cm^{-1}	1270 cm^{-1}	890 nm
[133]	SH-FTS	32 MZI	0.17 cm^{-1}	3 cm^{-1}	1550 nm
[134]	SH-FTS	42 MZI	2 cm^{-1}	42 cm^{-1}	$3.75 \mu\text{m}$
[108]	SH-FTS	20 MZI	15 cm^{-1}	132 cm^{-1}	$6.75 \mu\text{m}$
[135]	SH-FTS	16 MZI	0.34 cm^{-1}	2.4 cm^{-1}	1570 nm
[136]	SI-FTS	1 MZI	0.8 cm^{-1}	82 cm^{-1}	1560 nm
[137]	SI-FTS	1 MZI	13 cm^{-1}	233 cm^{-1}	1550 nm
This work	TT-SH-FTS	9 MZI	15 cm^{-1}	603 cm^{-1}	$7.7 \mu\text{m}$

Table 3.1.: Overview figures of merit of selected integrated FTS demonstrations.

3.1.1. Stationary wave integrated FTS

Inspired by Lippmann’s principle of colour photography, an integrated spectrometer approach was proposed in 2007 [131], named as stationary-wave integrated Fourier-transform spectrometer (SWIFTS). In that work, a co-propagating and counter-propagating wave generated a stationary interference pattern, as illustrated in Fig 3.1. Then, the light was partially scattered and the evanescent field collected by a detector array (gold nanowires). A Fourier-transform of the detected signal was later implemented to retrieve the output spectrum. This first demonstration of SWIFTS reported 4 nm resolution (16.6 cm^{-1} wavenumber) over a spectral range of 96 nm (400 cm^{-1} wavenumber), centered at 1550 nm wavelength. That work showed the possibility to perform compact spectrometers, with no moving parts and relatively high resolution. However, the maximal bandwidth may be compromised, as it is given by the physical spacing between consecutive detectors ($2.7 \mu\text{m}$ in that work).

Later in 2017, a SWIFTS demonstration reported a manner to alleviate the bandwidth constrain of previous works [132]. In that demonstration, the interference pattern was obtained by two co-propagating waves in CMOS-compatible silicon nitride waveguides, centered at 890 nm wavelength. The phase velocity of both waves was slightly shifted, leading to an expansion of the generated interferogram. Hence, the bandwidth constrains given by the separation between photodetectors can be significantly reduced. The experimental resolution reported in that work was 6 nm wavelength (76 cm^{-1} wavenumber) with an expected bandwidth of 100 nm (1270 cm^{-1} wavenumber). In fact, the experimental bandwidth reported in that work was limited to

a lower value, due to the performance constrains of the MMI used to divide the input signal in the two co-propagating waves. Recently, another work has introduced the use of electro-optic properties of a single thin-film lithium niobate waveguide to tune the interferogram and thus enhance the integrated FTS performance [138].

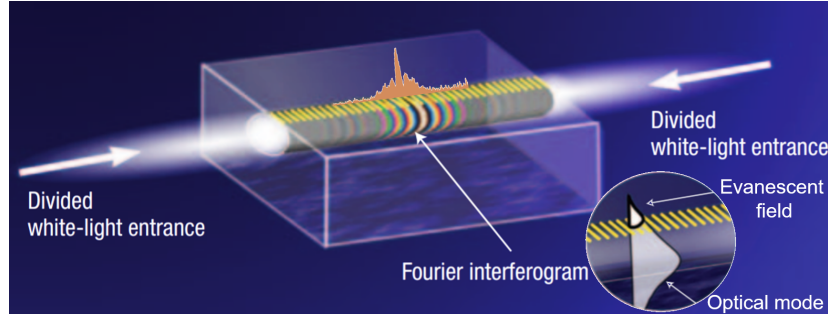


Figure 3.1.: SWIFTS approach schematic, where the input light is divided in both co- and counter-propagative waves. Then evanescent field is collected by an array of gold nanowires. Figure adapted from Ref. [131].

SWIFTS systems are an interesting solution to provide high performance spectrometers in a compact way. However, the demonstration of high-resolution and wideband SWIFTS operating in the MIR regime is still missing in the literature. In particular, the photonics integration of a narrow-gap photodetector array working in the MIR present several outstanding challenges.

3.1.2. Heterodyne integrated FTS

In heterodyne FTS, the input signal is divided to later interfere with a delayed version of itself. In this approach, the resulting interference intensity as a function of the relative delay between both signals (interference pattern) is obtained, to later perform a Fourier-transform to retrieve the input spectrum. Several integrated demonstrations have been reported in the literature, based on the collection of the interference pattern in the spatial or temporal domain. These two approaches are discussed below.

3.1.2.1. Spatial-heterodyne integrated FTS

In 2007, an integrated version of the classical FTS approach was proposed for the first time in Ref. [139], named here as spatial-heterodyne Fourier-transform spectrometer (SH-FTS). In this theoretical proposal, the interference pattern as a function of the path-length unbalance of the conventional free-space FTS is emulated by increasing the arm-length unbalance (ΔL) in an integrated MZI array. As seen in Fig. 3.2(a), the length difference between both arms is linearly increased along the array. Therefore, each MZI is understood as a sampling point of the interference pattern, corresponding to different displacement positions of the moving mirror in the classical free-space FTS. On one hand, and also ruled by Nyquist-Shannon theorem, the spectrometer resolution is given by the optical group index (n_g) and the maximal path-length

3. Integrated Fourier-transform spectrometer in the MIR

unbalance ΔL_{max} of the MZI array (Eq. 3.1). On the other hand, the bandwidth is given by the sampling period ΔL_{step} , which is the path-length difference between consecutive MZIs. The operational bandwidth is also understood as the FSR, which is the spectral range free of aliasing. It means that there is no overlap between the signal and image replicas after the Fourier-transform processing. It means that there is no overlap between the signal and image replicas after the Fourier-transform processing. For a given resolution ($\delta\sigma$), the bandwidth (FSR) is related to the number of MZIs in the array (N), as seen in Eq. 3.2. Therefore, the SH-FTS approach shows a tradeoff between bandwidth, resolution and number of MZIs required. In contrast, the main advantage of the SH-FTS is the calibration matrix procedure proposed to recover the input spectrum, because, unlike its dispersion-based integrated counterparts (e.g., AWG or echelle grating), fabrication imperfection can be mitigated.

$$\text{Resolution} : \delta\sigma = \frac{1}{\Delta L_{max} n_g} \quad [cm^{-1}] \quad (3.1)$$

$$\text{Bandwidth} : FSR_{\sigma} = \frac{\delta\sigma \times N}{2} \quad [cm^{-1}] \quad (3.2)$$

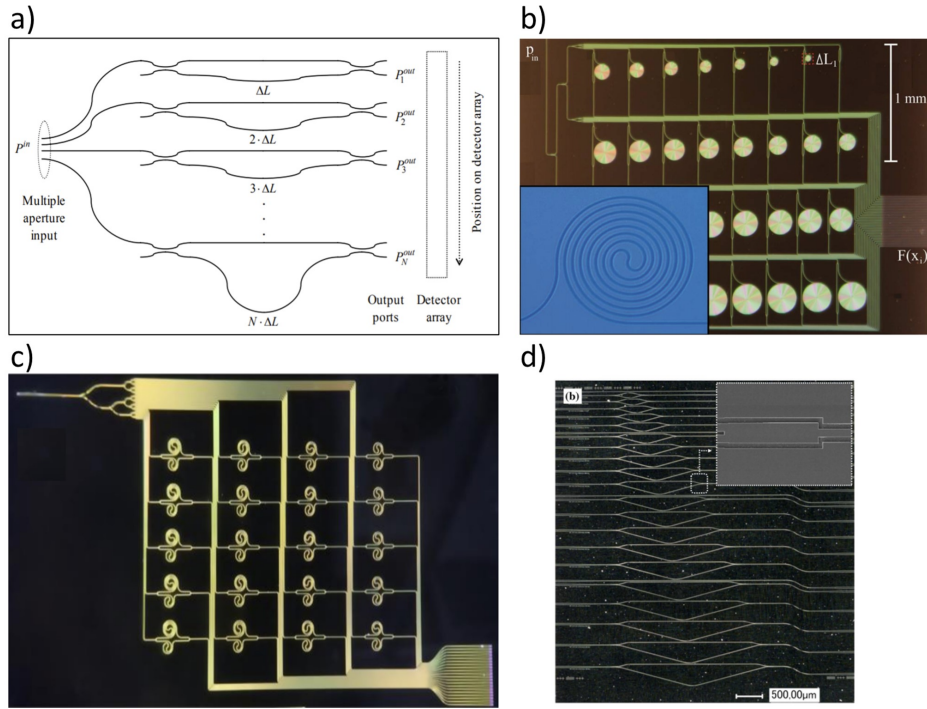


Figure 3.2.: (a) Schematic of SH-FTS based on a MZI array with increasing path-length unbalance between arms. (b) Top-view of SH-FTS based on 32 MZIs operating at 1550 nm wavelength. (c) Top-view of SH-FTS based on 42 MZIs operating at 3.75 μm wavelength. (d) Top-view of SH-FTS based on 20 MZIs operating between 5 and 8.5 μm wavelength. Figures taken from Refs. [108, 133, 134, 139].

Later in 2013, a SH-FTS spectrometer was experimentally demonstrated near 1550 nm wavelength. In that work, a remarkably 0.17 cm^{-1} wavenumber resolution was reported by mean of a 32 MZI array (Fig. 3.2(b)) [133]. Then, in 2015, a similar approach was carried out in the MIR regime, centered at 3.75 μm wavelength (Fig. 3.2(c)) [134]. A 42 MZI array was used to

perform 2 cm^{-1} wavenumber resolution, with a moderate 42 cm^{-1} bandwidth.

Going deeper in the MIR regime, a SH-FTS was experimentally demonstrated up to $8.5 \mu\text{m}$ wavelength in 2018 (Fig. 3.2(d)) [108]. That work was carried out in C2N lab during the PhD thesis of Q. Liu, using the graded-index SiGe platform. Although that spectrometer could operate in a wide spectral range ($5\text{-}8.5 \mu\text{m}$ wavelength range or 830 cm^{-1} wavenumber), the operational bandwidth was limited by the FSR to 132 cm^{-1} , given by the arm-length unbalance step (ΔL_{step}) of the fabricated 20 MZI array. Also, a moderate resolution near 15 cm^{-1} was achieved in the entire spectral range reported. Even though the wideband features of the graded-index SiGe platform were not fully exploited, that work showed the great potential of this platform to provide high-resolution spectrometers in a broad MIR range.

Since remarkably long path-length unbalances can be implemented in integrated MZIs, the SH-FTS approach is able to achieve high resolution features. However, in order to provide high resolution together with a large operational bandwidth, a large number of devices is required, thus increasing size of the device. Moreover, the signal division over a large number of MZIs strongly reduce the SNR.

3.1.2.2. Scanning interferometry integrated FTS

To overcome the SH-FTS limitations, and in particular the signal division over a large number of MZIs, alternative works have been reported in the literature. Among them, integrated scanning interferometry Fourier-transform spectrometers (SI-FTS) have emerged as an interesting approach. Similar to free-space FTS based on a Michelson interferometer (or SH-FTS), the optical path-delay between the two arms is discretely scanned to construct the interference pattern and later retrieve the spectrum. However, unlike SH-FTS in which the entire interference pattern is simultaneously discretized in a MZI array, in the SI-FTS approach the optical path-delay between both arms is externally tuned in time-domain. This modification is performed in a single interferometer, thus avoiding any signal division. Although Si-based SI-FTS demonstrations have not yet been reported in the MIR regime, different integrated SI-FTS works have been carried out in the NIR regime. Among them, two works are highlighted below.

On one hand, in Ref. [136] the path-delay unbalance of a single MZI is discretely scanned by changing the path-length distance in temporal domain. To that end, a reconfigurable interferometer is implemented thanks to a cascade of optical switches, based on a thermo-optic phase shifter design (Fig. 3.3). In this way, the bandwidth and resolution features exponentially scale up with the number of switches, while a compact design is achieved. Thanks to retrieval method techniques and 6 switches, that work reported a remarkable resolution of 0.8 cm^{-1} wavenumber and a moderate bandwidth of 82 cm^{-1} , centered at 1560 nm wavelength. By mean of temporal switching, that demonstration showed the possibility to achieve long path-delays (high resolution) in a compact design, while avoiding any signal division over a large number of MZIs. However, the bandwidth of this approach was still limited by the minimal path-length difference implemented in the reconfigurable interferometer.

3. Integrated Fourier-transform spectrometer in the MIR

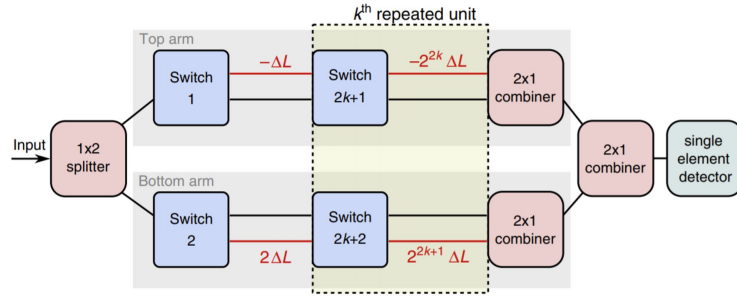


Figure 3.3.: Schematic of a SI-FTS design based on a reconfigurable MZI by mean of a cascade of optical switches. Image taken from Ref. [136].

On the other hand, thermo-optic effect has also been used to produce an interference pattern to later retrieve the input spectrum [140–143]. For instance, in Ref. [137] a MZI was composed by a pair of spiral waveguides, in which the group index of the propagating optical mode was tuned by thermo-optic effect, thanks to a heater on top of one of the MZI arms (Fig. 3.4). In this way, the path-delay can be finely tuned and a high sampling rate of the interference pattern can be achieved, leading to a large operational bandwidth. That work reported a modest resolution of 13 cm^{-1} wavenumber within a noticeable range of 233 cm^{-1} , centered at 1550 nm wavelength. This demonstration showed the possibility to achieve considerable wide operational bandwidths without any signal division. Nevertheless, the resolution was still limited by the maximal tunability of the path-delay. Indeed, since this approach was based on thermo-optic effect in a single MZI, relatively low delay unbalances were achieved. Therefore, unpractical spiral lengths should be implemented to reach a relatively high resolution.

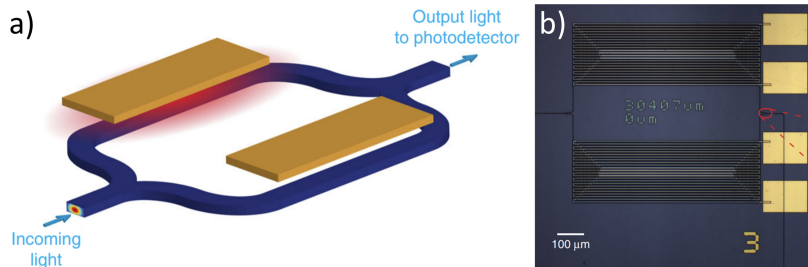


Figure 3.4.: (a) Schematic of a scanning interferometer design based on thermal tuning. (b) Top-view image of SI-FTS implementation. Image taken from Ref. [137].

In summary, several integrated FTS approaches have been reported in the literature during the last two decades. Interestingly, SH-FTS has demonstrated the possibility to achieve high resolution performances. However, it presents an intrinsic tradeoff between resolution, bandwidth and number of MZIs required. Alternatively, SI-FTS has showed the possibility to achieve a wide operational bandwidth by mean of finely tune the optical path-delay of a MZI by thermo-optic effect. Nevertheless, the resolution of this approach is limited by the maximal tunability of one of the MZI arms. Therefore, the bandwidth enhancement of integrated FTS without considerable penalty in terms of resolution or footprint is highly desirable, as a mean to provide high performance, compact and robust detectors that can be used in multiple sensing applications.

3.2. Integrated thermally-tuned spatial-heterodyne FTS: working principle and theoretical modeling

To overcome the limitations of previous integrated FTS reported in the literature, I propose in this section a novel approach of integrated FTS that gathers the advantages of SH-FTS and SI-FTS by thermo-optic effect, which has been named in this manuscript as thermally-tuned spatial heterodyne Fourier-transform spectrometer (TT-SH-FTS) [144]. As seen in Fig. 3.5(a), this approach is based on a MZI array with a linear increase of the path-length unbalance (ΔL_{step}), in which the first MZI is considered as symmetric. Additionally, a thermal heater of length L_H is placed in the longest MZI arm. In this way, the path-delay difference between both MZI arms is achieved by a combination of path-length unbalance and thermo-optic effect, providing an extra degree of freedom when compared to previous SH-FTS works. In the following, I generalize the model reported in Ref. [139] to include the thermal tuning. For simplification, a MZI array with N_L devices is considered for the mathematical analysis, based on a 1-by-2 MMI splitter and combiner. Nevertheless, it could also be implemented with multi-port MMI structures.

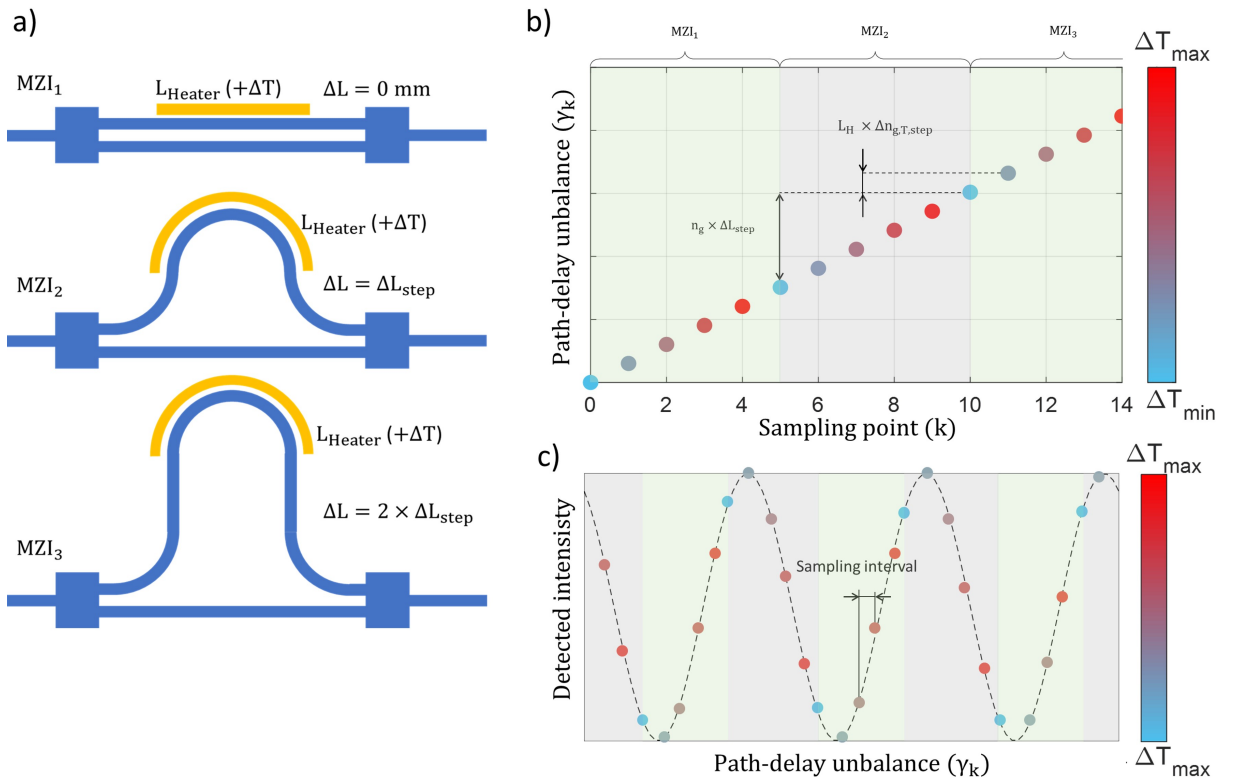


Figure 3.5.: (a) Schematic of TT-SH-FTS approach: the path delay is selected by thermo-optic effect and path-length unbalance. (b) Schematic representation of a linear optical path-delay as a function of the sampling point, for 3 different MZIs and 5 measurements at different temperatures. (c) Interference pattern illustration of a thermally-tuned MZI array.

First, the optical path-delay difference between both arms of the MZI (γ) can be expressed as in the Eq. 3.3, where n_{eff} is the effective index of the optical mode (similar for both MZI arm waveguides), ΔL the path-length difference between arms, L_H the heater length where the

3. Integrated Fourier-transform spectrometer in the MIR

temperatures increase is applied and $\Delta n_{eff,T}$ the effective index variation due to thermo-optic effect. The last effective index variation depends on the thermo-optic coefficient ($\partial n_{eff}/\partial T$) of the optical mode, as seen in Eq. 3.4, where ΔT is the temperature variation. The modification of the refractive index induced by the heater has been considered to be uniform along the heater length. Moreover, since this work is focused on Ge-rich waveguides operating in the MIR regime, the thermo-optic coefficient is considered to be of Ge material and constant as a function of the wavelength [145].

$$Delay : \gamma = n_{eff} \Delta L + L_H \Delta n_{eff,T} \quad (3.3)$$

$$\Delta n_{eff,T} = \frac{\partial n_{eff}}{\partial T} \Delta T \quad (3.4)$$

If loss-less and perfectly balanced 50:50 MMI are considered, the output power of a MZI (P_{out}) as a function of the path-delay unbalance γ and wavenumber (inverse of wavelength, $\sigma=\lambda^{-1}$) is expressed as in Eq. 3.5, where $P_{in}(\sigma)$ is the input spectrum to be retrieved. In practice, the path-delay shift due to thermo-optic effect will be much lower than the one due to path length difference ($\Delta L_{step} n_g \gg L_H \Delta n_{g,T,step}$). Therefore, a coarse sampling of the path-delay (γ) is performed by a linearly unbalancing the arm-length difference of the MZI array ($n_g \times \Delta L_{step}$), while a fine sampling is then achieved by thermally tuning each MZI ($L_H \times \Delta n_{g,T,step}$). In this way, as seen in Fig. 3.5(b-c), the sampling spacing of the collected interferogram as a function of the optical path-delay is inversely proportional to the number of measurements at different temperatures (N_T).

$$P_{out}(\sigma, \gamma) = \frac{P_{in}(\sigma)}{2} [1 + \cos(2\pi\sigma\gamma)] \quad (3.5)$$

Then, if a broadband photodetector with flat response as a function of the wavenumber (or wavelength) is considered, the collected output power of each MZI of the array at each measured temperature is integrated as a function of the wavenumber as in Eq. 3.6.

$$P_{out}(\gamma) = \int_0^\infty P_{out}(\sigma, \gamma) d\sigma = \frac{1}{2} P_{in} + \frac{1}{2} \int_0^\infty P_{in}(\sigma) \cos(2\pi\sigma\gamma) d\sigma \quad (3.6)$$

Therefore, the output power at each sampling point of γ ($P_{out}(\gamma)$) depends on the total input power (P_{in}) and the interferogram $I(\gamma)$, detailed in Eq. 3.7. Since the input spectrum has a limited range ($\Delta\sigma=\sigma_{max}-\sigma_{min}$) and the spectral power vanishes outside of this range, the limits of the integral can be extended to $\pm\infty$. Also, a shifted wavenumber variable is set in Eq. 3.7 as $\hat{\sigma}=\sigma-\sigma_{Littrow}$. This shift places the initial wavenumber of the spectral range (σ_{min}) to the wavenumber in which all the output powers are balanced with a uniform interference value ($\sigma_{Littrow}$). This wavenumber working point is known as Littrow condition and is related to the operative bandwidth of the system. Interestingly, an identical expression of the interference pattern is obtained in classical free-space FTS.

3.2. Integrated thermally-tuned spatial-heterodyne FTS: working principle and theoretical modeling

$$I(\gamma) = \int_0^{\infty} P_{in} \cos(2\pi\sigma\gamma) d\sigma = \int_{-\infty}^{+\infty} P_{in} \cos(2\pi\hat{\sigma}\gamma) d\hat{\sigma} \quad (3.7)$$

The interferogram collected at the output of the system is composed by cosine functions, which is the fundamental basis of the Fourier-transform. In fact, following the previous methodology, the obtained interferogram $I(\gamma)$ can be seen as the real part of the Fourier-transform of the input spectrum $P_{in}(\hat{\sigma})$. Therefore, the input spectrum can be retrieved as the inverse Fourier-transform of $I(\gamma)$, as in Eq. 3.8. Furthermore, since the cosine function is symmetric to respect zero value ($\gamma=0$), the interferogram, too. Hence, it is possible to integrate over half axis of the function, as in the right term of Eq. 3.8.

$$P_{in}(\hat{\sigma}) = \int_{-\infty}^{+\infty} I(\gamma) \cos(2\pi\hat{\sigma}\gamma) d\gamma = 2 \int_0^{\infty} I(\gamma) \cos(2\pi\hat{\sigma}\gamma) d\gamma \quad (3.8)$$

In practical implementations, the optical path-delay is scanned for discrete temperatures (N_T) and MZIs (N_L). Ideally, the discretized path-delay γ_k ($0 < \gamma_k < \gamma_{max}$) is composed by $N = N_T \times N_L$ equally space sampling points, as in Fig. 3.5. Thus, a similar inverse discrete Fourier-transform (IDFT) as in Ref. [139] can be applied to retrieve the input spectrum (Eq. 3.9). In fact, this IDFT is a discrete version of the interferogram integral of Eq. 3.8.

$$P_{in}(\hat{\sigma}) = 2 \gamma_{step} \sum_{k=0}^{N-1} I(\gamma_k) \cos(2\pi\hat{\sigma}\gamma_k) = \frac{2 \gamma_{max}}{N_T N_L - 1} \sum_{k=0}^{N_T N_L - 1} I(\gamma_k) \cos(2\pi\hat{\sigma}\gamma_k) \quad (3.9)$$

In Eq. 3.9, the first value of the summation ($k=0$) corresponds to $\gamma_0=0$, which mean no phase-delay unbalance. In other words, it means a totally balanced MZI with no thermal difference between arms. In such a case, the light is simply split and recombined, behaving similar to a straight waveguide. Therefore, no interference pattern is obtained and the detected output signal will always be the same as the total input power ($I(\gamma_0)=P_{in}$), thus not providing relevant information about the input spectrum. In this sense, this working point can be extracted from the summation to provide an expression that only depends on unbalanced MZIs, as in Eq. 3.10. Moreover, if we consider a relatively large number of measurements at different temperatures (N_T), the next consideration holds: $N_T N_L - 1 \simeq N_T N_L$. Finally, the input spectrum can be retrieved by using the expression of Eq. 3.11. It must be noted that this Fourier-transform is truncated to a limit number of values in the summation and this step-like cutoff leads to ripple oscillations in the retrieved spectrum. To avoid those oscillation features, it is possible to implement a signal apodization by weighting the collected interferogram values.

$$P_{in}(\hat{\sigma}) = \frac{2 \gamma_{max}}{N_T N_L - 1} I(\gamma_0) \cos(2\pi\hat{\sigma}\gamma_0) + \frac{2 \gamma_{max}}{N_T N_L} \sum_{k=1}^{k=N_T N_L - 1} I(\gamma_k) \cos(2\pi\hat{\sigma}\gamma_k) \quad (3.10)$$

3. Integrated Fourier-transform spectrometer in the MIR

$$P_{in}(\hat{\sigma}) = \frac{2 \gamma_{max} P_{in}}{N_T N_L} + \frac{2 \gamma_{max}}{N_T N_L} \sum_{k=1}^{k=N_T N_L} I(\gamma_k) \cos(2\pi \hat{\sigma} \gamma_k) \quad (3.11)$$

Similar to previous SH-FTS works, the TT-SH-FTS resolution is given by the maximal path-delay unbalance (γ_{max}). Following a similar procedure than in Ref. [139], the wavenumber resolution can be expressed as in Eq. 3.12. Likewise, the operational bandwidth (FSR) is related to the sampling interval step of the optical path-delay unbalance (γ_{step}), as in Eq. 3.13. In practice, for a fixed resolution, the operational bandwidth is proportional to the product of number of MZIs implemented (N_L) and the number of measurements of each MZI at different temperatures (N_T).

$$Resolution : \delta\sigma = \frac{1}{\gamma_{max}} = \frac{1}{\Delta L_{max} n_g + L_H \Delta n_{g,T,max}} \quad [cm^{-1}] \quad (3.12)$$

$$Bandwidth : FSR_{\sigma} = \frac{1}{2\gamma_{step}} = \frac{1}{\Delta L_{max} n_g + L_H \Delta n_{g,T,max}} \frac{N_T N_L}{2} \quad [cm^{-1}] \quad (3.13)$$

Interestingly, the resolution and FSR of TT-SH-FTS can be compared with previous SH-FTS works (Eq. 3.1 and 3.2). On one hand, the resolution of the proposed TT-SH-FTS approach is slightly enhanced, due to the extra unbalancing by thermo-optic effect of the path-delay difference of the most asymmetric MZI of the array. On the other hand, the operational bandwidth of TT-SH-FTS is significantly improved by N_T times, as the sampling step (γ_{step}) is inversely proportional to the number of measured temperatures (sampling points of γ). In summary, the TT-SH-FTS approach that I have proposed in this work can be understood as it introduces a new variable (the tuning by thermo-optic effect) in typical integrated SH-FTS to break the classical tradeoff between resolution, bandwidth and number of MZI required, thus providing superior performance features.

In this proposed model, a uniform sampling of the path-delay unbalance has been considered, meaning a linear increase of γ . To fulfill this condition, the maximal path-delay unbalance achieved by a MZI in the array must be continued by the minimal unbalance of the next MZI, as illustrated in Fig. 3.5(b). Therefore, the next relation must hold: $N_T L_H \Delta n_{g,T,step} = n_g \Delta L_{step}$. The minimal and maximal temperature variation required in each MZI to achieve a linear increase of γ are also provided in Eq. 3.14 and Eq. 3.15, respectively.

$$\Delta T_{step} = \frac{1}{\partial n_g / \partial T} \frac{n_g \Delta L_{step}}{N_T L_H} \quad (3.14)$$

$$\Delta T_{max} = (N_T - 1) \Delta T_{step} = (N_T - 1) \frac{1}{\partial n_g / \partial T} \frac{n_g \Delta L_{step}}{N_T L_H} \quad (3.15)$$

3.3. Application of calibration matrix method in TT-SH-FTS

Similar to classical integrated SH-FTS, the TT-SH-FTS approach here proposed may also suffer from phase and amplitude impairments due to fabrication imperfections. Moreover, thermal control deviations may also cause additional uncertainty in the collected interferogram. Therefore, the retrieval process chosen to obtain the input spectrum is no longer based on the canonical inverse Fourier-transform previously detailed, but on a calibration matrix procedure [74]. In this method, the transmission matrix is first obtained by scanning the FTS response with a monochromatic input signal within the operational spectral range of the spectrometer. This is done for each path-delay sampling point of the interferometer system, which corresponds to each working temperature of each MZI of the array (Fig. 3.6(a)). A total number of $N_T N_L M$ output intensity values are collected, where M is the number of measured wavenumbers (or wavelengths). As seen in Fig. 3.6(b), the transmission matrix is built up having a size of $N_T N_L \times M$.

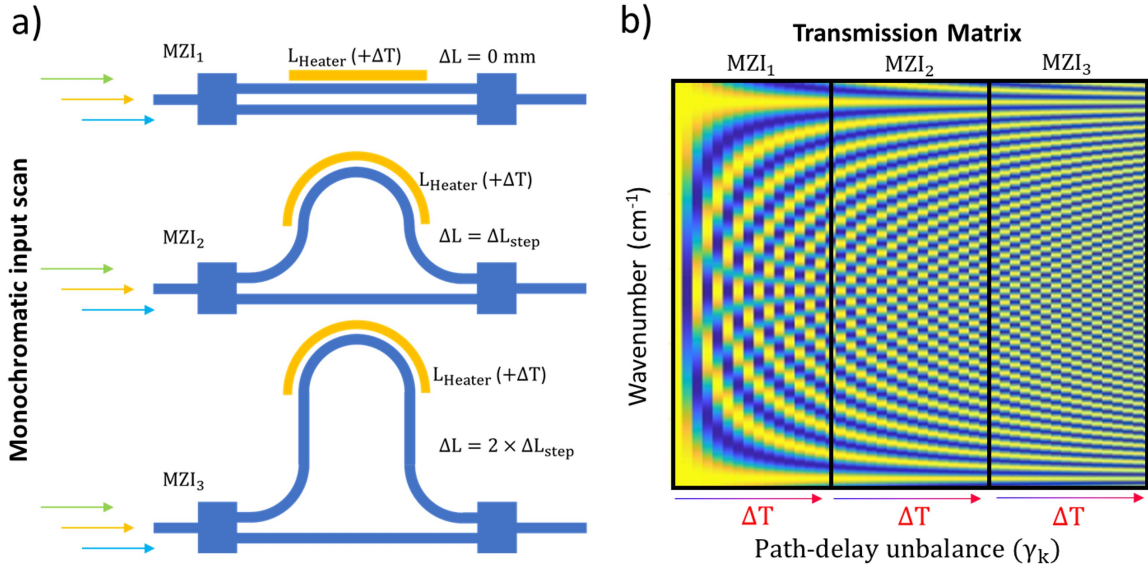


Figure 3.6.: (a) Schematic of wavenumber scan over a MZI array at different temperatures to construct the transmission matrix. (b) Transmission matrix schematic construction for 3 MZI and different temperatures.

As illustrated in Fig. 3.7(a), when a monochromatic input signal is sent to the spectrometer system, a discretized interference pattern is collected at the output, following a cosine shape. This process can be generalized for an arbitrary input signal by the following relation: $I(\gamma_k) = S(\sigma_M) \times T(\sigma_M, \gamma_k)$, where $S(\sigma_M)$ is the input spectrum for M discrete wavenumber points (σ_M) and $T(\sigma_M, \gamma_k)$ is the transmission matrix previously obtained. Then, since the pseudo-inverse of the transmission matrix (T^+) can be numerically calculated, the input spectrum can be consequently obtained by multiplying the output interferogram pattern by the pseudo-inverse matrix. This procedure is expressed as $S(\sigma_M) = I(\gamma_k) \times T^+(\gamma_k, \sigma_M)$ and illustrated in Fig. 3.7(b) for a sinusoidal interference pattern (monochromatic input). In order to

3. Integrated Fourier-transform spectrometer in the MIR

minimize ripple features due to the truncation of the interference pattern, a final apodization step can be implemented, too.

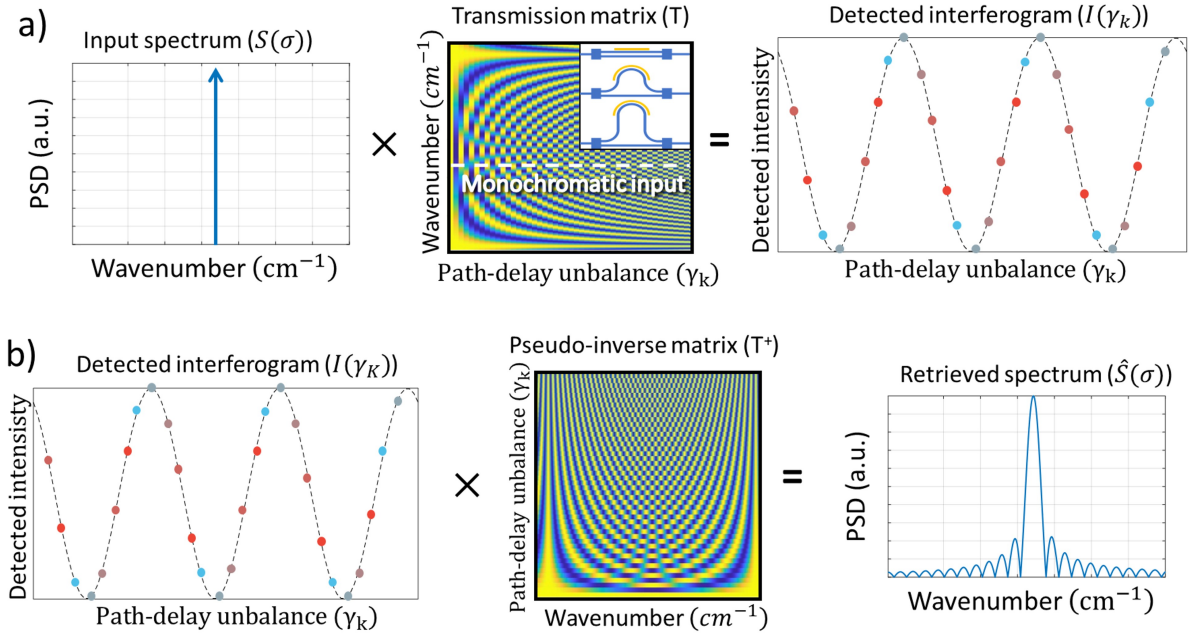


Figure 3.7.: Schematic of calibration matrix procedure. (a) If a monochromatic input is multiplied by the transmission matrix, a sinusoidal interferogram pattern is obtained. (b) If a sinusoidal interferogram pattern is multiplied by the corresponding pseudo-inverse transmission matrix, the monochromatic input spectrum is retrieved.

The calibration matrix method is a main advantage of integrated spectrograms based on FTS. With this method, fabrication imperfections are obviated, while providing a more stable performance. For instance, in Ref. [108], a retrieval process is repeated before and after a few weeks of its calibration, providing a retrieval inaccuracy difference below 2 cm^{-1} (original resolution of 15 cm^{-1}). Moreover, further numerical processing can be implemented to enhance the retrieval performances, such as Elastic-D1 method [136] or l1-norm minimization [146].

Interestingly, the calibration matrix method can be understood as a set of linear and independent equations that encode the input spectral information in the discrete values of the output interference pattern. In other words, the input spectrum can be transformed by a series of wideband and orthogonal functions to a list of coefficients. Therefore, if the orthogonal transformation basis and the output coefficients are known, the input spectrum can then be retrieved by using the inverse transformation. Indeed, the transmission matrix spectra at each path-delay working point (γ_k) shows a cosine shape, each of them with a different phase-velocity. Since cosine functions at different phase velocities are orthogonal, the normalized response of each MZI at each working point is also orthogonal with the others. In this regard, thanks to this calibration matrix method, the path-delay difference is no longer required to be uniformly sampled to properly retrieve the input spectrum. Indeed, it can be non-uniformly sampled, as long as the orthogonality between cosine-shape transfer functions of the transmission matrix is kept.

3.4. Numerical simulations and performance evaluation of integrated TT-SH-FTS in the MIR regime

As a next step, it is highly interesting to validate this novel approach, as a mean to provide high-performance integrated spectrometers. Also, since the aim of this chapter is to progress in the development of spectrometers operating in the fingerprint region of the MIR, the graded-index SiGe platform is here considered, as it has demonstrated to operate in a wide MIR spectral range. In the following, the TT-SH-FTS approach is expected to overcome the bandwidth limitations of classic integrated FTS, so that, unlike previous works, the broadband features of the graded-index SiGe platform can be fully exploited without any penalty in the resolution or a drastic increase in the number of required MZI devices.

To validate the advantages of TT-SH-FTS with respect to the classical SH-FTS approach, a similar spectrometer as the one reported in Ref. [108] but with half of the MZI devices, is considered. Therefore, a 10 MZI array with an increasing path-length difference of $\Delta L_{step}=18.8 \mu\text{m}$ is used for this assessment. The first MZI is balanced (no arm-length difference) and the last MZI of the array has a path-length difference of $\Delta L=169.2 \mu\text{m}$. Additionally, a thermal heater of 3.3 mm-length (L_H) is considered. Since the optical mode is guided through Ge-rich layers in the MIR regime, hereafter the thermo-optic coefficient of Ge is considered for numerical simulations, with a constant value of $\partial n_{eff}/\partial T = 4.1 \times 10^{-4} \text{ K}^{-1}$. Indeed, the thermo-optic coefficient experiences a maximal variation of $0.1 \times 10^{-4} \text{ K}^{-1}$ over the wavelength range between 5.5 and 8.5 μm (from 1180 to 1820 cm^{-1} wavenumber) [145]. In the following, I numerically evaluate the performance of such a spectrometer, to later confirm these results experimentally in the next section.

The transmission matrix is numerically obtained with Eq. 3.5. Then, the retrieval process of a monochromatic input centered at 1434 cm^{-1} wavenumber (7 μm wavelength), and depicted as black arrow in Fig. 3.8(e-h), is evaluated when different temperature variations are used. The numerical results when no temperature difference is induced ($N_T=1$) are reported in Fig. 3.8(a,e), which means the classical SH-FTS approach. In this case, four Littrow lines are observed in the transmission matrix and highlighted in red color. The Littrow lines correspond to the wavenumber condition in which all the MZI output signals that are collected have the same value. Since the MZIs show a cosine transfer function that is intrinsically periodic, this Littrow condition is also periodically obtained in the transmission matrix (or interferogram pattern) of the spectrometer. When a broadband spectral range is retrieved (1230 to 1790 cm^{-1} wavenumber or 5.6 to 8.1 μm wavelength), the repetition of the Littrow condition leads to signal aliasing. It means that signal images of the monochromatic input are present at both sides of each Littrow line position, as seen in Fig. 3.8(e). Nevertheless, if the path-delay difference between MZI arms is linearly sampled with 4 different temperature values, the commonly called Nyquist rate is thus increased. This fact results in a higher separation between Littrow condition wavenumbers, thus avoiding aliasing in a broader spectral range (Fig. 3.8(b,f)). The distance

3. Integrated Fourier-transform spectrometer in the MIR

between Littrow lines is given by twice the FSR, while the operative bandwidth free of aliasing corresponds to a FSR. Then, if the number of temperature differences is increased to 9, a theoretical FSR of 603 cm^{-1} is achieved. Therefore, as seen in Fig. 3.8(c,g), the monochromatic input can be properly retrieved in the full spectral range of 551 cm^{-1} wavenumber. Applying Eq. 3.15, a maximal temperature of 53 K must be achieved along the 3.3 mm-long heater. Therefore, even though this temperature can be achieved on-chip, it is also interesting to verify the previous assumption that a non-uniform sampling of the optical path-delay is still valid, as far as the orthogonality between the cosine-shape transfer functions at each MZI working point is kept. In this regard, as it will be later applied in the experimental validation, 9 temperature differences between MZI arms are considered, with a maximal temperature variation of 3 K and a temperature increment near 0.4 K. As it is seen in Fig. 3.8(d), a highly non-uniform sampling is obtained, where the missing points are seen as black areas. Nevertheless, even though such non-uniform sampling, the monochromatic input can be properly retrieved in the entire spectral range without any appreciable aggravation on the resolution (Fig. 3.8(h)).

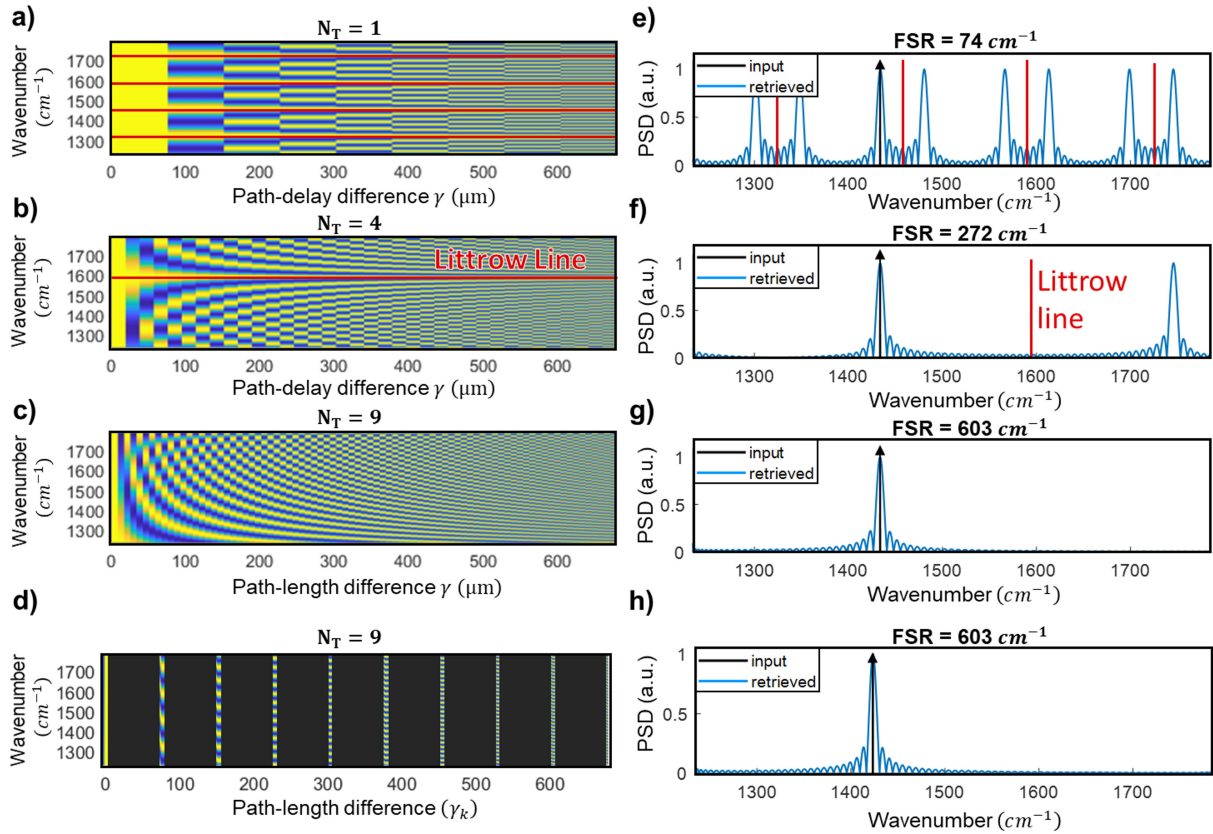


Figure 3.8.: Simulated retrieval process of a monochromatic input at 1434 cm^{-1} wavenumber, depicted as a black arrow. (a-d) Transmission matrix numerically obtained with no thermal tuning, 4 and 9 different working temperatures and 9 temperatures with no uniform sampling. (e-h) Power spectral density (PSD) of the retrieved signal for the similar cases. The Littrow line condition is depicted in red color.

Finally, I have also verified the correct retrieval process of a broadband input signal with different height values (right-side spectrum of Fig. 3.9(a)). The resolution performance is also checked in the left-side spectrum of Fig. 3.9(a), which is defined by Rayleigh criterion, meaning the retrieval of two distinguishable peaks separate by the resolution distance. Therefore, the center of two narrow peaks of 6.4 cm^{-1} width are separated by 13.4 cm^{-1} , which is the theoretical resolution obtained with Eq. 3.12. It means that the sides of both peaks are separated by half of the resolution distance (6.4 cm^{-1}). A similar retrieval process as the one previously reported for 9 different temperature values is performed. The results are shown in Fig. 3.9(b-c) for uniform and non-uniform path-delay sampling, respectively. Interestingly, the results reported with and without uniform sampling are equivalent, while the different height levels are properly identified and the two narrow peaks clearly distinguished.

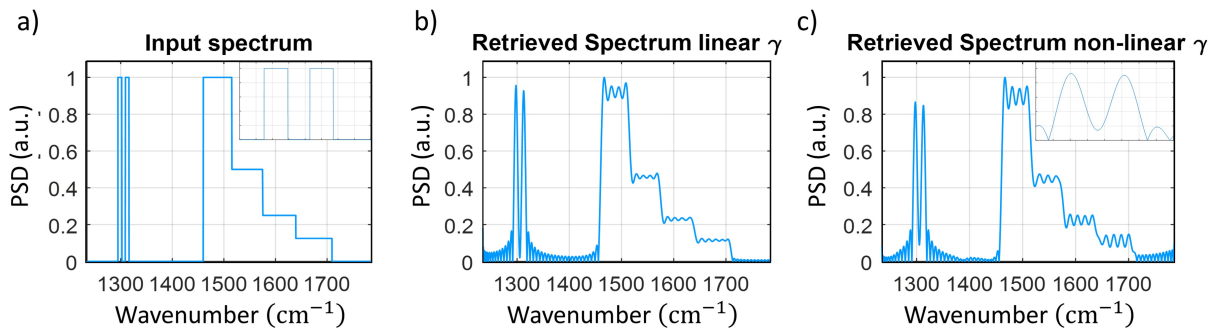


Figure 3.9.: Retrieval of a broadband input spectrum from $5.6 \mu\text{m}$ to $8.1 \mu\text{m}$ wavelength by mean of calibration matrix procedure and 9 temperature values. (a) Input power spectral density (PSD) with two narrow peaks separated by a theoretical resolution value of 13.4 cm^{-1} (left side) and different power levels (right side). (b) Retrieved spectrum with linear path-delay sampling. (c) Retrieved spectrum with non-linear path-delay sampling. Inset: zoom to the two narrow peaks.

Therefore, this new TT-SH-FTS approach has been numerically demonstrated to break the tradeoff of classical SH-FTS, thus providing superior bandwidth performances with no penalty in the number of required MZIs or resolution (even with a theoretically slightly increase). Moreover, thanks to the advantages of calibration matrix retrieval process, uniform sampling is no longer required. This fact enables the implementation of integrated TT-SH-FTS with low temperature increase, thus providing a faster time response and lower power consumption.

3.5. Experimental validation of MIR integrated TT-SH-FTS

This section reports an experimental demonstration that validates the advantages of the integrated TT-SH-FTS approach here proposed. To that end, a graded-index SiGe platform is used for the device design and fabrication. An array of 10 MZI is fabricated, by mean of 1-by-2 port MMI splitter and combiners with a size of $20 \times 105 \mu\text{m}$. An increasing path-length unbalance of $\Delta L_{step} = 18.8 \mu\text{m}$ is set and consecutive MZIs are separated by $50 \mu\text{m}$. Since the device had

3. Integrated Fourier-transform spectrometer in the MIR

been partially fabricated in previous works in my research group (Ref. [108]), the waveguides have both a width and etching depth of $4\ \mu\text{m}$. Then, as seen in Fig. 3.10, a gold metal path is added next to the shortest MZI arm, separated by $12\ \mu\text{m}$ to the waveguide. It must also be noted that, to simplify the structure definition, the heater is placed in the straight waveguide, which is the shortest arm of the MZI. Therefore, a temperature increase will balance the path-delay difference of the MZI, which is the opposite of the definition used in the theoretical model. To take into consideration this fact, the temperature increase (ΔT) can be easily modeled as taking negative values. If no thermal tuning is applied, the fabricated spectrometer is expected to perform with a theoretical resolution and bandwidth of $14.6\ \text{cm}^{-1}$ and $74\ \text{cm}^{-1}$, respectively. Those values are obtained by mean of classical integrated SH-FTS equations (Eq. 3.1 and 3.2).

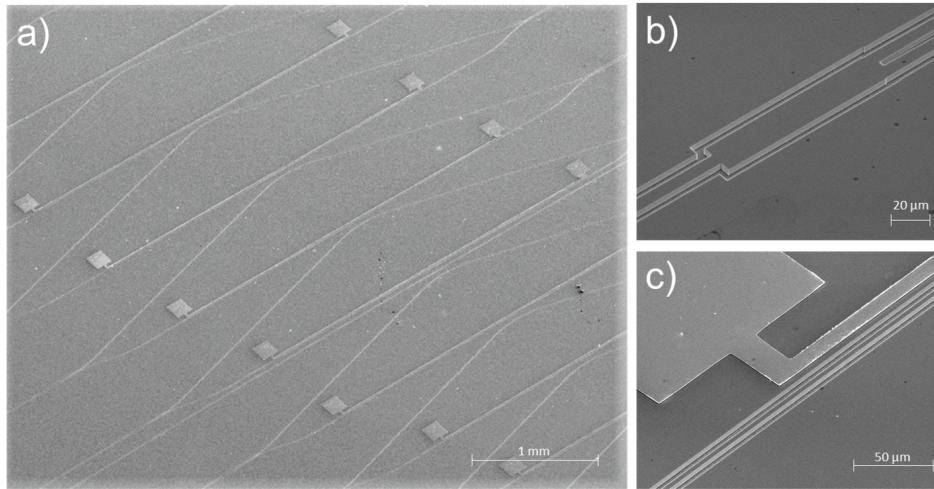


Figure 3.10.: SEM image of the integrated FTS. (a) General top view of the MZI array. (b) $20 \times 105\ \mu\text{m}$ MMI splitter and combiner. (c) Metallica gold path heater $12\ \mu\text{m}$ separated from the waveguide. A big path is added to enable tip contact access.

Next, the thermal heater performance is characterized. To that end, a free-space set-up similar to the one reported in previous chapter is used. As seen in Fig. 3.11(a), a pair of tip probes are added to the experimental characterization bench, to enable an electric contact. The injection of current through the metal path dissipates heat due to Joule effect, thus modifying the refractive index of the waveguide next to it, and consequently the path-delay unbalance between arms. In this demonstration I have done the measurements in TE polarization. The optical transmission in the MIR regime of each MZI is collected for 9 different dissipated powers in the thermal-heater, spanning from 0 to 1.6 W. The electrical power is obtained by multiplying the measured current and voltage applied with a Keithley 2400 power source. For instance, in Fig. 3.11(b) is reported the optical transmission as a function of the wavelength (centered at $7.75\ \mu\text{m}$) of a MZI with $\Delta L = 150.4\ \mu\text{m}$ path-length unbalance.

To evaluate the thermal heater performance, the phase shift of the MZI transmission as a function of the dissipated power is obtained as $2\pi \frac{\Delta\lambda_{meas}}{FSR_{meas}}$, where $\Delta\lambda_{meas}$ is the wavelength shift measured of a peak resonance and FSR_{meas} the spectral spacing between consecutive resonances. For example, the spectral resonance centered at $7.9\ \mu\text{m}$ wavelength (with no applied

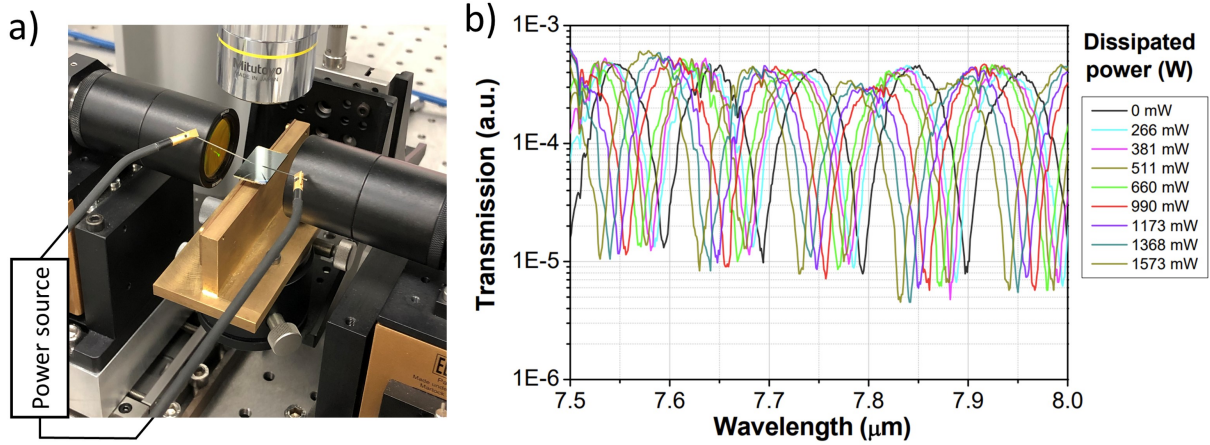


Figure 3.11.: (a) Photo of the device under test. (b) Transmission wavelength spectrum of a MZI with $150 \mu\text{m}$ arm-length unbalance for different heat dissipated powers.

power) is tracked as the dissipated power increases, and its phase shift is reported in Fig. 3.12(a). As seen in this figure, a maximal shift value of 1.25π is achieved with a dissipated power of 1.6 W. Then, the temperature increase as a function of the dissipated power is calculated as $\frac{\Delta\Phi_T \lambda}{L_H TOC 2\pi}$, where λ is the operational wavelength and $\Delta\Phi_T$ the thermal phase shift. I have also considered a 3.3 mm-length thermal heater (L_H) and a thermo-optic coefficient (TOC) value of $4.1 \times 10^{-4} \text{ K}^{-1}$. I have repeated this process for different peaks of the MZI transmission and the calculated thermal increase as a function of the dissipated power is reported in Fig. 3.12(b). As observed in this figure, an average heater efficiency of 0.5 W/K is deduced from the slope of the curve (linear fit in red color), achieving a modest maximal temperature increase of 3.5 K. Since the fabrication design was relatively conservative, the heater efficiency is expected to increase by locating the metal path closer to the waveguide (instead of $12 \mu\text{m}$ away from the waveguide). Further designs can also be implemented in future works to enhance the heat dissipation towards the waveguide and avoid heat leakage to the substrate, such as performing a thermal isolation by etching a trench around the metallic path.

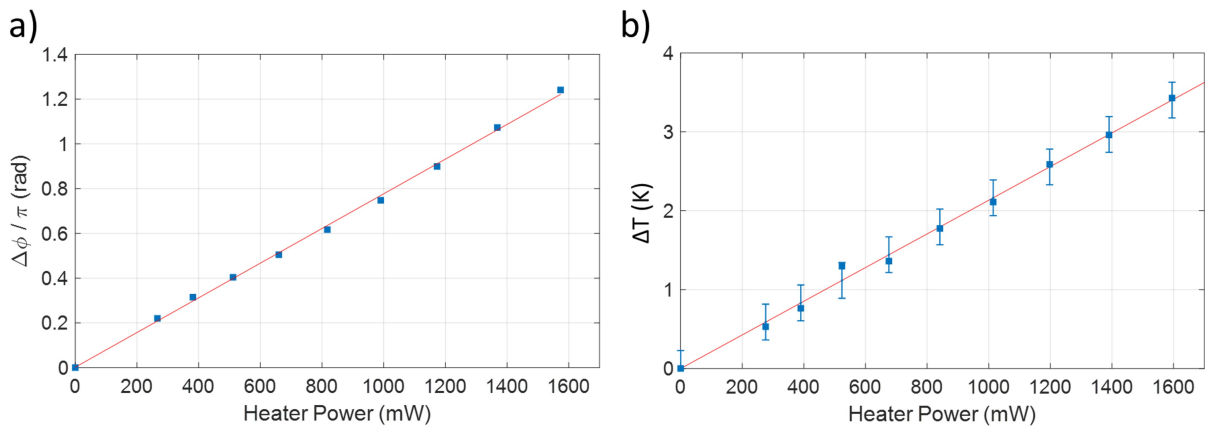


Figure 3.12.: Thermal tuning performance deduced from Fig. 3.11. (a) Phase shift variation of a peak centered at $7.9 \mu\text{m}$ wavelength as a function of the heat dissipated power. (b) Calculated temperature variation as a function of the dissipated power. A linear fit is reported in red color.

3. Integrated Fourier-transform spectrometer in the MIR

In order to reach a linear increase (uniform sampling) of the path-delay difference along the thermally tuned MZI array, a theoretical maximal temperature increase of 54 K should be achieved. This value is far from the maximal 3.5 K variation experimentally achieved. Moreover, due to fabrication errors, the first 3 MZI of the array were not available. Therefore a 7 MZI array is hereafter considered, with a path-length difference between 56.4 and 169.2 μm (increase step of $\Delta L=18.8 \mu\text{m}$). Interestingly, even though the high non-uniform sampling of the path-delay unbalance (γ), the calibration matrix method is expected to enable its use, showing remarkably flexibility and robustness in integrated FTS implementations.

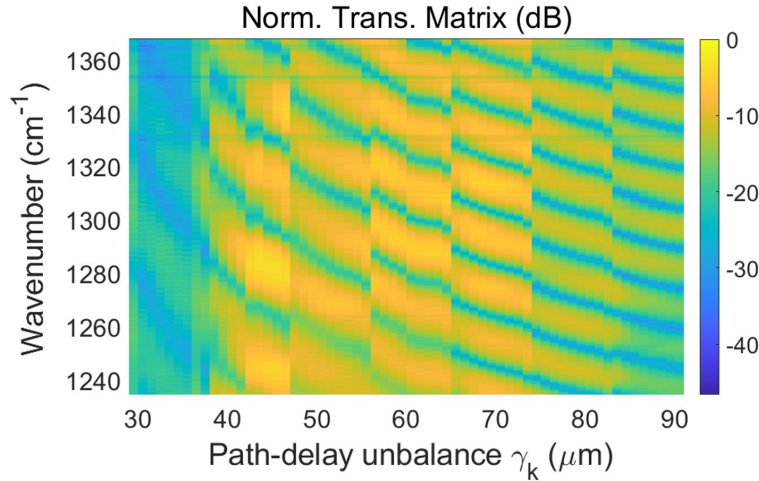


Figure 3.13.: Normalized experimental transmission matrix of 7 MZIs with arm-length difference from 56.4 to 169.2 μm , and 9 different temperature variations from 0 to 3.5 K. The characterized spectral range spans from 1235 to 1370 cm^{-1} wavenumber (7.1 to 8.3 μm wavelength).

In this regard, the transmission matrix is built by characterizing the spectral transmission of the 7 operative MZIs of the array at 9 different temperature increments (from 0 to 3.5 K). The measured spectral range spans from 7.3 to 8.1 μm wavelength (1235 to 1370 cm^{-1} in wavenumber), with a wavelength sampling step of 10 nm. It means a measured spectral range of 135 cm^{-1} . The transmission matrix is experimentally obtained and reported in Fig. 3.13. Then, the Moore-Penrose pseudo-inverse of this transmission matrix is obtained to implement the calibration matrix retrieval method. In order to evaluate the enhancement and compare the results when no thermal tuning is applied, I also obtained the transmission matrix with no thermal scanning implemented.

Finally, the retrieval process of a monochromatic input at different positions is evaluated with and without thermal tuning. To that end, a monochromatic input signal is multiplied by both transmission matrices previously obtained experimentally ($N_T=1$ and $N_T=9$), and later by its numerically calculated pseudo-inverse. A Gaussian function apodization is also implemented, in order to reduce ripple effects due to sampling truncation. The resulting retrieved spectra are reported in Fig 3.14. When no thermal sampling is applied, the theoretical operative bandwidth is 74 cm^{-1} , which is lower than the measured spectral range. Therefore, as it is observed in Fig 3.14(a), the retrieved spectrum may suffer from aliasing, depending on the monochromatic

input position (depicted as black arrow) relative to the Littrow line condition (depicted in red color). In contrast, the thermal tuning of the spectrometer device allows a theoretical operative bandwidth of 603 cm^{-1} wavenumber. Hence, the input tone is properly retrieved in the entire spectral range characterized. Moreover, a SNR enhancement is also observed, up to 7 dB. This fact can be understood from Fourier-transform theorem, in which the SNR is proportional to the number of sampling points. Therefore, since the thermal-scanning provides a higher number of sampling points of the optical path-delay unbalance (γ_k) for the same number of MZI devices, a clear SNR enhancement is observed.

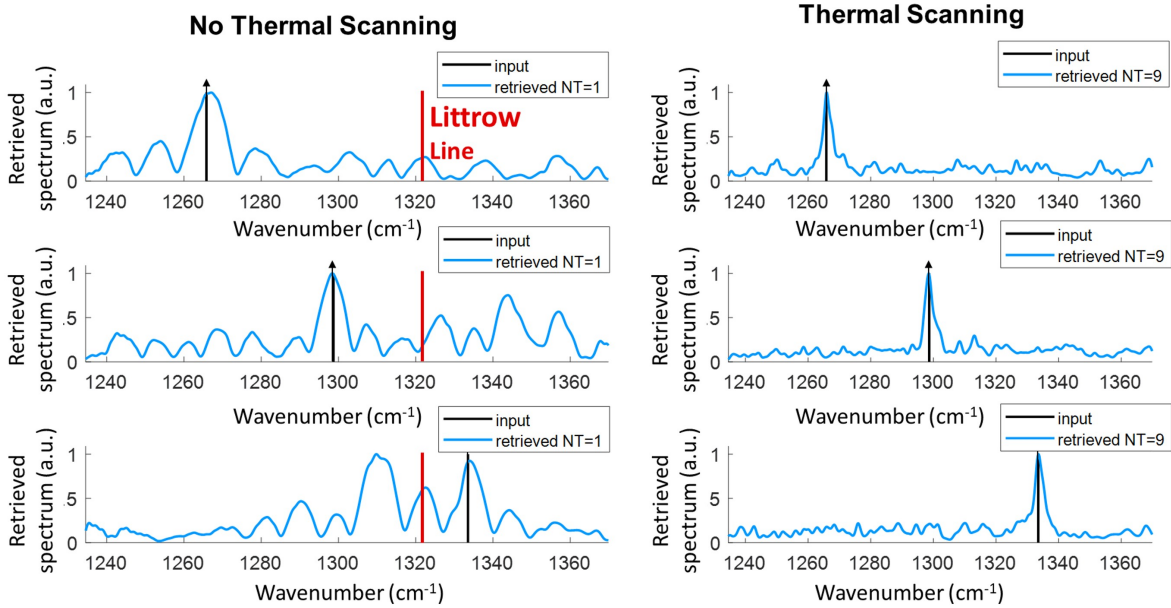


Figure 3.14.: Experimental normalized power spectral density (PSD) retrieved for a monochromatic input at 3 different position from 7.3 to $8.1 \mu\text{m}$ wavelength, depicted as a vertical black arrow: (a) when no thermal scanning is implemented ($N_T = 1$) and (b) for 9 measurements at different temperatures ($N_T = 9$). The Littrow line condition is depicted in red color.

In conclusion, the integrated spectrometer approach that I have proposed in this chapter has experimentally demonstrated to greatly enhance the operational bandwidth of classical integrated FTS operating in the MIR range, with the same number of MZIs and even performing a slightly better resolution, thus breaking the classical tradeoff between resolution, bandwidth and number of MZIs. To the best of my knowledge, this is the first experimental demonstration of an integrated FTS that exploits the advantages of the high resolution achieved with SH-FTS, together with the broadband features of SI-FTS by fine thermal tuning. Therefore, these results pave the way towards the implementation of high-performance integrated spectrometers operating in the fingerprint region of the MIR, that can be used in compact and robust multi-molecule sensor systems. Moreover, in future works multi-aperture injection can be implemented (each MZI is individually fed), to provide a higher optical throughput. For instance, a recent demonstration near 1570 nm wavelength has demonstrated the simultaneous feeding of 16 MZIs by mean of a wide two-way-fed Bragg coupling in a CMOS compatible SOI platform [135].

3. Integrated Fourier-transform spectrometer in the MIR

4

On-chip supercontinuum generation in the MIR

This chapter is dedicated to the achievement of an on-chip wideband source in the MIR regime by mean of nonlinear phenomena, and in particular by supercontinuum generation (SCG). First, a general overview of the interest and motivation of this work will be provided, in relation to other demonstrations reported in the literature. The basic underlying nonlinear dynamics that govern the SCG process will be also introduced. Then, a method to accurately obtain the dispersion properties of graded-index SiGe waveguides will be shown, as well as subsequent numerical group velocity dispersion (GVD) simulations. Finally, I will model, fabricate and characterize an on-chip SCG in the MIR regime, exploiting the graded-index SiGe platform.

4.1. State of the art and basic dynamics of SCG

4.1.1. Context and motivations for on-chip SCG in the MIR

Although relatively broadband MIR sources have been demonstrated [147, 148], some approaches have been proposed in the literature to extend the operational spectral range of a device, such as a QCL array [149]. For example, a QCL array with combined outputs has been shown by S. Nicoletti's group, to sequentially cover a wideband MIR spectrum [103, 150] (Fig. 4.1(a)). That work reported an AWG design that is capable to combine up to 67 laser sources and covering from 8.0 to 9.5 μm wavelength ($1050 - 1250 \text{ cm}^{-1}$ wavenumber). [151]. As another example, a spectral generation from 6.2 to 9.1 μm wavelength ($1100 - 1610 \text{ cm}^{-1}$) has also been demonstrated with a single emitting aperture, by mean of eight sampled grating distributed feedback (SG-DFB) laser array and a beam combiner [152] (Fig. 4.1(b)).

Alternatively, the wavelength conversion by mean of nonlinear phenomena has also been reported in the literature. In particular, SCG is an interesting solution that provides several advantages, notably obtaining an ultra-wide and coherent light source, while a single laser source

4. On-chip supercontinuum generation in the MIR

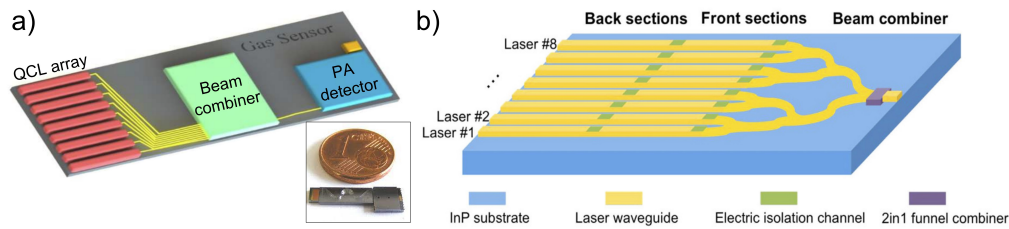


Figure 4.1.: Integrated broadband source by mean of a QCL array. (a) Schematic of a integrated sensor based on a QCL array, a beam combiner (AWG) and a photo-acoustic detector. Inset: real prototype implementation with a 1 cent coin to size comparison. Image adapted from [151] and www.leti-cea.com. (b) Schematic of a 8 SG-DFB laser array with a single output. Image taken from [152].

is required. In this regard, different SCG demonstrations have been reported in the literature in free-space configuration, successfully achieving multi-octave spectral broadening by mean of bulk crystals, such as 3.3 octave broadening with yttrium aluminum garnet (YAG) crystal [153]. Also, by mean of fiber optics, a spectral broadening has been reported from 2 to 16 μm wavelength, with a 2.29 MW peak power and 6.3 μm wavelength pump [154], or from 1.4 to 13.3 μm with 11.5 mW average pump power at 7 μm wavelength [155]. However, despite the greatly spectrum expansion of these works, they remain bulky and unpractical for compact and wide-spread sensing implementations. Therefore, SCG based on integrated waveguides has compelling interest to enable simultaneous multi-molecule detection in a compact device.

In this regard, several SCG demonstrations have been reported in the MIR regime based on different photonic integrated platforms. For example, a 1-octave SCG has been reported on SOI waveguides up to 3.6 μm wavelength, reaching the upper multiphonon absorption limit of silica material [156]. By avoiding the use of silica cladding, 1.9-6 μm wavelength range expansion has been demonstrated in SOS nanowires [157]. Also, a considerable 2-10 μm wavelength spectral expansion has been reported by mean of chalcogenide waveguides (GeAsSe/GeAsS) [72]. Nevertheless, even though broadband and efficient on-chip SCG in the MIR regime has been already reported in the literature, the development of SCG with similar performances, but based on Si-compatible platforms would enable cost-effective devices for sensing applications. However, achieving an efficient and broad SCG in the MIR regime by mean of Si-compatible integrated waveguides present different challenges. First, a strong modal nonlinear coefficient is required, together with a high light-matter interaction, which means high optical mode confinement. Second, the GVD must be accurately tailored to provide an appropriate phase-matching condition over a wide spectral range. In this sense, some previous works have reported interesting results. For example, by properly engineering the GVD of CMOS-compatible N-rich silicon nitride waveguides, my research group has remarkably demonstrated 2-octave expansion, spanning from 400 to 1600 nm wavelength in 2020 [158]. Also, reaching the MIR regime, the work reported in Ref. [159] has noticeably demonstrated 35% power conversion and milliwatt-level output powers in the 3-4 μm wavelength range, by properly engineering the GVD profile. Third, low propagation losses must be achieved in the full spectral range generated. In this sense, the

use of Ge-based platforms is a promising solution to achieve a wide SCG in the MIR regime, as Ge shows a wide transparency window beyond the Si multiphonon absorption around $7.5 \mu\text{m}$ wavelength. For instance, the work reported in Ref. [160] has demonstrated 1-octave SCG, spanning from 3 to $8.5 \mu\text{m}$ wavelength, thanks to $\text{Si}_{0.6}\text{Ge}_{0.4}$ waveguides.

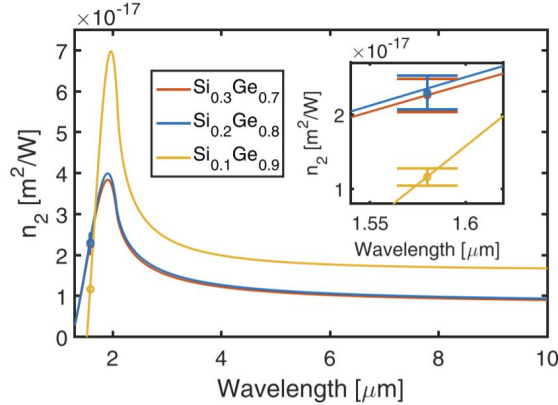


Figure 4.2.: Theoretical Kerr nonlinear refractive index (n_2) as a function of the wavelength for $\text{Si}_{1-x}\text{Ge}_x$ alloys with x values of 0.7, 0.8 and 0.9. Inset: zoomed area near $1.58 \mu\text{m}$ wavelength, where experimental results are also reported. Figure taken from [161].

The development of SCG in the MIR regime, and particularly including the LWIR range ($\lambda > 8 \mu\text{m}$), is highly interesting, as many important molecules for sensing applications (e.g., ozone or alkanes) have strong absorption lines in the spectral range from 7 to $13 \mu\text{m}$ wavelength. However, the demonstration of such SCG by mean of Si-compatible waveguides was still missing in the literature at the beginning of this thesis, while it would pave the way towards high-performance and cost-effective sensors. Interestingly, it is possible to take advantage of the unique features of Ge-rich graded-index SiGe waveguides to address the different requirements for efficient on-chip SCG. First, a high optical mode confinement is achieved, thanks to the refractive index contrast between Ge-rich SiGe layers and the air cladding, while also benefiting from a higher nonlinear coefficient of Ge-rich SiGe alloys when compared to Si [161]. This last fact has been proven during the PhD of S. Serna, in which an experimental and theoretical modeling showed a Kerr coefficient (n_2) increase when raising the Ge concentration of SiGe alloys (Fig. 4.2). Interestingly, a low dependency of n_2 with the wavelength was also reported for wavelengths longer than approximately $4 \mu\text{m}$. Second, the graded-index profile provides an extra degree of freedom to perform GVD engineering and achieve relatively flat and anomalous dispersion condition over a broad MIR spectral range. Such dispersion tailoring was theoretically reported for the first time in Ref. [110], predicting a high SCG performance in the MIR regime. Third, as detailed in Chapter 2, Ge-rich graded-index SiGe platform has demonstrated to perform low propagation losses over a wide spectral range, experimentally reported from 5 to $11 \mu\text{m}$ wavelength. Therefore, this kind of waveguides has compelling interest to perform broadband and efficient SCG in the MIR regime. Accordingly, I provide in the following sections the design, fabrication and characterization of such a SCG by mean of the Si-compatible, Ge-rich, graded-index SiGe platform.

4.1.2. Basic nonlinear dynamics of SCG

In order to develop an on-chip SCG, it is necessary to first understand the basic principles behind it. The SCG phenomena is a complex process that can be simplified and explained from a time-domain perspective as the following [162–164]. A high power and femtosecond pump pulse is sent to a dispersive medium (e.g., bulk crystal, optical fiber or integrated waveguide). Although a few works have reported SCG in all-normal dispersion waveguides [165, 166], for simplicity, an isolated pulse in anomalous dispersion is considered, without any further interaction with other pulses. Also, since Si and Ge are centrosymmetric materials, second order nonlinear phenomena are not considered (e.g., second harmonic generation), thus only considering a third order nonlinear response (Kerr effect). For instance, self-phase modulation (SPM) is an effect that arises from the intensity-dependence of the refractive index, given by $n = n_0 + n_2 I$, where n is the resulting refractive index, n_0 the unperturbed material refractive index, n_2 the Kerr coefficient and I the optical intensity. Since the pulse is considerably short in time domain, its spectrum has a certain bandwidth. Then, it can be understood that the input pulse is compressed in time-domain via SPM, while the anomalous GVD tends to expand it. Under appropriate conditions, the SPM effect can be perfectly compensated by the anomalous dispersion condition. Therefore, the pulse envelope remains invariant while propagating through the nonlinear medium. This effect is commonly known as distortionless soliton propagation. In fact, as depicted in Fig. 4.3, the optical propagating pulse experiences a time-dependent phase variation by SPM, in which the lower frequency components are pushed towards the rising edge of the temporal pulse, whereas the higher frequency components to the falling edge. In contrast, the pulse experiences an inverse effect while being propagated in an anomalous dispersive medium, thus compensating each other effect and keeping the envelope of the pulse invariant.

If the energy of the input pulse (I) is higher than the optimal energy that sustains the equilibrium between GVD and SPM of the fundamental soliton, a higher order soliton (HOS) is obtained. The order of the HOS is given by $N = \sqrt{\gamma P_0 L_D}$, where γ is the effective nonlinear coefficient, P_0 the input peak power and L_D the dispersive length, which is calculated as $L_D = T_0^2 / |\beta_2|$, where T_0 is the input pulse duration and β_2 the group velocity dispersion [168]. HOS lead to a more complex dynamics, in which the pulse envelope is no longer invariant, but periodically compresses and stretches along the propagating distance, alternatively in frequency and time domain (Fig. 4.4). The maximal spectral bandwidth depends on how short the envelope of the propagating pulse is when compressed in the time domain. Since a remarkable high peak power and a significant short pulse envelope are achieved, an ultra-wide spectral expansion is thus obtained. This periodic oscillation dynamics in a nonlinear medium is commonly known as breather solitons. In fact, breathers include all the solutions, in which the fundamental one is the distortionless soliton and the rest are HOS. In an ideal case, with perfectly flat GVD and zero propagation loss, the N-order breather invariably propagates in a periodic manner. In principle, these dynamics are robust and breathers can experience elastic collisions with other breathers when propagating, remaining unperturbed after the interaction. However,

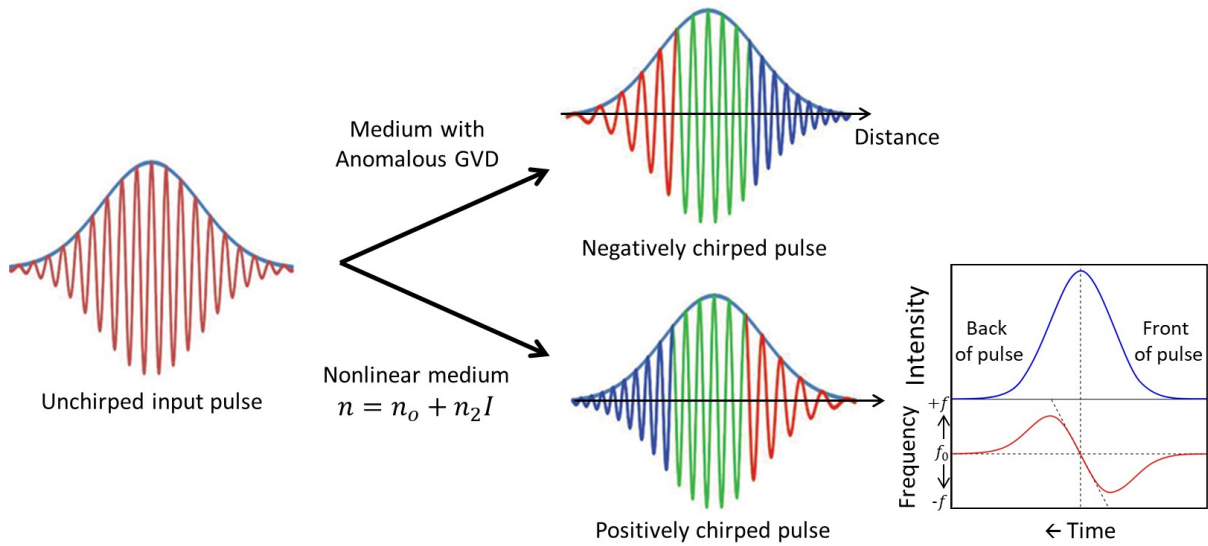


Figure 4.3.: Illustration of linear and nonlinear chirp effect in a temporal Gaussian pulse. The linear effect by anomalous GVD is depicted on top and the nonlinear SPM effect by a Kerr medium is depicted on bottom side. The SPM effect is also depicted in the right side, where the input pulse (blue color) experiences a temporal shelf frequency shift (red color). The front of the pulse is shifted to lower frequencies, the back of the pulse to higher ones and the center of the pulse shows an approximately linear shift. Image adapted from [167].

in more realistic dispersive mediums, after the first pulse compression, the breather mechanism is perturbed by third or higher order dispersion terms (also FCPD effect due to multiphoton absorption or Raman scattering, among others [169]). Therefore, the periodic oscillating dynamic of the N-order HOS breaks, and the HOS is sequentially split in N fundamental solitons, each one centered at a different wavelength and propagating with a different velocity. The wavelength shift between each newly generated fundamental soliton mainly depends on the optical power that it contains [170]. This process is known as soliton fission and is the basis of the SCG to achieve an ultra-wide output spectrum. Interestingly, in this whole process, part of the energy is radiated to resonant frequency bands (with perfect phase-matching condition), generating the commonly called dispersive waves (DW) and typically showing a double-wing output spectral shape. Indeed, when a maximal pulse compression is reached, the spectral expansion partially overlaps phase-matched wavelengths, thus efficiently transferring energy to those. The DW excitation is also known as non-solitonic radiation, as the ultra-wide generated bandwidth can include normal GVD condition, in where soliton propagation is not possible [171].

In summary, SCG is a complex nonlinear phenomenon that typically requires a Kerr nonlinear medium, anomalous GVD features and a short pulsed source (femtosecond laser) centered within the anomalous dispersion condition. If those requirements are accurately addressed, a multi-octave output spectrum can be achieved and extended at both limits by a pair of DW. Furthermore, the output spectrum can be highly coherent in the entire generated bandwidth. Both facts makes SCG highly interesting for a plethora of applications that require a broadband and coherent light source in a single device, such as optical coherent tomography.

4. On-chip supercontinuum generation in the MIR

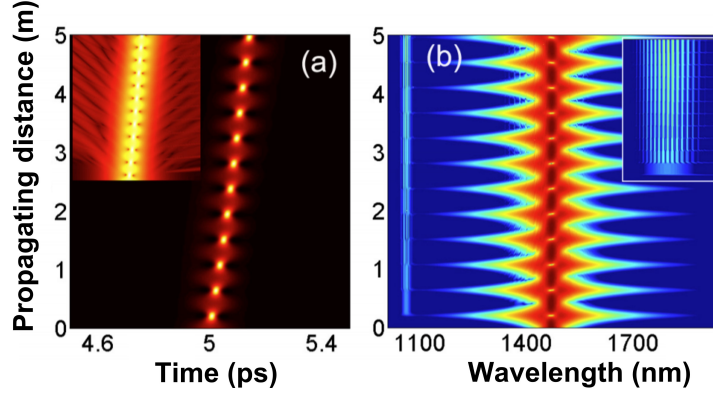


Figure 4.4.: Spatial evolution of 2-order soliton (breather) under low third-order dispersion medium. (a) In temporal domain. Inset: normalized signal to appreciate low intensity waves. (b) In spectral domain. Inset: zoom-in to 1030-1080 nm wavelength range. Image taken from [172].

4.2. SCG design with graded-index SiGe waveguides

In this work, the Ge-rich graded-index SiGe platform is investigated to achieve an efficient and wideband SCG in the MIR regime. Since the dispersion features play an important role in the SCG, I have developed a method that considers both the modal and material dispersion to accurately calculate the total GVD (in particular at the lowest MIR wavelengths) to later obtain a more precise SCG numerical simulations. This method is detailed in the following.

First, the refractive index of Si and Ge are obtained at each wavelength by the fitting equations reported in Ref. [80]. Then, the vertical refractive index profile $n(z)$ is calculated by weighting the $\text{Si}_{1-x}\text{Ge}_x$ alloy as a function of the vertical position z in the layer stack (as in Fig. 2.3 and Fig. 2.4). Next, the vertical refractive index profile $n(z)$ is introduced to a numerical solver (Mode, Lumerical) at each wavelength, within a 2-15 μm range and a step of 10 nm. Thanks to optical simulations, the effective refractive index value (n_{eff}) of the fundamental TE and TM modes are acquired. In this way, the n_{eff} is obtained as a function of the wavelength in an accurate manner. Then, the second derivative of n_{eff} as a function of the wavelength ($\partial^2 n_{eff} / \partial \lambda^2$) is calculated by finite differences method in central configuration with an accuracy order of 8 (i.e., 9 different coefficients) as in Eq. 4.1, where n_{eff_i} are the effective refractive indexes calculated at different wavelengths, uniformly sampled with the same wavelength step (λ_{step}) and weighted by different coefficient values (C_i). I have chosen this derivative method due to its robustness against numerical instabilities and its facility to be employed. Finally, the GVD is obtained as: $GVD = -\frac{\lambda}{c} \frac{\partial^2 n_{eff}}{\partial \lambda^2}$.

$$\frac{\partial^2 n_{eff0}}{\partial \lambda^2} \approx \frac{\sum_{i=-4}^{i=4} C_i n_{eff_i}}{\lambda_{step}^2} \quad (4.1)$$

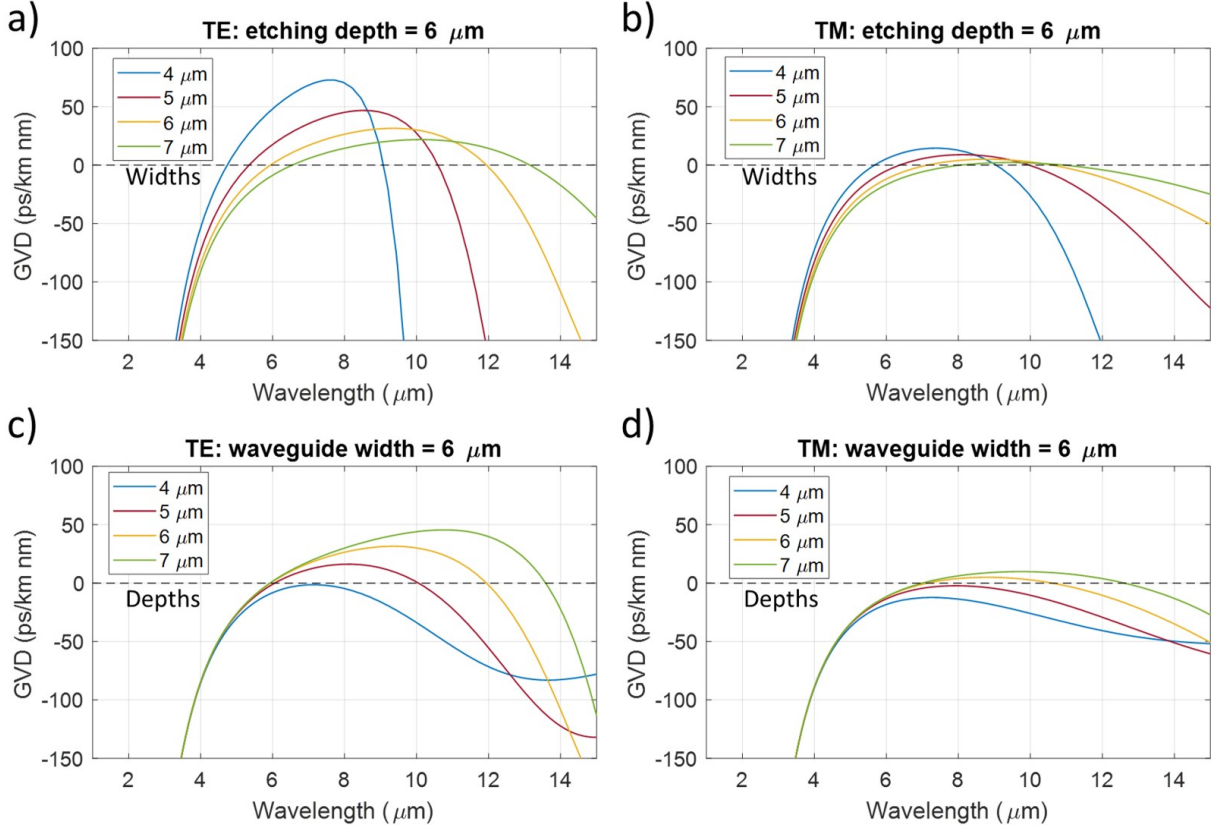


Figure 4.5.: Dispersion profiles for TE and TM polarization in the 13 μm thick graded-index SiGe platform. (a-b) Simulated profiles with fixed 6 μm etching depth and different waveguide widths. (c-d) Simulated profiles with fixed 6 μm waveguide widths and different etching depths.

This method can be used to further implement dispersion engineering for SCG optimization. For instance, different dispersion profiles are reported in Fig. 4.5 for the graded-index SiGe platform. As observed in this figure the waveguide width and height, as well as the optical mode polarization, have a strong influence on the spectral dispersion profile. Since the waveguides detailed in Chapter 2 are later used for SCG experiments, similar waveguides dimensions are considered hereafter: 6.2 μm width and 6.1 μm etching depth (Fig. 4.6(a)). As seen in Fig. 4.6(b) and for these waveguide dimensions, anomalous dispersion condition is obtained in a wide MIR wavelength range for both polarizations, but in particular for the fundamental TE optical mode, spanning from 6 to 13 μm . Therefore, only TE polarization is investigated in the following. Furthermore, at the same time as n_{eff} values are obtained with the mode solver at each wavelength, the effective modal area (A_{eff}) is also calculated. The effective modal area is reported in the right vertical axis of Fig. 4.6(c). The effective nonlinear coefficient is also calculated as $\gamma = \omega_0 n_2 / c A_{eff}$ (left vertical axis of Fig. 4.6(c)), where c is the light speed and ω_0 the pulsation. A constant Kerr nonlinear index value of $n_2 = 1 \times 10^{-17} \text{ m}^2/\text{W}$ is considered for this calculation [161]. This value has been taken from Fig. 4.2 and for $\text{Si}_{0.2}\text{Ge}_{0.8}$ alloy, as the optical mode is guided through high Ge concentration layers and the pump is located in this work in anomalous dispersion condition (6-13 μm wavelength). It has also been considered constant, as it experiences a weak variation along the MIR range with anomalous GVD. As

4. On-chip supercontinuum generation in the MIR

observed in Fig. 4.2(c), since the waveguides operate in the MIR regime, the A_{eff} is relatively large (especially when compare to the NIR regime), thus reducing the nonlinear coefficient γ . In fact, depending on the wavelength position, γ experiences approximately an order of magnitude variation, due to the large variation of A_{eff} .

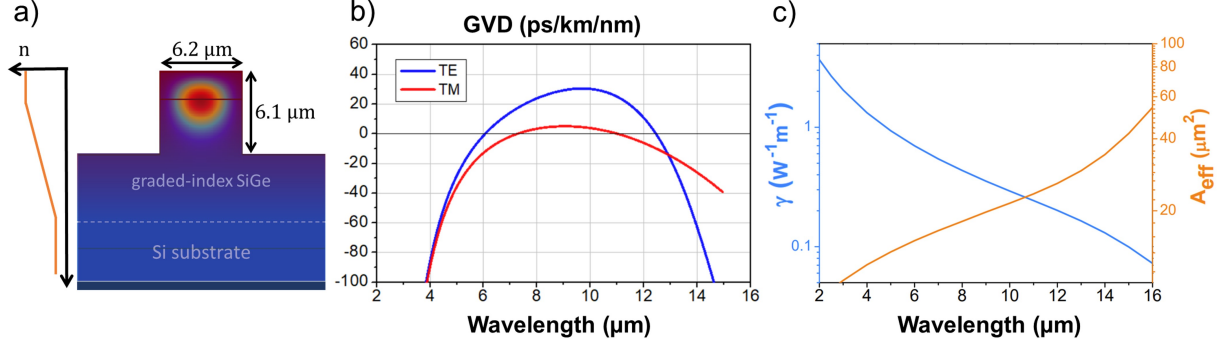


Figure 4.6.: SiGe waveguide features. (a) Schematic of waveguide dimensions and optical field distribution of the fundamental TE mode at 8 μm wavelength. Left side: illustration of refractive index profile. (b) GVD profile for TE and TM polarizations. (c) Effective nonlinear coefficient (left vertical axis) and effective area (right vertical axis) as a function of the wavelength.

4.3. Numerical SCG simulations

Once an accurate GVD profile and the γ parameter are obtained, it is now possible to numerically model the SCG properties. As a first step, the spectral position of a pair of generated dispersive waves (DW) are analyzed, as a mean to predict the SCG bandwidth. To that end, I employ the Eq. 4.2 [173] to obtain the phase-matching condition, where $\beta(\omega)$ is the frequency-dependent dispersion, ω_{DW} the pulsation position of the DW, ω_s the pulsation position of most energetic soliton (related to the pump wavelength), $v_{g,s}$ the group velocity at ω_s position and P the peak power of the most energetic soliton, which can be obtained from the input peak power (P_0) as $P = P_0 \frac{(2N-1)^2}{N^2}$, where N is the order of the initial HOS (breather). The left term of Eq. 4.2 is commonly called the integrated dispersion (β_{int}), which is equivalent to the summation of all the higher order dispersion terms. Therefore, the β_{int} is understood as the phase mismatch between the pump and the generated wavelengths, and can also be calculated as Eq. 4.3 [158], where the pulsation of the most energetic soliton (ω_s) corresponds to the input pump pulsation (ω_{pump}).

$$\beta(\omega_{DW}) - \beta(\omega_s) - \frac{\omega_{DW} - \omega_s}{v_{g,s}} = \frac{\gamma P}{2} \quad (4.2)$$

$$\beta_{int}(\omega) = \beta(\omega) - \frac{\omega - \omega_{pump}}{v_{g,pump}} - \beta_{pump}(\omega) - \gamma P_0 \frac{(2N-1)^2}{2N^2} \quad (4.3)$$

To investigate in detail the SCG, three different pump wavelength positions (λ_{pump}) are selected within the anomalous dispersion condition: 7.5, 8.5 and 9.4 μm . Then, the integrated dispersion is calculated as a function of the wavelength for those three pump positions and selected pulse peak powers. For a better comparison, the same peak powers have been applied. As seen in Fig. 4.7, for the three λ_{pump} , the cross of β_{int} with zero (horizontal dash line) is produced near 3 and 19 μm wavelength, with a variation depending on the input peak power. It means that the SCG generated may expand between those two wavelength positions in where a pair of DW would be generated. Furthermore, this figure is a direct illustration of the wavelength conversion efficiency, since the closer is β_{int} to zero, the better is the phase-matching. Interestingly, this calculation predicts an efficient SCG that expands over an ultra-wide spectral range, achieving more than 2-octaves broadening.

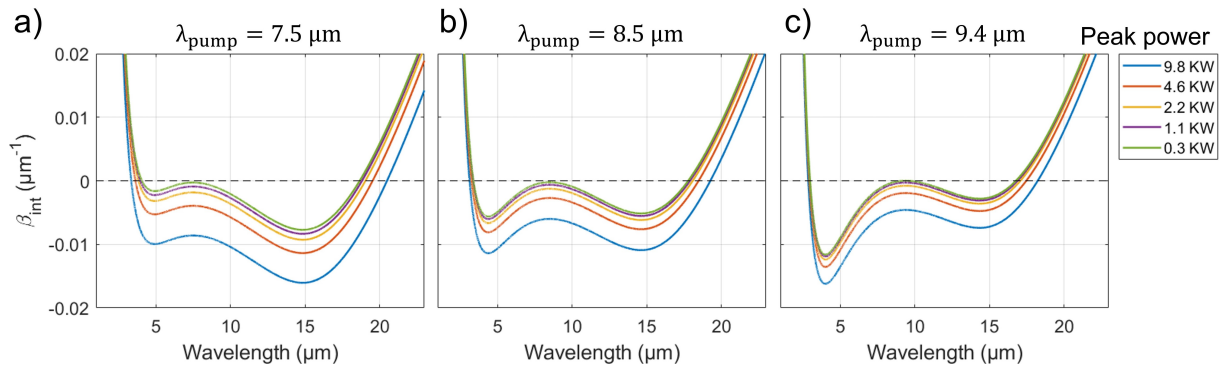


Figure 4.7.: Integrated dispersion profile for different pump peak powers and input wavelengths of (a) 7.5 μm , (b) 8.5 μm and (c) 9.4 μm . The cross with zero (horizontal dash line) predicts the apparition of a DW.

To confirm these results and to deepen in the knowledge of such SCG in graded-index SiGe waveguides, spatio-temporal simulations are performed by mean of the generalized nonlinear Schrodinger equation (GNLSE) shown in Eq. 4.4 [158, 173]. It must be noted that, since the Raman intensity decays as a function of the wavelength proportionally to λ^{-4} [174], Raman effect is considered negligible for the wavelengths under study, and thus has not been considered in this work ($f_R=0$ in the classical GNLSE formulation). For such simulation, I have adapted previous algorithms (Matlab code) developed by C. Lafforgue in C2N lab, in which a 4-order Runge-Kutta method is implemented [175]. The pump pulse is assumed to have a quadratic hyperbolic secant shape (sech^2) in time domain, with 220 fs duration at full-width of half-maximum. Furthermore, similar waveguide propagation losses as the ones reported in Chapter 2 are considered. However, they have only been experimentally characterized from 5 to 11 μm wavelength. On one hand, the propagation losses below 5 μm wavelength have been considered as the ones experimentally obtained at 5 μm (near 1 dB/cm). On the other hand, the propagation losses at wavelength longer than 11 μm wavelength have been considered as the ones obtained at 11 μm (near 3 dB/cm).

4. On-chip supercontinuum generation in the MIR

$$\frac{\partial A}{\partial z} = -\frac{\alpha}{2}A + i \sum_{k \geq 2} \beta_k \frac{i^k}{k!} \frac{\partial^k A}{\partial t^k} + i\gamma \left(i + i\tau_{shock} \frac{\partial}{\partial t} \right) |A|^2 A \quad (4.4)$$

The propagating evolution of a single input pulse is reported in Fig. 4.8 in wavelength and time domain, for a pump wavelength of $7.5 \mu\text{m}$ and an input peak power of 9.8 kW . As we can see in Fig. 4.8(a), a wide spectral broadening is obtained after a remarkable short propagating distance of $1.5\text{-}2 \text{ mm}$. This spectral expansion is related to a pulse compression in time domain (Fig. 4.8(b)), followed by a soliton fission process, in where an initial 77 -order soliton is sequentially divided in fundamental solitons. A remarkable spectral broadening is numerically obtained between 3 and $19 \mu\text{m}$ wavelength, corresponding, as predicted, to the position of a pair of generated DW. In the aim to minimize the size dimensions and provide a device as compact as possible, a propagating length of 5.5 mm is assumed to be large enough to provide a SCG in the area of interest, which is the transparency window of Ge (i.e., between 2 and $15 \mu\text{m}$ wavelength). The 5.5 mm -length position is depicted as an horizontal dash line in Fig. 4.8.

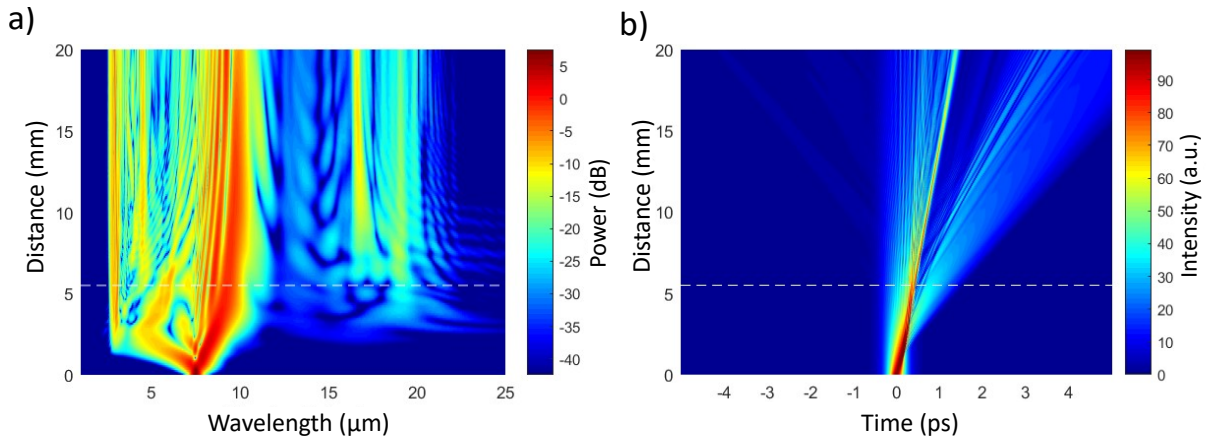


Figure 4.8.: Pulse evolution along the propagating distance for a pump pulse at $7.5 \mu\text{m}$ wavelength and 9.8 kW peak power. (a) In wavelength domain. (b) In time domain. Horizontal dashed line indicated 5.5 mm propagating length.

4.4. On-chip 2-octaves SCG: experimental results

As next step, the SCG has been experimentally investigated. To that end, the same sample as the one used in Chapter 2 is used for the experimental measurements, in which a 5.5 mm -length waveguide was available. Likewise, to optimize the coupling efficiency, a 1.5 mm -length taper transition is used to adapt the optical mode profile from the free-space beam to the $50 \mu\text{m}$ -width access waveguide and then to the $6.2 \mu\text{m}$ -width waveguide. Since the effective area (A_{eff}) of the optical mode is much larger in those transitions than in the central waveguide, the $50 \mu\text{m}$ -width access waveguide and the taper transition are assumed to have a low impact in the nonlinear phenomena, and thus were not considered in the previous simulations.

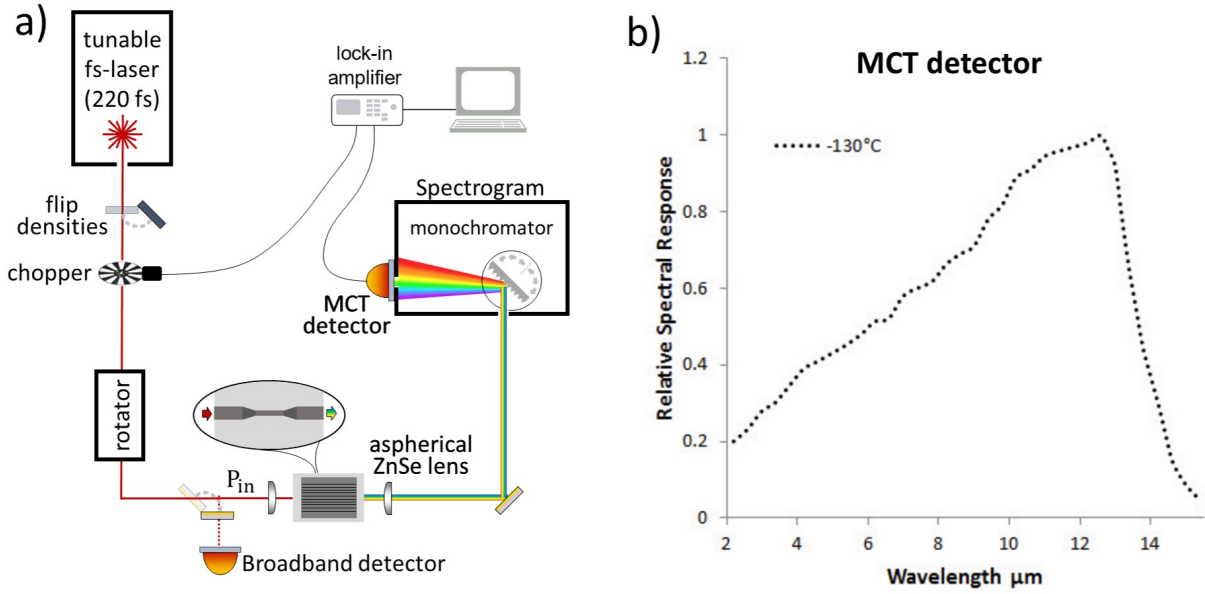


Figure 4.9.: (a) Schematic of the experimental setup used for SCG characterization. (b) MCT detector (DSS-MCT(14)020) response as a function of the wavelength. Image taken from www.horiba.com

In order to experimentally demonstrate SCG phenomena, the experimental set-up depicted in Fig. 4.9(a) is deployed. In this, a tunable femtosecond laser is used, with a pulse duration of 220 fs and a repetition rate of 1 MHz. The beam is rotated to obtain TE polarization by mean of a free-space scheme (Fig. 2.9(b)). Thanks to a pair of ZnSe aspherical lenses, the MIR light beam is injected into the integrated waveguide and the output signal is collected in a spectrometer system, based on a grating array monochromator and a MCT photodetector (DSS-MCT(14)020, Horiba). The response of the MCT detector is shown in Fig. 4.9(b). Two grating arrays are used in the monochromator for the experiments, with a central reflected wavelength position at 4 and 9 μm . A lock-in system is also used to perform synchronous detection and thus improve the detection sensitivity, thanks to a chopper that is placed in the input beam path. In order to tune the injected power, different MIR densities can also be introduced in the beam path to reduce the input peak power. To later calculate the injected power, the average input power (P_{in}) is obtained with a high-power and broadband photodetector that is selectively placed before the injecting lens. To construct the output SCG spectrum, I optimized the position of the output aspherical lens at each 1 μm wavelength step within 2-16 μm range and performed a full spectrum scan with both grating arrays (centered at 4 and 9 μm wavelength). Then, all the traces are overlapped and the envelop of them is obtained to retrieve the output spectrum.

The experimental results are provided in Fig. 4.10(a-c) for three input wavelengths (7.5, 8.5 and 9.4 μm) and different estimated average powers injected to the waveguide, based on P_{in} measurements and assuming 14 dB insertion loss (IL). For the sake of clarity, each trace is shifted in the vertical axis by 30 dB. As the maximal power delivered by the femtosecond laser rapidly decreases with the wavelength, a wide SCG is not reached with 9.4 μm pump wavelength. Nevertheless, a remarkable wide SGC, spanning up to 3-13 μm wavelength range (at

4. On-chip supercontinuum generation in the MIR

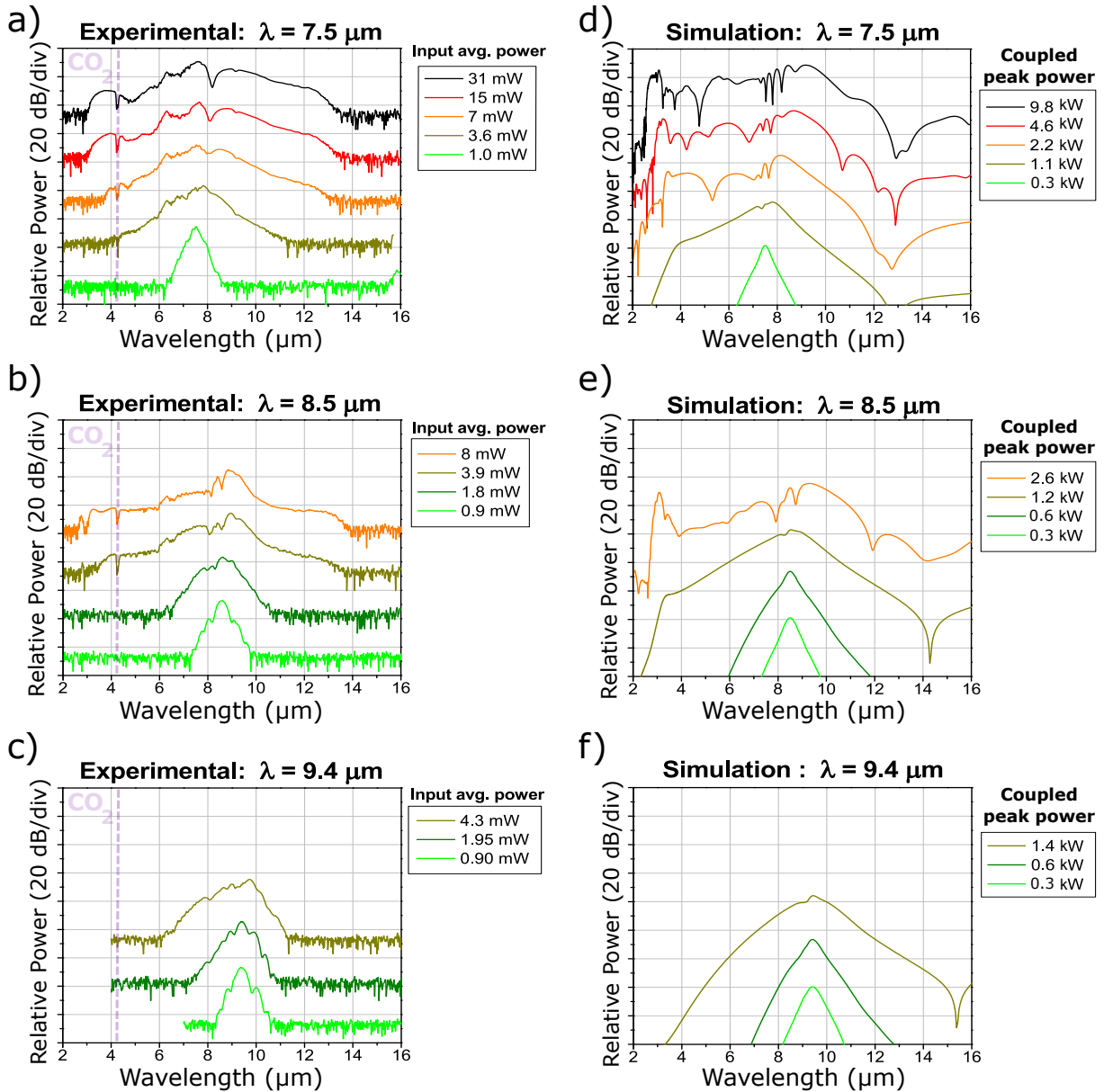


Figure 4.10.: Experimental and simulated SCG spectrum after a 5.5 mm long waveguide propagation. (a-c) Experimental measurements for 7.5, 8.5 and 9.4 μm input pump wavelength and different estimated mean powers injected into the waveguide, calculated from the average input power P_{in} and assuming 14 dB insertion losses. A vertical dashed line at 4.25 μm wavelength is added to indicate the atmospheric absorption of CO₂. (d-f) Simulated results for same input wavelengths and equivalent injected peak powers. For the sake of clarity, each trace has been vertically shifted by 30 dB in each figure.

-30 dB from the maximum value), is achieved for 7.5 and 8.5 μm pump wavelengths. Since the experimental setup is based on a free-space configuration, an absorption peak is observed at 4.25 μm wavelength, corresponding to the carbon dioxide present in the atmosphere. To compare those results with the previous modeling, I provide equivalent simulations in Fig. 4.10(d-f). To obtain the injected peak power, a squared pulse duration of 220 fs at 1 MHz rate is assumed. Also, a 14 dB of IL is considered, based on previous propagation loss measurements by cut-

back method. An IL of 9-15 dB was previously calculated and then a 14 dB value is obtained for the three pump wavelengths by fitting numerical and experimental results. It must be also noted that, numerical simulations theoretically expand up to near 19 μm wavelength, but the trace has been shortened to 16 μm to better compare with the experiments.

To evaluate the influence of the pump wavelength on the SCG, the experimental bandwidth (at -30 dB from the maximum value) as a function of the pump power is reported in Fig. 4.11(a). As we can see in this figure, the most efficient pump wavelength is 8.5 μm , which means that is possible to achieve the widest spectral expansion (up to 10 μm wavelength bandwidth) with the minimal pump power. This fact can be understood from integrated dispersion calculations (Fig. 4.7), in which a pump wavelength located near the center of the anomalous dispersion regime may lead to a higher phase-matching condition over the entire bandwidth (β_{int} closer to zero).

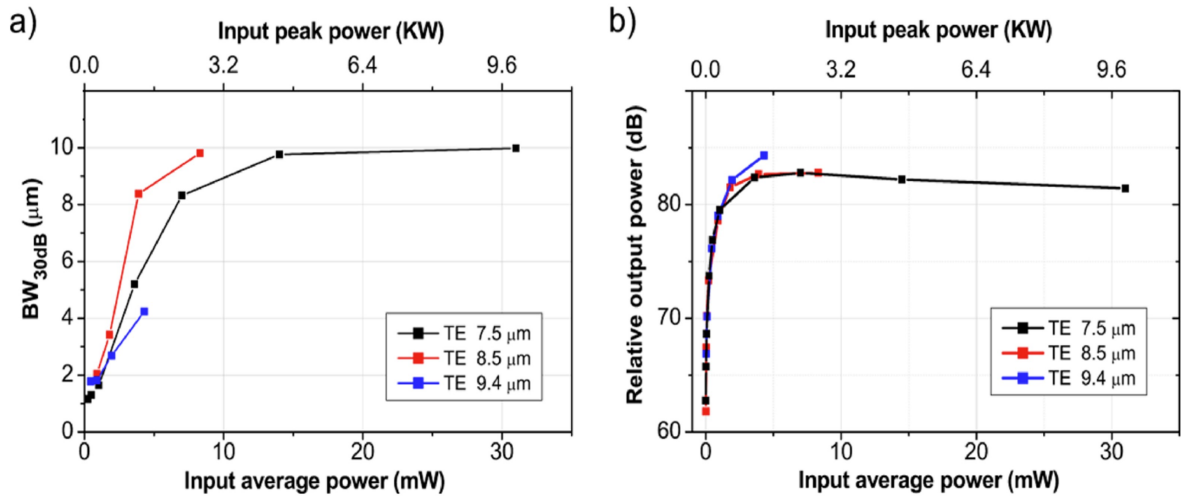


Figure 4.11.: SCG efficiency comparative for three different pump wavelengths in TE polarization: 7.5, 8.5, and 9.4 μm . (a) SCG bandwidth as a function of the input power, calculated as -30 dB of the maximum value. (b) Integrated total output power as a function of the input power. The input power is shown as averaged values (bottom x-axis) or peak pulse values (top x-axis).

The total output power (numerically integrated over the entire measured bandwidth) is also reported in Fig. 4.11(b). As we can see in this figure, for the three pump wavelengths the total output power saturates for input peak powers higher than around 1.5 kW (5 mW input average power), and even slightly decrease when increasing the pump power, as it is appreciated for 7.5 μm pump wavelength. This fact is assumed to not be caused by interband absorption loss coming from multiphoton absorption, meaning that the energy addition of multiple photons that simultaneously coincide in the same position is higher than the material bandgap. The photon energy is calculated as $E = \frac{hc}{\lambda}$, where λ is the wavelength of the photons, h is the Planck's constant and c the speed of light. Therefore, those photons would be absorbed and generate free-carriers that reduce the optical transmission, even in a stronger way than in NIR regime (FCPD effect is stronger in the MIR than in the NIR regime). An indirect gap of Si material of

4. On-chip supercontinuum generation in the MIR

$E_{g,Si} = 1.12$ eV, $E_{g,Ge} = 0.66$ eV for germanium and $E_{g,Si_{0.2}Ge_{0.8}} = 0.94$ eV for the $Si_{0.2}Ge_{0.8}$ alloy are obtained [176]. As seen in Fig. 4.12, for pump wavelengths longer than $6.5 \mu\text{m}$, up to 5-photon absorption is not enough to overpass the 0.94 eV bandgap of $Si_{0.2}Ge_{0.8}$ material. Hence, the nonlinear loss from multiphoton absorption is considered as negligible.

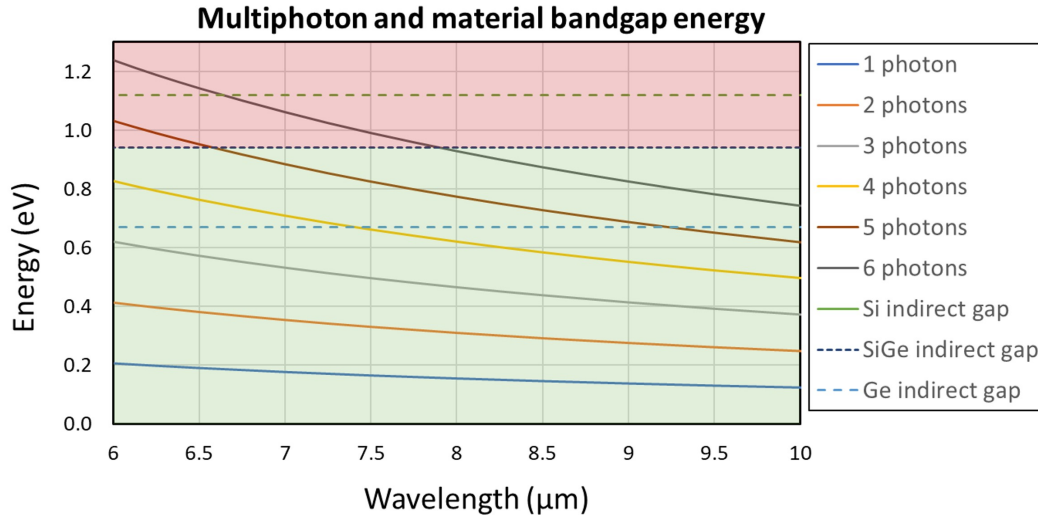


Figure 4.12.: Multiphoton energy as a function of the wavelength in solid lines. Horizontal dash lines indicate the bandgap energy of Si, Ge and weighted $Si_{0.2}Ge_{0.8}$ material. If the multiphoton energy overlaps the upper red colored area means that its energy is higher than the bandgap of the SiGe alloy, and thus will be absorbed by the waveguide material.

To understand the output power limitation that is experimentally observed, experimental and numerical results are compared. In fact, the SCG theoretically expand up to near $19 \mu\text{m}$ wavelength, while linear losses have been experimentally calculated only up to $11 \mu\text{m}$ wavelength. At longer wavelengths, and in particular higher than $15 \mu\text{m}$, the generated signal is expected to experience high propagation losses due to the intrinsic multiphonon absorption of Ge material. Furthermore, as seen in Fig. 4.9(b), the MCT detector of the experimental setup show a spectral response cutoff near $13 \mu\text{m}$ wavelength. It means that any light generated at wavelength longer than approximately $13 \mu\text{m}$ is not detected in the experimental setup, even though the SCG could expand slightly further up to $15 \mu\text{m}$ (limit of Ge). On one hand, this fact limits the maximal SCG wavelength bandwidth to around $10 \mu\text{m}$ value (Fig. 4.11(a)). On the other hand, when increasing the pump power, the energy transferred at wavelength longer than $13 \mu\text{m}$ is either not collected or vanished by multiphonon absorption, thus showing a saturating effect of the total output power in Fig. 4.11(b). Moreover, the increase of the pump peak power also leads to a moderate higher phase mismatch (Fig. 4.7), thus reducing the SCG efficiency. These facts can be an explanation of the slightly decrease of the total SCG output power when increasing the pump peak power in Fig. 4.11(b).

4.5. Simulated SCG coherence

Finally, since broadband but coherent light sources are often required for many MIR applications, such as free-space communications or imaging purposes, the coherence of the SCG is also investigated. To that end, the first order degree of mutual coherence g_{12} is calculated according to Eq. 4.5 [173], where the angle brackets denote an averaging over a series of independently generated output spectra \tilde{A} , where a random noise has been applied at each sampling point in temporal domain as Eq. 4.6. Therefore, the spectra \tilde{A} are obtained from the Fourier transform of the temporal pulses $A_{tot}(t)$, including a quantum shot noise in amplitude such that $a(t)$ follows a Gaussian distribution with variance $hf_0/(2T_e)$ [177, 178], where h is the Plank constant, f_0 the frequency of the initial input pulse and T_e the sampling time. The quantum shot noise in the phase of the initial pulse ($\phi(t)$) also follows a Gaussian distribution with variance π .

$$g_{12}(\omega) = \frac{\left| \left\langle \tilde{A}_i^*(\omega) \tilde{A}_j(\omega) \right\rangle_{i \neq j} \right|}{\sqrt{\left| \left\langle \tilde{A}_i(\omega) \right\rangle \right|^2 \left| \left\langle \tilde{A}_j(\omega) \right\rangle \right|^2}} \quad (4.5)$$

$$A_{tot}(t) = A_0(t) + a(t)e^{j\phi(t)} \quad (4.6)$$

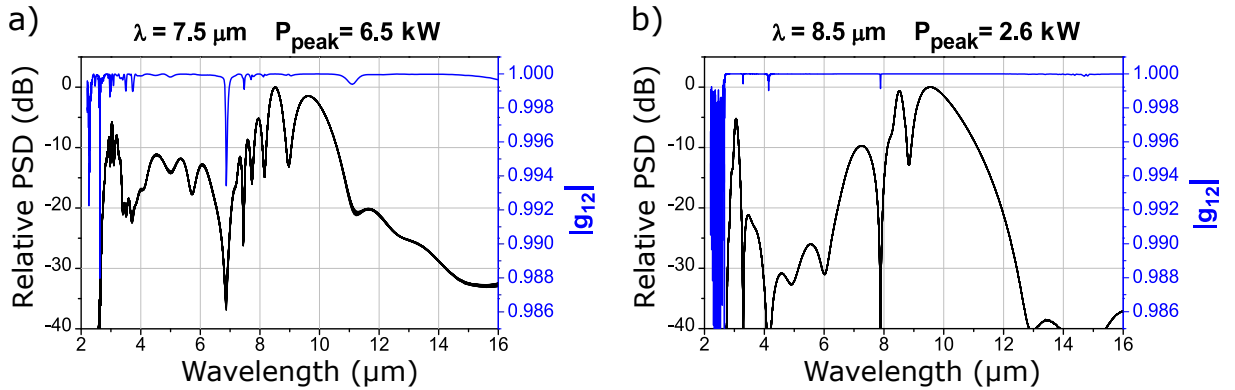


Figure 4.13.: First order degree of mutual coherence g_{12} as a function of wavelength in blue color (right y-axis) and superposition of 40 simulated SCG spectra used for statistical calculation in black color (left y-axis), after 5.5 mm propagating length: (a) for a 7.5 μm wavelength and 6.5 kW peak power of the input pump pulse, and (b) for a 8.5 μm wavelength and 2.6 kW peak power of the input pump pulse.

The calculations have been performed by my colleague C. Lafforgue with 40 different SCG simulations at both 7.5 and 8.5 μm pump wavelength and 6.5 and 2.6 kW peak power, respectively. The results are reported in Fig. 4.13, where the trace in black is the superposition of the 40 output spectra. This figure has also been shortened to a maximum wavelength of 16 μm , as no signal was experimentally detected at longer wavelengths and to better compare with previous figures. As it is seen in blue color, a high degree of coherence is predicted in the entire spectral bandwidth generated. Interestingly, since the quantum shot noise is considered as the main

4. *On-chip supercontinuum generation in the MIR*

source of incoherence and it is directly related to the single photon energy, a higher simulated coherence is achieved when operating at longer MIR wavelengths (lower photon energy).

4.6. Conclusions and routes for improvement of SCG in SiGe waveguides

In summary, a remarkable 2-octave SCG has been achieved in this chapter, spanning from 3 up to 13 μm wavelength, and by mean of a 5.5 mm-length Si-compatible waveguide. This experimental demonstration achieves two-fold the spectral expansion of previous works reported in the literature, providing an ultra-wideband and coherent MIR source by mean of a single and compact device. The demonstration of this building-block opens exciting perspectives to perform on-chip absorption spectroscopy of a significant large number of molecules, as it covers the full fingerprint region. Moreover, this SCG almost covers the both MIR atmospheric transparency windows (3-5 and 8-14 μm wavelength), thus showing compelling interest for many other high-impact applications, too.

In future works, some routes for improvement could be addressed. For example, since this work used available waveguides, the waveguide dimension or even the graded-index profile can be engineered to tailor the GVD profile, and thus optimize the SCG efficiency. It would be also interesting to explore the possibility of modifying the waveguide width along the propagating distance to improve the SCG performance or efficiency [179–181].

5

Integrated MIR electro-optical modulator

This chapter is devoted to the development of an integrated electro-optic modulator (EOM) operating in a broad spectral range of the MIR, by mean of free-carrier plasma dispersion (FCPD) effect. First, the state of the art and motivation of this work will be briefly introduced. Then, I will model and experimentally characterize the FCPD absorption effect in a wide MIR range, thanks to all-optical modulation in Ge-rich waveguides. Subsequently, I will address the design, fabrication and characterization of an integrated EOM device.

5.1. Motivation and state-of-the-art for broadband integrated EOM in the MIR regime

During the last two decades, several photonic integrated platforms capable to guide the MIR regime have been reported in the literature, and many related passive building blocks have been demonstrated. However, the development of an integrated EOM operating in the fingerprint region (3-13 μm wavelength range) is still missing in the literature, while it would enable efficient and simultaneous multi-molecule detection in compact sensing systems. In fact, the further development of an integrated EOM operating at room temperature would pave the way towards the implementation of efficient on-chip sensors, as they could benefit from a great sensitivity enhancement via synchronous detection [182]. Moreover, the realization of high-speed EOM in the MIR would open exciting perspectives in free-space communications, from short distance access networks to satellite communications [13, 79].

Indeed, only a few narrowband demonstrations have reported EOMs working at the longest wavelengths of the MIR regime. For example, a recent demonstration has shown a remarkable 1.5 Gbps optical modulation at 10 μm wavelength, by exploiting intersubband transitions in III-V material quantum-well structures and at room temperature [183]. However, this work was based on a free-space configuration and performing an intrinsic narrowband operation, given by the fabricated hetero-structure dimensions. Alternatively, since FCPD effect has been extensively used to implement optical modulators in the NIR [184], the wavelength extension of this

5. Integrated MIR electro-optical modulator

effect is a promising solution to implement MIR broadband modulators. Among the different MIR platform approaches, Si-based ones have emerged as a strong candidate to provide cost-effective devices, and in particular by mean of SiGe waveguides, as they can potentially operate up to $15\ \mu\text{m}$ wavelength (Ge transparency window). Interestingly, FCPD effect has been theoretically studied, first in Si and then in Ge material [122, 185], predicting a stronger FCPD effect at increasing wavelengths. Nevertheless, these models have not yet been experimentally evaluated at the longest MIR wavelengths.

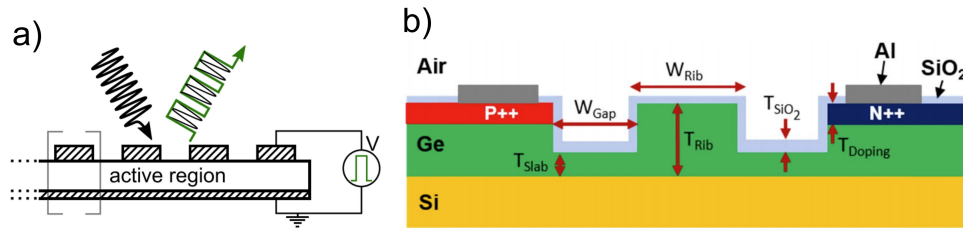


Figure 5.1.: Schematic of efficient MIR EOMs reported in the literature. (a) Free-space modulator operating at 1.5 Gbps in a narrow spectral band centered at $10\ \mu\text{m}$ wavelength, by mean of III-V quantum-well structures. Image taken from Ref. [183]. (b) Integrated modulator by mean of GOS waveguides and FCPD absorption effect. Image taken from Ref. [186].

Some works have exploited the FCPD effect to demonstrate optical modulation in the MIR regime, by mean of a diode embedded in Si-based waveguides. For example, a SOI-based EOM has shown up to 125 Mbps data-rate at $3.8\ \mu\text{m}$ wavelength [187], close to the transparency limit of SOI waveguides. In order to extend the optical modulation to longer wavelengths, an EOM based on GOS waveguides has also been reported in Ref. [186], showing up to 60 MHz on-off keying modulation at $3.8\ \mu\text{m}$ wavelength. That work also reported a preliminary absorption modulation at $8\ \mu\text{m}$ wavelength, by collecting with a MIR camera the output light of a grating array. Then, the modulation efficiency was obtained from the difference of the integrated pixel intensities when the input laser was injected or not. To the best of my knowledge, this is the only preliminary work of an integrated EOM working in the LWIR range of the MIR regime.

The absence of cost-effective and broadband integrated EOMs in the literature is due to the fact that reaching efficient on-chip MIR modulation present several challenges. First, the intrinsic material absorption of most of materials commonly used in Si-based PICs prevents its use at the longest wavelengths of the MIR. In this sense, the remarkable bandwidth performance of Ge-rich SiGe waveguides makes them a promising candidate to develop an integrated EOM. However, since Si and Ge are centro-symmetric material, Pockels effect cannot be exploited in this kind of platforms. Also, thermo-optic effect is not practical for high-speed modulation, as thermal effect is commonly slow. Therefore, FCPD effect is the remaining option to implement direct modulation in the MIR (without further wavelength conversion). Nevertheless, reaching efficient on-chip FCPD also present different difficulties, mainly related to the larger optical mode size at increasing wavelengths. On one hand, the injection or depletion region of diodes embedded in optical waveguides is fixed for an applied voltage. Therefore, as the optical mode

size increases at longer wavelengths, its overlap with the area in which the carrier concentration is modulated may be reduced (especially in depletion operation), thus reducing the modulation efficiency, too. On the other hand, EOMs based on FCPD effect typically requires highly doped layers to enable electric contact access to the diode electrodes. Those doped layers strongly absorb the optical light, and even more intensively in the MIR than in the NIR regime, as predicted in theoretical models and later experimentally demonstrated in this manuscript. Therefore, since the optical mode size and the free-carrier absorption increases with the wavelength, those doped layers must be placed further away from the waveguide core to minimize its overlap with the large optical mode. However, the longer distance between doped layers in the diode structure increases the access resistance, and consequently the maximal modulation speed, too.

In summary, the development of a broadband integrated EOM working in the longest wavelengths of the MIR is crucial for SNR enhancement in compact spectroscopy sensing system, among others, while has not been demonstrated yet. Among the different modulation phenomena, FCPD effect has aroused as a promising candidate for its implementation. However, its development presents different challenges that must be addressed. As a first step, the FCPD absorption effect in Ge material must be experimentally evaluated in a wide MIR range. This characterization is critical to confirm current prediction models and enable the further design and optimization of electrically driven optical modulators based on a diode embedded in Ge-rich SiGe waveguides.

5.2. Broadband validation of FCPD absorption in the MIR

In order to evaluate the FCPD absorption effect in a wide MIR spectral range, I have first carried out an all-optical modulation experiment by using the graded-SiGe waveguides. In this, a NIR pump at $1.33 \mu\text{m}$ wavelength is coupled to the waveguide, as illustrated in Fig. 5.2. The NIR wavelength value is given by the optimal working condition of the optical amplifier that was available in the experimental setup. As the photon energy at $1.33 \mu\text{m}$ wavelength is higher than the indirect gap of $\text{Si}_{0.2}\text{Ge}_{0.8}$ material, the light is absorbed, thus generating free-carriers. Consequently, if a co-propagating MIR beam is simultaneously coupled and guided through the waveguide, it will experience an absorption increase due to the newly generated carriers. Therefore, if the NIR signal is modulated, the MIR transmission will be, too. Finally, if the increase of the free-carrier concentration due to the NIR pump is properly modeled and the MIR wavelength is scanned, the FCPD absorption effect can be evaluated in a wide MIR spectral range.

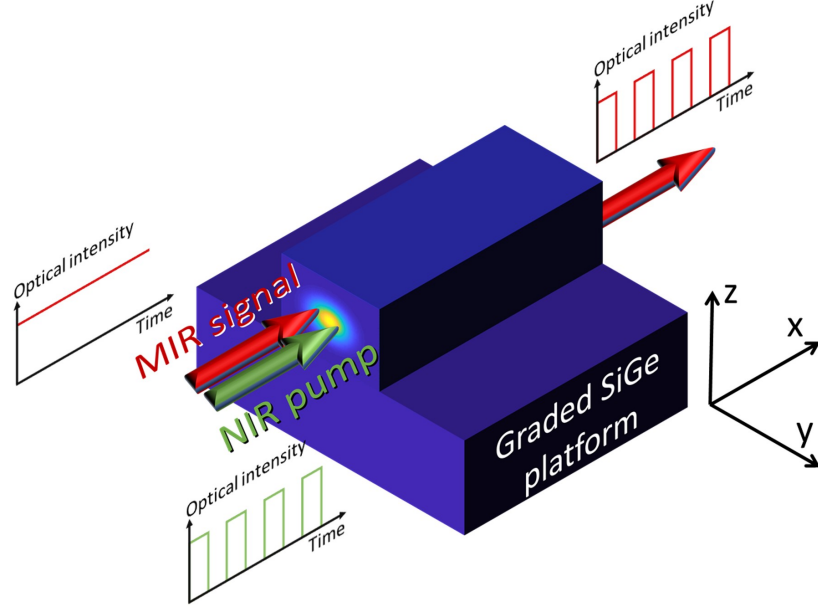


Figure 5.2.: Basic schematic of all optical modulation experiment. A NIR pump at $1.33 \mu\text{m}$ wavelength is coupled to the graded-index SiGe waveguide, together with a tunable MIR beam.

5.2.1. Modeling of free-carrier absorption in Ge-rich SiGe waveguides

In order to simulate the generation of free-carriers in the waveguide due to the interband absorption of the NIR pump, I used the carrier distribution model in semiconductor materials proposed in Ref. [188]. Therefore, a NIR beam at $1.33 \mu\text{m}$ wavelength is considered as a source of photons that propagates in the x-direction, with a two-dimensional (2D) Gaussian shape in the yz-plane. As externally applied electric fields are not considered in this model, the generated free-carriers can experience recombination given by the carrier lifetime (τ), or a diffusion in the semiconductor material. The carrier distribution generated along the waveguide can be described as in Eq. 5.1, where Δn is the carrier density increase with respect to the intrinsic waveguide concentration, x the propagating distance position, D the ambipolar diffusion coefficient (as in Ref. [189]), α the NIR absorption coefficient, Φ_0 the incident photon flux and $G(y, z)$ is the normalized 2D-Gaussian function that describes the free-carrier distribution in the yz-plane, with a standard deviation of R . The diffusion length of the carriers is calculated as $L_D = \sqrt{D\tau}$, and if it is larger than the NIR input beam size, the value of R can be considered as the diffusion length L_D . The photon flux value Φ_0 can also be obtained from the NIR input power (P_{NIR}) as $\Phi_0 = \frac{P_{NIR}}{h c / \lambda_{NIR}}$, where h is the Planck constant, c the speed of light and λ_{NIR} the pump wavelength (i.e., $1.33 \mu\text{m}$).

$$\frac{\Delta n(x, y, z)}{\tau} - D \frac{\partial^2 \Delta n(x, y, z)}{\partial x^2} = \alpha \Phi_0 G(y, z) e^{-\alpha x} \quad (5.1)$$

Next, the boundary conditions are considered as the free-carrier density vanishes at $x=+\infty$ and a surface recombination rate of S_0 is assumed at $x=0$ (input facet). Hence, the generated carrier density excess can be expressed as in Eq. 5.2.

$$\Delta n(x, y, z) = \frac{\alpha \tau \Phi_0 G(y, z)}{(\alpha L_D)^2 - 1} \left(\frac{\frac{S_0}{D} + \alpha}{\frac{S_0}{D} + 1/L_D} e^{-x/L_D} - e^{-\alpha x} \right) \quad (5.2)$$

Since most of the NIR light propagates mainly through the upper constant composition layer of $\text{Si}_{0.2}\text{Ge}_{0.8}$, an absorption coefficient of $\alpha = 20 \text{ cm}^{-1}$ has been assumed [190]. Likewise, an ambipolar coefficient of $D = 65 \text{ cm}^2\text{s}^{-1}$ has also been considered in this modeling [189, 191]. The recombination rate at the input facet has been considered as the Ge material, with a value of $S_0 = 250 \text{ cm s}^{-1}$ [192]. Also, since the carrier recombination time strongly depends on the growth conditions and the waveguide fabrication process, the value of τ is later adjusted to fit the simulations with the subsequent experimental results. A τ value of 15 ns has been obtained, which is consistent with other works reported in the literature. For instance, a similar work of all-optical modulation in the 2-3 μm wavelength range was reported in Ref. [193], showing an estimated value of $\tau = 18 \text{ ns}$ in GOS waveguides. A diffusion length of $L_D = 10 \mu\text{m}$ is then obtained. Since this value is larger than the NIR input beam spot size (estimated to be approximately 5 μm), the L_D value has also been considered as the standard deviation of the 2D-Gaussian distribution of the free-carriers in the yz -plane $G(y, z)$: $R = 10 \mu\text{m}$.

Once the free-carrier density increase (Δn) generated by the NIR pump has been modeled, this modification of the free-carrier density can be translated to variations of the refractive index and absorption coefficient, by the predictions reported in Ref. [122] for Ge material. Since the MIR optical mode is propagated through Ge-rich layers, those predictions are considered to be also valid for the Ge-rich SiGe alloy waveguides. Therefore, the absorption coefficient increase $\Delta\alpha$ can be expressed as in Eq. 5.3, where the values of the wavelength-dependent coefficients $c(\lambda)$ are also taken from Ref. [122]. Moreover, as each photon will excite an electron, generating an electron-hole pair, the increase in both $\Delta n_{\text{electrons}}$ and Δn_{holes} concentrations have been assumed to be equivalent in this model.

$$\Delta\alpha(\lambda) = c_1(\lambda)\Delta n_{\text{electrons}}^{c_2(\lambda)} + c_3(\lambda)\Delta n_{\text{holes}}^{c_4(\lambda)} \quad (5.3)$$

To do a preliminary analysis, I calculated the carrier density excess generated along the center of the waveguide (at the maximum of the NIR input beam) for three different NIR powers: 4, 8 and 12 mW. The maximum pump power value was limited by the experimental setup equipment used for the experiments and the coupling losses from the free-space setup to the integrated graded-SiGe waveguide. As seen in Fig. 5.3(a), the generated carrier density excess at the waveguide input strongly increases with the pump power, taken a value up to $3.9 \times 10^{15} \text{ cm}^{-3}$ for 12 mW pump power. Also, the generated free-carrier density exponentially decreases along the propagating distance, as the NIR pump is rapidly absorbed. Then, the FCPD absorption effect predicted in Ref. [122] is applied by considering these carrier distributions. For instance, in Fig. 5.3(b) is shown the absorption coefficient increase as a function of the wavelength, for a combined contribution of electrons and holes with an equal density of $3.9 \times 10^{15} \text{ cm}^{-3}$. As seen in this figure, the absorption coefficient due to free-carriers increases with the wavelength,

5. Integrated MIR electro-optical modulator

and in particular between 5 and 9 μm wavelength, while a slightly saturation effect is observed at wavelengths longer than 9 μm . Finally, the absorption coefficient increase along the center of the waveguide as a function of the propagating length is reported in Fig. 5.3(c), for 12 mW pump power and different MIR wavelengths. As observed in this figure, since the NIR light is strongly absorbed in the first millimeter of the waveguide, the MIR modulation will occur in that distance, too. Also, as expected, the modulation efficiency shown in Fig. 5.3(c) is also higher for longer MIR wavelengths.

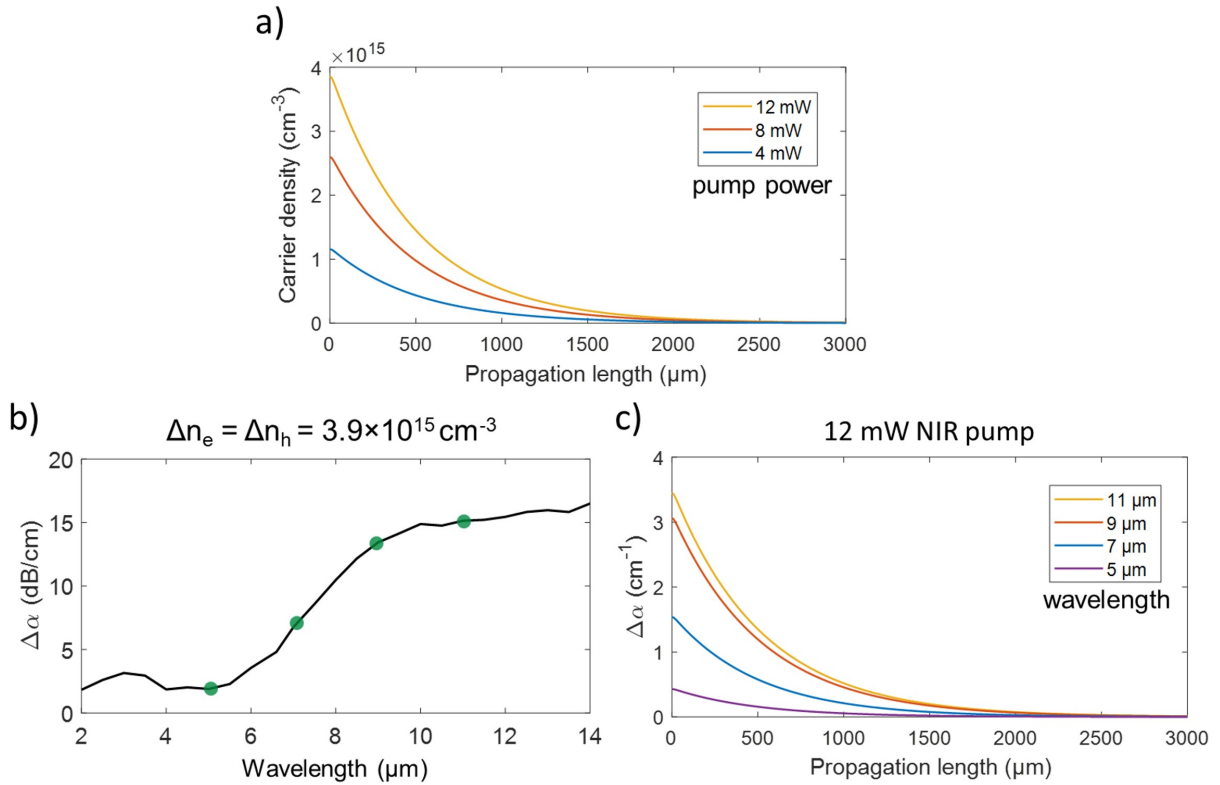


Figure 5.3.: (a) Carrier density distribution along the propagating axis at the center of input NIR beam and for different pump powers. (b) Absorption coefficient as a function of the wavelength for a combined electron and hole contribution at $3.9 \times 10^{15} \text{ cm}^{-3}$ density [122]. (c) Absorption coefficient distribution at the center of the waveguide for the corresponding carrier density distribution and for different MIR wavelengths.

To model the modulation efficiency of the subsequent fabricated device, a 50 μm -width access waveguide has been considered. As seen in Fig. 5.4(a), the input waveguide is 1 mm long, followed by a 2 mm-length taper transition. This structure is later used in the experimental setup to adapt the MIR optical beam from the free-space setup to the 7 μm -width waveguide. In this regard, since the NIR beam is mainly absorbed in first millimeter, the MIR light will be mainly modulated in the 50 μm -width input waveguide, which can be considered as a slab waveguide. To illustrate the vertical confinement of this approximately slab waveguide, Fig. 5.4(b) reports the graded-index concentration and the optical intensity profiles at 1.33, 5 and 11 μm wavelength as a function of the vertical z -axis. As it is appreciated in this figure, the maximum of the field intensity is shifted downwards at longer wavelengths. It must be noted that this vertical

shift at increasing wavelengths leads to an overlap mismatch between the MIR light and NIR beam responsible for electron-hole generation, and thus a slight reduction of the modulation efficiency is expected at longer MIR wavelengths.

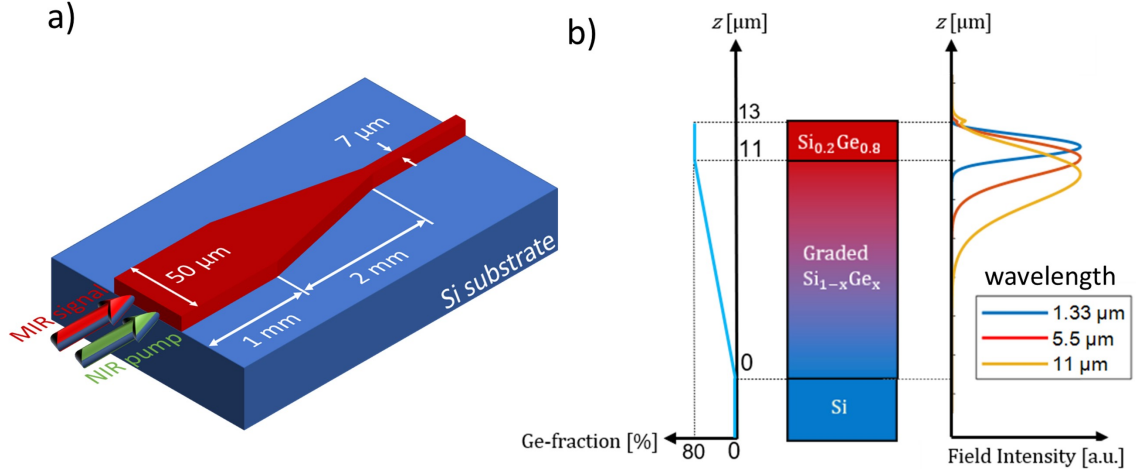


Figure 5.4.: (a) Scaleless schematic of the input coupling structure. (b) Cut-view schematic of the graded-index SiGe platform. On the left side is shown the Ge-concentration profile. In the right side is shown the normalized field intensity as a function of the vertical z -axis for three different wavelengths.

Next, an analytical description of the propagating MIR light is considered as the following. First, a non-uniform 2D-Gaussian shape is assumed for the MIR field profile that is being propagated. Therefore, a different standard deviation values are used in each axis of the 2D-Gaussian profile: R_y and R_z . Also, to consider the mismatch position between the MIR and NIR beams, the position of the MIR non-uniform Gaussian profile is vertically shifted as a function of the wavelength. On one hand, the vertical MIR confinement (R_z) and the z -axis position are estimated from optical simulations. On the other hand, due to the large 50 μm-width input waveguide, the horizontal confinement (R_y) is lower than the free-space input beam size. Therefore the R_y value of the MIR profile is considered in this model as the MIR beam spot size at the input facet of the waveguide. This value has been experimentally estimated with a MIR camera, where a value of $R_y=12$ μm at 5.5 μm wavelength was obtained. For longer wavelengths, the following relation is used: $R_y = R_{5.5\mu\text{m}} \sqrt{\lambda_{MIR}/5.5}$, where λ_{MIR} is the MIR light wavelength in μm and $R_{5.5\mu\text{m}}$ is the horizontal confinement value at 5.5 μm wavelength (i.e., 12 μm).

Then, the MIR non-uniform 2D-Gaussian beam is analytically propagated through the waveguide along the x -axis direction as in Eq. 5.4, considering 2.5 dB/cm propagation losses (α_{losses}) when no NIR pump is injected (from Fig. 2.15), $\Delta\alpha_{carriers}$ the absorption coefficient excess due to the generated free-carriers and $P_{in}(y, z)$ and $P_{out}(y, z)$ the respectively input and output MIR power profiles in the yz -plane after the x propagating distance. By mean of Eq. 5.2, the carrier density increase due to the NIR pump is analytically obtained at each spatial position of the waveguide, and is subsequently translated to an absorption loss coefficient distribution through

5. Integrated MIR electro-optical modulator

Eq. 5.3. This additional loss distribution in the three spatial dimensions of the SiGe waveguide is then applied to the MIR propagating field. The propagating MIR power can thus be calculated by numerically integrating the MIR field profile along the yz -plane at each propagating distance (x). For instance, the transmitted MIR power along the first 3 mm propagating distance is reported in Fig. 5.5, when zero or 12 mW NIR pump power are applied. Finally, the output modulation is obtained from the difference between the MIR transmission when the 1.33 μm wavelength pump is injected (P_{on}) or not (P_{off}). As expected, the modulation is mainly produced in the first 1 mm propagation length, where the orange color trace exponentially decays, while the blue trace remains with a linear decay at 2.5 dB/cm considered in the model. For propagating distances longer than approximately 1 mm, the NIR pump has been mainly absorbed and free-carriers are no longer generated, thus the slope of both traces (orange and blue) remains similar, only driven by the 2.5 dB/cm propagation loss.

$$P_{out}(y, z) = P_{in}(y, z) e^{-(\alpha_{losses} + \Delta\alpha_{carriers}) x} \quad (5.4)$$

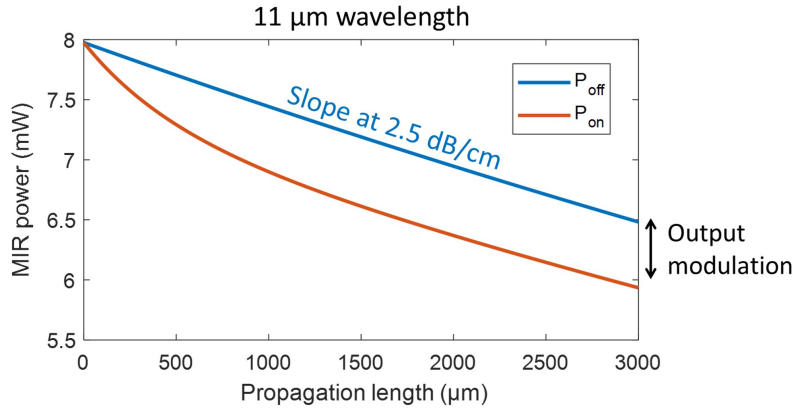


Figure 5.5.: Power distribution along the propagating axis of a 11 μm wavelength signal when the 12 mW NIR pump is injected (orange color) or not (blue color). A 2.5 dB/cm propagation loss is considered in both cases.

Finally, the modulation depth (MD) is calculated from the simulated output transmission difference as in Eq. 5.5, where P_{on} and P_{off} is the numerically integrated output MIR power when the NIR pump is sent to the waveguide or not, respectively. This method is implemented for different MIR wavelengths between 5.5 and 11 μm and three NIR pump powers (i.e., 4, 8 and 12 mW). The numerically obtained MD is reported in Fig. 5.6. As expected, those results predict an increase of the modulation efficiency between 5.5 and 9 μm wavelength. For longer wavelengths, a saturation and even a slight decrease is observed. This effect can be explained from the modest saturation of the FPCD absorption predicted in the literature (Fig. 5.3(b)) and a minor overlap mismatch between the NIR and the MIR field profiles at increasing wavelengths (Fig. 5.4(b)), where the MIR is shifted towards the Si substrate.

$$MD = \frac{P_{off} - P_{on}}{(P_{off} + P_{on})/2} \quad [\%] \quad (5.5)$$

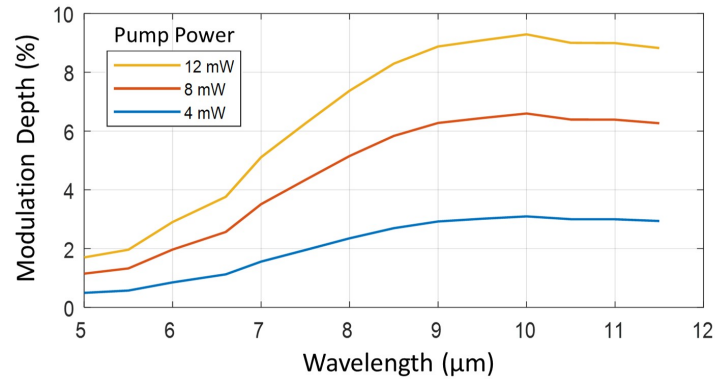


Figure 5.6.: Simulated all-optical modulation depth as a function of the wavelength, for a NIR pump at $1.33 \mu\text{m}$ wavelength and powers of 4, 8 and 12 mW.

5.2.2. Experimental characterization of all-optical modulation in the MIR

In order to experimentally validate the FCPD absorption effect in the graded-index Ge-rich SiGe platform by mean of all-optical modulation characterization, a set of straight waveguides are patterned by laser lithography and fabricated with an RIE-ICP equipment (in Polifab). As seen in Fig. 5.7(a), the waveguide width and etching depth are measured with a SEM, having a value of $7 \mu\text{m}$ and $3.8 \mu\text{m}$, respectively. A $50 \mu\text{m}$ -width and 1 mm-length access waveguide is also implemented, followed by a 2 mm-length taper transition (Fig. 5.4(a)).

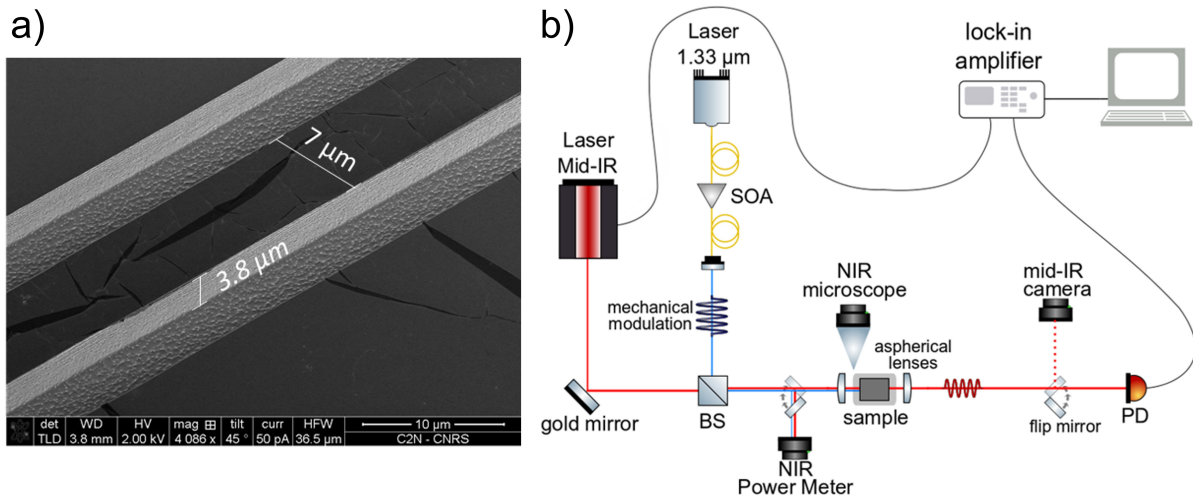


Figure 5.7.: (a) SEM image of the fabricated waveguides used in all-optical measurements. (b) Schematic of the experimental setup used for all-optical characterization in graded-index SiGe waveguides.

To characterize the all-optical modulation in the fabricated samples, the experimental setup depicted in Fig. 5.7(b) is deployed. In this, a continuous-wave laser at $1.33 \mu\text{m}$ wavelength is amplified by a semiconductor optical amplifier (SOA) and sent to free-space by a collimator objective. Thanks to a beam splitter, the NIR beam is superposed with the MIR one. Similar to previous characterization setups, the MIR beam can be tuned from 5.1 to $11.2 \mu\text{m}$ wavelength,

5. Integrated MIR electro-optical modulator

with a pulse duty cycle of 5% and 100 kHz repetition rate. Also, both beams are coupled to the fabricated waveguides and collected in a MCT detector thanks to a pair of ZnSe aspherical lenses. Likewise, a lock-in amplification system is used for SNR enhancement. Since the voltage values delivered by the lock-in equipment are proportional to the optical power collected by the MCT detector, the reading voltages (V_{on} and V_{off}) can be used for the MD calculations, instead of P_{on} and P_{off} . In order to select the NIR pump power, the SOA gain is tuned. Then, the pump power injected to the waveguide is estimated by measuring the NIR optical power before coupling to the sample with a broadband photodetector, and assuming 5 dB insertion loss.

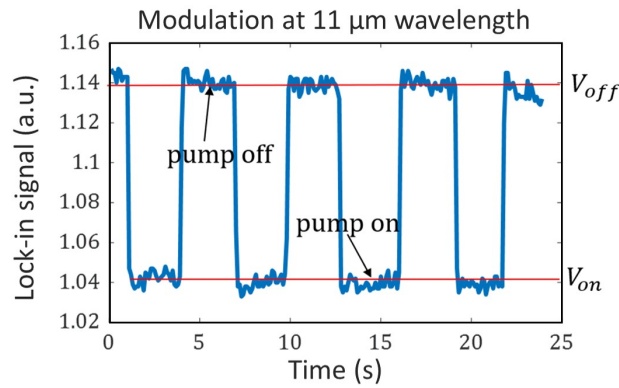


Figure 5.8.: Experimental all-optical modulation at 11 μm wavelength, mechanically actuated with a 12 mW pump at 1.33 μm wavelength.

To perform the MD measurements, the NIR pump has been modulated by manually activating a shutter that selectively blocked the NIR beam path. An example of all-optical modulation measurement performed at 11 μm wavelength is reported in Fig. 5.8, where the values V_{on} and V_{off} are the ones used for the MD calculations. As shown in this figure, clear modulation is observed when the mechanical shutter is activated or deactivated in time domain up to 8 times.

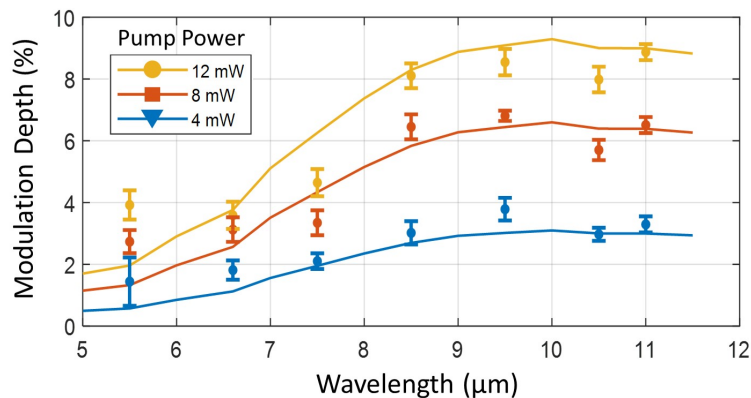


Figure 5.9.: Experimental all-optical modulation in a wide MIR range. The modulation depth is reported as a function of the wavelength and for three estimated NIR pump powers coupled to the SiGe waveguide, at 1.33 μm wavelength. The experimental data is shown as dots and simulated result as solid lines. The error bar of each experimental data corresponds to the MD standard deviation after a minimum of 10 repeated measurements.

Finally, the MD is experimentally obtained in a set of measurements, in which the MIR wavelength is scanned from 5.5 to 11 μm , and for 3 NIR pump powers coupled to the waveguide: 4, 8 and 12 mW. The results are reported as dots in Fig. 5.9, showing a good agreement with previously simulated results depicted as solid lines. These measurements are repeated a minimum of 10 times at each working point, in order to provide the MD standard deviation (shown as vertical bars). Interestingly, a saturation and even a slight decrease predicted by the model at wavelengths longer than 9 μm is also observed experimentally. It must be noted that small variations can be observed at low wavelengths (i.e., 5.5-7.5 μm), which are expected to be due to the different modeling assumptions. These experimental data have also been used to fit the carrier lifetime τ in the previous numerical model.

In summary, this work is the first experimental validation of FCPD absorption effect in a wide MIR spectral range, spanning from 5.5 to 11 μm wavelength and reaching the LWIR regime. Although the modest MD values obtained, the experimental results are in good agreement with the numerical modeling. Hence, these experimental results confirm previous models reported in the literature, enabling the further design and optimization of efficient integrated EOMs based on FCPD effect.

5.3. Integrated EOM in the MIR

The FCPD absorption effect has been experimentally validated in the previous section. As a next step, I will demonstrate the first integrated EOM operating in a wide MIR spectral range in the following subsections.

5.3.1. Design of the integrated EOM structure

In this work, a Ge-rich graded-index SiGe platform is used to implement the integrated EOM. However, unlike previous demonstrations in this thesis, the platform proposed now has a Ge concentration that linearly increases from 0% (Si substrate) to pure Ge, along a 6 μm -thickness layer. This graded-index platform was reported for the first time in Ref. [95] and has been chosen for this demonstration due to its higher compactness when compared to the previous 13 μm -thickness graded-SiGe platform. In this way, a reduced distance between the electrodes is expected to provide a lower access resistance, and thus a larger modulation bandwidth. Moreover, the graded-SiGe layer is epitaxially grown on top of a 500 μm -thickness heavily n-doped Si substrate in order to provide a bottom access contact and simplify the fabrication process, as only one etching step and an easy bottom metal deposition are required. To complete the vertical diode embedded in the SiGe waveguide and to exploit the FCPD effect driven by an electric signal, a metal layer is deposited in the bottom of the device and a metal strip on top of the waveguide. Both contacts are formed by a 300 nm-thickness layer of gold. A schematic cut-view of the EOM structure is reported in Fig. 5.10.

5. Integrated MIR electro-optical modulator

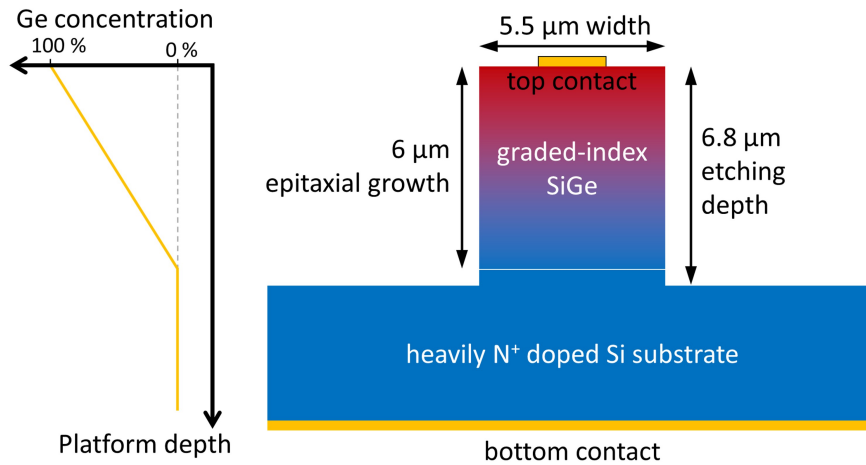


Figure 5.10.: Schematic cut-view of the EOM structure. Left side: illustration of the Ge concentration as a function of the SiGe platform depth.

To properly model the diode, the residual doping type of the graded-index layer is experimentally obtained by hot-probe characterization [194]. In this, a soldering iron is placed on top of the wafer in which epitaxial growth was done. Then, a voltmeter is used, placing one of the electrodes next to the iron tip and the other one relatively far away, both touching the sample surface. The thermal difference between the electrodes creates a voltage, which sign depends on the residual doping characteristics of the SiGe layer (p-type or n-type). In the platform used for this demonstration, a residual n-type doping was obtained. This result is later confirmed by a SIMS characterization, too. Therefore, since the Si substrate and the graded-index layer have both a n-type free-carrier concentration, a potential barrier between the top metal strip and the graded-index layer is expected to perform a vertical Schottky diode. In this regard, if a bias voltage is applied between the top and bottom metal electrodes, the free-carrier concentration in the top area of the waveguide will vary. Moreover, if a certain voltage is appropriately applied, the potential barrier can be surpassed, thus creating a current that traverses the diode in the vertical direction. In both cases, the carrier concentration variation modifies the refractive index and absorption coefficient experienced by the optical mode that is being propagated through the waveguide, thus modulating its intensity or phase. In this first integrated EOM design, straight waveguides are considered. Hence, only absorption modulation will be exploited, benefiting from previous experimental evaluations of FCPD effect.

To preliminary evaluate the optical influence of the highly doped Si substrate in this design, numerical simulations of the optical mode profile are performed. For instance, Fig. 5.11 shows three different mode profiles at three wavelengths that will be later used in the experiments: 6.4, 8.5 and 10.7 μm. Likewise, a 5.5 μm-width and 6.8 μm-high waveguides have been considered for the simulations, with a top metal (gold) layer of 300 nm thickness. As we can observe in this figure, the optical mode in TE polarization is well confined on top of the waveguide, with a relative low modal area. Therefore, the free-carrier absorption due to the highly doped substrate is estimated by optical simulations to have a negligible contribution up to 7 μm wavelength.

However, it increases at longer wavelength, as the optical field profile enlarges towards the Si substrate, reaching a simulated value of 3 dB/cm near 11 μm . I have obtained this value by multiplying the power fraction of the optical mode by the absorption coefficient caused by the free-carriers in the Si substrate ($2 \times 10^{19} \text{ cm}^{-3}$ electron density). Although the optical mode profile is well confined in Ge-rich layers, as seen in Fig. 5.11, this optical expansion at longer wavelengths may also lead to an increase of the propagation losses due to Si multiphonon absorption. In this sense, it is interesting to experimentally study the optical propagation loss at different MIR wavelengths. Hence, this evaluation is later experimentally performed in a dedicated sample with similar waveguide dimensions and without metal contacts deposited. Furthermore, the influence of the top metal strip is expected by simulations to prevent the use of TM polarization as, due to the electric field orientation to respect the EOM structure, the top metal introduces high propagation losses in this polarization. Therefore, only TE polarization is considered hereafter. The experimental influence of the top metal strip is later evaluated, too.

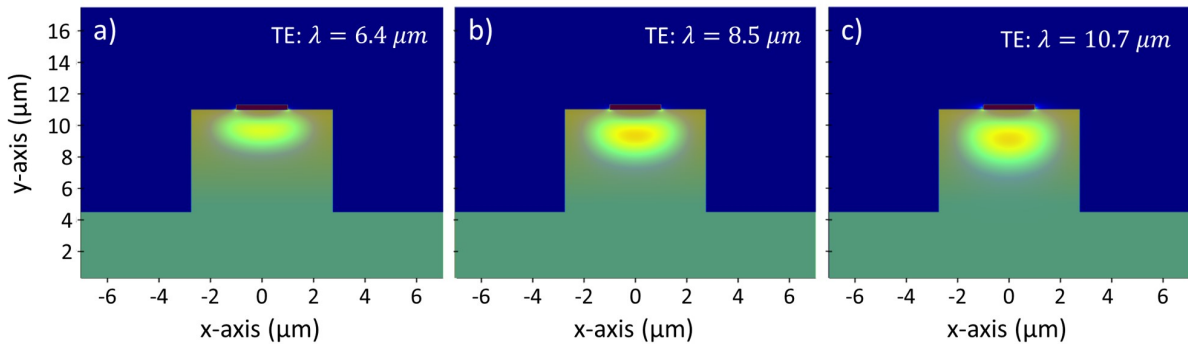


Figure 5.11.: Simulation of the fundamental TE optical mode profile in the EOM device at selected wavelengths: (a) 6.4 μm , (b) 8.5 μm and (c) 10.7 μm .

5.3.2. Integrated EOM fabrication and experimental insertion losses

To implement the EOM design, I have developed the fabrication process illustrated in Fig. 5.12. First, the 6 μm -thickness platform is grown on top of a highly n-doped Si substrate, with an estimated arsenic concentration of $2 \times 10^{19} \text{ cm}^{-3}$. The epitaxial growth process is similar to the other graded-index SiGe platform previously detailed in this manuscript and is likewise carried out by G. Isella's group of Politecnico di Milano (Como, Italy). Then, a 1 mm long and 2 μm wide top metal strip is deposited on the sample surface by lift-off process. The metal layer is composed by 10 nm of titanium and 300 nm of gold, in order to enable a good adhesion to the sample surface. Next, the waveguides are patterned by e-beam lithography, developed and defined with an RIE-ICP dry etching process (in C2N facilities). It must be noted that, since the total metal thickness is only 310 nm and the CSAR layer is approximately 1.3 μm , a uniform electronic photoresist (CSAR-18) deposition is achieved in the spin coating step. The fabricated waveguide dimensions are measured with a SEM, having 5.5 μm width and 6.8 μm height. Then,

5. Integrated MIR electro-optical modulator

the fabricated structure is protected with a thick optical photoresist (AZ-4562) and the bottom of the sample is mechanically polished. This step is performed to enable a good and uniform electric contact to the highly doped substrate, avoiding any possible isolating dielectric layer due to Si substrate oxidation. A similar metal layer is subsequently deposited in the bottom of the device (10 nm of Ti and 300 nm of Au). Then, the sample must be accurately cleaned to remove the protecting optical photoresist and the electronic photoresist remaining from the dry etching step. A cut-view SEM image of the structure is also reported in Fig. 5.12. Finally, in order to facilitate the later electro-optical characterization, the sample is glued to a metal holder with a conducting indium paste.

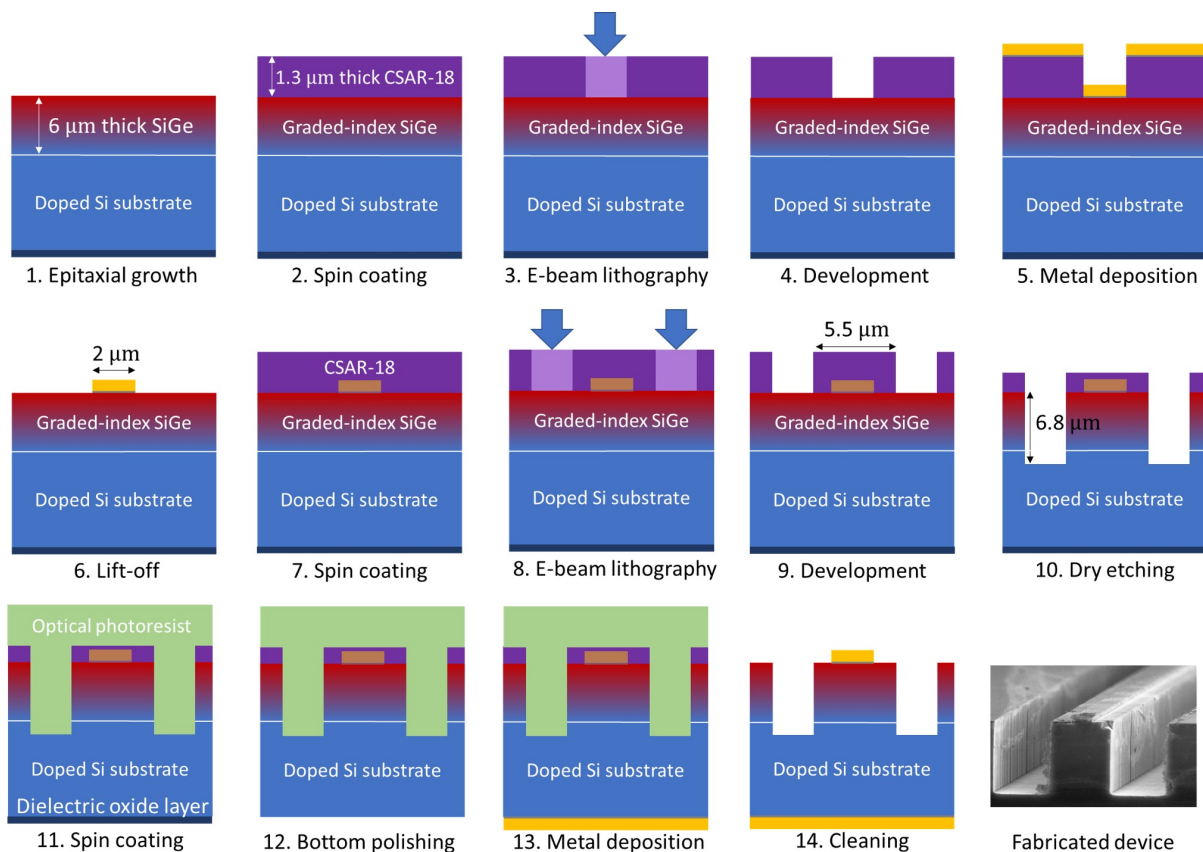


Figure 5.12.: Fabrication process steps of the proposed integrated EOM structure. A cut-view SEM image of the fabricated structure is also given in the bottom-right corner.

A proper optimization of each fabrication step is essential to ensure the reliability and repeatability of the fabrication process flow. Furthermore, the correct optimization of each step allows its further reuse in the fabrication of other structure designs. Therefore, optical and SEM pictures are methodically taken. For instance, Fig. 5.12 shows the metal deposition of the top metal strip with different widths, just before the lift-off process step carried out in a 2-butanone bath.

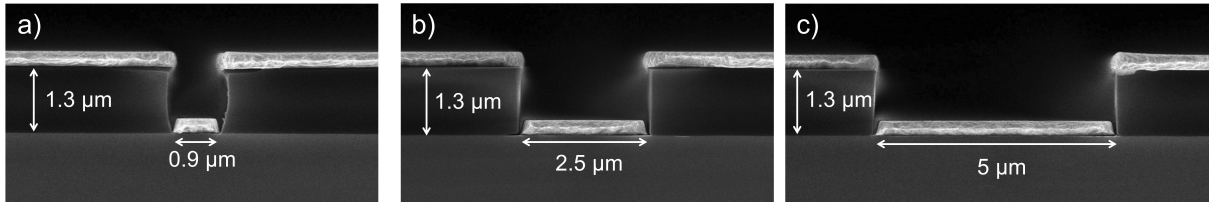


Figure 5.13.: Cut-view SEM image of the top metal deposition step. A $1.3\ \mu\text{m}$ -thick electronic photoresist (CSAR-18) is patterned and a long metal strip (10 nm Ti and 300 nm gold) is deposited with three different widths: (a) $0.9\ \mu\text{m}$, (b) $2.5\ \mu\text{m}$ and (c) $5\ \mu\text{m}$.

To apply a bias voltage in the Schottky diode, the top and bottom metals must be contacted with a positive and negative electrode, typically by mean of external tip probes. The large bottom metal layer enables an easy electric contact access. However, the narrow $2\ \mu\text{m}$ -width top metal strip prevents a practical contact, in which a minimum of $100\ \mu\text{m}$ squared metal size is typically required. In this regard, as shown in the scaleless top-view schematic of Fig. 5.14(a), the $5.5\ \mu\text{m}$ -width SiGe waveguide (in blue color) widens up to $100\ \mu\text{m}$ through a $1.5\ \text{mm}$ -length taper transition. In this way, from right to left in the Fig. 5.14(a), the $1\ \text{mm}$ -length top metal strip (in yellow color) is extended through the waveguide taper, to later enlarge along a $100\ \mu\text{m}$ -length transition from $2\ \mu\text{m}$ to $98\ \mu\text{m}$ width. Hence, a feasible top contact access is allowed with an electric tip probe. Furthermore, the $100\ \mu\text{m}$ -width access waveguide can be used to improve the optical coupling efficiency, similar to the previously used $50\ \mu\text{m}$ -width access waveguides. A SEM image of the EOM structure is also reported in Fig. 5.14(b). For simplicity, a taper transition and access waveguide with similar dimensions are also placed at the output of the EOM device (without a metal strip deposited on top) to improve the collection efficiency, too.

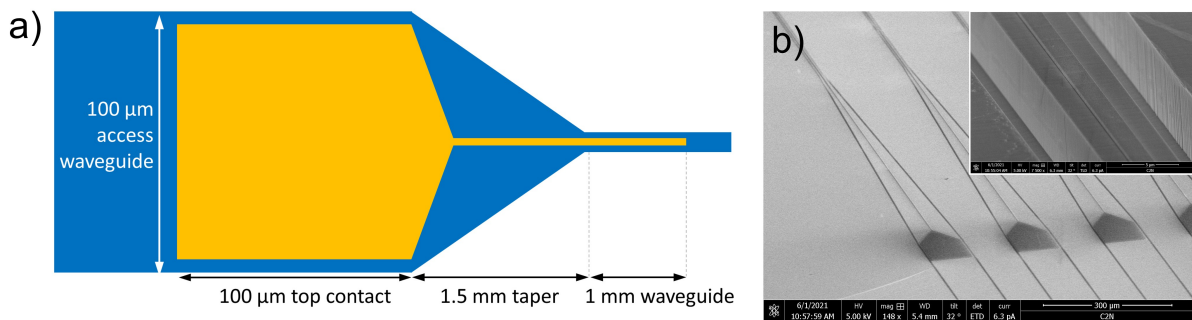


Figure 5.14.: (a) Top-view and scaleless schematic of the EOM device. The optical waveguide is depicted in blue color, which narrows down from the $100\ \mu\text{m}$ -width input access to the $5.5\ \mu\text{m}$ -width waveguide along a $1.5\ \text{mm}$ -length transition. The top metal contact is depicted in yellow color and narrows down from the $98\ \mu\text{m}$ -width metal path to the $2\ \mu\text{m}$ -width and $2.4\ \text{mm}$ -long metal strip, along $100\ \mu\text{m}$ -length transition. (b) SEM image of the EOM structure. Inset: SEM image of the $5.5\ \mu\text{m}$ -width waveguide section.

Once the EOM device has been fabricated, its related optical losses are experimentally investigated at three different MIR wavelengths: 6.4 , 8.5 and $10.7\ \mu\text{m}$. The different loss values

5. Integrated MIR electro-optical modulator

are summarized in Table 5.1. On one hand, the influence of the top metal strip is experimentally obtained by comparing the transmission of an EOM structure with and without metal on top. An insertion loss contribution of 3.5, 7 and 12 dB at 6.4, 8.0 and 10.7 μm wavelength are respectively obtained for the top metal contact. On the other hand, the optical propagation loss contribution due to the SiGe waveguide (and the highly-doped substrate) is also investigated in a dedicated sample, in which a set of waveguides with increasing length were fabricated, but omitting both metal depositions (top and bottom contacts). The fabricated waveguides have similar dimensions to the EOM structure (5.5 μm width and 6.8 μm height). Then, the propagation losses have been characterized by cut-back method together with my colleague N. Koompai (PhD student in C2N), similarly to previous waveguide characterizations in this manuscript. The obtained propagation losses were 2, 4 and 12 dB/cm at the selected wavelengths (6.4, 8.0 and 10.7 μm). As appreciated in both experimental investigations, the insertion loss rapidly increases at longer wavelengths, mainly due to an expansion of the optical mode towards the top metal contact and the bottom highly doped Si substrate. Also, the top metal strip shows a stronger interaction with the optical mode than the Si substrate, thus introducing higher insertion loss values for the three selected wavelengths. The total insertion losses of the 2.6 mm-length modulator have thus been determined as 4, 8 and 16 dB at 6.4, 8.0 and 10.7 μm wavelength. It must be finally noted that, although the different loss contributions can be improved in further optimized designs, they are acceptable for this first demonstration of an integrated EOM operating in a broad spectral range of the MIR regime.

Experimental losses of the 2.6 mm-length EOM	Wavelength		
	6.4 μm	8.5 μm	10.7 μm
Total insertion loss	4 dB	8 dB	16 dB
Contribution of metal contacts	3.5 dB	7 dB	12 dB
Contribution of optical waveguide & substrate	0.5 dB	1.0 dB	3.6 dB
Waveguide propagation losses	2 dB/cm	4 dB/cm	14 dB/cm

Table 5.1.: Optical losses of the 2.6 mm-length EOM device at 6.4, 8.5, and 10.7 μm wavelength.

5.3.3. Schottky diode mesa study and electrical characterization

Before reporting electro-optical modulation experiments, it is interesting to investigate the static electrical properties of the EOM structure. On one hand, it is important to confirm the Schottky diode behavior on top of the waveguide. In fact, if a p-type doping concentration is obtained during the epitaxial growth of the graded-index SiGe layer, the carriers will recombine or deplete in the interface between this layer and the n-doped substrate. As this would be produced far from the upper part of the waveguide, where the optical mode is mainly propagated, the free-carrier depletion would slightly affect the optical mode, and thus a weak electro-optical modulation would be achieved. On the other hand, it is also interesting to obtain the electrical

resistivity of the Si substrate and graded-index SiGe layer, in order to better understand the modulation efficiency in further experiments. In this regard, my colleague N. Koompai fabricated and characterized squared mesa diodes with different sizes, from 60 to 150 μm side-length. To fabricate these structures, a similar fabrication process as for the EOM device was performed. As an example, Fig. 5.15 shows an optical microscope image of fabricated squared mesas with 70 and 150 μm side-length. Inset: zoomed image to a single mesa structure.

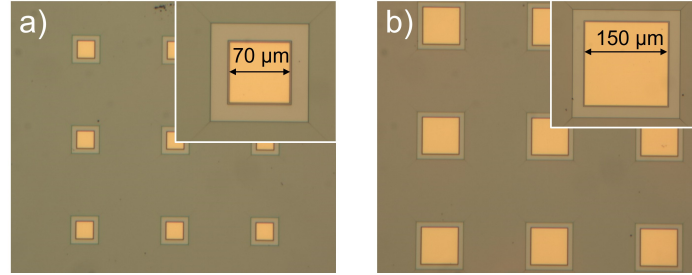


Figure 5.15.: Optical microscope image of fabricated Schottky diode squared mesas with (a) 70 μm side length and (b) 150 μm side length. Inset: zoomed image to a single mesa structure.

To experimentally characterize the Schottky mesas, a pair of tip probe electrodes are placed on the top and bottom metal contacts of the sample. Then, a voltage is applied in the diode with a power source (Keithley-2400) and the injected current value required to achieve that voltage is obtained. The Fig. 5.16(a) shows the resulting I-V traces for different squared mesa diodes with side-length between 70 and 100 μm . From these measurements, following the methods reported in the literature [195, 196] and considering a Richardson constant of $120 \times 0.12 \text{ A}/(\text{cm}^2\text{K}^2)$, an ideality factor of 1.43 and a Schottky barrier of 0.6 eV are obtained. Furthermore, to calculate the access resistance of the mesa diode, the derivative of the voltage with respect to the injected current is calculated. The results for equivalent squared mesa diodes (from 70 to 100 side-length) are reported in Fig. 5.16(b). The total resistivity of the complete structure (Si substrate and graded-index layer) is calculated as 2.7-3.6 Ω .

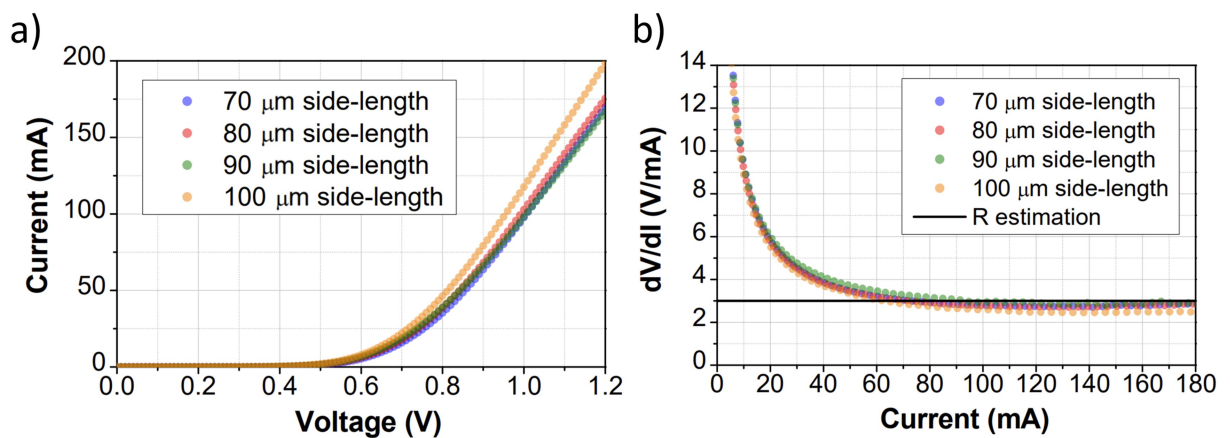


Figure 5.16.: (a) Measured current intensity as a function of the applied voltage in squared mesas with side-length of 70-100 μm . (b) Measured voltage derivative to respect the current intensity of similar diode mesas. A horizontal line represents a 3 Ω resistivity value.

5. Integrated MIR electro-optical modulator

To support these results and to allow further accurate electro-optical simulations, the arsenic (n-type), phosphorous (n-type) and boron (p-type) concentration of the graded-index platform is evaluated by a SIMS characterization, performed by an external company (Eurofins Scientific). The collected data are reported in Fig. 5.17. Since the measured dopant concentration values depend on the ratio of the SiGe alloy, that is gradually modified along the platform depth, these results have a certain incertitude. Nevertheless, the graded-index SiGe layer is estimated to have a low residual n-type doping density of $10^{15} - 10^{16} \text{ cm}^{-3}$. This value has been considered by comparing the different concentration values in Fig. 5.17, and subtracting the p-type contribution (B) to the n-type concentrations (P and As). As observed in this figure, the As dopant (green color) is the predominant one in the PIC platform. In fact, the relatively high As concentration in the $6 \mu\text{m}$ -thickness SiGe layer is expected to have been produced from a dopant diffusion coming from the highly-doped Si substrate (As concentration of $2 \times 10^{19} \text{ cm}^{-3}$).

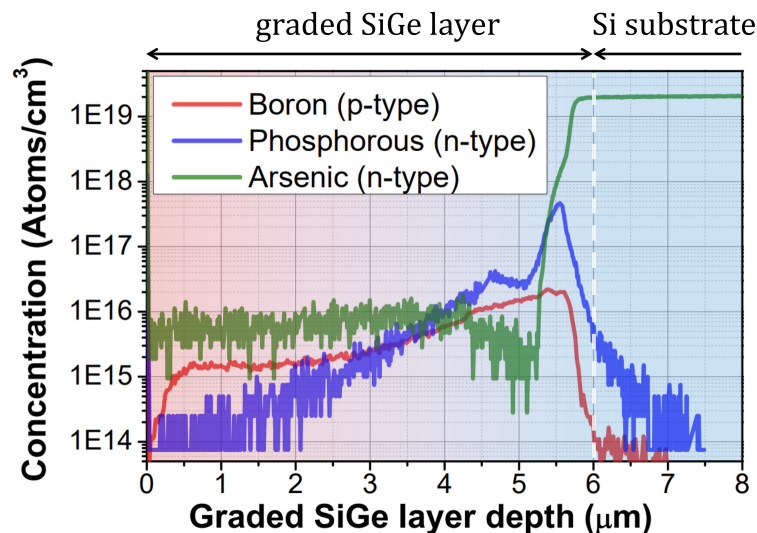


Figure 5.17.: SIMS characterization of the EOM structure. The boron (red), phosphorous (blue) and arsenic (green) concentration is shown as a function of the vertical z-axis, where zero means the top surface of the $6 \mu\text{m}$ -thickness graded-index SiGe platform.

Finally, the integrated EOM device is fabricated and the voltage-current intensity curve (I-V) is experimentally obtained. As seen in Fig. 5.18, the injected current exponentially increases for positive voltages larger than 0.6 V (the Schottky barrier), while no strong current increase is appreciated for negative applied voltages. These results are in good agreement with theoretical models and confirms the Schottky diode behavior of the EOM structure. Interestingly, the Schottky diode operation allows the characterization of the device in both current injection (positive voltages) and carrier depletion (negative voltages) configuration. Therefore, electro-optical modulation characterization is investigated below in both regimes. It must also be noted that the I-V curve does not depend on the MIR operational wavelength but on the electrical features of the EOM device.

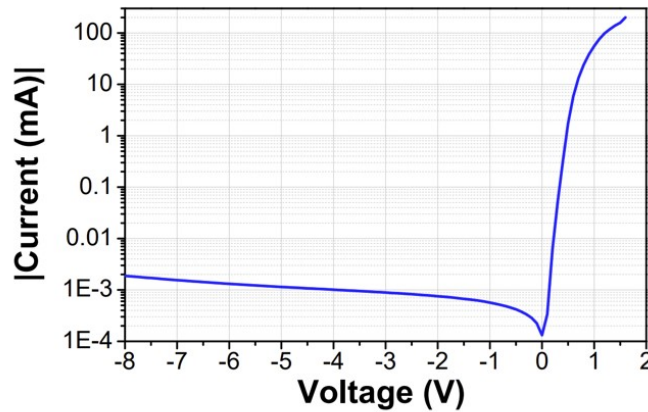


Figure 5.18.: I-V curve of the diode used in the integrated EOM: absolute current intensity value as a function of the voltage applied in the EOM structure.

5.3.4. Experimental characterization of integrated EOM in the MIR: modulation efficiency and bandwidth

To characterize the modulation efficiency of the fabricated EOM device, I have used a similar experimental setup as the one detailed in Chapter 3. In this, I have obtained the optical transmission of the EOM at different MIR wavelengths, while different bias voltages were applied to the EOM structure in a static regime. The selected wavelengths are 6.4, 8.5 and 10.7 μm . For a better comparison, the optical transmission at different voltages have been normalized with the transmission when no voltage was applied. On one hand, the EOM has been characterized in current injection regime. It means that positive voltages are applied to the EOM with a power source equipment, while the injected current required to achieve that voltage is also measured. The normalized optical transmission as a function of the measured injected current is reported in Fig. 5.19(a). The higher the injected current in the structure is, the higher the carrier density that traverses the waveguide and interacts with the optical mode is. Hence, as seen in Fig. 5.19(a), the optical transmission decreases with the current values due to FCPD effect and, as expected, the modulation is more efficient at longer MIR wavelengths. A maximum variation of 1.3 dB is achieved at 10.7 μm wavelength for a current of 170 mA, which is, to date, the largest electro-optical modulation reported on-chip at wavelengths longer than 8 μm . On the other hand, I have performed similar measurements in depletion configuration (negative voltages). The optical transmission as a function of the applied voltage is reported in Fig. 5.19(b). In this case, the higher the voltage applied to the EOM structure is, the larger the depletion region inside of the waveguide is, in which the residual free-carriers are extracted. Therefore, since the total free-carrier density that overlaps with the optical mode is globally reduced, the transmission losses due to FCPD effect are also reduced, thus increasing the optical transmission. As seen in Fig. 5.19(b), a maximal variation of 0.4 dB is obtained at -8 V applied to the EOM structure, and an improvement of the FCPD effect is also observed at longer MIR wavelengths. These

5. Integrated MIR electro-optical modulator

moderate results can be explained by a non-optimal overlap between a small carrier depletion area and the large optical mode profiles, possibly caused by both a difference in size and relative position between them.

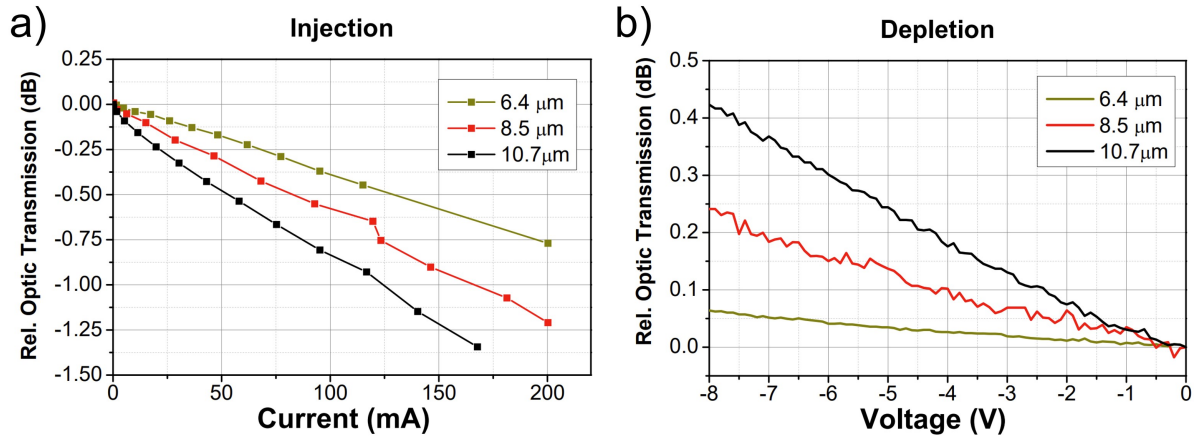


Figure 5.19.: Static EOM characterization: (a) Optical normalized transmission as a function of the injected current. (b) Optical normalized transmission as a function of the applied voltage in depletion configuration.

To investigate the modulation speed of the fabricated EOM device, I have also performed a dynamic characterization of the EOM device. To that end, some modifications were introduced in the experimental setup. First, a continuous wave laser source (Mircat, Daylight Solutions) at 8 μm wavelength was used. It must be noted that the maximal modulation speed only depends on the electrical features of the Schottky diode, and not on the working MIR wavelength. Then, the output light was collected in a high-speed MCT detector and amplified by a pre-amplifier device that has an operational range up to 600 MHz (PVI-4TE-10.6, Vigo System). The photodetected signal was then sent to an electrical signal analyzer (MS2830A, Anritsu). At the same time, a sinusoidal signal obtained from a RF generator (MG3694C, Anritsu) was injected to the EOM through electrical tip probes. A Python code script was used to control the different equipment and perform the dynamic measurements. To experimentally obtain the modulation speed, the signal generator frequency was scanned while the detected signal peak amplitude was collected.

The peak amplitude detected in the electrical spectrum analyzer as a function of the signal frequency is reported in Fig. 5.20, in injection and depletion regimes. In both cases, the background noise is also reported in black color, which has been obtained by performing similar measurements, but when the MIR laser was turned off. As observed in this figure, the relatively high noise level prevents an accurate characterization at the highest modulation frequencies by mean of the experimental setup that was used. This high noise can be attributed to electromagnetic radiation produced by the electrode paths, that was then collected with the spectrum analyzer equipment. Nevertheless, a relatively high-speed operation has been achieved in this first EOM demonstration. As observed in injection regime in Fig. 5.20(a), the modulation amplitude decreases almost linearly at frequencies higher than 50 MHz, due to the carrier life-time limit. In contrast, a different behavior is obtained in depletion regime in Fig. 5.20(b), where a

nearly flat modulation amplitude is achieved up to 225 MHz, while the high noise level prevents a correct characterization beyond this frequency. It must be also mentioned that a signal drop observed in this figure near 200 MHz can be similarly attributed to the radiation noise.

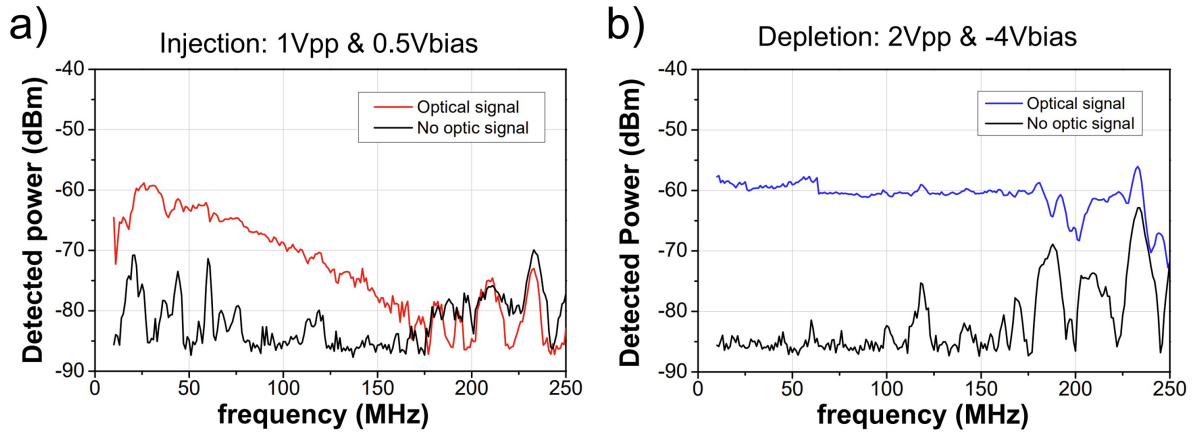


Figure 5.20.: Amplitude of the photodetected peak tone as a function of the sinusoidal signal frequency applied to the EOM: (a) in carrier injection regime with 0.5 V bias and 1 Vpp electrical signal and (b) in depletion regime with -4 V bias and 2 Vpp. The background noise obtained when the MIR laser source not activated is also reported in black color.

Finally, the photodetected signal was also collected in a sampling oscilloscope, in order to verify the correct on-chip electro-optical modulation. For instance, as seen in Fig. 5.21, clear modulation is observed at 30 MHz and 150 MHz in injection and depletion regime, respectively. These results also confirm the previous modulation speed results of the EOM device.

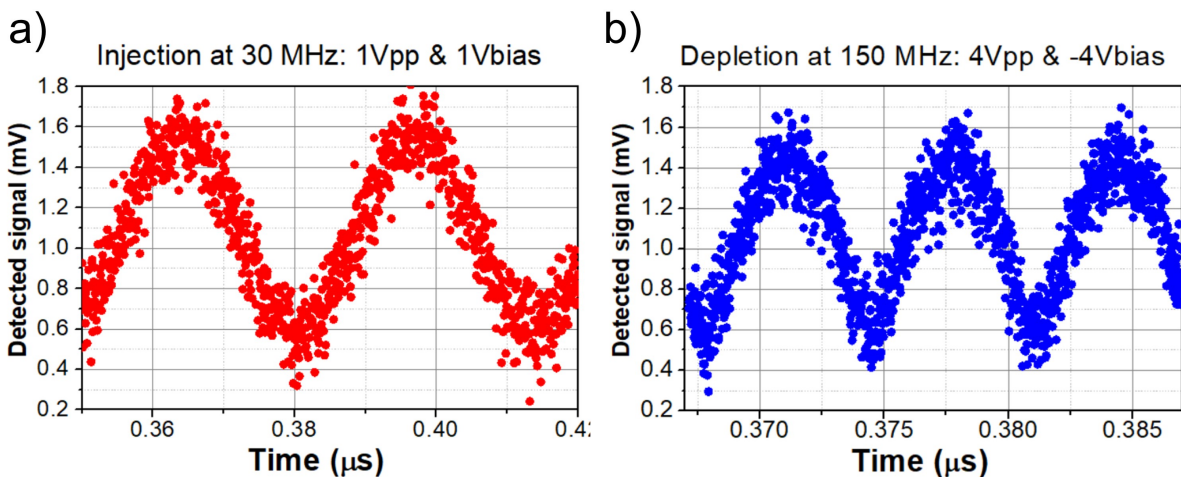


Figure 5.21.: Temporal characterization of the integrated EOM at 8 μm MIR wavelength. (a) Photodetected signal in carrier injection regime with a sinusoidal electric signal applied at 30 MHz with 1 Vpp and 1 V bias. (b) Photodetected signal in depletion configuration with a sinusoidal electric signal applied at 150 MHz with 4 Vpp and -4 V bias.

5.3.5. Numerical modeling of FCPD effect modulation in depletion regime

To investigate the limitations of the EOM device and enable its optimization in further designs, I have also developed a numerical modeling of the electro-optical modulation. For simplicity and since the experimental modulation speed in depletion configuration was considerable higher than in current injection, only carrier depletion regime has been considered in the following numerical model and in a static regime. To that end, I have simulated the carrier concentration profile of the EOM structure (Device, Lumerical) at different applied voltages, from 0 to -8 V. In these simulations, a residual n-type concentration of $4 \times 10^{15} \text{ cm}^{-3}$ has been assumed in the $6 \mu\text{m}$ -thickness graded-SiGe layer. As seen in dark blue in Fig. 5.22(a-b), thanks to the vertical Schottky diode embedded in the waveguide, the residual free-carriers are extracted from the top metal strip. Moreover, the higher the negative voltage applied is, the larger the depletion region is. Then, optical simulations at different wavelengths are performed with a mode solver (Mode, Lumerical). The optical field profiles at simulated wavelengths and the carrier density profiles at different voltages are next exported and combined with a Python script code. In this algorithm, the simulated carrier density profile is translated to an absorption coefficient map at each selected wavelength, by locally considering the carrier density at each sampling point of the simulated mesh-grid and later apply the corresponding nonlinear FCPD absorption effect. Then, each absorption coefficient map is applied to the different optical mode profiles, thus obtaining the absorption loss per unit of length at different MIR wavelengths. Finally, the total absorption at different voltages and wavelengths are normalized with respect to zero voltage, and a 2.6 mm-length device is considered.

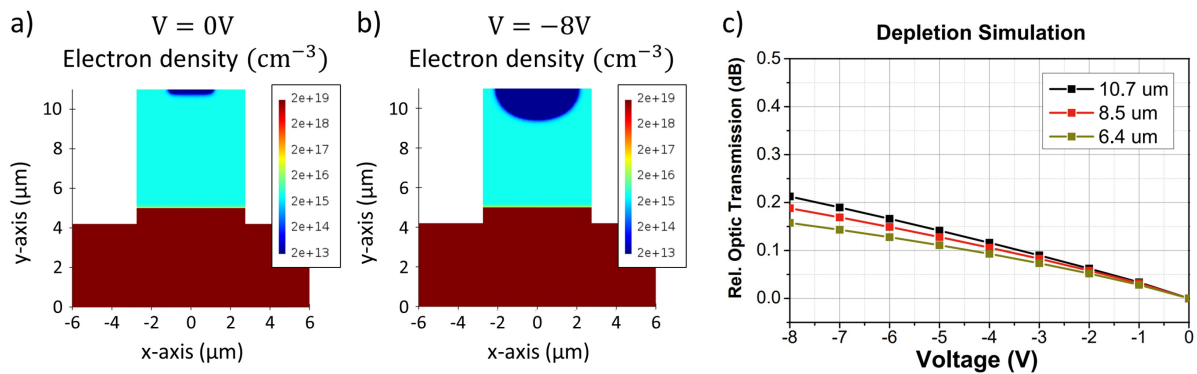


Figure 5.22.: Simulated free-carrier depletion area in the EOM structure when (a) 0 V and (b) 8 V are applied. A n-type concentration of 2×10^{19} and $4 \times 10^{15} \text{ cm}^{-3}$ have been considered for the Si substrate and the graded-SiGe layer, respectively. A 300 nm-thick gold metal strip has been assumed for the top access contact. (c) Simulated optical transmission with respect to zero voltage applied as a function of the bias voltage and at three selected MIR wavelengths.

The simulated modulation results in depletion configuration are reported in Fig. 5.22(c). As seen in this figure, they are in good agreement with the experiments performed in static configuration in Fig. 5.19(a). Firstly, the modulation efficiency increases with the operational MIR wavelength. Secondly, the higher the negative voltage applied is, the higher the depletion re-

gion is, and thus the optical transmission. Interestingly, the modeling and experiment values are particularly similar at $8.5 \mu\text{m}$ wavelength, obtaining 0.19 dB modulation in simulations and 0.24 dB in experiments. Therefore, this numerical model is sufficiently validated with the experimental results obtained, thus allowing the further design and optimization of future EOM structures, to enhance the modulating performances or to reduce the insertion losses.

5.3.6. Routes for improvement and new MIR integrated EOM designs

In the aim to progress in the development of efficient integrated EOMs in the MIR regime, some improvements are proposed for future demonstrations. For instance, by tailoring the graded-index profile, optical confinement engineering can be performed to optimize the overlap between the optical mode and the carrier depletion area. In this way, the modulation efficiency is expected to be enhanced. Moreover, the interaction between the optical mode and the metal contacts and highly doped layers can also be minimized by this kind of confinement engineering, thus reducing the insertion loss of the EOM device.

In this regard, I have explored several structures with different shapes and graded-index profiles. Among them, I propose the structure design shown in Fig. 5.23(a) for further EOM demonstrations, in which a slightly n-doped SiGe layer is grown to perform a Schottky diode, similarly to the previous demonstration. In contrast, instead of using a heavily n-doped Si substrate, a highly n-doped layer is placed between 7 and $8 \mu\text{m}$ depth in the SiGe platform. In this way, the deposition of a side contact in an etched trench next to the waveguide performs a more compact diode with a shorter distance between the top and side electrodes. Therefore, this new design is expected to reduce the electric access resistance ($2.7\text{-}3.6 \Omega$ in previous design), thus achieving a higher modulation bandwidth. Although the fabrication process is more complex due to the side metal deposition (when compared to the previous design), a maximal etching depth up to $8 \mu\text{m}$ can already be properly achieved with the fabrication process I have developed in this manuscript (Section 2.2), also allowing wide etching trenches at each side of the waveguide. It must be also noted that the use of a highly p-doped bottom layer between 7 and $8 \mu\text{m}$ depth and a slightly p-doped graded-SiGe layer could also be explored to perform a diode embedded in the optical waveguide, and profit from a higher FCPD effect for holes than for electrons. However, the optical propagation losses would be increased in this implementation. Similarly, if the dopant concentration of the slightly n-type SiGe layer of the proposed Schottky diode design is increased, the modulation efficiency would be increased, too. However, in both cases, a tradeoff between the modulation efficiency and the propagation losses is predicted.

Moreover, in order to reduce the insertion loss of the EOM device, the graded-index profile shown in Fig. 5.23(b) is also proposed. In this, a reduction of the Ge-concentration on the top 500 nm-thickness of the platform to 70% (instead of 100% of Ge in the previous design) is expected to confine the optical mode slightly deeper in the waveguide. This offset is expected to reduce the interaction between the optical mode and the metal strip deposited on top of the waveguide. Hence, the 3.5, 7 and 12 dB top metal contributions to the insertion loss ex-

5. Integrated MIR electro-optical modulator

perimentally obtained in the previous design at 6.4, 8.5 and 10.7 μm wavelengths (Table 5.1), respectively, are expected to be reduced. To increase the optical confinement towards the center of the waveguide and far from the Si substrate, a bottom constant composition layer at 40% of Ge is also conceived in this proposed profile. However, since the depleted region is expected to be produced on top of the waveguide (Fig. 5.22(b)), in the interface between the slightly doped SiGe layer and the top metal strip, a tradeoff between insertion losses and modulation efficiency is also predicted. Finally, although some rough estimations of the enhanced performance could be estimated, further experimental fabrication and characterizations must be performed.

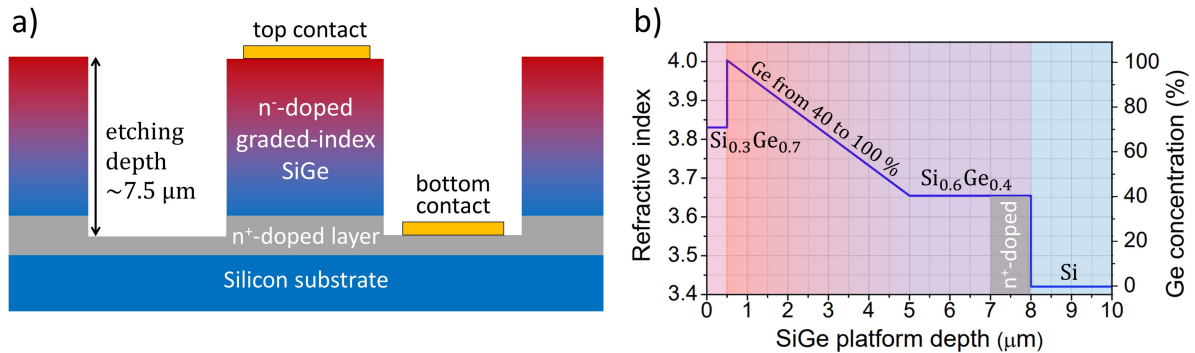


Figure 5.23.: Proposed EOM designs for future implementations. (a) Cut-view schematic of the proposed EOM structure, with top and side contacts. (b) Refractive index or Ge-concentration profile as a function of the platform depth.

5.4. Conclusion of integrated EOM operating the MIR

In this chapter I have addressed an experimental validation of the FCPD effect in a wide MIR range that was previously missing in the literature, to later implement the first demonstration of a broadband integrated EOM in the MIR. A Schottky diode embedded in the optical waveguide has been proposed to perform electro-optical modulation, and a highly doped Si substrate has been used to facilitate the EOM fabrication. Thanks to the unique broadband and confinement features graded-SiGe platforms, I have experimentally demonstrated an EOM operating from 6.4 to 10.7 μm wavelength in both carrier injection and depletion configuration. A maximal absorption modulation of 1.3 dB has been reported by carrier injection at 10.7 μm wavelength with 170 mA, while a considerable modulation bandwidth of 225 MHz has been demonstrated in carrier depletion regime. Interestingly, the modulation bandwidth value has been limited by the measurement noise of the experimental setup. In addition, thanks to the numerical model that I have reported and experimentally evaluated, a complete optimization process can be conceived. In this, the graded-index platform profile and the waveguide dimensions could be optimized, in order to enhance the required performances, such as modulation bandwidth, insertion loss or EOM efficiency (bias voltage or injected current required). Finally, I have also introduced possible routes for improvement by proposing a new EOM structure and SiGe platform profile.

5.4. Conclusion of integrated EOM operating the MIR

In conclusion, this work paves the way for the development of efficient and high-frequency integrated EOMs operating in the full fingerprint region and in both MIR atmospheric transparency windows. This development is highly interesting for high-sensitivity sensor systems via synchronous detection or free-space communications, among others.

5. Integrated MIR electro-optical modulator

6

Conclusions and perspectives

6.1. General conclusions

The work I have presented in this PhD manuscript leverages on previous works to go a step further towards the implementation of a complete on-chip MIR photonics system. While previous demonstrations were only dedicated to passive devices, the main objective of this thesis has been to develop different functionalities based on thermal-tuning, nonlinear and electro-optic effects, that were previously missing in the literature. To achieve these objectives, I have developed and optimized several fabrication processes in two cleanroom facilities and addressed the design, modeling and characterization of different integrated photonic circuits.

In terms of results, I have first achieved a remarkably low propagation loss over an unprecedentedly wide wavelength range, spanning from 5.1 to 11.2 μm , and in both TE and TM polarizations. Then, I have investigated the insights of the propagation losses, identifying the residual free-carriers and Si multiphonon absorption as the main contributions at wavelengths longer than 7.5 μm . I have also reported the experimental characterization of two MZIs devices that confirm the broadband features of this kind of platforms and the possibility to operate with multimode SiGe waveguides.

Next, I have proposed a novel integrated FTS approach that gathers the advantages of high-resolution spatial heterodyne schemes and the wide bandwidth of fine scanning interferometry FTS in time-domain. A theoretical model, simulations and experimental results have been provided, showing the possibility to break the classical SH-FTS tradeoff between bandwidth, resolution and number of required interferometric structures, by introducing a temporal tuning of the path-delay with thermo-optic effect. This first TT-SH-FTS demonstration is an interesting contribution to the development of robust and compact spectrometers that are capable to operate with high-resolution and in the full fingerprint region of the MIR.

Then, I have exploited nonlinear phenomena to provide a coherent and broadband MIR light source, and in particular by mean of SCG. Thanks to the unique and versatile GVD features of graded-SiGe waveguides, the phase-matching condition can be tailored by not only the wave-

6. Conclusions and perspectives

guide dimensions, but also by the vertical refractive index profile. In this sense, I have achieved in this work a wide spectral expansion, ranging from 3 to 13 μm wavelength, by mean of a relatively short 5.5 mm-length integrated waveguide. This result is two-fold the bandwidth achieved in previous works reported in the literature, covering the full fingerprint region.

Finally, I have reported the first experimental demonstration of an integrated EOM working in a wide MIR spectral range. As a first step, I have reported an experimental evaluation of the FCPD absorption effect in a wide MIR range (from 5.5 to 11 μm wavelength), by mean of all-optical measurements and an accurate modeling. This experimental evaluation confirms previous predictions reported in the literature, in which a more efficient FCPD effect was shown at increasing MIR wavelengths. These results enable the further appropriately design and optimization of electrically driven modulators. Therefore, as next step, I have proposed and fabricated an innovative EOM design based on a Schottky diode embedded in a graded-SiGe waveguide and a highly n-doped Si substrate. Then, I have investigated the electro-optic absorption modulation in both current injection and carrier depletion configurations, from 6.4 to 10.7 μm wavelength. Interestingly, a maximal 1.3 dB extinction ratio has been achieved in carrier injection with 170 mA, while a maximal 225 MHz modulation bandwidth could be experimentally measured in carrier depletion. These results are, to date, the most efficient and fastest on-chip EOM at wavelengths longer than 8 μm . Moreover, I have provided a numerical model to simulate the EOM performance in carrier depletion, showing a good agreement with the experiments, and thus allowing a further design optimization. A new EOM structure and graded-SiGe platform are also proposed for future demonstrations.

In conclusion, this thesis has successfully addressed the development of integrated waveguides and three critically missing building blocks operating in a wide MIR spectral range: FTS, SCG and EOM. Hence, among many other purposes, this work paves the way towards the long-term development of an integrated sensor system capable to simultaneously identify multiple molecules, thus opening exciting perspectives in a plethora of high-impact applications.

6.2. Perspectives and future works

In addition, this PhD thesis opens different routes for improvement and interesting investigations to explore. I will highlight some of them in the following. First, the graded-index SiGe platforms have been experimentally demonstrated to perform relatively low propagation losses up to 11.2 μm wavelength. However, since Ge material is transparent up to approximately 15 μm , the use of richer Ge concentrations is expected to provide lower propagation losses up to longer MIR wavelengths. Therefore, it is highly interesting to explore new and Ge-richer graded-index platforms to enhance the optical propagation performance in the LWIR range. Eventually, the integrated waveguides can also be characterized up to longer MIR wavelengths.

Second, a 2-octave SCG has been reported in this manuscript with an input peak power near 3 kW. Nevertheless, it is also interesting to explore the possibility to achieve a more efficient

wavelength conversion. It means to achieve a similar wavelength expansion, but with a lower input peak power. In this regard, the waveguide dimensions and graded-index profile can be optimized for this purpose in future works. Moreover, alternative possibilities can also be explored, such as the modulation of the waveguide width along the propagating length.

Third, regarding the EOM device, this first experimental demonstration opens multiple possibilities. For example, it will be interesting to evaluate the refractive index variations due to FCPD effect in a MZI device, in order to explore the possibility of phase-modulation. Also, a new EOM structure design and graded-index SiGe platform have been proposed to enhance the modulating and insertion loss features. Therefore, the further fabrication and characterization of this new EOM design is highly interesting to progress in the development of efficient and broadband EOMs working in the MIR regime. These devices are also expected to be later used in multiple schemes, from lock-in amplification systems to electro-optical frequency comb generation.

Finally, the integration of a QCL laser is also highly desirable to progress in the development of a fully integrated sensor system. In this sense, I highlight a work carried out by E. Tournié's group in Montpellier University, in which they demonstrated the monolithical growth of a QCL in a Si substrate [197]. Interestingly, the development of a similar work in a graded-SiGe platform would enable the on-chip integration of MIR laser sources with broadband graded-index SiGe waveguides. In the framework of a French national project (ANR-19 CE24-0002-01), I have collaborated in the initial development of different fabrication processes to pattern integrated waveguides based on III-V material hetero-structures on top of the graded-index SiGe platform. Although this project is at its initial stages, the successful development of the laser integration in the broadband SiGe platform would open exciting perspective in the development of fully on-chip MIR systems.

6. *Conclusions and perspectives*

Bibliography

- [1] J. Byrnes, *Unexploded Ordnance Detection and Mitigation*, 2009.
- [2] B. Schrader, *Infrared and Raman Spectroscopy: Methods and Applications*, 1995.
- [3] R. M. Balabin, R. Z. Safieva, and E. I. Lomakina, “Comparison of linear and nonlinear calibration models based on near infrared (nir) spectroscopy data for gasoline properties prediction,” *Chemometr. Intell. Lab.*, vol. 88, no. 2, pp. 183–188, 2007.
- [4] D. Popa and F. Udrea, “Towards integrated mid-infrared gas sensors,” *Sensors*, vol. 19, no. 9, p. 2076, 2019.
- [5] C. Moreirinha, J. Trindade, J. A. Saraiva, A. Almeida, and I. Delgado, “Mir spectroscopy as alternative method for further confirmation of foodborne pathogens salmonella spp. and listeria monocytogenes,” *J. Food Sci. Technol.*, vol. 55, no. 10, pp. 3971–3978, 2018.
- [6] I. E. Gordon, L. S. Rothman, C. Hill, R. V. Kochanov, Y. Tan, P. F. Bernath, M. Birk, V. Boudon, A. Campargue, K. V. Chance, B. J. Drouin, J.-M. Flaud, R. R. Gamache, J. T. Hodges, D. Jacquemart, V. I. Perevalov, A. Perrin, K. P. Shine, M.-A. H. Smith, J. Tennyson, G. C. Toon, H. Tran, V. G. Tyuterev, A. Barbe, A. G. Császár, V. M. Devi, T. Furtenbacher, J. J. Harrison, J.-M. Hartmann, A. Jolly, T. J. Johnson, T. Karman, I. Kleiner, A. A. Kyuberis, J. Loos, O. M. Lyulin, S. T. Massie, S. N. Mikhailenko, N. Moazzen-Ahmadi, H. S. P. Müller, O. V. Naumenko, A. V. Nikitin, O. L. Polyansky, M. Rey, M. Rotger, S. W. Sharpe, K. Sung, E. Starikova, S. A. Tashkun, J. V. Auwera, G. Wagner, J. Wilzewski, P. Wcislo, S. Yu, and E. J. Zak, “The HITRAN2016 molecular spectroscopic database,” *J. Quant. Spectros. Ra.*, vol. 203, pp. 3–69, 2017. [Online]. Available: <https://www.sciencedirect.com/science/article/pii/S0022407317301073>
- [7] Tematys, “Mid-ir photodetectors and systems: applicatinos and markets,” Paris, France, Tech. Rep. 4858085, Dec 2019.
- [8] H. Lin, Z. Luo, T. Gu, L. C. Kimerling, K. Wada, A. Agarwal, and J. Hu, “Mid-infrared integrated photonics on silicon: a perspective,” *Nanophotonics*, vol. 7, no. 2, pp. 393–420, 2018. [Online]. Available: <https://doi.org/10.1515/nanoph-2017-0085>
- [9] A. T. Young, “Rayleigh scattering,” *Appl. Opt.*, vol. 20, no. 4, pp. 533–535, Feb 1981. [Online]. Available: <http://ao.osa.org/abstract.cfm?URI=ao-20-4-533>
- [10] R. Martini, R. Paiella, C. Gmachl, F. Capasso, E. Whittaker, H. Liu, H. Hwang, D. Sivco, J. Baillargeon, and A. Cho, “High-speed digital data transmission using mid-infrared quantum cascade lasers,” *Electron. Lett.*, vol. 37, pp. 1290–1292, 11 2001.

Bibliography

- [11] P. Corrigan, R. Martini, E. A. Whittaker, and C. Bethea, “Quantum cascade lasers and the kruse model in free space optical communication,” *Opt. Express*, vol. 17, no. 6, pp. 4355–4359, Mar 2009. [Online]. Available: <http://www.opticsexpress.org/abstract.cfm?URI=oe-17-6-4355>
- [12] X. Pang, O. Ozolins, R. Schatz, J. Storck, A. Udalcovs, J. R. Navarro, A. Kakkar, G. Maisons, M. Carras, G. Jacobsen, S. Popov, and S. Lourdudoss, “Gigabit free-space multi-level signal transmission with a mid-infrared quantum cascade laser operating at room temperature,” *Opt. Lett.*, vol. 42, no. 18, pp. 3646–3649, Sep 2017. [Online]. Available: <http://ol.osa.org/abstract.cfm?URI=ol-42-18-3646>
- [13] Y. Su, W. Wang, X. Hu, H. Hu, X. Huang, Y. Wang, J. Si, X. Xie, B. Han, H. Feng, Q. Hao, G. Zhu, T. Duan, and W. Zhao, “10 gbps dpsk transmission over free-space link in the mid-infrared,” *Opt. Express*, vol. 26, no. 26, pp. 34 515–34 528, Dec 2018. [Online]. Available: <http://www.opticsexpress.org/abstract.cfm?URI=oe-26-26-34515>
- [14] L. C. Kelly, “Low-emissivity topcoats for the reduction of thermal infrared emissions from military platforms,” *COATINGSTECH*, vol. 17, no. 4, pp. 18–31, 2020.
- [15] C. Kieleck, A. Berrou, C. Kneis, B. Donelan, and M. Eichhorn, “2 μm and mid-IR fiber-laser-based sources for OCM,” in *Technologies for Optical Countermeasures XI; and High-Power Lasers 2014: Technology and Systems*, D. H. Titterton, M. A. Richardson, R. J. Grasso, W. L. Bohn, and H. Ackermann, Eds., vol. 9251, International Society for Optics and Photonics. SPIE, 2014, pp. 49–60. [Online]. Available: <https://doi.org/10.1117/12.2070355>
- [16] E.-C. Koch, “Pyrotechnic countermeasures: Ii. advanced aerial infrared countermeasures,” *Propel. Explos. Pyrot.*, vol. 31, no. 1, pp. 3–19, 2006.
- [17] G. Rybicki and A. Lightman, “Radiative processes in astrophysics,” 1979.
- [18] J. Faist, F. Capasso, D. Sivco, C. Sirtori, A. Hutchinson, and A. Cho, “Quantum cascade laser,” *Science*, vol. 264, pp. 553–556, 04 1994.
- [19] J. Meyer, J. Meyer, I. Vurgaftman, R. Yang, and R. Ram-Mohan, “Type-ii and type-i interband cascade lasers,” *Electron. Lett.*, vol. 32, pp. 45 – 46, 02 1996.
- [20] M. Kim, C. Canedy, W. Bewley, C. S. Kim, J. Lindle, J. Abell, I. Vurgaftman, and R. Meyer, “Interband cascade laser emitting at $\lambda=3.75 \mu\text{m}$ in continuous wave above room temperature,” *Appl. Phys. Lett.*, vol. 92, pp. 191 110 – 191 110, 2008.
- [21] R. Pecharromás-Gallego, “Quantum cascade lasers: Review, applications and prospective development,” *Laser Eng.*, vol. 24, pp. 277–314, 01 2013.
- [22] R. Won, “Shining the mid-infrared,” *Nature*, vol. 5, pp. 457–458, 2011.

- [23] A. Hugi, G. Villares, S. Blaser, H. Liu, and J. Faist, “Mid-infrared frequency comb based on a quantum cascade laser,” *Nature*, vol. 492, pp. 229–33, 12 2012.
- [24] S. Jackson, “Towards high-power mid-infrared emission from a fibre laser,” *Nat. Photonics*, vol. 6, pp. 423–431, 07 2012.
- [25] A. Elbaz, D. Buca, N. von den Driesch, K. Pantzas, G. Patriarche, N. Zerounian, E. Herth, X. Checoury, S. Sauvage, I. Sagnes, A. Foti, R. Ossikovski, J.-M. Hartmann, F. Boeuf, Z. Ikonc, P. Boucaud, D. Grützmacher, and M. El Kurdi, “Ultra-low-threshold continuous-wave and pulsed lasing in tensile-strained gesn alloys,” *Nat. Photonics*, vol. 14, 06 2020.
- [26] D. Romanini, A. Kachanov, N. Sadeghi, and F. Stoeckel, “Cw cavity ring down spectroscopy,” *Chem. Phys. Lett.*, vol. 264, no. 3-4, pp. 316–322, 1997.
- [27] M. D. Wheeler, S. M. Newman, A. J. Orr-Ewing, and M. N. Ashfold, “Cavity ring-down spectroscopy,” *J. Chem. Soc. Faraday T.*, vol. 94, no. 3, pp. 337–351, 1998.
- [28] G. Berden, R. Peeters, and G. Meijer, “Cavity ring-down spectroscopy: Experimental schemes and applications,” *Int. Rev. Phys. Chem.*, vol. 19, no. 4, pp. 565–607, 2000.
- [29] G. Berden and R. Engeln, *Cavity ring-down spectroscopy: techniques and applications*. John Wiley & Sons, 2009.
- [30] J. F. McClelland, “Photoacoustic spectroscopy,” *Anal. Chem.*, vol. 55, no. 1, pp. 89–105, 1983.
- [31] C. Du, R. Linker, and A. Shaviv, “Identification of agricultural mediterranean soils using mid-infrared photoacoustic spectroscopy,” *Geoderma*, vol. 143, no. 1-2, pp. 85–90, 2008.
- [32] F. J. Harren and S. M. Cristescu, “Photoacoustic spectroscopy in trace gas monitoring,” *Encyclopedia of Analytical Chemistry*, pp. 1–29, 2006.
- [33] J.-G. Coutard, A. Glière, J.-M. Fedeli, O. Lartigue, J. Skubich, G. Aoust, A. Teulle, T. Strahl, S. Nicoletti, M. Carras, and L. Duraffourg, “Photoacoustic cell on silicon for mid-infrared qcl-based spectroscopic analysis,” in *MOEMS and Miniaturized Systems XVIII*, vol. 10931. International Society for Optics and Photonics, 2019, p. 109310V.
- [34] H. Schiff, G. Mackay, and J. Bechara, “The use of tunable diode laser absorption spectroscopy for atmospheric measurements,” *Res. Chem. Intermediat.*, vol. 20, no. 3, pp. 525–556, 1994.
- [35] M. Lackner, “Tunable diode laser absorption spectroscopy (tdlas) in the process industries—a review,” *Rev. Chem. Eng*, vol. 23, no. 2, pp. 65–147, 2007.

Bibliography

- [36] C. Zheng, W. Ye, N. P. Sanchez, C. Li, L. Dong, Y. Wang, R. J. Griffin, and F. K. Tittel, “Development and field deployment of a mid-infrared methane sensor without pressure control using interband cascade laser absorption spectroscopy,” *Sens. Actuat., B*, vol. 244, pp. 365–372, 2017.
- [37] R. J. Tancin, Z. Chang, M. Gu, V. Radhakrishna, R. P. Lucht, and C. S. Goldenstein, “Ultrafast laser-absorption spectroscopy for single-shot, mid-infrared measurements of temperature, co, and ch 4 in flames,” *Opt. Lett.*, vol. 45, no. 2, pp. 583–586, 2020.
- [38] Z. Du, S. Zhang, J. Li, N. Gao, and K. Tong, “Mid-infrared tunable laser-based broadband fingerprint absorption spectroscopy for trace gas sensing: A review,” *Appl. Sci.*, vol. 9, no. 2, 2019. [Online]. Available: <https://www.mdpi.com/2076-3417/9/2/338>
- [39] A. Glière, J. Rouxel, M. Brun, B. Parvitte, V. Zéninari, and S. Nicoletti, “Challenges in the design and fabrication of a lab-on-a-chip photoacoustic gas sensor,” *Sensors*, vol. 14, no. 1, pp. 957–974, 2014.
- [40] Z. Yang, T. Albrow-Owen, W. Cai, and T. Hasan, “Miniaturization of optical spectrometers,” *Science*, vol. 371, no. 6528, 2021.
- [41] Y. Li, D. L. García-González, X. Yu, and F. R. van de Voort, “Determination of free fatty acids in edible oils with the use of a variable filter array ir spectrometer,” *J. Am. Oil Chem. Soc.*, vol. 85, no. 7, pp. 599–604, 2008.
- [42] A. Wang and Y. Dan, “Mid-infrared plasmonic multispectral filters,” *Sci. Rep.*, vol. 8, no. 1, pp. 1–7, 2018.
- [43] D. B. Nash, “Mid-infrared reflectance spectra (2.3–22 μm) of sulfur, gold, kbr, mgo, and halon,” *Appl. Opt.*, vol. 25, no. 14, pp. 2427–2433, 1986.
- [44] J. Bao and M. G. Bawendi, “A colloidal quantum dot spectrometer,” *Nature*, vol. 523, no. 7558, pp. 67–70, 2015.
- [45] E. Huang, Q. Ma, and Z. Liu, “Etalon array reconstructive spectrometry,” *Sci. Rep.*, vol. 7, p. 40693, 01 2017.
- [46] C. H. Smith, C. M. Wright, D. K. Aitken, P. F. Roche, and J. H. Hough, “Studies in mid-infrared spectropolarimetry-ii. an atlas of spectra,” *Mon. Not. R. Astron. Soc.*, vol. 312, no. 2, pp. 327–361, 2000.
- [47] L. Nugent-Glandorf, T. Neely, F. Adler, A. J. Fleisher, K. C. Cossel, B. Bjork, T. Dinneen, J. Ye, and S. A. Diddams, “Mid-infrared virtually imaged phased array spectrometer for rapid and broadband trace gas detection,” *Opt. Lett.*, vol. 37, no. 15, pp. 3285–3287, 2012.

- [48] A. Malik, M. Muneeb, S. Pathak, Y. Shimura, J. Van Campenhout, R. Loo, and G. Roelkens, "Germanium-on-silicon mid-infrared arrayed waveguide grating multiplexers," *IEEE Photon. Technol. Lett.*, vol. 25, no. 18, pp. 1805–1808, 2013.
- [49] A. Malik, A. Spott, Y. Wang, E. J. Stanton, J. Peters, and J. E. Bowers, "High resolution, high channel count mid-infrared arrayed waveguide gratings in silicon," *Opt. Lett.*, vol. 45, no. 16, pp. 4551–4554, 2020.
- [50] E. J. Stanton, N. Volet, and J. E. Bowers, "Silicon arrayed waveguide gratings at 2.0- μm wavelength characterized with an on-chip resonator," *Opt. Lett.*, vol. 43, no. 5, pp. 1135–1138, 2018.
- [51] M. P. Fuller and P. R. Griffiths, "Diffuse reflectance measurements by infrared fourier transform spectrometry," *Anal. Chem.*, vol. 50, no. 13, pp. 1906–1910, 1978.
- [52] E. N. Lewis, P. J. Treado, R. C. Reeder, G. M. Story, A. E. Dowrey, C. Marcott, and I. W. Levin, "Fourier transform spectroscopic imaging using an infrared focal-plane array detector," *Anal. Chem.*, vol. 67, no. 19, pp. 3377–3381, 1995.
- [53] M. J. Persky, "A review of spaceborne infrared fourier transform spectrometers for remote sensing," *Rev. Sci. Instrum.*, vol. 66, no. 10, pp. 4763–4797, 1995.
- [54] J. L. Hall, "Nobel lecture: Defining and measuring optical frequencies," *Rev. Mod. Phys.*, vol. 78, no. 4, p. 1279, 2006.
- [55] P. Del'Haye, A. Schliesser, O. Arcizet, T. Wilken, R. Holzwarth, and T. J. Kippenberg, "Optical frequency comb generation from a monolithic microresonator," *Nature*, vol. 450, no. 7173, pp. 1214–1217, 2007.
- [56] S. Ozharar, F. Quinlan, I. Ozdur, S. Gee, and P. Delfyett, "Ultraflat optical comb generation by phase-only modulation of continuous-wave light," *IEEE Photon. Technol. Lett.*, vol. 20, no. 1, pp. 36–38, 2007.
- [57] C. Wang, M. Zhang, M. Yu, R. Zhu, H. Hu, and M. Loncar, "Monolithic lithium niobate photonic circuits for kerr frequency comb generation and modulation," *Nat. Commun.*, vol. 10, no. 1, pp. 1–6, 2019.
- [58] A. Schliesser, N. Picqué, and T. W. Hänsch, "Mid-infrared frequency combs," *Nat. Photonics*, vol. 6, no. 7, pp. 440–449, 2012.
- [59] A. Hugi, G. Villares, S. Blaser, H. Liu, and J. Faist, "Mid-infrared frequency comb based on a quantum cascade laser," *Nature*, vol. 492, no. 7428, pp. 229–233, 2012.
- [60] S. Schiller, "Spectrometry with frequency combs," *Opt. Lett.*, vol. 27, no. 9, pp. 766–768, 2002.

Bibliography

- [61] F. Keilmann, C. Gohle, and R. Holzwarth, “Time-domain mid-infrared frequency-comb spectrometer,” *Opt. Lett.*, vol. 29, no. 13, pp. 1542–1544, 2004.
- [62] M. J. Thorpe, D. Balslev-Clausen, M. S. Kirchner, and J. Ye, “Cavity-enhanced optical frequency comb spectroscopy: application to human breath analysis,” *Opt. Express*, vol. 16, no. 4, pp. 2387–2397, 2008.
- [63] N. R. Newbury, I. Coddington, and W. Swann, “Sensitivity of coherent dual-comb spectroscopy,” *Opt. Express*, vol. 18, no. 8, pp. 7929–7945, 2010.
- [64] I. Coddington, N. Newbury, and W. Swann, “Dual-comb spectroscopy,” *Optica*, vol. 3, no. 4, pp. 414–426, 2016.
- [65] M. Yu, Y. Okawachi, A. G. Griffith, N. Picqué, M. Lipson, and A. L. Gaeta, “Silicon-chip-based mid-infrared dual-comb spectroscopy,” *Nat. Commun.*, vol. 9, no. 1, pp. 1–6, 2018.
- [66] G. Ycas, F. R. Giorgetta, E. Baumann, I. Coddington, D. Herman, S. A. Diddams, and N. R. Newbury, “High-coherence mid-infrared dual-comb spectroscopy spanning 2.6 to 5.2 μm ,” *Nat. Photonics*, vol. 12, no. 4, pp. 202–208, 2018.
- [67] M. Yan, P.-L. Luo, K. Iwakuni, G. Millot, T. W. Hänsch, and N. Picqué, “Mid-infrared dual-comb spectroscopy with electro-optic modulators,” *Light Sci. Appl.*, vol. 6, no. 10, pp. e17076–e17076, 2017.
- [68] Y. Qi and Y. Li, “Integrated lithium niobate photonics,” *Nanophotonics*, vol. 9, no. 6, pp. 1287–1320, 2020. [Online]. Available: <https://doi.org/10.1515/nanoph-2020-0013>
- [69] S. Jung, D. Palaferri, K. Zhang, F. Xie, Y. Okuno, C. Pinzone, K. Lascola, and M. A. Belkin, “Homogeneous photonic integration of mid-infrared quantum cascade lasers with low-loss passive waveguides on an inp platform,” *Optica*, vol. 6, no. 8, pp. 1023–1030, 2019.
- [70] M. Sieger, F. Balluff, X. Wang, S.-S. Kim, L. Leidner, G. Gauglitz, and B. Mizaikoff, “On-chip integrated mid-infrared gaas/algaas mach-zehnder interferometer,” *Anal. Chem.*, vol. 85, 11 2012.
- [71] H. Lin, L. Li, Y. Zou, S. Danto, J. D. Musgraves, K. Richardson, S. Kozacik, M. Murakowski, D. Prather, P. Lin, V. Singh, A. Agarwal, L. Kimerling, and J. Hu, “Demonstration of high-q mid-infrared chalcogenide glass-on-silicon resonators,” *Opt. Lett.*, vol. 38, pp. 1470–2, 05 2013.
- [72] Y. Yu, X. Gai, P. Ma, K. Vu, Z. Yang, R. Wang, D. Choi, S. Madden, and B. Luther-Davies, “Experimental demonstration of linearly polarized 2-10 $\hat{\text{C}}\text{m}$ supercontinuum generation in a chalcogenide rib waveguide,” *Opt. Lett.*, vol. 41, p. 958, 03 2016.

- [73] G. Mashanovich, M. Milosevic, M. Nedeljkovic, N. Owens, B. Xiong, E. J. Teo, and Y. Hu, “Low loss silicon waveguides for the mid-infrared,” *Opt. Express*, vol. 19, pp. 7112–9, 04 2011.
- [74] M. Nedeljkovic, A. Khokhar, A. Delage, P. Cheben, and G. Mashanovich, “Mid-infrared silicon-on-insulator fourier-transform spectrometer chip,” *IEEE Photon. Technol. Lett.*, vol. 28, pp. 1–1, 11 2015.
- [75] S. Miller, M. Yu, X. Ji, A. Griffith, J. Cardenas, A. Gaeta, and M. Lipson, “Low-loss silicon platform for broadband mid-infrared photonics,” *Optica*, vol. 4, 03 2017.
- [76] S. Khan, J. Chiles, J. Ma, and S. Fathpour, “Silicon-on-nitride optical waveguides for mid- and near-infrared integrated photonics,” *Appl. Phys. Lett.*, vol. 102, 03 2013.
- [77] G. Reed, G. Mashanovich, F. Gardes, D. Thomson, Y. Hu, J. Soler Penades, M. Nedeljkovic, A. Khokhar, P. Thomas, C. Littlejohns, A. Ahmed, S. Reynolds, R. Topley, C. Mitchell, S. Stankovic, P. Wilson, K. Li, T. Ben Masaud, A. Tarazona, and H. Chong, “Silicon photonic devices for the near- and the mid-infrared wavelength ranges,” 05 2014, pp. 1–3.
- [78] J. S. Penadés, C. Alonso-Ramos, A. Z. Khokhar, M. Nedeljkovic, L. A. Boodhoo, A. O.-M. nux, I. Molina-Fernández, P. Cheben, and G. Z. Mashanovich, “Suspended soi waveguide with sub-wavelength grating cladding for mid-infrared,” *Opt. Lett.*, vol. 39, no. 19, pp. 5661–5664, Oct 2014. [Online]. Available: <http://ol.osa.org/abstract.cfm?URI=ol-39-19-5661>
- [79] R. Soref, “Mid-infrared photonics in silicon and germanium,” *Nat. Photonics*, vol. 4, no. 8, pp. 495–497, Aug. 2010. [Online]. Available: <https://doi.org/10.1038/nphoton.2010.171>
- [80] L. Zhang, A. Agarwal, L. Kimerling, and J. Michel, “Nonlinear group iv photonics based on silicon and germanium: From near-infrared to mid-infrared,” *Nanophotonics*, vol. 3, 08 2014.
- [81] G. Mashanovich, M. Nedeljkovic, J. Soler Penades, Z. Qu, W. Cao, A. Osman, Y. Wu, C. Stirling, Y. Qi, Y. Cheng, L. Reid, C. Littlejohns, J. Kang, Z. Zhao, M. Takenaka, T. Li, Z. Zhou, F. Gardes, D. Thomson, and G. Reed, “Group iv mid-infrared photonics [invited],” *Opt. Mater. Express*, vol. 8, p. 2276, 08 2018.
- [82] J.-M. Fedeli and S. Nicoletti, “Mid-infrared (mid-ir) silicon-based photonics,” *Proceedings of the IEEE*, vol. PP, pp. 1–11, 07 2018.
- [83] D. Marris-Morini, V. Vakarín, J. M. Ramírez, Q. Liu, A. Ballabio, J. Frigerio, M. Montesinos Ballester, C. Alonso-Ramos, L. R. Xavier, S. Serna, D. Benedikovic,

Bibliography

- D. Chrastina, L. Vivien, and G. Isella, “Germanium-based integrated photonics from near- to mid-infrared applications,” *Nanophotonics*, vol. 7, 09 2018.
- [84] Y.-C. Chang, V. Paeder, L. Hvozدارa, J.-M. Hartmann, and H. P. Herzig, “Low-loss germanium strip waveguides on silicon for the mid-infrared,” *Opt. Lett.*, vol. 37, no. 14, pp. 2883–2885, Jul 2012. [Online]. Available: <http://ol.osa.org/abstract.cfm?URI=ol-37-14-2883>
- [85] A. Malik, M. Muneeb, Y. Shimura, J. Van Campenhout, R. Loo, and G. Roelkens, “Germanium-on-silicon mid-infrared waveguides and mach-zehnder interferometers,” in *2013 IEEE Photonics Conference*. IEEE, 2013, pp. 104–105.
- [86] A. Malik, M. Muneeb, Y. Shimura, J. Van Campenhout, R. Loo, and G. Roelkens, “Germanium-on-silicon planar concave grating wavelength (de) multiplexers in the mid-infrared,” *Appl. Phys. Lett.*, vol. 103, no. 16, p. 161119, 2013.
- [87] A. Malik, M. Muneeb, S. Pathak, Y. Shimura, J. Van Campenhout, R. Loo, and G. Roelkens, “Germanium-on-silicon mid-infrared arrayed waveguide grating multiplexers,” *IEEE Photon. Technol. Lett.*, vol. 25, no. 18, pp. 1805–1808, 2013.
- [88] M. Nedeljkovic, J. S. Penadés, C. J. Mitchell, A. Z. Khokhar, S. Stanković, T. D. Bucio, C. G. Littlejohns, F. Y. Gardes, and G. Z. Mashanovich, “Surface-grating-coupled low-loss ge-on-si rib waveguides and multimode interferometers,” *IEEE Photon. Technol. Lett.*, vol. 27, no. 10, pp. 1040–1043, 2015.
- [89] M. Nedeljkovic, J. S. Penades, V. Mittal, G. S. Murugan, A. Z. Khokhar, C. Littlejohns, L. G. Carpenter, C. B. Gawith, J. S. Wilkinson, and G. Z. Mashanovich, “Germanium-on-silicon waveguides operating at mid-infrared wavelengths up to 8.5 μm ,” *Opt. Express*, vol. 25, no. 22, pp. 27 431–27 441, 2017.
- [90] K. Gallacher, R. Millar, U. Griškevičiūtė, L. Baldassarre, M. Sorel, M. Ortolani, and D. Paul, “Low loss ge-on-si waveguides operating in the 8–14 μm atmospheric transmission window,” *Opt. Express*, vol. 26, no. 20, pp. 25 667–25 675, 2018.
- [91] U. Griskeviciute, R. W. Millar, K. Gallacher, J. Valente, and D. J. Paul, “Ge-on-si waveguides for sensing in the molecular fingerprint regime,” *Opt. Express*, vol. 28, no. 4, pp. 5749–5757, 2020.
- [92] D. A. Kozak, N. F. Tyndall, M. W. Pruessner, W. S. Rabinovich, and T. H. Stievater, “Germanium-on-silicon waveguides for long-wave integrated photonics: ring resonance and thermo-optics,” *Opt. Express*, vol. 29, no. 10, pp. 15 443–15 451, 2021.
- [93] L. Carletti, P. Ma, Y. Yu, B. Luther-Davies, D. Hudson, C. Monat, R. Orobchouk, S. Madden, D. Moss, M. Brun, S. Ortiz, P. Labeye, S. Nicoletti, and C. Grillet, “Nonlin-

- ear optical response of low loss silicon germanium waveguides in the mid-infrared,” *Opt. Express*, vol. 23, no. 7, pp. 8261–8271, 2015.
- [94] M. Brun, P. Labeye, G. Grand, J.-M. Hartmann, F. Boulila, M. Carras, and S. Nicoletti, “Low loss sige graded index waveguides for mid-ir applications,” *Opt. Express*, vol. 22, no. 1, pp. 508–518, 2014.
- [95] J. M. Ramírez, Q. Liu, V. Vakarin, J. Frigerio, A. Ballabio, X. Le Roux, D. Bouville, L. Vivien, G. Isella, and D. Marris-Morini, “Graded sige waveguides with broadband low-loss propagation in the mid infrared,” *Opt. Express*, vol. 26, no. 2, pp. 870–877, 2018.
- [96] A. Malik, S. Dwivedi, L. Van Landschoot, M. Muneeb, Y. Shimura, G. Lepage, J. Van Campenhout, W. Vanherle, T. Van Opstal, R. Loo, and G. Roelkens, “Ge-on-si and ge-on-soi thermo-optic phase shifters for the mid-infrared,” *Opt. Express*, vol. 22, no. 23, pp. 28 479–28 488, 2014.
- [97] S. Radosavljevic, N. T. Beneitez, A. Katumba, M. Muneeb, M. Vanslembrouck, B. Kuyken, and G. Roelkens, “Mid-infrared vernier racetrack resonator tunable filter implemented on a germanium on soi waveguide platform,” *Opt. Mater. Express*, vol. 8, no. 4, pp. 824–835, 2018.
- [98] J. Kang, M. Takenaka, and S. Takagi, “Novel ge waveguide platform on ge-on-insulator wafer for mid-infrared photonic integrated circuits,” *Opt. Express*, vol. 24, no. 11, pp. 11 855–11 864, 2016.
- [99] W. Li, P. Anantha, S. Bao, K. H. Lee, X. Guo, T. Hu, L. Zhang, H. Wang, R. Soref, and C. S. Tan, “Germanium-on-silicon nitride waveguides for mid-infrared integrated photonics,” *Appl. Phys. Lett.*, vol. 109, no. 24, p. 241101, 2016.
- [100] T.-H. Xiao, Z. Zhao, W. Zhou, M. Takenaka, H. K. Tsang, Z. Cheng, and K. Goda, “Mid-infrared germanium photonic crystal cavity,” *Opt. Lett.*, vol. 42, no. 15, pp. 2882–2885, 2017.
- [101] T.-H. Xiao, Z. Zhao, W. Zhou, M. Takenaka, H. K. Tsang, Z. Cheng, and K. and Goda, “High-q germanium optical nanocavity,” *Photonics Res.*, vol. 6, no. 9, pp. 925–928, 2018.
- [102] T.-H. Xiao, Z. Zhao, W. Zhou, C.-Y. Chang, S. Y. Set, M. Takenaka, H. K. Tsang, Z. Cheng, and K. Goda, “Mid-infrared high-q germanium microring resonator,” *Opt. Lett.*, vol. 43, no. 12, pp. 2885–2888, 2018.
- [103] P. Barritault, M. Brun, P. Labeye, J.-M. Hartmann, F. Boulila, M. Carras, and S. Nicoletti, “Design, fabrication and characterization of an awg at 4.5 μm ,” *Opt. Express*, vol. 23, no. 20, pp. 26 168–26 181, 2015.

Bibliography

- [104] J. M. Ramírez, V. Vakarín, C. Gilles, J. Frigerio, A. Ballabio, P. Chaisakul, X. Le Roux, C. Alonso-Ramos, G. Maisons, L. Vivien *et al.*, “Low-loss ge-rich $\text{Si}_{0.2}\text{Ge}_{0.8}$ waveguides for mid-infrared photonics,” *Opt. Lett.*, vol. 42, no. 1, pp. 105–108, 2017.
- [105] V. Vakarín, J. M. Ramírez, J. Frigerio, A. Ballabio, X. Le Roux, Q. Liu, D. Bouville, L. Vivien, G. Isella, and D. Marris-Morini, “Ultra-wideband ge-rich silicon germanium integrated mach–zehnder interferometer for mid-infrared spectroscopy,” *Opt. Lett.*, vol. 42, no. 17, pp. 3482–3485, 2017.
- [106] Q. Liu, J. M. Ramírez, V. Vakarín, J. Frigerio, A. Ballabio, L. Vivien, C. Alonso-Ramos, G. Isella, and D. Marris-Morini, “Mid-ir integrated cavity based on ge-rich graded sign waveguides with lateral bragg grating,” in *Mid-Infrared Coherent Sources*. Optical Society of America, 2018, pp. MM3C–4.
- [107] J. M. Ramírez, Q. Liu, V. Vakarín, X. Le Roux, J. Frigerio, A. Ballabio, C. Alonso-Ramos, E. T. Simola, L. Vivien, G. Isella, and D. Marris-Morini, “Broadband integrated racetrack ring resonators for long-wave infrared photonics,” *Opt. Lett.*, vol. 44, no. 2, pp. 407–410, 2019.
- [108] Q. Liu, J. M. Ramírez, V. Vakarín, X. Le Roux, C. Alonso-Ramos, J. Frigerio, A. Ballabio, E. T. Simola, D. Bouville, L. Vivien, G. Isella, and D. Marris-Morini, “Integrated broadband dual-polarization ge-rich sign mid-infrared fourier-transform spectrometer,” *Opt. Lett.*, vol. 43, no. 20, pp. 5021–5024, 2018.
- [109] V. Vakarín, W. N. Ye, J. M. Ramírez, Q. Liu, J. Frigerio, A. Ballabio, G. Isella, L. Vivien, C. Alonso-Ramos, P. Cheben, and D. Marris-Morini, “Ultra-wideband ge-rich silicon germanium mid-infrared polarization rotator with mode hybridization flattening,” *Opt. Express*, vol. 27, no. 7, pp. 9838–9847, 2019.
- [110] J. M. Ramírez, V. Vakarín, J. Frigerio, P. Chaisakul, D. Chrastina, X. Le Roux, A. Ballabio, L. Vivien, G. Isella, and D. Marris-Morini, “Ge-rich graded-index $\text{Si}_{1-x}\text{Ge}_x$ waveguides with broadband tight mode confinement and flat anomalous dispersion for nonlinear mid-infrared photonics,” *Opt. Express*, vol. 25, no. 6, pp. 6561–6567, 2017.
- [111] V. Vakarín, J. M. Ramírez, J. Frigerio, Q. Liu, A. Ballabio, X. Le Roux, C. Alonso-Ramos, G. Isella, P. Cheben, W. N. Ye, L. Vivien, and D. Marris-Morini, “Wideband ge-rich sign polarization-insensitive waveguides for mid-infrared free-space communications,” *Appl. Sci.*, vol. 8, no. 7, p. 1154, 2018.
- [112] Thorlabs. (2021) Silicon windows: total transmission of 5 nm thick, uncoated Si windows. [Online]. Available: https://www.thorlabs.com/newgrouppage9.cfm?objectgroup_id=3979

- [113] P. Douglas J. (2021) Misfit dislocations. [Online]. Available: <http://userweb.eng.gla.ac.uk/douglas.paul/SiGe/misfit.html>
- [114] G. Isella, D. Chrastina, B. Rössner, T. Hackbarth, H.-J. Herzog, U. König, and H. Von Känel, “Low-energy plasma-enhanced chemical vapor deposition for strained si and ge heterostructures and devices,” *Solid State Electron.*, vol. 48, no. 8, pp. 1317–1323, 2004.
- [115] N. P. Barnes and M. S. Piltch, “Temperature-dependent sellmeier coefficients and non-linear optics average power limit for germanium,” *JOSA*, vol. 69, no. 1, pp. 178–180, 1979.
- [116] E. D. Palik, *Handbook of optical constants of solids*. Academic press, 1998, vol. 3.
- [117] L. H. Gabrielli, D. Liu, S. G. Johnson, and M. Lipson, “On-chip transformation optics for multimode waveguide bends,” *Nat. Commun.*, vol. 3, no. 1, pp. 1–6, 2012.
- [118] K. Byron, “Optical waveguide theory,” *Physics Bulletin*, vol. 35, no. 9, p. 391, 1984.
- [119] E. Artacho, F. Ynduráin, B. Pajot, R. Ramírez, C. P. Herrero, L. I. Khirunenko, K. M. Itoh, and E. E. Haller, “Interstitial oxygen in germanium and silicon,” *Phys. Rev. B*, vol. 56, no. 7, p. 3820, 1997.
- [120] I. Yonenaga, M. Nonaka, and N. Fukata, “Interstitial oxygen in gesi alloys,” *Physica B*, vol. 308, pp. 539–541, 2001.
- [121] M. Lorenc and J. Humlicek, “Localized vibrational modes of interstitial oxygen in $\text{si}_x\text{ge}_{1-x}$ alloys,” *Acta Phys. Pol. A*, vol. 94, no. 3, pp. 436–440, 1998.
- [122] M. Nedeljkovic, R. Soref, and G. Z. Mashanovich, “Predictions of free-carrier electroabsorption and electrorefraction in germanium,” *IEEE Photonics J.*, vol. 7, no. 3, pp. 1–14, 2015.
- [123] M. Montesinos-Ballester, V. Vakarin, J. M. Ramírez, Q. Liu, C. Alonso-Ramos, X. Le Roux, J. Frigerio, A. Ballabio, A. Barzaghi, L. Deniel, D. Bouville, L. Vivien, G. Isella, and D. Marris-Morini, “Optical modulation in ge-rich sige waveguides in the mid-infrared wavelength range up to 11 μm ,” *Commun. Mat.*, vol. 1, no. 1, pp. 1–6, 2020.
- [124] F. Payne and J. Lacey, “A theoretical analysis of scattering loss from planar optical waveguides,” *Opt. Quantum Electron.*, vol. 26, no. 10, pp. 977–986, 1994.
- [125] F. Grillot, L. Vivien, S. Laval, and E. Cassan, “Propagation loss in single-mode ultrasmall square silicon-on-insulator optical waveguides,” *J. Lightwave Technol.*, vol. 24, no. 2, p. 891, 2006.

Bibliography

- [126] F. Johnson, “Lattice absorption bands in silicon,” *Proc. Phys. Soc.*, vol. 73, no. 2, p. 265, 1959.
- [127] S. Fray, F. Johnson, J. Quarrington, and N. Williams, “Lattice bands in germanium,” *Proc. Phys. Soc.*, vol. 85, no. 1, p. 153, 1965.
- [128] J. Connes and P. Connes, “Near-infrared planetary spectra by fourier spectroscopy. i. instruments and results,” *JOSA*, vol. 56, no. 7, pp. 896–910, 1966.
- [129] T. Hirschfeld, “Fellgett’s advantage in uv-vis multiplex spectroscopy,” *Appl. Spectrosc.*, vol. 30, no. 1, pp. 68–69, 1976.
- [130] P. R. Griffiths and J. A. De Haseth, *Fourier transform infrared spectrometry*. John Wiley & Sons, 2007, vol. 171.
- [131] E. Le Coarer, S. Blaize, P. Benech, I. Stefanon, A. Morand, G. Léronnel, G. Leblond, P. Kern, J. M. Fedeli, and P. Royer, “Wavelength-scale stationary-wave integrated fourier-transform spectrometry,” *Nat. Photonics*, vol. 1, no. 8, pp. 473–478, 2007.
- [132] X. Nie, E. Ryckeboer, G. Roelkens, and R. Baets, “Cmos-compatible broadband co-propagative stationary fourier transform spectrometer integrated on a silicon nitride photonics platform,” *Opt. Express*, vol. 25, no. 8, pp. A409–A418, 2017.
- [133] A. V. Velasco, P. Cheben, P. J. Bock, A. Delâge, J. H. Schmid, J. Lapointe, S. Janz, M. L. Calvo, D.-X. Xu, M. Florjańczyk, and M. Vachon, “High-resolution fourier-transform spectrometer chip with microphotonic silicon spiral waveguides,” *Opt. Lett.*, vol. 38, no. 5, pp. 706–708, 2013.
- [134] M. Nedeljkovic, A. V. Velasco, A. Z. Khokhar, A. Delâge, P. Cheben, and G. Z. Mashanovich, “Mid-infrared silicon-on-insulator fourier-transform spectrometer chip,” *IEEE Photon. Technol. Lett.*, vol. 28, no. 4, pp. 528–531, 2015.
- [135] T. T. D. Dinh, D. González-Andrade, M. Montesinos-Ballester, L. Deniel, B. Szelag, X. Le Roux, E. Cassan, D. Marris-Morini, L. Vivien, P. Cheben, A. V. Velasco, and C. Alonso-Ramos, “Silicon photonic on-chip spatial heterodyne fourier transform spectrometer exploiting the jacquinots advantage,” *Opt. Lett.*, vol. 46, no. 6, pp. 1341–1344, 2021.
- [136] D. M. Kita, B. Miranda, D. Favela, D. Bono, J. Michon, H. Lin, T. Gu, and J. Hu, “High-performance and scalable on-chip digital fourier transform spectroscopy,” *Nat. Commun.*, vol. 9, no. 1, pp. 1–7, 2018.
- [137] M. C. Souza, A. Grieco, N. C. Frateschi, and Y. Fainman, “Fourier transform spectrometer on silicon with thermo-optic non-linearity and dispersion correction,” *Nat. Commun.*, vol. 9, no. 1, pp. 1–8, 2018.

- [138] D. Pohl, M. R. Escalé, M. Madi, F. Kaufmann, P. Brotzer, A. Sergeyev, B. Guldemann, P. Giaccari, E. Alberti, U. Meier *et al.*, “An integrated broadband spectrometer on thin-film lithium niobate,” *Nat. Photonics*, vol. 14, no. 1, pp. 24–29, 2020.
- [139] M. Florjańczyk, P. Cheben, S. Janz, A. Scott, B. Solheim, and D.-X. Xu, “Multiaperture planar waveguide spectrometer formed by arrayed mach-zehnder interferometers,” *Opt. Express*, vol. 15, no. 26, pp. 18 176–18 189, 2007.
- [140] S. Zheng, H. Cai, Y. D. Gu, L. K. Chin, and A. Q. Liu, “High-resolution on-chip spectrometer with a tunable micro-ring resonator filter,” in *CLEO: Applications and Technology*. Optical Society of America, 2016, pp. AM1J–2.
- [141] S. Zheng, Y. Chen, H. Cai, Y. Gu, and A. Liu, “High-resolution and large-bandwidth on-chip microring resonator cavity-enhanced fourier-transform spectrometer,” in *CLEO: Applications and Technology*. Optical Society of America, 2018, pp. ATh4O–2.
- [142] R. A. Soref, F. De Leonardis, V. M. Passaro, and Y. Fainman, “On-chip digital fourier-transform spectrometer using a thermo-optical michelson grating interferometer,” *J. Lightwave Technol.*, vol. 36, no. 22, pp. 5160–5167, 2018.
- [143] R. A. Soref, F. De Leonardis, and V. M. Passaro, “Scanning spectrometer-on-a-chip using thermo-optical spike-filters or vernier-comb filters,” *J. Lightwave Technol.*, vol. 37, no. 13, pp. 3192–3200, 2019.
- [144] M. Montesinos-Ballester, Q. Liu, V. Vakarín, J. M. Ramírez, C. Alonso-Ramos, X. Le Roux, J. Frigerio, A. Ballabio, E. Talamas, L. Vivien, G. Isella, and D. Marris-Morini, “On-chip fourier-transform spectrometer based on spatial heterodyning tuned by thermo-optic effect,” *Sci. Rep.*, vol. 9, no. 1, pp. 1–10, 2019.
- [145] B. J. Frey, D. B. Leviton, and T. J. Madison, “Temperature-dependent refractive index of silicon and germanium,” in *Optomechanical technologies for Astronomy*, vol. 6273. International Society for Optics and Photonics, 2006, p. 62732J.
- [146] H. Podmore, A. Scott, P. Cheben, A. V. Velasco, J. H. Schmid, M. Vachon, and R. Lee, “Demonstration of a compressive-sensing fourier-transform on-chip spectrometer,” *Opt. Lett.*, vol. 42, no. 7, pp. 1440–1443, 2017.
- [147] S. Höfling, J. Heinrich, J. Reithmaier, A. Forchel, J. Seufert, M. Fischer, and J. Koeth, “Widely tunable single-mode quantum cascade lasers with two monolithically coupled fabry-pérot cavities,” *Applied physics letters*, vol. 89, no. 24, p. 241126, 2006.
- [148] A. Bismuto, R. Terazzi, M. Beck, and J. Faist, “Electrically tunable, high performance quantum cascade laser,” *Applied Physics Letters*, vol. 96, no. 14, p. 141105, 2010.

Bibliography

- [149] B. G. Lee, M. A. Belkin, R. Audet, J. MacArthur, L. Diehl, C. Pflügl, F. Capasso, D. C. Oakley, D. Chapman, A. Napoleone *et al.*, “Widely tunable single-mode quantum cascade laser source for mid-infrared spectroscopy,” *Applied Physics Letters*, vol. 91, no. 23, p. 231101, 2007.
- [150] P. Labeye, A. Koshkinbayeva, M. Dupoy, P. Barritault, O. Lartigue, M. Fournier, J.-M. Fedeli, S. Boutami, S. Garcia, S. Nicoletti, and L. Duraffourg, “Multiplexing photonic devices integrated on a silicon/germanium platform for the mid-infrared,” in *Integrated Optics: Devices, Materials, and Technologies XXI*, vol. 10106. International Society for Optics and Photonics, 2017, p. 101060Y.
- [151] S. Nicoletti, J.-M. Fédéli, M. Fournier, P. Labeye, P. Barritault, A. Marchant, A. Glière, A. Teulle, J.-G. Coutard, and L. Duraffourg, “Miniaturization of mid-ir sensors on si: challenges and perspectives,” in *Silicon Photonics XIV*, vol. 10923. International Society for Optics and Photonics, 2019, p. 109230H.
- [152] W. Zhou, N. Bandyopadhyay, D. Wu, R. McClintock, and M. Razeghi, “Monolithically, widely tunable quantum cascade lasers based on a heterogeneous active region design,” *Sci. Rep.*, vol. 6, no. 1, pp. 1–7, 2016.
- [153] F. Silva, D. Austin, A. Thai, M. Baudisch, M. Hemmer, D. Faccio, A. Couairon, and J. Biegert, “Multi-octave supercontinuum generation from mid-infrared filamentation in a bulk crystal,” *Nat. Commun.*, vol. 3, no. 1, pp. 1–5, 2012.
- [154] C. R. Petersen, U. Møller, I. Kubat, B. Zhou, S. Dupont, J. Ramsay, T. Benson, S. Sujecki, N. Abdel-Moneim, Z. Tang, D. Furniss, A. Seddon, and O. Bang, “Mid-infrared supercontinuum covering the 1.4–13.3 μm molecular fingerprint region using ultra-high na chalcogenide step-index fibre,” *Nat. Photonics*, vol. 8, no. 11, pp. 830–834, 2014.
- [155] Z. Zhao, B. Wu, X. Wang, Z. Pan, Z. Liu, P. Zhang, X. Shen, Q. Nie, S. Dai, and R. Wang, “Mid-infrared supercontinuum covering 2.0–16 μm in a low-loss telluride single-mode fiber,” *Laser Photonics Rev.*, vol. 11, no. 2, p. 1700005, 2017.
- [156] R. K. Lau, M. R. Lamont, A. G. Griffith, Y. Okawachi, M. Lipson, and A. L. Gaeta, “Octave-spanning mid-infrared supercontinuum generation in silicon nanowaveguides,” *Opt. Lett.*, vol. 39, no. 15, pp. 4518–4521, 2014.
- [157] N. Singh, D. D. Hudson, Y. Yu, C. Grillet, S. D. Jackson, A. Casas-Bedoya, A. Read, P. Atanackovic, S. G. Duvall, S. Palomba, B. Luther-Davies, S. Madden, D. J. Moss, and B. J. Eggleton, “Midinfrared supercontinuum generation from 2 to 6 μm in a silicon nanowire,” *Optica*, vol. 2, no. 9, pp. 797–802, 2015.
- [158] C. Lafforgue, S. Guerber, J. M. Ramírez, G. Marcaud, C. Alonso-Ramos, X. Le Roux, D. Marris-Morini, E. Cassan, C. Baudot, F. Boeuf, S. Cremer, S. Monfray, and L. Vivien,

- “Broadband supercontinuum generation in nitrogen-rich silicon nitride waveguides using a 300 mm industrial platform,” *Photonics Res.*, vol. 8, no. 3, pp. 352–358, 2020.
- [159] D. Grassani, E. Tagkoudi, H. Guo, C. Herkommer, F. Yang, T. J. Kippenberg, and C.-S. Brès, “Mid infrared gas spectroscopy using efficient fiber laser driven photonic chip-based supercontinuum,” *Nat. Commun.*, vol. 10, no. 1, pp. 1–8, 2019.
- [160] M. Sinobad, C. Monat, B. Luther-Davies, P. Ma, S. Madden, D. J. Moss, A. Mitchell, D. Allieux, R. Orobtcouk, S. Boutami, J.-M. Hartmann, J.-M. Fedeli, and C. Grillet, “Mid-infrared octave spanning supercontinuum generation to 8.5 μm in silicon-germanium waveguides,” *Optica*, vol. 5, no. 4, pp. 360–366, 2018.
- [161] S. Serna, V. Vakarin, J. M. Ramírez, J. Frigerio, A. Ballabio, X. Le Roux, L. Vivien, G. Isella, E. Cassan, N. Dubreuil, and D. Marris-Morini, “Nonlinear properties of ge-rich $\text{Si}_{1-x}\text{Ge}_x$ materials with different ge concentrations,” *Sci. Rep.*, vol. 7, no. 1, pp. 1–11, 2017.
- [162] A. Demircan and U. Bandelow, “Supercontinuum generation by the modulation instability,” *Opt. Commun.*, vol. 244, no. 1-6, pp. 181–185, 2005.
- [163] J. M. Dudley and J. R. Taylor, *Supercontinuum generation in optical fibers*. Cambridge University Press, 2010.
- [164] R. R. Alfano, *The supercontinuum laser source: the ultimate white light*. Springer, 2016.
- [165] M. Sinobad, A. DellaTorre, R. Armand, B. Luther-Davies, P. Ma, S. Madden, A. Mitchell, D. J. Moss, J.-M. Hartmann, J.-M. Fedeli, C. Monat, and C. Grillet, “Mid-infrared supercontinuum generation in silicon-germanium all-normal dispersion waveguides,” *Opt. Lett.*, vol. 45, no. 18, pp. 5008–5011, 2020.
- [166] H. Saghaei and V. Van, “Broadband mid-infrared supercontinuum generation in dispersion-engineered silicon-on-insulator waveguide,” *JOSA B*, vol. 36, no. 2, pp. A193–A202, 2019.
- [167] N. Badraoui, “Propagation problems of solitons in fibers.”
- [168] S. Roy, S. K. Bhadra, and G. P. Agrawal, “Effects of higher-order dispersion on resonant dispersive waves emitted by solitons,” *Opt. Lett.*, vol. 34, no. 13, pp. 2072–2074, 2009.
- [169] C. Ciret, S.-P. Gorza, C. Husko, G. Roelkens, B. Kuyken, and F. Leo, “Physical origin of higher-order soliton fission in nanophotonic semiconductor waveguides,” *Sci. Rep.*, vol. 8, no. 1, pp. 1–11, 2018.

Bibliography

- [170] I.-W. Hsieh, X. Chen, X. Liu, J. I. Dadap, N. C. Panoiu, C.-Y. Chou, F. Xia, W. M. Green, Y. A. Vlasov, and R. M. Osgood, “Supercontinuum generation in silicon photonic wires,” *Opt. Express*, vol. 15, no. 23, pp. 15 242–15 249, 2007.
- [171] S. Roy, S. K. Bhadra, and G. P. Agrawal, “Dispersive wave generation in supercontinuum process inside nonlinear microstructured fibre,” *Curr. Sci.*, pp. 321–342, 2011.
- [172] R. Driben, A. Yulin, and A. Efimov, “Resonant radiation from oscillating higher order solitons,” *Opt. Express*, vol. 23, no. 15, pp. 19 112–19 117, 2015.
- [173] J. M. Dudley, G. Genty, and S. Coen, “Supercontinuum generation in photonic crystal fiber,” *Rev. Mod. Phys.*, vol. 78, no. 4, p. 1135, 2006.
- [174] A. Cox, A. J. DeWeerd, and J. Linden, “An experiment to measure mie and rayleigh total scattering cross sections,” *Am. J. Phys.*, vol. 70, no. 6, pp. 620–625, 2002.
- [175] J. Hult, “A fourth-order runge–kutta in the interaction picture method for simulating supercontinuum generation in optical fibers,” *J. Lightwave Technol.*, vol. 25, no. 12, pp. 3770–3775, 2007.
- [176] J. Weber and M. Alonso, “Near-band-gap photoluminescence of si-ge alloys,” *Phys. Rev. B*, vol. 40, no. 8, p. 5683, 1989.
- [177] R. Paschotta, “Noise of mode-locked lasers (part i): numerical model,” *Appl. Phys. B*, vol. 79, no. 2, pp. 153–162, 2004.
- [178] A. Ruehl, M. J. Martin, K. C. Cossel, L. Chen, H. McKay, B. Thomas, C. Benko, L. Dong, J. M. Dudley, M. E. Fermann, I. Hartl, and J. Ye, “Ultrabroadband coherent supercontinuum frequency comb,” *Phys. Rev. A*, vol. 84, no. 1, p. 011806, 2011.
- [179] N. Singh, D. Vermulen, A. Ruocco, N. Li, E. Ippen, F. X. Kärtner, and M. R. Watts, “Supercontinuum generation in varying dispersion and birefringent silicon waveguide,” *Opt. Express*, vol. 27, no. 22, pp. 31 698–31 712, 2019.
- [180] J. Wei, C. Ciret, M. Billet, F. Leo, B. Kuyken, and S.-P. Gorza, “Supercontinuum generation assisted by wave trapping in dispersion-managed integrated silicon waveguides,” *Phys. Rev. Appl.*, vol. 14, no. 5, p. 054045, 2020.
- [181] C. Ciret and S.-P. Gorza, “Generation of ultra-broadband coherent supercontinua in tapered and dispersion-managed silicon nanophotonic waveguides,” *JOSA B*, vol. 34, no. 6, pp. 1156–1162, 2017.
- [182] M. Meade, “Advances in lock-in amplifiers,” *J. Phys. E: Sci. Instrum.*, vol. 15, no. 4, p. 395, 1982.

- [183] S. Pirotta, N.-L. Tran, A. Jollivet, G. Biasiol, P. Crozat, J.-M. Manceau, A. Bousseksou, and R. Colombelli, “Fast amplitude modulation up to 1.5 ghz of mid-ir free-space beams at room-temperature,” *Nat. Commun.*, vol. 12, no. 1, pp. 1–6, 2021.
- [184] G. T. Reed, G. Mashanovich, F. Y. Gardes, and D. Thomson, “Silicon optical modulators,” *Nat. Photonics*, vol. 4, no. 8, pp. 518–526, 2010.
- [185] M. Nedeljkovic, R. Soref, and G. Z. Mashanovich, “Free-carrier electrorefraction and electroabsorption modulation predictions for silicon over the 1-14 μm infrared wavelength range,” *IEEE Photonics J.*, vol. 3, no. 6, pp. 1171–1180, 2011.
- [186] T. Li, M. Nedeljkovic, N. Hattasan, W. Cao, Z. Qu, C. G. Littlejohns, J. S. Penades, L. Mastronardi, V. Mittal, D. Benedikovic, D. J. Thomson, F. Y. Gardes, H. Wu, Z. Zhou, and G. Z. Mashanovich, “Ge-on-si modulators operating at mid-infrared wavelengths up to 8 μm ,” *Photonics Res.*, vol. 7, no. 8, pp. 828–836, 2019.
- [187] M. Nedeljkovic, C. G. Littlejohns, A. Z. Khokhar, M. Banakar, W. Cao, J. Soler-Penades, D. T. Tran, F. Y. Gardes, D. J. Thomson, G. T. Reed, H. Wang, and G. Z. Mashanovich, “Silicon-on-insulator free-carrier injection modulators for the mid-infrared,” *Opt. Lett.*, vol. 44, no. 4, pp. 915–918, 2019.
- [188] E. Rosencher and B. Vinter, “Optoélectronique, dunod,” 2002.
- [189] D. GIBBS, “Mckelvey, jp-solid state and semiconductor physics,” 1967.
- [190] R. Braunstein, A. R. Moore, and F. Herman, “Intrinsic optical absorption in germanium-silicon alloys,” *Phys. Rev.*, vol. 109, no. 3, p. 695, 1958.
- [191] I. Institute. (2001) Iofee. [Online]. Available: <http://www.ioffe.ru/SVA/NSM/Semicond/>
- [192] D. T. Stevenson and R. J. Keyes, “Measurements of the recombination velocity at germanium surfaces,” *Physica*, vol. 20, no. 7-12, pp. 1041–1046, 1954.
- [193] L. Shen, N. Healy, C. J. Mitchell, J. S. Penades, M. Nedeljkovic, G. Z. Mashanovich, and A. C. Peacock, “Mid-infrared all-optical modulation in low-loss germanium-on-silicon waveguides,” *Opt. Lett.*, vol. 40, no. 2, pp. 268–271, 2015.
- [194] G. Golan, A. Axelevitch, B. Gorenstein, and V. Manevych, “Hot-probe method for evaluation of impurities concentration in semiconductors,” *Microelectron. J.*, vol. 37, no. 9, pp. 910–915, 2006.
- [195] C.-D. Lien, F. So, and M.-A. Nicolet, “An improved forward iv method for nonideal schottky diodes with high series resistance,” *IEEE Trans. Electron. Devices*, vol. 31, no. 10, pp. 1502–1503, 1984.
- [196] S. Sze, “Physics of semiconductor devices, pp. 103,” 1969.

Bibliography

- [197] H. Nguyen-Van, A. N. Baranov, Z. Loghmari, L. Cerutti, J.-B. Rodriguez, J. Tournet, G. Narcy, G. Boissier, G. Patriarche, M. Bahriz *et al.*, “Quantum cascade lasers grown on silicon,” *Sci. Rep.*, vol. 8, no. 1, pp. 1–8, 2018.



Publication List

This PhD thesis has contributed to the following international peer-reviewed research articles:

1. T. T. D. Dinh, D. González-Andrade, M. Montesinos-Ballester, L. Deniel, B. Szlag, X. Le Roux, E. Cassan, D. Marris-Morini, L. Vivien, P. Cheben, A. Velasco, and C. Alonso-Ramos, "Silicon photonic on-chip spatial heterodyne Fourier transform spectrometer exploiting the Jacquinot's advantage," *Opt. Lett.*, vol. 46, no. 6, p. 1341, 2021.
2. M. Montesinos-Ballester, C. Lafforgue, J. Frigerio, A. Ballabio, V. Vakarín, Q. Liu, J. M. Ramírez, X. Le Roux, D. Bouville, A. Barzaghi, C. Alonso-Ramos, L. Vivien, G. Isella, and D. Marris-Morini, "On-chip mid-infrared supercontinuum generation from 3 to 13 μm wavelength," *ACS Photonics*, vol. 7, no. 12, p. 3423, 2020.
3. M. Montesinos-Ballester, V. Vakarín, Q. Liu, X. Le Roux, J. Frigerio, A. Ballabio, A. Barzaghi, C. Alonso-Ramos, L. Vivien, G. Isella, and D. Marris-Morini, "Ge-rich graded SiGe waveguides and interferometers from 5 to 11 μm wavelength range," *Opt. Express*, vol. 28, no. 9, p. 12771, 2020.
4. M. Montesinos-Ballester, V. Vakarín, J. M. Ramírez, Q. Liu, C. Alonso-Ramos, X. Le Roux, J. Frigerio, A. Ballabio, A. Barzaghi, L. Deniel, D. Bouville, L. Vivien, G. Isella, and D. Marris-Morini, "Optical modulation in Ge-rich SiGe waveguides in the mid-infrared wavelength range up to 11 μm ," *Commu. Mater.*, vol. 1, p. 6, 2020.
5. M. Montesinos-Ballester, Q. Liu, V. Vakarín, J. M. Ramírez, C. Alonso-Ramos, X. Le Roux, J. Frigerio, A. Ballabio, E. Talamas, L. Vivien, G. Isella, and D. Marris-Morini, "On-chip Fourier-transform spectrometer based on spatial heterodyning tuned by thermo-optic effect," *Sci. Rep.*, vol. 9, p. 14633, 2019.
6. D. Marris-Morini, V. Vakarín, J. M. Ramírez, Q. Liu, A. Ballabio, J. Frigerio, M. Montesinos, C. Alonso-Ramos, X. Le Roux, S. Serna, D. Benedikovic, D. Chrastina, L. Vivien, and G. Isella, "Germanium-based integrated photonics from near to mid-infrared applications," *Nanophotonics*, vol. 7, no. 11, p. 1781, 2018 (Invited).

Titre: Circuits photoniques SiGe exploitant l'optique non linéaire et les effets électro-optiques dans l'infrarouge moyen

Mots clés: infrarouge moyen, circuits photoniques intégrés, silicium

Résumé: La gamme spectrale de l'infrarouge moyen (MIR), communément définie entre 2 et 20 μm de longueur d'onde), a suscité un grand intérêt au cours des deux dernières décennies en raison de ses caractéristiques uniques pour la détection et la sécurité. En particulier, la «fingerprint region» (de 3 à 13 μm de longueur d'onde) permet une détection à haute sensibilité de la plupart des molécules, grâce à leurs modes de vibration fondamentaux qui conduisent à des lignes d'absorption spécifiques dans cette gamme spectrale.

Le travail que je présente ici s'appuie sur les démonstrations précédentes de dispositifs passifs basés sur des plateformes SiGe à gradient d'indice riche en Ge pour aller plus loin dans la mise en oeuvre d'un système photonique MIR complet sur puce. À cette fin, j'ai développé et optimisé de nouveaux processus de fabrication dans deux salles blanches, pour ensuite aborder la conception, la modélisation et la caractérisation de trois fonctionnalités manquantes basées sur l'accord thermique, les effets non linéaires et électro-optiques, montrant un fonctionnement à large bande dans la gamme MIR.

Tout d'abord, j'ai démontré des pertes de propagation inférieures à 4.6 dB/cm de 5 à 11 μm de longueur d'onde, qui sont compatibles avec la plupart des applications MIR intégrées. J'ai également confirmé les performances large bande des plateformes SiGe à gradient d'indice par la caractérisation de deux dispositifs MZI. J'ai ensuite développé une approche de spectromètre intégré basée sur une configuration hétérodyne spatiale, dans laquelle j'ai

ajusté thermiquement le déséquilibre du délai de propagation d'un réseau MZI pour surmonter le compromis classique entre la résolution, la largeur de bande opérationnelle et le nombre de structures interférométriques requises. Ces résultats facilitent le développement de spectromètres compacts et robustes fonctionnant dans le MIR. Ensuite, j'ai démontré une génération de supercontinuum qui s'étend de 3 à 13 μm de longueur d'onde dans un guide d'onde SiGe graduel de 5.5 mm de long. Cette démonstration fournit une lumière MIR large bande et cohérente au moyen d'un seul dispositif, ouvrant ainsi des perspectives passionnantes pour la détection simultanée de plusieurs molécules. Enfin, j'ai évalué expérimentalement l'effet de la dispersion du plasma de porteurs libres dans une large gamme MIR, pour ensuite démontrer un modulateur électro-optique intégré fonctionnant de 6.4 à 10.7 μm de longueur d'onde et montrant jusqu'à 1.3 dB de rapport d'extinction en régime d'injection de courant et 225 MHz de bande passante de modulation en déplétion de porteuse. Ce dispositif est essentiel pour mettre en oeuvre la détection synchrone et ainsi améliorer significativement la sensibilité des systèmes de détection intégrés.

En conclusion, cette thèse a abordé avec succès le développement de guides d'ondes intégrés et de trois fonctionnalités associées manquantes dans la littérature opérant dans une large bande spectrale MIR. Par conséquent, ce travail ouvre des perspectives excitantes dans une grande gamme d'applications à fort impact, et ouvre la voie au développement à long terme de systèmes de capteurs multimoléculaires compacts

Title: SiGe photonics circuits exploiting nonlinear optics and electro-optic effects in the mid-infrared

Keywords: mid-infrared, integrated photonic circuits, silicon

Abstract: The mid-infrared (MIR) spectral range, commonly defined from 2 to 20 μm wavelengths, has attracted a great interest over the past two decades due to its unique characteristics for detection and security purposes. In particular, the fingerprint region (from 3 to 13 μm wavelength) allows a high sensitivity detection of most of molecules due to fundamental molecular vibrational modes that lead to specific absorption lines in this spectral range.

The work I present here leverages on previous passive devices demonstrations based on Ge-rich graded-index SiGe platforms to go a step further towards the implementation of a complete on-chip MIR photonics system. To that end, I developed and optimized new fabrication processes in two clean-room facilities, and also addressed the design, modeling and characterization of three missing functionalities based on thermal-tuning, nonlinear and electro-optic effects, showing a broadband operation in the MIR range.

First, I demonstrated propagation losses lower than 4.6 dB/cm from 5 to 11 μm wavelength, which are compatible with most of integrated MIR applications. I also confirmed the broadband performance of graded-index SiGe platforms by the characterization of two MZI devices. Then, I discussed an integrated spectrometer approach based on a spatial-heterodyne configuration, in which I thermally tuned the path-delay unbalance of a MZI

array to overcome the classical tradeoff between resolution, operational bandwidth, and number of interferometric structures required. These results facilitate the development of compact and robust spectrometers operating in the MIR fingerprint region. Next, I demonstrated a supercontinuum generation that spans from 3 to 13 μm wavelength in a 5.5 mm long graded-SiGe waveguide. This demonstration provides a broadband and coherent MIR light by mean of a single device, opening exciting perspectives for the simultaneous detection of multiple molecules. Finally, I experimentally evaluated the free-carrier plasma dispersion effect in a wide MIR range, to later demonstrate an integrated electro-optical modulator operating from 6.4 to 10.7 μm wavelength, showing up to 1.3 dB extinction ratio in current injection regime and 225 MHz modulation bandwidth in carrier depletion. This device is essential to implement synchronous detection and thus significantly improve the sensitivity of integrated detection systems.

In conclusion, this thesis has successfully addressed the development of integrated waveguides and three associated functionalities missing in the literature operating in a wide MIR spectral band. Therefore, this work opens exciting perspectives in a plethora of high-impact applications, paving the way towards the long-term development of compact multi-molecular sensor systems.